UNIVERSITÀ DEGLI STUDI DI NAPOLI FEDERICO II

CHEMISTRY SCIENCE DOCTORATE

XXX CYCLE

Hierarchical self-assembly and crystallization across length scales of block-copolymers from metallorganic catalysis

TUTORS:
Prof. Claudio De Rosa
Prof. Finizia Auriemma

SUPERVISOR:
Prof. Michele Pavone

CANDIDATE:
Claudia Cioce

UNIVERSITÀ DEGLI STUDI DI NAPOLI FEDERICO II

DOTTORATO DI RICERCA IN

SCIENZE CHIMICHE

XXX CICLO

Organizzazione strutturale gerarchica in copolimeri a blocchi semicristallini guidata da self-assembly e cristallizzazione

TUTORI:
Prof. Claudio De Rosa
Prof. Finizia Auriemma

RELATORE:
Prof. Michele Pavone

CANDIDATA:
Claudia Cioce

SUMMARY

Block copolymers (BCPs) are important materials in which the properties of distinct polymer chains are combined or ‘‘alloyed’’ to yield materials with hybrid properties. The solid state organization of the BCPs is extremely interesting. In fact, when chemical incompatibility between the different blocks in the melt occurs, a phase separation is observed, leading to the formation of different domains with geometries and dimensions depending on the volume fraction and the molecular mass of the blocks, respectively.[1,2] In fully amorphous BCPs, the solid state organization is driven by the self-assembly in the melt: the same morphology developing in the melt is observed, since it is trapped by vitrification (i.e. by cooling the system below its glass transition temperature, T_g). In the case of semicrystalline BCPs, in which at least a crystallizable block is present, the final structure that develops in the solid state is not predictable as it is the result of the competition between microphase separation and crystallization.[3] The interplay between these two processes results in morphological richness and kinetic complexity. The intrinsic possibility of semicrystalline BCPs of being able to create a “structure within a structure” thanks to development of a hierarchical morphology of nanoelements which results from coupling the self-assembly occurring in the melt, and the confined crystallization of a block within the phase separated nanodomains, makes these complex systems extremely interesting.

The present work aims at exploring the self-assembly properties of a novel class of semicrystalline BCPs, i.e. block copolymers having crystallizable blocks made of stereoregular polyolefins or polyethylene obtained with living insertion metallorganic catalysts. The interest towards these systems is driven by the possibility of creating thermally resistant nanostructured materials with improved mechanical properties thanks to the presence of a high temperature melting crystalline phase. In particular, in this work a structural and morphological characterization at different length scales, of different classes of polyolefin-based semicrystalline block-copolymers obtained through metallorganic catalysis has been performed. The physical properties of these BCPS have been also analysed. The first class of polyolefin-based semicrystalline BCPs consists of di-block copolymers in which a crystalline block made of polyethylene (PE) or isotactic polypropylene (iPP) is covalently linked to different amorphous or slightly crystalline blocks made of ethylene-based or propylene-based copolymers.

The second class of semicrystalline BCPs studied, consists of multi-block (MBCP) ethylene-norbornene copolymers obtained via chain shuttling polymerization (CSP).

1. Polyolefin-based semicrystalline di-block copolymers:

The first series of PE-based semicrystalline di-block copolymers consists of BCPs wherein the PE block is linked to an amorphous rubbery poly(1,5-hexadiene) (PHD) block (**PE-*b*-PHD**). Samples with different relative length of the blocks have been synthesized by using a fluorinated bis(phenoxyimine) Ti complex. In particular, the mass fraction of the PE block (w_{PE}) in the different samples varies from 0.27 to 0.79.

The structural characterization reveals that these samples crystallize in the orthorhombic form of PE, with an overall crystallinity index (x_c) decreasing with decreasing the mass fraction of the PE block (w_{PE}). When the crystallinity index is normalized for the mass fraction of the PE block, similar values among the different samples are observed.

The DSC analysis shows that the melting of the PE crystals occurs in a temperature range of 100-120°C, slightly lower than the typical melting temperature of high density PE (HDPE) ($T_m \approx 130$°C), because of the presence of 1,5-hexadiene units within the PE block. The crystallization temperature of the PE crystals varies in the range 84-97°C. The glass transition temperature of the PE-*b*-PHD BCPs, relative to the amorphous PHD block, occurs at -19°C.

The SAXS/WAXS analysis as a function of temperature reveals that when PE-*b*-PHD BCPs are melted, a non-homogeneous phase is obtained because of the scarce chemical affinity of the two blocks and the high molecular mass of the BCPs. This phase-separated melt is still present at high temperatures, i.e. 280°C, with correlation distances of the different domains varying in the range 28-60nm depending on the relative block length of the two blocks. These data also indicate that the crystallization of PE occurs from a microphase separated melt. The values of the average periodicity of the PE lamellar domains vary in the range 16-20nm. By calculating the one-dimensional normalized (self-) correlation function of electron density fluctuations, further information about the structural organization in the crystalline PE block have been obtained, namely the thickness of the amorphous (l_a) and crystalline (l_c) layers of the stacked arrays of lamellar PE crystals. The values of l_c vary in the range 3.6–7nm, those of l_a in the range of

10.7-14.2nm. In particular, it has been observed that the higher the molecular mass of PE blocks, the shorter the thickness of lamellar crystals. We speculate that this is due to the different morphologies occurring in the melt, and therefore to the different geometries of the crystallisable PE domains.

The mechanical characterization of the PE-*b*-PHD BCPs reveals that these samples span different mechanical behaviors depending on the relative block length of the PE and PHD blocks. In fact, by changing the sole mass fraction of one of the two blocks, it is possible to design materials with tailored properties ranging from those of stiff plastomers (similar to PE) at high w_{PE} values, to those of materials with high flexibility and ductility with partial elastomeric properties at lower w_{PE} values. In addition, it is worth reminding that good thermal resistance is also guaranteed thanks to the presence of the crystalline PE block.

The study of the structural changes occurring in these BCPs during tensile deformation shows that upon deformation, gradual orientation of PE crystals in the stretching direction is obtained, and that the longer the relative length of PE blocks, the higher the degree of orientation achieved by PE crystals. In fact, the increase of the relative length of PE blocks implies the decrease of the volume fraction of PHD amorphous blocks which, indeed perform a damping effect, transmitting the stress to the crystals less efficiently.

A second type of PE-based semicrystalline BCP shows the PE block linked to an amorphous block made of a random copolymer of ethylene and vinyl cyclohexene (P(E-*co*-VCH)). One **PE-*b*-P(E-*co*-VCH)** BCP sample with w_{PE}=0.59 has been synthesized, by using a C_s-symmetric pyridylamidohafnium dimethyl complex. The structural and thermal characterizations show that the sample crystallizes in the orthorhombic form of PE, with melting and crystallization temperatures of the PE crystals equal to 133°C and 120°C, respectively. It is worth mentioning that in this case, according to the adopted synthetic procedure, no VCH units are present in the PE block. Therefore, the PE block shows a high melting temperature, comparable to that of HDPE.

The SAXS/WAXS analysis as a function of temperature shows that when PE-*b*-P(E-*co*-VCH) BCP is melted, no inhomogeneities are observed, thus indicating either that phase separation does not occur, or that the periodicity of the phase separated domains of PE and P(E-*co*-VCH) incompatible blocks occurs at higher length scales than those accessible in our

measurements, i.e. >90nm. The analysis also shows that the lamellar crystals of PE of characteristic size equal to ≈8 nm are organized in stacks with a periodicity of ≈60nm, separated by amorphous domains of thickness equal to ≈56 nm.

The mechanical behavior of the PE-*b*-P(E-*co*-VCH) BCP has been compared with that of an amorphous P(E-*co*-VCH) random copolymer synthesized with the same catalyst and in the same reaction conditions as the P(E-*co*-VCH) block in the PE-*b*-P(E-*co*-VCH) BCP. The random copolymer shows the typical behavior of an amorphous, rubbery material with a low value of the Young's modulus, no yield point and high deformation at break. The mechanical characterization of the PE-*b*-P(E-*co*-VCH) BCP shows that by linking the crystalline PE block to the amorphous P(E-*co*-VCH) block, a rather rigid material is obtained, with a higher value of the Young's modulus, a lower value of the deformation at break and high strain hardening with respect to the amorphous P(E-*co*-VCH) random copolymer.

The series of the iPP-based semicrystalline di-block copolymers consist in BCPs wherein the iPP block is linked to an amorphous block made of a random copolymer of propylene and vinyl cyclohexene (P(P-*co*-VCH)), or to an amorphous block made of a random copolymer of propylene and 1-octadecene P(P-*co*-C18). Samples of **iPP-*b*-P(P-*co*-VCH)** and **iPP-*b*-P(P-*co*-C18)** BCPs differing in the relative lengths of the blocks have been synthesized with the same C_s-symmetric pyridylamidohafnium dimethyl complex used for the synthesis of the PE-*b*-P(E-*co*-VCH) BCP. The structural and thermal characterizations of these samples reveal that both classes of BCPs mainly crystallize in the α form of iPP, with melting and crystallization temperatures of the iPP blocks of 133°C and ≈95°C, respectively. In the case of iPP-*b*-P(P-*co*-C18) BCPs, additional PE-like crystallinity is observed when cooling the samples below room temperature, due to the crystallization of the side chains of the C18 units in the P(P-*co*-C18) block.

SAXS/WAXS analysis as a function of temperature reveals that for both the iPP-based BCPs classes, either a homogeneous melt is obtained or a possible phase separation due to chemical incompatibility between the two different blocks occurs at higher length scales than those accessible in our measurements. The crystallization of the iPP block from the melt results in lamellar stacks having a periodicity of ≈12-14nm, comparable to what observed for a iPP homopolymer synthesized with the same catalyst and in the

same reaction conditions as the iPP-based BCPs. Moreover, for the iPP-*b*-P(P-*co*-VCH) BCPs, a lamellar thickness of ≈11nm and an amorphous layer thickness of ≈3nm have also been evaluated by calculating the self-correlation function from the SAXS data recorded at 25°C.
In the case of the iPP-*b*-P(P-*co*-C18) BCPs, low temperature SAXS analysis reveals that the PE-like crystallites formed by the C18 units arrange in crystalline domains having a periodicity of ≈5nm.

The mechanical behavior of the iPP-based BCPs has been compared to that of the iPP homopolymer. In the case of the iPP-*b*-P(P-*co*-VCH) BCPs, having w_{iPP}=0.67 and 0.78, lower ductility, but similar values of the stress at the yield and break point with respect to iPP homopolymer are observed. In the case of the iPP-*b*-P(P-*co*-C18) BCPs having w_{iPP}=0.31 and 0.44, similar ductility, but lower values of the stress at yield and break point are observed with respect to the iPP homopolymer. These data indicate that when an amorphous block is linked to the crystalline iPP block, the mechanical behavior is changed. With high values of w_{iPP} the mechanical resistance due to the iPP block prevails, but a decrease of the ductility is observed, while at lower w_{iPP}, high ductility is achieved at the expense of the mechanical stress and rigidity.

The study of the structural changes occurring in these BCPs during tensile deformation reveals that while in the iPP homopolymer a complete transformation of the α form crystals into the mesophase is observed, in the case of the iPP-*b*-P(P-*co*-VCH) and iPP-*b*-P(P-*co*-C18) BCPs, only partial transformation of the α form crystals into mesophase occurs. As in the case of PE-*b*-PHD BCPs, this behavior is due to the presence of an amorphous random copolymer block, linked to the crystalline block, that performs a damping effect, so that the stress level experienced by amorphous tie chains is transmitted to the crystals less efficiently.

In the case of iPP-*b*-P(P-*co*-C18) BCPs, stretching experiments performed at low temperature while recording X-ray diffraction data reveal that the drawing of the samples induces the orientation of the PE-like crystallites formed by the C18 units with their chain axes perpendicular to the drawing direction. However, above a threshold value of deformation, which depends on the concentration of the C18 units in the P(P-*co*-C18) block, the PE-crystals are destroyed by effect of tension, probably because the mean distance between the side chains increases to an extent that they are not able to organize in PE-like crystallites anymore.

It is well known that iPP homopolymer, by effect of fast cooling to 0°C of the melt (quench), crystallizes in the mesomorphic form which shows interesting mechanical properties.[4] The ability of iPP-based BCPs to undergo the same structural change observed for iPP homopolymer quenched from the melt, has been studied. In particular, for both iPP-based BCPs classes, the quenching of the samples from the melt down to 0°C induces the crystallization of the iPP block into the mesomorphic form, thus indicating that the presence of the amorphous block does not influences the properties of the iPP block.

The mechanical behavior of the iPP-*b*-P(P-*co*-C18) BCPs crystallized in iPP mesophase are similar in terms of ductility to that of the same samples crystallized in α form, but strain hardening is observed, thus leading to higher values of the stress at break. This mechanical behavior is probably dictated by the different morphology developing in the samples quenched from the melt, which may somehow influence the mechanisms of deformation and fracture. In fact, the study of the morphology by polarized optical microscopy (POM) shows that all the samples slowly crystallized from the melt are characterized by the presence of birefringent lamellar aggregates of not well defined shape, and dimensions 5-10μm, which are relative to the iPP block crystallized in α form. When the iPP block crystallizes in the mesomorphic form, a different morphology is observed. POM images do not show birefringence. However, AFM analysis reveals a nodular morphology with aggregates having dimensions ≈90-100nm, resembling that of the iPP homopolymer, in the case of samples with high values of w_{iPP}. For BCP samples with low w_{iPP} values the nodular morphology is not observed. This may be due to the presence of a high amount of the amorphous block that prevents the formation of nodular aggregates. We speculate that for BCPs with low w_{iPP} values, isolated mesomorphic aggregates are formed, which are not well discernible, by AFM analysis, from the surrounding amorphous matrix in which they are embedded.

The interest towards PE-based and iPP-based BCPs relies on the possibility of coupling crystalline blocks having high melting temperatures with amorphous blocks, to yield peculiar properties and therefore materials suitable for tailored application. For instance, the PE-*b*-PHD BCPs wherein the PE crystalline block is linked to a rubbery PHD block are interesting systems in which the final mechanical properties may be finely tuned by varying the relative block length of the two blocks, while preserving the high

melting temperature due to the PE block. Moreover, since the polymerization of 1,5-hexadiene leads to the formation of vinyl groups as side chains, functional BCPs may be obtained. In this way, materials for advanced applications can be obtained, as a result of the combination of the good mechanical properties provided by the main chain of the BCP and the specific properties provided by the functional side chains. Similar interest relies on the PE-*b*-P(E-*co*-VCH) BCPs and of the iPP-P(P-*co*-VCH) BCPs, because of the possibility to have high melting temperature functional thermoplastic materials. In fact, on one side the PE and iPP blocks show high melting temperatures (≈130°C), on the other side the VCH units in the amorphous blocks bear pendant reactive moieties that provide easy access to a wide range of functionalities. Moreover, in the case of the iPP-based BCPs, further interest arises from the polymorphism of iPP. In fact, by choosing the proper crystallization conditions, it is possible to control the type of crystallinity in order to further tailor the properties of the final materials.
In the case of the iPP-*b*-P(P-*co*-C18) BCPs the interest relies on the possibility of combining the peculiar structural and thermal properties of the iPP and P(P-*co*-C18) blocks: on one hand the high melting temperature iPP block that can possibly crystallize in different crystalline forms depending on the thermal processing, on the other hand the P(P-*co*-C18) block that whilst amorphous at room temperature, can develop crystallinity when cooled below room temperature due to the crystallization of the side chains of the 1-octadecene (C18) units.

2. Semicrystalline ethylene/norbornene-based multi-block copolymers:

The ethylene-norbornene multi-block copolymers (E/N MBCPs) have been synthesized via chain shuttling polymerization (CSP).[5] Chain shuttling mechanism is realized when two catalysts, which produce chemically different polymeric chains, are put in the same reaction environment together with a chain-transfer agent (CTA) that is able to transfer the growing chain from one catalyst to another, providing a multi-block architecture in the resultant polymeric chain.[6]

The E/N MBCPs were synthesized with two *ansa*-metallocene Zr-based catalysts, labelled B1 and A3, having different selectivity toward norbornene incorporation, and diethyl zinc ($Zn(Et)_2$) as chain transfer agent (CTA). The structure and properties of the E/N MBCPs are compared with those of reference samples, obtained by copolymerization of E and N with the sole

catalyst A3 and the sole catalyst B1. MBCPs and the reference samples were prepared by fixing the N/E feed ratio equal to 1.3, and using different concentrations of CTA. The copolymer prepared with the sole catalyst A3 is amorphous and includes a major amount of N units. The copolymers prepared with the sole catalyst B1 includes a lower content of N units, and shows a small degree of crystallinity, due to presence of long ethylene sequences melting at ≈120°C, and crystallizing from the melt at ≈115°C. Also the E/N MBCPs show a slight crystallinity due to the presence of long ethylene sequences, with melting and crystallization temperatures similar to those of the reference sample from catalyst B1, and glass transition temperatures intermediate between those of the reference samples from A3 and B1 catalysts.

SAXS/WAXS analysis as a function of temperature reveals that the E/N MBCPs and the reference sample synthesized with the sole B1 catalyst, show heterogeneities in the melt due to the presence of different chain sequences having different N contents and different microstructures. The size of the different domains forming in the melt is in the range 7-10.5nm. On the contrary, the melt of the reference sample synthesized with the sole A3 catalyst is homogeneous, confirming the homogeneous distribution of E and N along the polymer chain. The present results do not clearly indicate that the samples obtained with A3+B1 in presence of the CTA are truly multi-block copolymers. Therefore, the effect of CTA in presence of the *ansa*-metallocene catalysts A3+B1 in the copolymerization of E and N to multi-block architectures remains an open question.

The interest towards this class of materials obtained through CSP strategy relies on the possibility to obtain multi-blocks copolymers where different microstructures are bonded together in an alternate sequence to form a polymer chain. The advantage of obtaining such molecular architectures is that the different properties of the diverse microstructural blocks are combined in a single polymer chain showing hybrid properties. In fact, in this particular case of ethylene/norbornene copolymers, CSP may allow to obtain a component rich in ethylene and a component rich in norbornene, bonded in an alternate multi-block sequence resulting in polymers showing, at the same time, elastic properties and rigidity typical of P(E-*co*-N) copolymers.

References

1. Bates, F.S.; Fredrickson, G.H. *Annu. Rev. Phys. Chem.* **1990**, *41*, 525.
2. Fasolka, M.J.; Mayes, A.M. *Annu. Rev. Mater. Res.* **2001,** *31*, 323.
3. a) I.W. Hamley; *The Physics of Block Copolymers*, New York: Oxford University Press, **1998**; b) I.W. Hamley; *Development in Block Copolymer Science and Technology*, John Wiley & Sons. Chichester, **2005**.
4. C. De Rosa, F. Auriemma, R. Di Girolamo, O. Ruiz de Ballesteros; *J. Polym. Sci., Part B: Polym. Phys.*, **2014**, *52*, 677.
5. D. Sidari, *Cyclolefin Copolymers via Chain Shuttling*, XXVII cycle Doctorate in Chemical Sciences, Università Degli Studi Di Milano Bicocca, **2015**.
6. D.J. Arriola, E.M. Carnahan, P.D. Hustad, R.L. Kuhlman, T.T. Wenzel; *Science*, **2006**, *312*, 714.

INDEX

CHAPTER 2

Isotactic polypropylene-based semicrystalline di-block copolymers

INTRODUCTION

Semicrystalline block copolymers

Block copolymers (BCPs) are important materials in which the properties of distinct polymer chains are combined or ‘‘alloyed’’ to yield materials with hybrid properties. A block copolymer macromolecule consists of two or more polymer chains attached at their ends by chemical links. The simplest molecular architecture is obtained by connecting a block of A units with a block of B units, both having uniform length (Figure 1 a). Immiscibility between A and B blocks in the melt may induce a segregation into different domains with geometries and dimensions depending on the volume fraction and on the molecular mass of the blocks, respectively.[1,2] Moreover, since all domains have uniform size (varying from a few to hundred nanometers), they can arrange in a regular and periodic manner. For an A-B di-block copolymer, depending on the volume fraction of the blocks, the self-assembly process may lead to cubic arrays of spheres, hexagonal arrays of cylinders, bicontinuous cubic phases or lamellae (Figure 1 b).

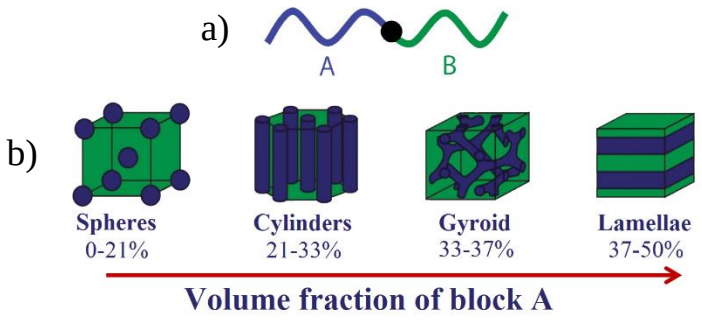

Figure 1 a) Scheme of an A-B di-block copolymer; **b)** Nanostructures formed by self-assembly in di-block copolymers.

The present work is aimed at studying a novel class of polyolefin-based block copolymers i.e. block copolymers having crystallizable blocks made of stereoregular polyolefins. The self-assembly of stereoregular polyolefin based BCPs leads to the formation nanostructures characterized by high melting temperature domains.

The techniques generally used for BCPs’ synthesis are: cationic, anionic and controlled radical polymerizations.[3] These methods ensure a consecutive

enchainment of monomer units without the occurrence of termination events (*living polymerization*) thus providing a precise control over the molecular weight of the resultant polymers and the possibility to synthesize polymers with a wide range of architectures. In particular, anionic and controlled radical polymerization techniques are well established methods for the preparation of BCPs containing blocks made of polystyrene, poly(1,4-butadiene), polyoxyethylene, polyoxypropylene, poly(acrylates), poly(ε-caprolactone) and poly(d,l-lactide), whereas sequential living cationic polymerization is especially used to prepare BCPs containing vinyl ether or polyisobutilene blocks. Ring opening metathesis polymerization (ROMP) is exploited to build blocks from cyclic olefins, e.g. for the synthesis of polynorbornenes. BCPs containing polyethylene blocks have been typically obtained by anionic polymerization of poly(1,4-butadiene) followed by hydrogenation, since ethylene polymerizes too slowly with carbanionic initiators. Hydrogenation of polydiene blocks synthesized by anionic polymerization techniques is also used to obtain blocks consisting of head-to-head polypropylene, poly(ethyl ethylene), poly(ethylene-*co*-propylene).

BCPs containing stereoregular polyolefin blocks cannot be synthesized with these methodologies and, because of the difficulty of the synthetic strategy, have been subject of a small number of studies. Only in the last decade, the living synthesis of these systems has emerged thanks to the development of metal-based insertion polymerization methods which are able to ensure a high stereochemical control in olefins polymerization.[4] Depending on the ligand framework of the catalyst and the nature of the coordination metal center, linear or branched polyethylene, atactic, isotactic and syndiotactic poly(α-olefins), poly(cycloolefins), random copolymers of ethylene with branched α-olefins, can now be efficiently synthesized in a living manner. Examples of catalyst precursors for the living and stereocontrolled polymerization of 1-alkene monomers are shown in Figure 2. In particular, the bis(phenoxyimine) titanium complex (**1**) activated with methylaluminoxane (MAO) produces BCPs containing highly stereoregular syndiotactic polypropylene (sPP) and/or polyethylene (PE) blocks;[5] the phenoxyketimine titanium complex (**2**) activated with MAO produces BCPs with stereoregular isotactic polypropylene (iPP) blocks;[6] the chiral, C_2-symmetric, nickel diimine complex (**3**) activated with MAO produces BCPs containing iPP blocks (at low temperatures) and regioirregular polypropylene (PP) blocks at higher temperatures;[7] the ammine-phenolate zirconium

complex (**4**) (Bn standing for the benzyl group) activated with $B(C_6F_5)_3$ produces BCPs containing highly isotactic poly(1-hexene) or poly(1-octene), iPP and PE blocks;[8] C_s-symmetric pyridylamidohafnium dimethyl complex (**5**) activated with $B(C_6F_5)_3$ produces iPP, PE and isotactic poly(4-methyl-1-pentene) (iP4MP) blocks[9].

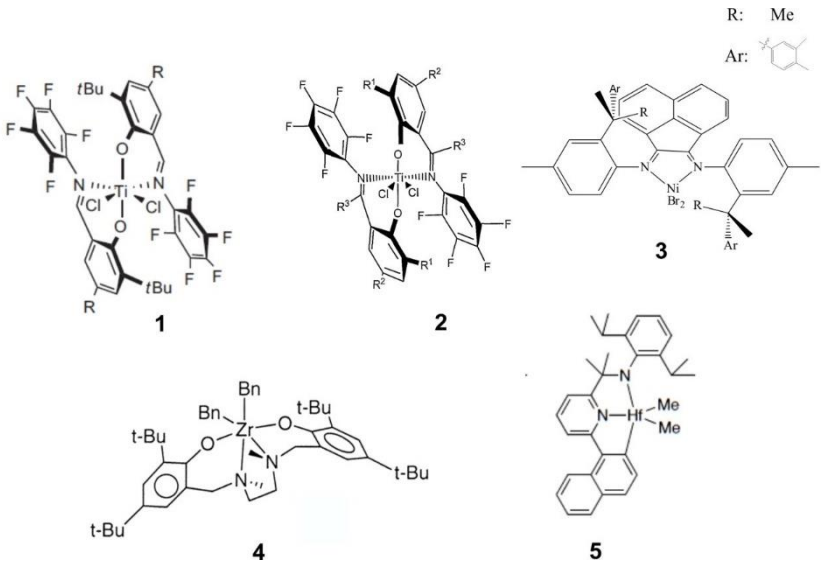

Figure 2 Catalyst precursors for the synthesis, through living polymerization, of BCPs containing tactic poly(1-alkene) blocks.

The important achievement is that polyolefin blocks with relatively high melting temperature are obtained. Depending on the degree of crystallinity, melting temperatures up to 150°C are observed in the case of sPP and up to 160°C in the case of iPP. Also for PE blocks higher degree of crystallinity and higher melting temperatures are achieved in comparison to those obtained via hydrogenation of poly(1,4-butadiene).

There are several aspects that make semicrystalline polyolefin-based BCPs extremely attractive. From the practical point of view, it is worth mentioning that two-thirds of all thermoplastic polymers are polyolefins, because of their versatile thermal, mechanical and optical properties, excellent melt processability, good chemical and solvent resistance and last but not least, the low-cost of monomers and production process.

As an example, in the field of thermoplastic elastomers, there are great research efforts aimed at developing cost-effective methods for the synthesis of polyolefin-based BCPs containing hard and soft blocks that ensure an overall elastic behavior in a wide range of temperatures. This goal has been

recently achieved thanks to the aforementioned living polymerization catalysts which are able to synthesize hard crystalline blocks, such as PE, iPP, sPP, and soft rubbery blocks, such as regioirregular polypropylene, random copolymers of ethylene with propene or other olefins, and thus lead to systems having, at the same time, high melting and low glass transition temperatures that allow them to be used in high-performance applications so far inaccessible to polyolefins.[4]

Other important applications of polyolefin BCPs containing highly crystalline blocks may be envisaged in their use as compatibilizer in polymer blending, in nanotechnological applications to build nanofibers for the setting up of reinforced polymer composites, template structures for lithography, photonic crystals to bound and guide the light and to construct highly selective nanocatalysts.[4]

From the point of view of basic research, semicrystalline BCPs are interesting systems *per se*. Indeed, the phase behavior of BCPs has been well understood only in the case of amorphous systems.[3]

In these systems, if the chemical incompatibility between the different blocks is sufficiently high, a phase separated melt is originated and, in the solid state, the same morphology developing in the melt is observed, since it is trapped by vitrification (i.e. by cooling the system below its glass transition temperature, T_g). To a first approximation, the phase behavior of di-blocks BCPs may be represented in terms of two variables within a morphology diagram, the variables being the reduced parameter χN and the volume fraction of one of the blocks, *f*. In particular, χ is the Flory-Huggins interaction parameter, which reflects the interaction energy between the different monomers. It is assumed to be inversely proportional to the temperature, according to the empirical relation $\chi = A/T + B$. N is the degree of polymerization of the copolymer. In other words, the parameter χN is a measure of the degree of incompatibility of the blocks, the higher its value, the higher the degree of incompatibility. For a given molecular architecture, an increase of χN may be achieved by increasing the chemical incompatibility of the blocks, decreasing the temperature or increasing the degree of polymerization *N*. The schematic phase diagram of amorphous di-block BCPs is shown in Figure 3 as an example. For sufficient low χN values, i.e. at high temperatures, the polymer chains are homogeneously mixed as in any polymer melt (*disordered melt*). When χN is higher than a critical value, χN_{ODT} (where ODT stands for Order-Disorder Transition), i.e. by lowering the temperature

below a critical value, T_{ODT}, the BCP separates in a periodically ordered microstructure. The geometry of the ordered structure that develops at $\chi N > \chi N_{ODT}$ (typically $\chi N_{ODT}=10$) depends mainly on the BCP composition (indicated by f).

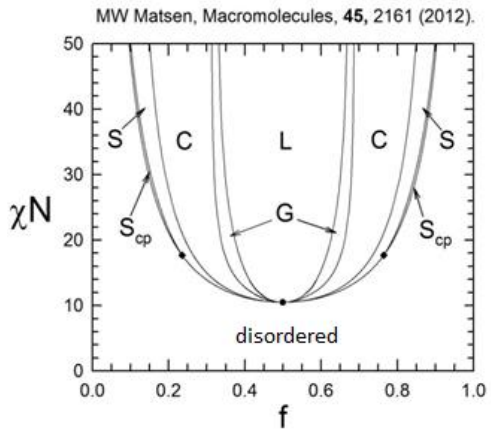

Figure 3 Schematic phase diagram of amorphous BCPs.

In the case of semicrystalline BCPs, in which at least a crystallizable block is present, the final structure that develops in the solid state is not predictable as it is the result of the competition between microphase separation and crystallization.[3] The interplay between these two processes results in morphological richness and kinetic complexity.

Generally, the energy of crystallization, of order of 100J/g, is significantly larger than the energy associated with microphase separation, ≈1J/g. Crystallization may occur either from a homogeneous melt, or from a microphase separated (heterogeneous) melt. In the latter case, the prevailing of the crystallization may induce structural changes in the morphology of the microphase separated melt or, even further, completely disrupt it. There are at least three types of crystallization modes for semicrystalline BCPs occurring in the bulk from heterogeneous melts: *break-out, confined* and *templated crystallization*. *Break-out* describes situations where a nanostructure generated by microphase separation is destroyed, and replaced by a lamellar morphology eventually giving rise to spherulitic superstructures similar to those formed from a homogeneous melt. Breakout generally occurs when the melt is weakly segregated.[10-13]

The nanostructured morphology may be retained for BCPs with high and medium values of χN. In particular, *confined crystallization*[14] may occur for

BCPs in the high segregation limit. It entails nucleation events and growth of crystals in the individual crystallizable microdomains, with no bridge between them. Also in the *templated crystallization*,[14-16] the phase separated microdomain nanostructure of the melt is retained. However, due to the lower segregation strength, occasional bridging events may occur, generating formation of multiple crystalline microdomains from a single nucleus, and consequent acceleration of the crystallization kinetics. In general, templated and confined crystallizations are directional processes, where the crystallization is preferred for the crystals growing unhindered with the fastest growth direction parallel to the long axis of the microdomain.

In the weak segregation limit, a fourth type of crystallization, addressed as *pass-through* crystallization, has been also described, entailing preservation of the overall domain morphology of the melt, no crystal orientation, and growth of the crystallites nucleated in confined domains, with branches *passing-through* the complementary domains.[17]

In general, in the weak segregation limit (low χN values), the crystallization behavior of BCPs containing crystallizable blocks is controlled by the BCP constitution (length and number of blocks) and key temperatures, such as the crystallization temperature T_c of the crystalline blocks, the glass transition temperature T_g of the amorphous blocks and the order-disorder transition temperature T_{ODT} of the BCP. In particular, confining the attention to di-block copolymers in which a crystallizable block is covalently linked to an amorphous block, and the crystallization takes place from a non-homogeneous melt ($T_{ODT} < T_c$), if the crystallizable block is the major component, break-out crystallization is expected to occur regardless of the T_g value of the amorphous blocks.[18,19] In BCPs in which the crystalline block is the minor component, instead, templated crystallization is expected to occur if the crystallization temperature is lower than T_g ($T_{ODT} > T_g > T_c$), whereas crystallization may either be templated or occur by disrupting the domain morphology of the melt (break-out) for BCPs crystallizing at temperatures higher than T_g ($T_{ODT} > T_c > T_g$). The crystallization mode in this latter case depends on the BCP segregation strength, and the relative length of the blocks. Notably, templated and confined crystallizations occurring in lamellar, cylindrical and spherical domains, are processes involving crystallization in 1-, 2- or 3 dimensions.[20]

Regardless of melt morphology, in the case of break-out crystallization, a lamellar morphology is often obtained, where lamellar stacks are organized in

spherulitic entities, as shown in the case of poly(ε-caprolactone)-*b*-poly(butadiene),[15] polyethylene-*b*-poly(ethylene-*alt*-propylene),[13] polyethylene-*b*-poly(ethylethylene)[21] and poly(ethyleneoxide)-*b*-polyisoprene.[22.]

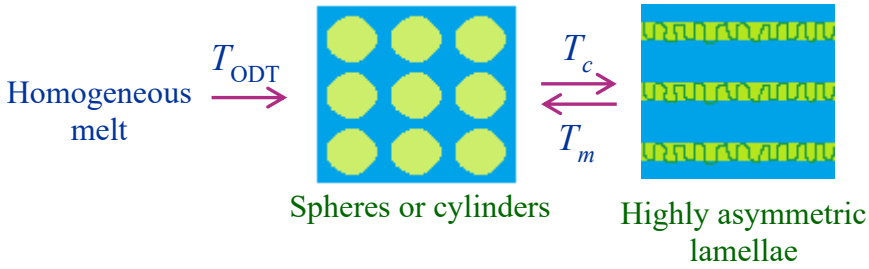

Figure 4 Scheme for the reversible phase transition between highly asymmetric lamellar structure and sphere or cylinder structure switched by crystallization and melting.

A possible model for the lamellar structure developing from break-out crystallization (Figure 4) may imply large differences in thickness between the two lamellar microdomains formed by the crystalline and the amorphous blocks, resulting in a high asymmetry. Therefore, whereas the morphology of amorphous di-block copolymers depends on the volume fraction of the blocks and a lamellar structure is formed for symmetric BCPs characterized by volume fractions of the blocks in the range 30-70%, in crystalline BCPs the lamellar morphology may take place upon break-out crystallization even in cases where morphologies of hexagonally packed cylinders or close packed spheres are expected to occur. This is due to the high enthalpy change involved in the crystallization process, overwhelming the small gain in free energy associated with the formation by self-assembly of ordered nanostructures.[3]

In the case of confined crystallization, the morphology of the BCP before and after crystallization is the same, as schematically depicted in Figure 5.

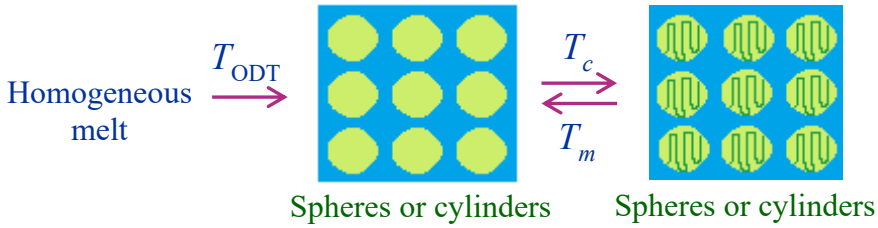

Figure 5 Scheme for confined crystallization of BCPs.

It is worth noting that the crystallization mode of a block in a BCP (templated/confined vs. break out) may be controlled by the maximum temperature achieved in the melt and the cooling rate, resulting in increased number of possibilities to tailor the final morphology. Since the properties of BCPs depend not only on the chemical constitution of the blocks but also on the morphology, also the properties can be tailored by controlling the crystallization mode. As an example, the Young modulus, the mechanical strength and the viscoelastic properties of a semicrystalline BCP characterized by the confined crystallization of blocks in phase separated domains are expected to be completely different from those of the same BCPs obtained by break-out crystallization.

A further mode for controlling the crystallization mode of BCPs and therefore also the morphology and the properties may be achieved also by adjusting the molecular mass. In fact, since the segregation strength of BCPs depends on the product χN, confined crystallization may occur even for BCPs constituted by blocks of similar chemical affinity, entailing low χ values, by simply increasing the molecular mass (proportional to N). This entails that under the same crystallization conditions break-out crystallization may be switched to confined or templated crystallization, in BCPs having similar relative length of the blocks but higher molecular mass.

Objective of the thesis work

The intrinsic possibility of semicrystalline BCPs of being able to create a “structure within a structure” thanks to development of a hierarchical morphology of nanoelements which results from coupling the self-assembly occurring in the melt, and the confined crystallization of a block within the phase separated nanodomains, makes these complex systems extremely interesting.

The present work aims at exploring the self-assembling properties of a novel class of semicrystalline BCPs, i.e. block copolymers having crystallizable blocks made of stereoregular polyolefins obtained with living insertion metallorganic catalysts. The interest towards these systems is driven by the possibility of creating thermally resistant nanostructured materials with improved mechanical properties thanks to the presence of a high temperature melting crystalline phase. Moreover, the possibility to switch from confined/templated crystallization to break out crystallization offers a unique opportunity to control the properties of these BCPs by simply adjusting the crystallization conditions. In particular, the effect of coupling polyolefin-based blocks having different mechanical properties, on the BCPs global properties, is studied in detail for systems in which highly rigid blocks, such as polyethylene or isotactic polypropylene, are covalently linked to highly flexible blocks, such as propene-, ethylene-based copolymers. The study of the mechanical properties of these systems allows identifying new classes of materials with tailorable properties.

In particular, in this work the structural and morphological characterizations on different length scales, as well as the study of the physical properties of different classes of polyolefin-based semicrystalline BCPs obtained through metallorganic catalysis have been performed. The first class of polyolefin-based semicrystalline BCPs consists of di-block copolymers in which a crystalline block made of polyethylene (PE) or isotactic polypropylene (iPP) is covalently linked to different amorphous or slightly crystalline blocks. The second class of polyolefin-based semicrystalline BCPs consists of multi-block ethylene-norbornene copolymers obtained via chain shuttling polymerization.

The study performed on semicrystalline BCPs belonging to the first class, PE-based semicrystalline BCPs and iPP-based semicrystalline BCPs is

reported in Chapter 1 and 2 respectively. The BCPs taken into account are listed below:

- Polyethylene-*block*-poly(1,5-hexadiene) (PE-*b*-PHD).
- Polyethylene-*block*-poly(ethylene-*co*-vinylcyclohexene) (PE-*b*-(E-*co*-VCH));
- Isotactic polypropylene-*block*-poly(propene-*co*-vinylcyclohexene) (iPP-*b*-(P-*co*-VCH));
- Isotactic polypropylene-*block*-poly(propene-*co*-1-octadecene) (iPP-*b*-(P-*co*-C18));

For each type of BCP, several samples with different volume fractions of the blocks have been studied.

The study performed on the multi-block ethylene-norbornene copolymers is reported in Chapter 3.

CHAPTER 1

Polyethylene-based semicrystalline di-block copolymers

1.1 Polyethylene-*b*-poly(1,5-hexadiene) di-block copolymers PE-*b*-PHD

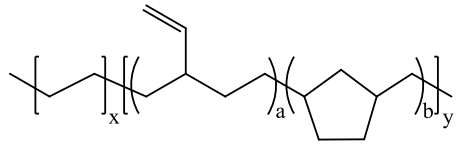

Figure 1.1 Structure of the polyethylene-*block*-poly(1,5-hexadiene) di-block copolymers.

Semicrystalline di-block copolymers having a crystalline block made of polyethylene (PE) and an amorphous block made of poly(1,5-hexadiene) (PHD) (Figure 1.1) have been studied.
Due to the difference in the molecular structure between the PE block and the PHD block, phase segregation in the melt is expected for these BCPs. The coupling of a crystalline block of PE having a high melting temperature with a rubbery block of PHD, makes these BCPs extremely interesting for their mechanical properties. Moreover, since the polymerization of 1,5-hexadiene leads to the formation of vinyl groups as side chains, functional BCPs may be obtained. In fact, the side reactive moieties provide easy access to a wide range of functionalities through chemical modifications. In this way, materials for advanced applications can be obtained, as a result of the combination of the good mechanical properties provided by the main BCP chain and the specific properties provided by the functional side chains.

1.1.1 Materials and methods

Samples of PE-*b*-PHD BCPs were synthesized by living polymerization with a fluorinated bis(phenoxyimine) Ti complex activated with methylaluminoxane (MAO). The synthetic procedure, consisting in the sequential synthesis of the PHD and PE blocks, is shown in Scheme 1.1.
The polymerization of 1,5-hexadiene by the fluorinated bis(phenoxyimine) Ti catalyst results in a copolymer containing not only the expected comonomeric

units of methylene-1,3-cyclopentane (MCP) but also 3-vinyl tetramethylene (VTM) units.[23]

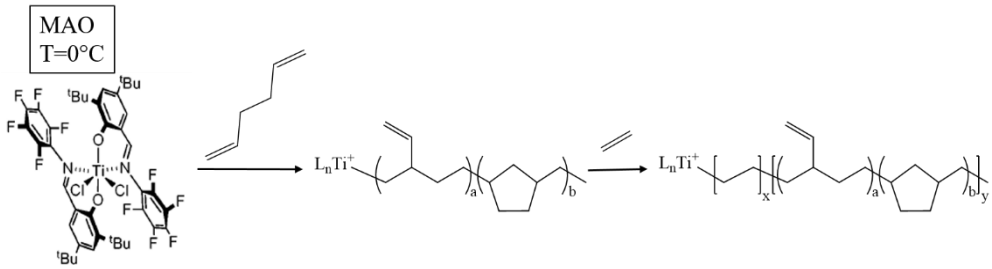

Scheme 1.1 Structure of the fluorinated bis(phenoxyimine) titanium complex used as catalyst for the preparation of the PE-*b*-PHD BCPs and scheme of the sequential polymerization procedure.

A PHD homopolymer and several samples with different mass fractions (w_{PHD}) of the PHD block were synthesized.

In particular, for the synthesis of the PHD homopolymer, a 200mL Lab-Crest® pressure reaction vessel (Andrews Glass) equipped with a magnetic stir bar was charged with d-PMAO, toluene and 1,5-hexadiene. The flask was equilibrated at 0°C and the catalyst solution in toluene was added via a gas-tight syringe. After 20min, the reaction was carefully quenched with a methanol/HCl solution and the polymer was precipitated in copious methanol/HCl, filtered, washed with methanol, and then dried in vacuum to constant weight.

For the synthesis of the PE-*b*-PHD BCPs, a 200mL Lab-Crest® pressure reaction vessel (Andrews Glass) equipped with a magnetic stir bar was charged with a desired amount of d-PMAO, toluene and 1,5-hexadiene. The reactor was the equilibrated at 0°C and the catalyst solution in toluene was then added via a gas-tight syringe. After 10-30min, depending on the desired molecular weight, an aliquot of the polymerization medium (PHD block) was removed for GPC analysis and stored in a vial equipped with a magnetic stir-bar; this aliquot was quenched by addition of methanol. The second stage of the polymerization was allowed to proceed under a constant feed of ethylene. After the desired time had elapsed (1-2min depending on the desired poly(ethylene-*co*-1,5-hexadiene) block length), the polymerization was quenched by the addition of a methanol/HCl solution. The polymer was precipitated in copious methanol, collected via filtration, and dried to constant weight in vacuum at 25 °C.

The molecular characteristics of the samples are shown in Table 1.1.

Table 1.1 Total molecular mass ($M_{n\ TOT}$), molecular mass of the PHD block ($M_{n\ PHD}$) and of the PE block ($M_{n\ PE}$), polydispersity index (M_w/M_n), mass fraction (w_{PHD}) and volume fraction (f_{PHD}) of the PHD block, mass fraction of the PE block (w_{PE}) and concentration of the 3-vinyl tetramethylene units.

SAMPLE	M_n[a] TOT (Kg/mol)	M_n[a] PHD (Kg/mol)	M_n[b] PE (Kg/mol)	$\frac{M_w}{M_n}$[a]	w[c] PHD	f[d] PHD	w[c] PE	VTM[e] (mol%)
RDG-1-13	78.4	-	-	1.34	1	1	0	33
RDG-1-26	146.4	106.7	39.7	1.53	0.73	0.74	0.27	16
RDG-1-20	175.7	113.4	62.3	1.33	0.64	0.66	0.36	18
RDG-1-29	203.5	114.3	89.2	1.29	0.56	0.58	0.44	-
RDG-1-36	232.6	68.8	163.8	1.29	0.30	0.31	0.70	10
RDG-1-15	466.4	97.6	368.8	1.45	0.21	0.22	0.79	3.9

a evaluated from GPC analysis; **b** calculated from $M_{n\ TOT}$ and $M_{n\ PHD}$ as $M_{n\ PE}=M_{n\ TOT}-M_{n\ PHD}$; **c** calculated as $M_{n\ PHD}/M_{n\ TOT}$; **d** calculated from the molecular masses $M_{n\ PHD}$ and $M_{n\ PE}$ and the densities of PHD (0.940 g/cm^3) and PE (0.996 g/cm^3) as $f_{PHD}=(M_{n\ PHD}/0.940)/((M_{n\ PHD}/0.940)+(M_{n\ PE}/0.996))$. The density of the PHD has been experimentally determined by flotation (see Appendix 3) using a PHD homopolymer synthesized with the same Ti-based catalyst used for the synthesis of the PE-*b*-PHD copolymers; the density of PE is the theoretical value for a sample having 100% crystallinity; **e** evaluated from ^{1}H-NMR as described in Appendix 1 section 1; in the case of the sample RDG-1-13, it indicates the amount of VTM units in PHD homopolymer, while in the case of the BCPs samples (from RDG-1-26 to RDG-1-15) it indicates the amount of VTM in the whole BCP molecule.

The characterization of the samples has been performed on as prepared samples and/or on compression moulded samples. The compression molded samples have been prepared by heating the as prepared samples at ≈140°C under a press at very low pressure, keeping it at this temperature for 5 min, and cooling it down to room temperature at a cooling rate of about 15°C/min.

The thermal characterization of the samples has been carried out by calorimetric measurements performed with a differential scanning calorimeter (DSC-822 by Mettler Toledo) in a flowing N_2 atmosphere and at a scanning rate of 10°C/min.

The structural characterization has been carried out by X-ray scattering technique using a Ni-filtered CuKα radiation. Wide angle X-ray scattering (WAXS) analysis has been performed on unoriented (powder) and oriented (fiber) samples using an automatic diffractometer (Philips) and a cylindrical camera equipped with a MS (MultiSensitive) phosphor storage imaging plate (Fujifilm), respectively. Small angle X-ray scattering (SAXS) analysis has been performed with a Kratky compact camera working in line collimation geometry (SAXSess by Anton Paar) equipped with a MS imaging plate (Fujifilm) and conventional X-ray source. The apparatus allows collecting simultaneously WAXS and SAXS data. The WAXS/SAXS data recorded on MS imaging plates have been read with a digital imaging reader Cyclone Plus (Perkin Elmer) and then processed with SAXSquant2D and SAXSquant1D software by Anton Paar to obtain the calculated (desmeared) SAXS profiles in point collimation geometry.

Mechanical characterization has been performed at room temperature with a universal mechanical tester (Zwicky by Zwick Roell) following the standard test method for tensile properties of thin plastic sheets, ASTM D882-83. The mechanical parameters reported for each sample are averaged results from at least five independent experiments.

Morphological characterization has been performed with a Transmission Electron Microscope (TEM) Philips EM 208S operating at 100kV on thin films (thickness <100nm) of the polymer material.

1.1.2 WAXS and thermal analyses of as prepared and compression molded samples

X-ray powder diffraction profiles of as prepared samples (A) and of compression molded samples (A') of the PHD homopolymer synthesized with the same catalyst and in the same experimental conditions as PE-*b*-PHD block copolymers, and of the PE-*b*-PHD BCPs with different blocks lengths are shown in Figure 1.2. The X-ray powder diffraction profiles of as prepared and compression molded samples of the PHD homopolymer (curves a of Figure 1.2 A and A' respectively), show an amorphous halo centered at 2θ=18°. X-ray powder diffraction profiles of as prepared and compression moulded samples of the PE-*b*-PHD BCPs (curves b-f in Figure 1.2 A and A' respectively), show Bragg peaks at 2θ≈21° and 2θ≈24°, corresponding to the 110 and 200 reflections of the PE blocks in the orthorhombic form, overlaying the amorphous halo of the PE amorphous phase and of the amorphous PHD block. The values of the crystallinity index of the PE-*b*-PHD BCPs increase with increasing the PE mass fraction (Table 1.2), but after normalization for the weight fraction of the PE blocks, become more similar among the different samples.

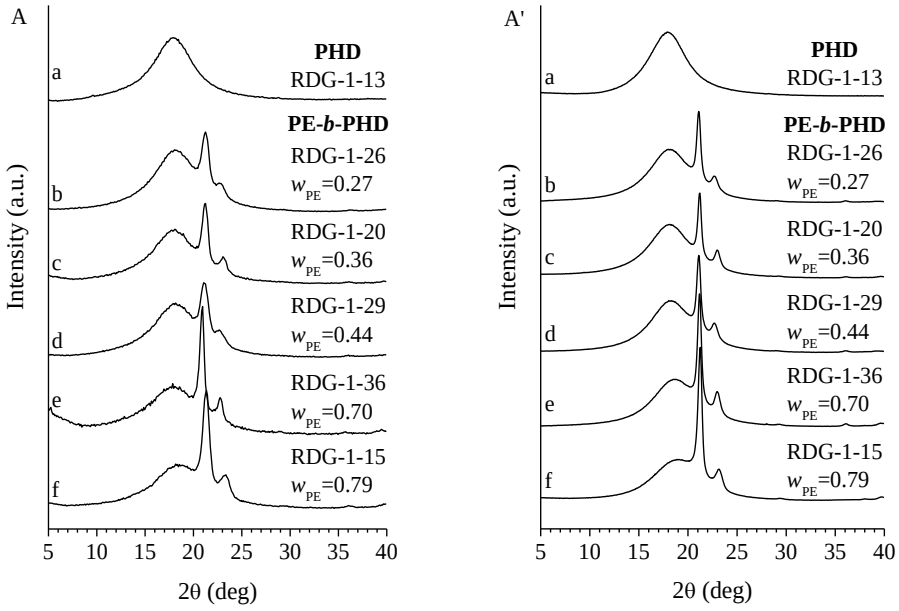

Figure 1.2 X-ray powder diffraction profiles of as prepared (A) and compression molded (A') samples of PHD homopolymer (a) and of PE-*b*-PHD block copolymers (b-f).

Table 1.2 Mass fraction of the PHD (w_{PHD}) and PE (w_{PE}) block and degree of crystallinity of the as prepared ($x_{c\,TOT}$ a.p., $x_{c\,PE}$ ap) and compression moulded ($x_{c\,TOT}$ c.m., $x_{c\,PE}$ cm) samples, relative to the whole sample (subscript TOT) and to the sole PE block (subscript PE).

SAMPLE	w_{PHD}	w_{PE}	$x_{c\,TOT}$ **a.p. (%)**	$x_{c\,TOT}$ **c.m. (%)**	$x_{c\,PE}$ **a.p.=** $x_{c\,TOT}$ **a.p.**/w_{PE} **(%)**	$x_{c\,PE}$ **c.m.=** $x_{c\,TOT}$ **c.m.**/w_{PE} **(%)**
RDG-1-13	1	0	0	0	0	0
RDG-1-26	0.73	0.27	9	11	33	41
RDG-1-20	0.64	0.36	17	12	47	33
RDG-1-29	0.56	0.44	18	16	41	36
RDG-1-36	0.30	0.70	28	21	40	30
RDG-1-15	0.21	0.79	27	27	34	34

DSC thermograms of the as prepared and compression moulded samples of the PHD homopolymer and PE-*b*-PHD BCPs are shown in Figure 1.3 and Figure 1.4 respectively. The DSC thermograms of PHD homopolymer (curves a of Figure 1.3 and 1.4), show an inflection point relative to the glass transition at -19°C, confirming that it is amorphous. DSC heating thermograms of the crystalline PE-*b*-PHD BCPs (curves b-f of Figure 1.3 A, C and 1.4 A, C) show that the melting peak of PE crystals occurs at temperatures in the range 100-120°C, which are lower than the typical melting temperature of high density PE (HDPE) ($T_m \approx 130$°C). This indicates that since the synthesis of PE blocks follows that of the PHD blocks in the sequential approach, the chains of the PE blocks contain a fraction of comonomeric units due to the enchainment of unreacted 1,5-hexadiene molecules which are left in the reaction medium. In the cooling step, the DSC thermograms of the BCP samples (curves b-f of Figure 1.3 B and 1.4 B), show an exothermic peak in the range of T=84-97°C due to the crystallization of the PE. The glass transition relative to the PHD blocks at -19°C is also observed in the DSC thermograms of the BCPs (curves b-f in Figure 1.3 and 1.4). The relevant thermal parameters extracted from DSC analysis are reported in Table 1.3 and 1.4 for the as prepared and compression molded samples respectively.

Table 1.3 Mass fraction of the PHD (w_{PHD}) and PE (w_{PE}) block, melting temperature and melting enthalpy recorded during the first (T_m^I, ΔH_m^I) and second (T_m^{II}, ΔH_m^{II}) heating, crystallization temperature and crystallization enthalpy (T_c, ΔH_c), glass transition temperature (T_g) of as prepared samples of the PHD homopolymer and of PE-*b*-PHD BCPs.

SAMPLE	w_{PHD}	w_{PE}	T_m^I (°C)	ΔH_m^I (J/g)	T_m^{II} (°C)	ΔH_m^{II} (J/g)	T_c (°C)	ΔH_c (J/g)	T_g (°C)
RDG-1-13	1	0	-	-	-	-	-	-	-19
RDG-1-26	0.73	0.27	105	-32.2	107	-21.3	82	25.6	-22
RDG-1-20	0.64	0.36	112	-39.5	108	-31.0	89	32.20	-19
RDG-1-29	0.56	0.44	107	-27.9	103	-20.6	85	22.6	-18
RDG-1-36	0.30	0.70	114	-65.0	108	-47.3	91	44.2	-21
RDG-1-15	0.21	0.79	119	-96.6	108	52.5	91	56.7	-22

Table 1.4 Mass fraction of the PHD (w_{PHD}) and PE (w_{PE}) block, melting temperature and melting enthalpy recorded during the first (T_m^I, ΔH_m^I) and second (T_m^{II}, ΔH_m^{II}) heating, crystallization temperature and crystallization enthalpy (T_c, ΔH_c), glass transition temperature (T_g) of compression molded samples of the PHD homopolymer and of PE-*b*-PHD BCPs.

SAMPLE	w_{PHD}	w_{PE}	T_m^I (°C)	ΔH_m^I (J/g)	T_m^{II} (°C)	ΔH_m^{II} (J/g)	T_c (°C)	ΔH_c (J/g)	T_g (°C)
RDG-1-13	1	0	-	-	-	-	-	-	-18
RDG-1-26	0.73	0.27	105	-23.9	106	-25.5	84	31.4	-18
RDG-1-20	0.64	0.36	108	-33.8	108	-34.4	91	35.6	-19
RDG-1-29	0.56	0.44	104	-30.9	104	-28.6	86	33.1	-19
RDG-1-36	0.30	0.70	108	-56.8	109	-58.8	92	63.1	-19
RDG-1-15	0.21	0.79	110	-63.4	110	-65.3	97	68.4	-21

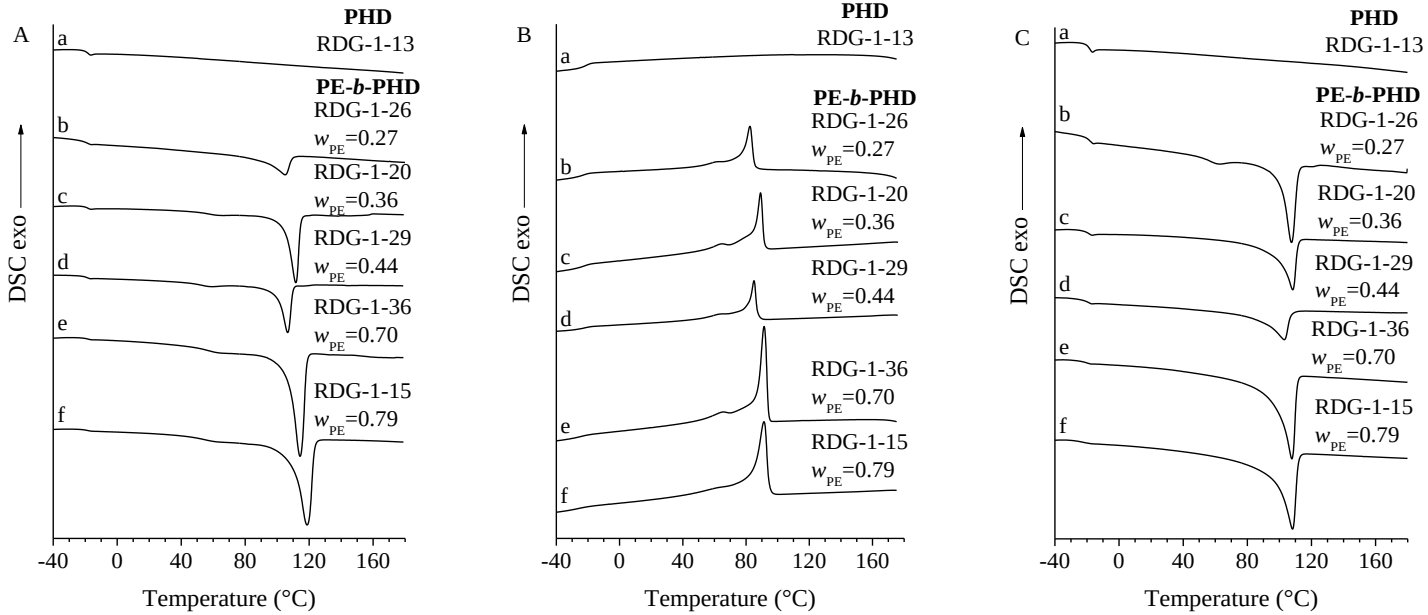

Figure 1.3 DSC thermograms recorded during heating (A), successive cooling (B) and second heating (C) of as prepared samples of PHD homopolymer (a) and of PE-*b*-PHD BCPs (b-f).

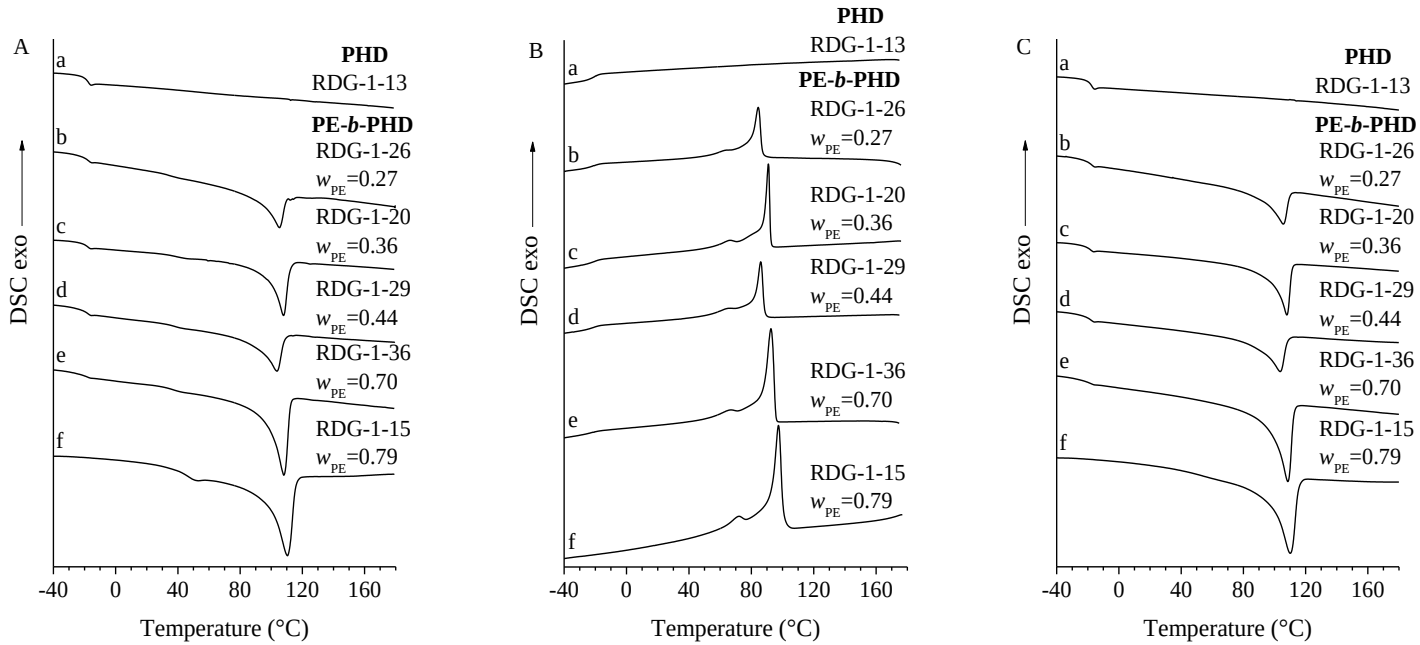

Figure 1.4 DSC thermograms recorded during heating (A), successive cooling (B) and second heating (C) of compression molded samples of PHD homopolymer (a) and of PE-*b*-PHD BCPs (b-f).

1.1.3 SAXS/WAXS analysis as a function of temperature

Samples of the PE-*b*-PHD BCPs have been also analyzed by SAXS and WAXS measurements, as a function of temperature. Data were collected on melt cooled samples, obtained by compression molding. WAXS and SAXS data were collected simultaneously, step-wise, in the temperature range 25-180°C (or up to 240-280°C) in a heating/cooling run. Room temperature measurements were extended also to the PHD homopolymer. Data are shown in Figure 1.5–1.10. For BCP samples, the SAXS intensity profiles corrected for the Lorentz factor are also reported.

The SAXS profile of the PHD homopolymer recorded at 25°C (Figure 1.5) shows a q^{-4} decay in all the sampled angular range, in agreement with its amorphous nature.

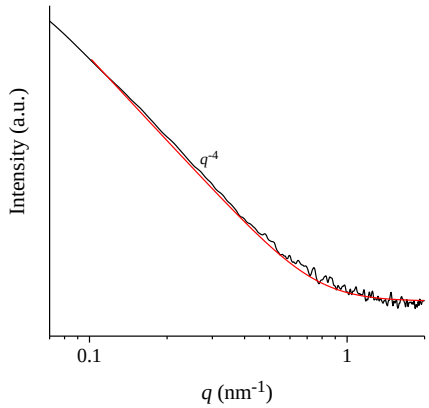

Figure 1.5 SAXS intensity profile of the PHD homopolymer RDG-1-13, recorded at 25°C.

The SAXS profiles of PE-*b*-PHD BCPs in the melt (180°C) show inflection points at q less than 0.2 nm^{-1} (curve b of Figure 1.6 A-1.10 A) which remain also at 240° or 280°C (Figure 1.6 A'-1.8 A' and 1.10 A'). With decreasing the temperature, starting from the onset of crystallization at ≈90°C (curves e-g of Figure 1.6 A-1.10 A) a second inflection at q higher than 0.2 nm^{-1} superimposes the first one, indicating that crystallization of PE occurs from a microphase separated melt. Whether crystallization of PE is a confined (directional) process, or it involves breakout or passthrough crystallization, cannot be established from SAXS data of Figure 1.6-1.10. We just observe a non-homogeneous melt, up to 240° or 280°C due to the scarce chemical affinity of the two blocks and the high molecular mass of the BCPs, (higher than 146Kg/mol). That is, the order-disorder transition of the BCPs RDG-1-

26, RDG-1-29 and RDG-1-15 (w_{PE}=0.27, 0.44, 0.79, respectively) is higher than 280°C, regardless of relative length of the blocks. The melting/crystallization of the samples inferred from SAXS profiles collected as a function of the temperature is confirmed by the appearance/disappearance of the Bragg reflection at 2θ≈21° and 24° in the WAXS profiles of Figure 1.6 B-1.10 B.

The correlation distance of heterogeneities in the melt, and the average periodicity of the PE lamellar domains may be roughly calculated from the position $q_{inflection}$ of the inflection point in the SAXS profiles of Figure 1.6 A-1.10 A, and/or the position q_{max} of the correlation peak in the corresponding Lorentz corrected profiles of Figure 1.6 C-1.10 C using the Bragg law. The so determined values are reported in Table 1.5.

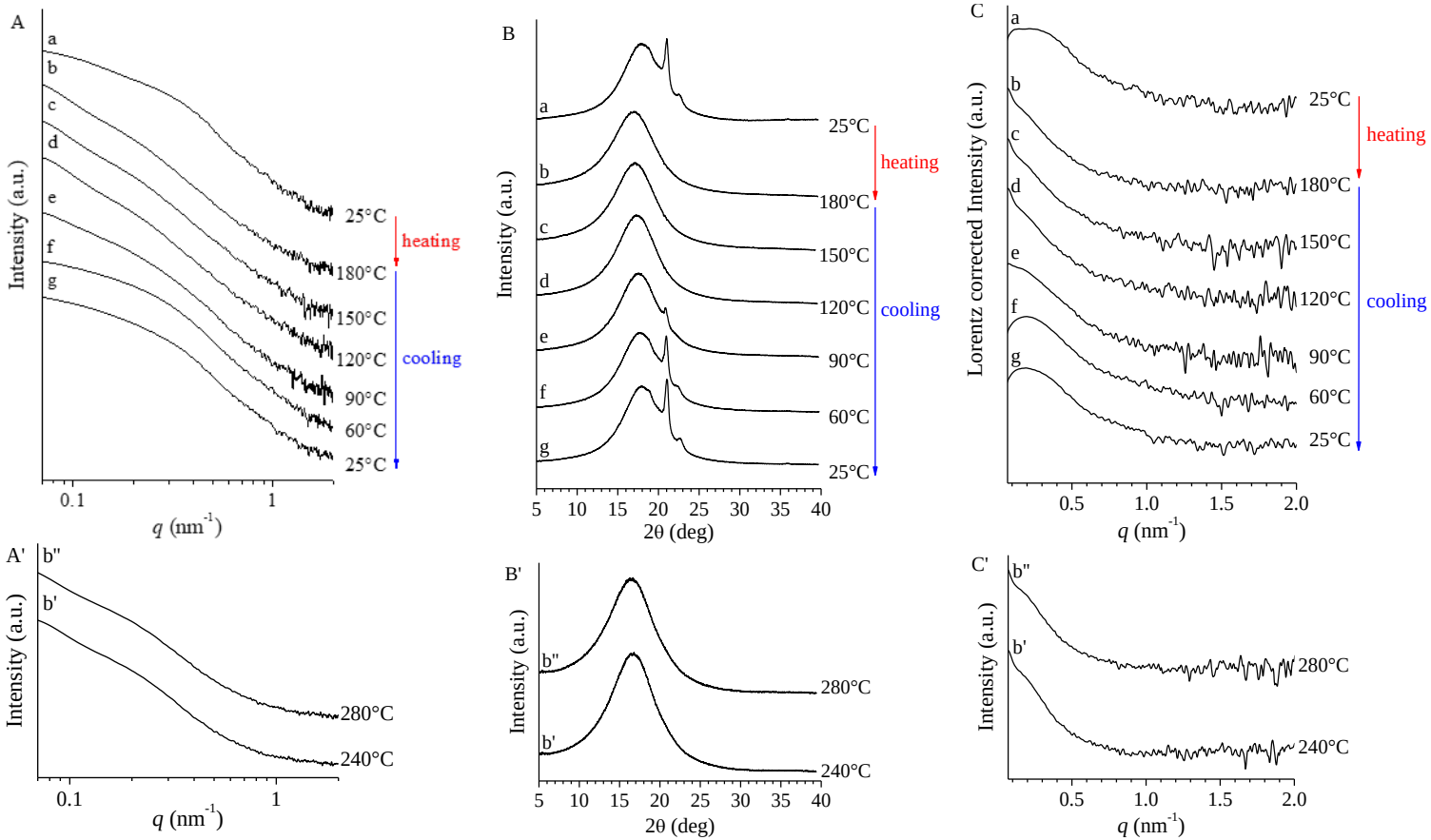

Figure 1.6 SAXS (A), WAXS (B) and Lorentz corrected (C) intensity profiles recorded at the indicated temperatures during heating and successive cooling of the sample RDG-1-26 (w_{PE}=0.27). SAXS (A'), WAXS (B') and Lorentz corrected (C') intensity profiles recorded at the indicated temperatures in a different experiment.

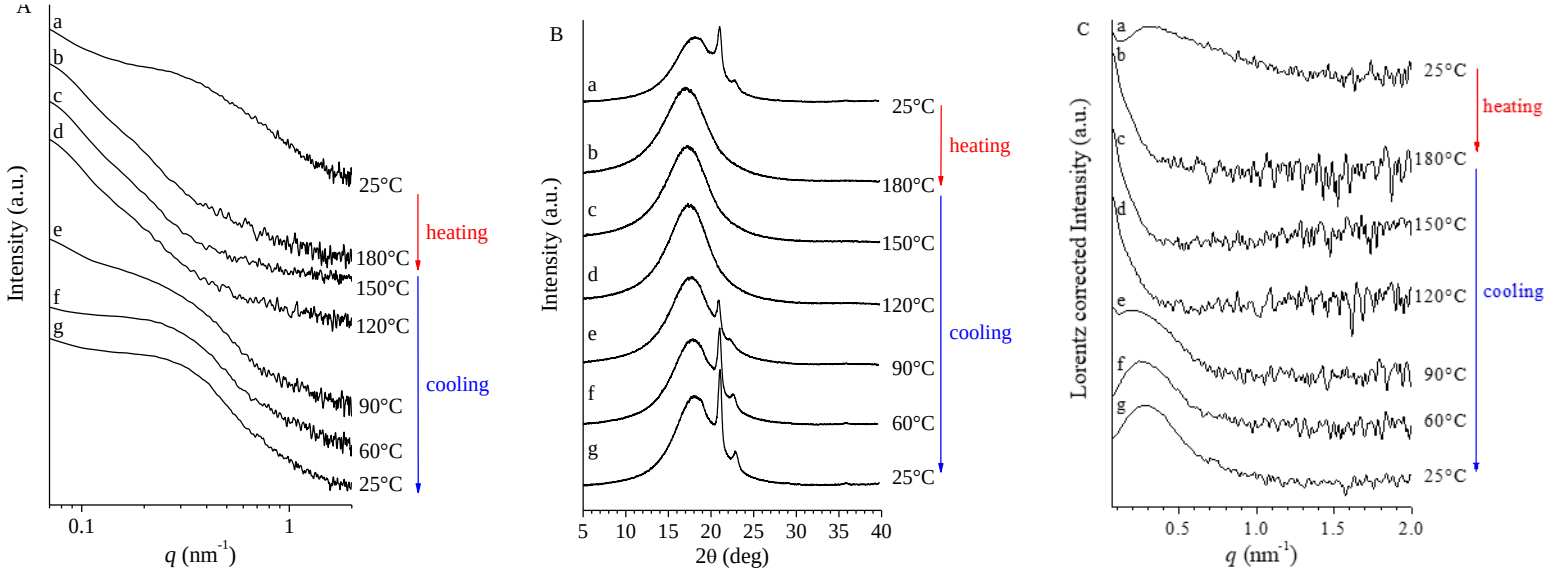

Figure 1.7 SAXS (A), WAXS (B) and Lorentz corrected (C) intensity profiles recorded at the indicated temperatures during heating and successive cooling of the sample RDG-1-20 (w_{PE}=0.36).

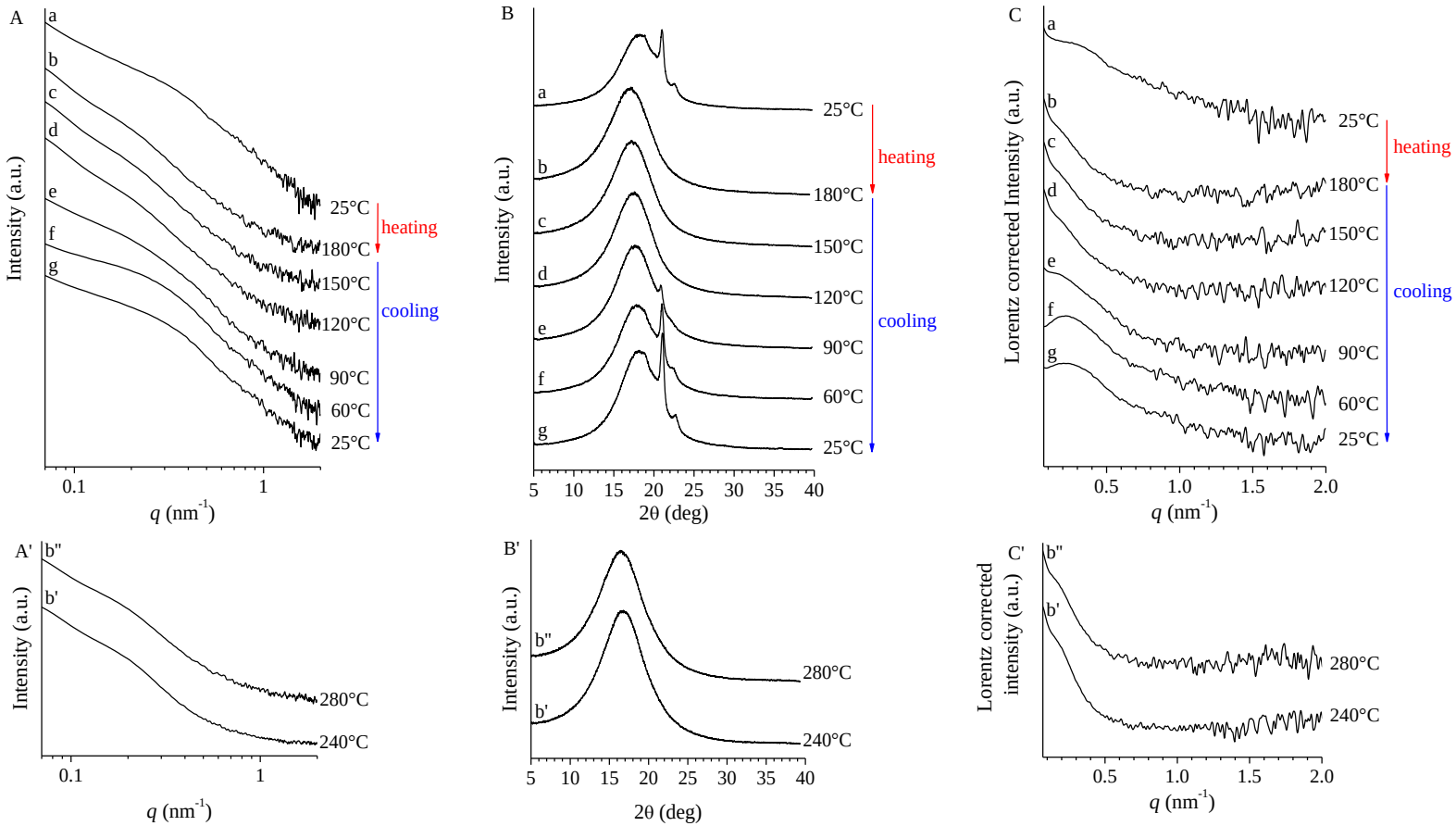

Figure 1.8 SAXS (A), WAXS (B) and Lorentz corrected (C) intensity profiles recorded at the indicated temperatures during heating and successive cooling of the sample RDG-1-29 (w_{PE}=0.44). SAXS (A'), WAXS (B') and Lorentz corrected (C') intensity profiles recorded at the indicated temperatures in a different experiment.

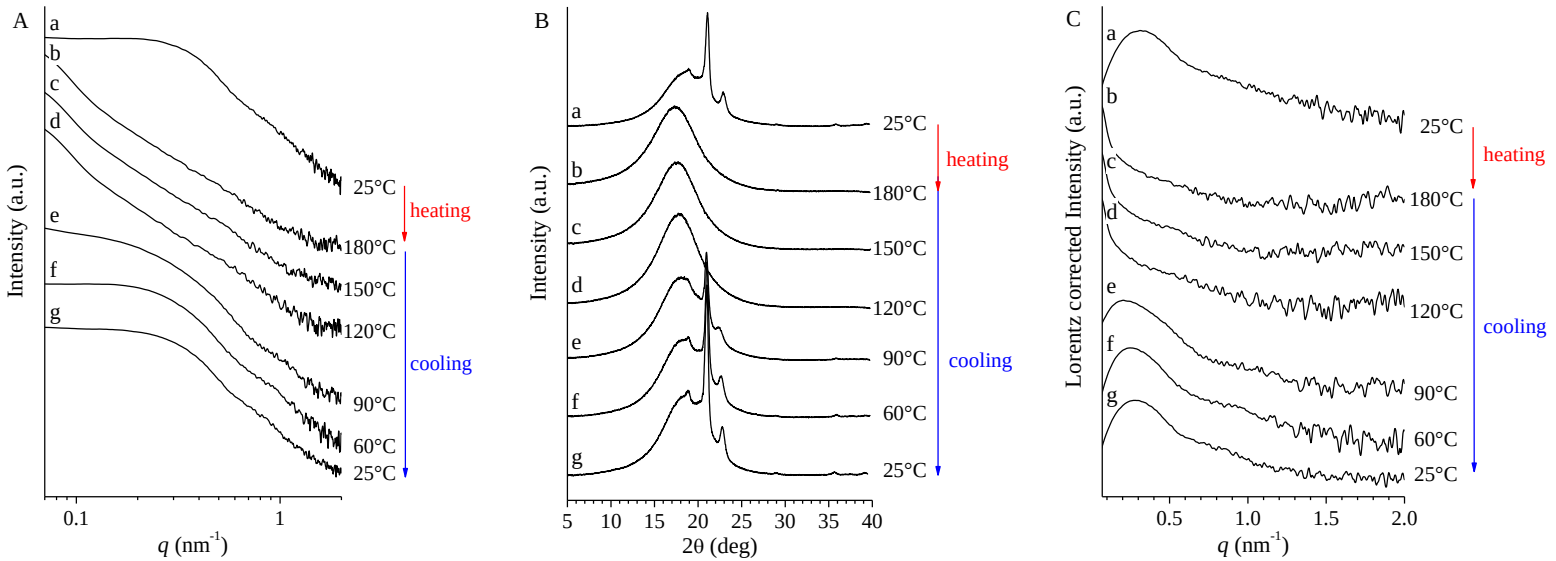

Figure 1.9 SAXS (A), WAXS (B) and Lorentz corrected (C) intensity profiles recorded at the indicated temperatures during heating and successive cooling of the sample RDG-1-36 (w_{PE}=0.70).

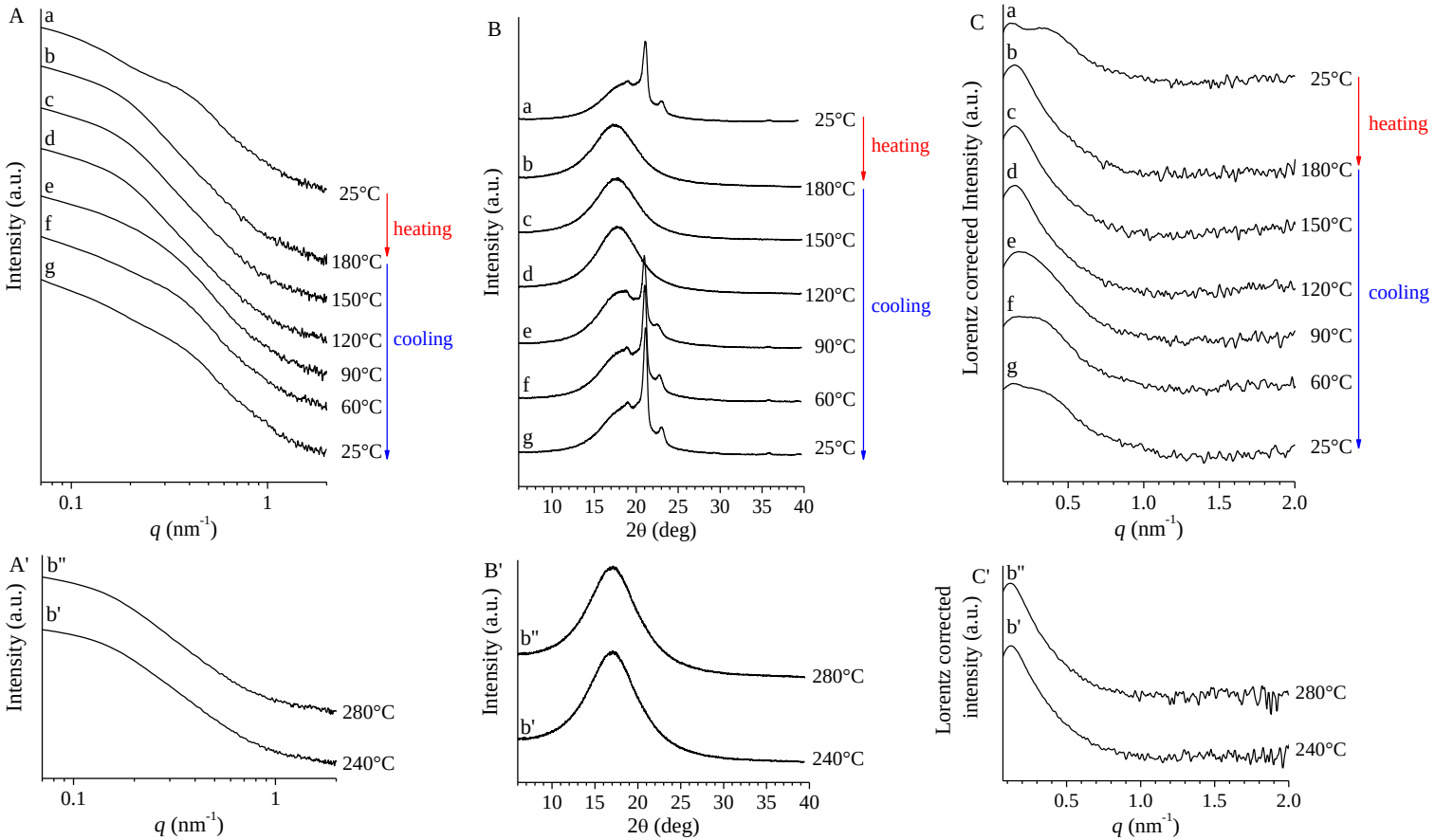

Figure 1.10 SAXS (A), WAXS (B) and Lorentz corrected (C) intensity profiles recorded at the indicated temperatures during heating and successive cooling of the sample RDG-1-15 (w_{PE}=0.79). SAXS (A'), WAXS (B') and Lorentz corrected (C') intensity profiles recorded at the indicated temperatures in a different experiment.

Table 1.5 Number average molecular mass ($M_{n\ TOT}$), mass fraction of the PE (w_{PE}) block, position of the correlation peak read in the SAXS profiles recorded at 25°C (q* 25°C) and 180°C (q* 180°C) and value of corresponding Bragg distances (L_B 25°C, L_B 180°C) for PE-*b*-PHD BCPs.

SAMPLE	$M_{n\ TOT}$ (Kg/mol) [a]	w_{PE}	q* 25°C (nm^{-1})	L_B 25°C (nm)	q* 180°C (nm^{-1})	L_B 180°C (nm)
RDG-1-13	78.4	0	-	-	-	-
RDG-1-26	146.4	0.27	0.36	17	0.20	31
RDG-1-20	175.7	0.36	0.33	19	<0.1	>60
RDG-1-29	203.5	0.44	0.37	17	0.22	28
RDG-1-36	232.6	0.70	0.32	20	<0.1	>60
RDG-1-15	466.4	0.79	0.40	16	0.15	42

Further information about the structural organization in the crystalline PE block may be obtained by calculating the one-dimensional normalized (self-)correlation function of electron density fluctuations (correlation function) from the SAXS data obtained for the samples crystallized from the melt, in particular those recorded at 25°C after cooling. This function is defined by Eq.1 and is related to a lamellar biphasic morphology.[24,25]

$$p(r) = \frac{\int_0^\infty q^2 I_c(q)\cos(qr)dq}{\int_0^\infty q^2 I_c(q)dq} \qquad \text{Eq.1}$$

The contribution to SAXS intensity due to sole lamellar arrangement is obtained by subtracting from the SAXS data recorded at 25 °C, the SAXS profile of the melt (recorded at 180°C) after scaling. In the hypothesis that the so obtained SAXS profiles are relative to a biphasic system consisting in the alternation of crystalline and amorphous layers, the (self-)correlation function of electron density fluctuations (correlation function) (Eq. 1) may be calculated. As an example, the method is illustrated in the case of the sample RDG-1-26 (w_{PE}=0.27) in Figure 1.11 A, where the SAXS profiles obtained at 25°C before (black curve) and after (blue curve) subtraction of the SAXS profile recorded at 180°C (red curve) are reported. This procedure allows evidencing the correlation peak at $q \approx 0.4$ nm^{-1} due to the sole contribution from lamellar stacking. The correlation function obtained from the blue profile in Figure 1.11 A is shown in Figure 1.11 B. Using a similar procedure, calculations of the correlation functions have been performed also for the other

BCPs and the results are shown Figure 1.12-1.15. In general, the correlation function assumes the maximum value at origin, i.e. $p(0)=1$, for $r=0$ nm, then decreases until becoming negative up to reach a minimum, and then increases again up to reach a positive secondary maximum. The relevant parameters of the stacked array of lamellar crystals are the lamellar periodicity P, the thickness of amorphous layers (l_a) and the lamellar thickness (l_c), where $P= l_a + l_c$. These parameters may be extracted from the correlation function. In particular, the position of the secondary maximum corresponds to P, whereas the minimum layer thickness corresponds to the abscissa of the intersection point between the line AC and the horizontal line BC fitting the minimum of $p(r)$ in Figure 1.11 B. Depending on the degree of crystallinity value x_c, the minimum layer thickness corresponds to l_a for x_c higher than 50% and to l_c, for x_c lower than 50%.

Based on the data of Table 1.2, all the samples within the series show a degree of crystallinity relative to the sole PE blocks $x_{c\,PE}<50\%$ (see also Table 1.6). Therefore, the minimum layer thickness evaluated from the correlation function corresponds to l_c. All samples show a secondary maximum corresponding to P. However, in the correlation function of the samples RDG-1-26 (Figure 1.11 B) and RDG-1-29 (Figure 1.13), the secondary maximum is not well defined, probably because of the low contrast. For these samples, the periodicity P of the layered structure may not be determined from the correlation function but it may be assumed as coincident with the value determined with the Bragg law, L_B, from the position of the correlation peak in the Lorentz corrected intensity profile (Figure 1.6 C, and 1.8 C). Finally, l_a is determined as $l_a=L_B-l_c$. The values of $x_{c\,PE}$, L_B, P, l_c, l_a obtained for the PE-*b*-PHD BCPs are reported in Table 1.6.

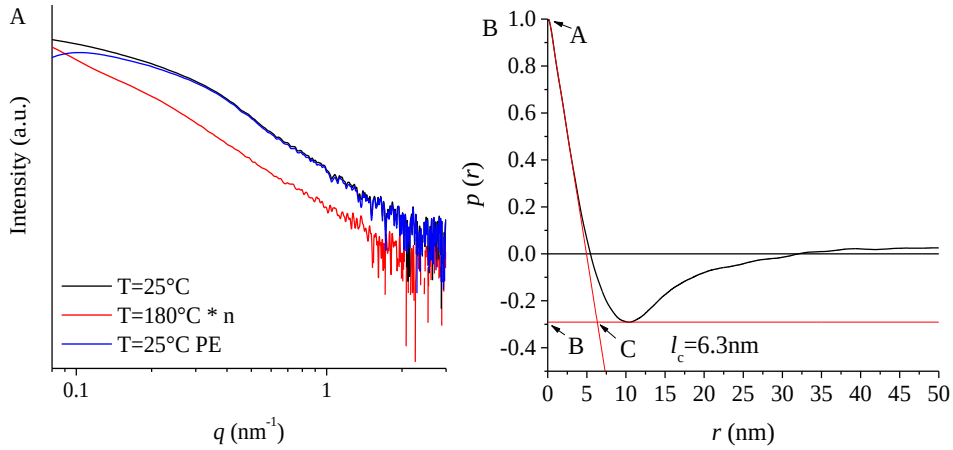

Figure 1.11 Sample RDG-1-26 (w_{PE}=0.27): (A) Experimental SAXS profile recorded at 25°C before (black) and after (blue) the subtraction of the profile recorded at T=180°C (red) after scaling. (B) Normalized correlation function obtained from the SAXS profile calculated for the crystalline PE block (blue profile).

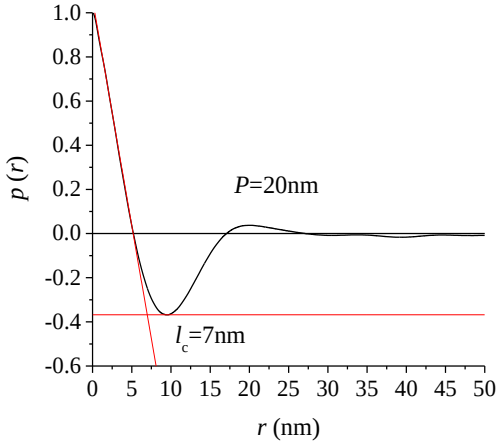

Figure 1.12 Normalized correlation function obtained for the sample RDG-1-20 (w_{PE}=0.36) from the experimental SAXS profile recorded at 25°C.

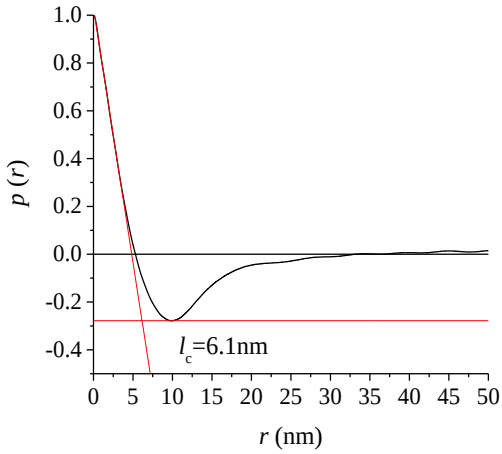

Figure 1.13 Normalized correlation function obtained for the sample RDG-1-29 (w_{PE}=0.44) from the SAXS profile calculated for the crystalline PE block.

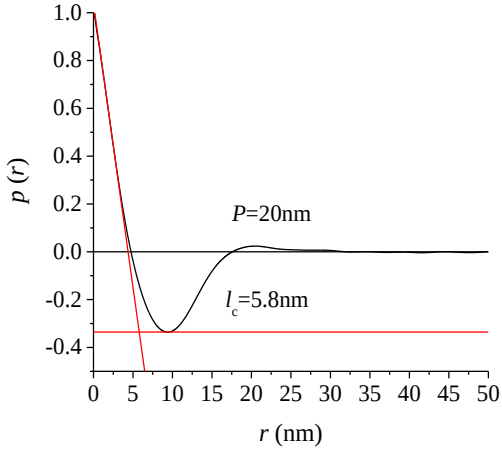

Figure 1.14 Normalized correlation function obtained for the sample RDG-1-36 (w_{PE}=0.70) from the experimental SAXS profile recorded at 25°C.

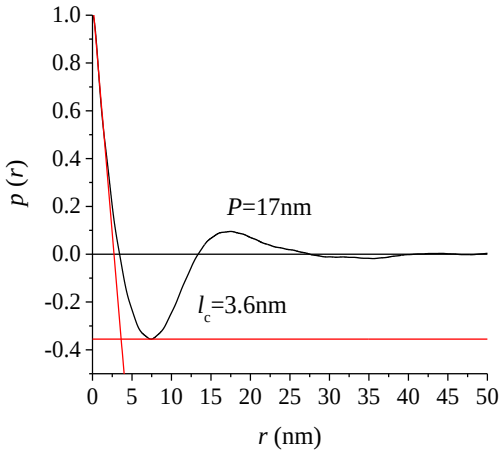

Figure 1.15 Normalized correlation function obtained for the sample RDG-1-15 (w_{PE}=0.79) from the SAXS profile calculated for the crystalline PE block.

Table 1.6 Molecular mass ($M_{n\ PE}$), mass fraction (w_{PE}) and degree of crystallinity ($xc_{\ PE}$) of the PE block. Values of the Bragg distance (L_B), periodicity of the lamellar stacks (P), crystalline (l_c) and amorphous layers (l_a) of the crystalline PE block in PE-*b*-PHD BCPs.

SAMPLE	$M_{n\ TOT}$ (Kg/ mol)	$M_{n\ PE}$ (Kg/ mol)	w_{PE}	$xc_{\ PE}$ (%)	L_B (nm)	P (nm)	l_c (nm)	l_a (nm)
RDG-1-13	78.4	-	0	-	-	-	-	
RDG-1-26	146.4	39.7	0.27	41	17	-	6.3	10.7
RDG-1-20	175.7	62.3	0.36	33	19	20	7	13
RDG-1-29	203.5	89.2	0.44	36	17	-	6.1	10.9
RDG-1-36	232.6	163.8	0.70	30	20	20	5.8	14.2
RDG-1-15	466.4	368.8	0.79	34	16	17	3.6	13.4

A general model describing the solid state organization in PE-*b*-PHD BCPs in the hypothesis of confined crystallization, and no breakout, is shown in Figure 1.16. The periodicity of the nanostructure is given by the Bragg distance obtained from the position of the correlation peak in the SAXS profile recorded at 180°C (L_B 180°C, Table 1.5), while the periodicity of the amorphous and crystalline layers within the PE block is given by the Bragg distance obtained from the SAXS profile recorded at 25°C, or the position of the secondary maximum in the correlation function (L_B 25°C and P, Table 1.6). In Figure 1.16, the lamellar crystals with thickness l_c and the amorphous layers with thickness l_a are also indicated.

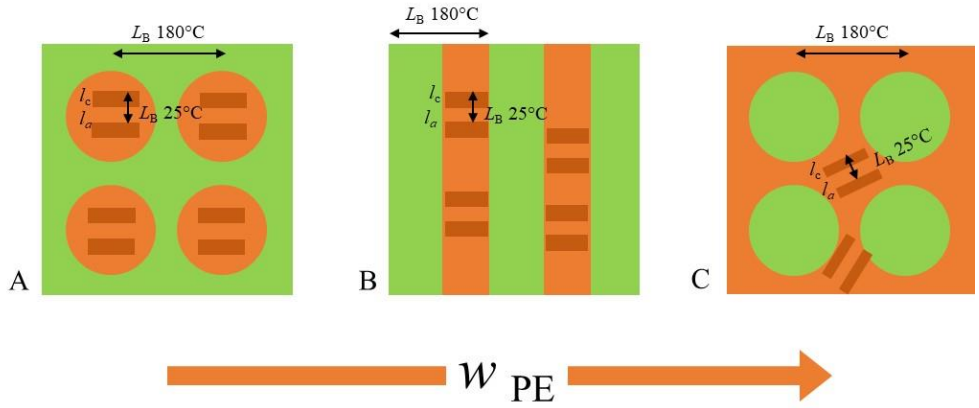

Figure 1.16 Scheme of the solid state organization of PE-*b*-PHD BCPs, for which crystallization occurs from a phase separated melt with no breakout, as a function of the mass fraction of the PE block.

A curious result obtained from SAXS analysis consists in a paradox. The higher the molecular mass of PE blocks, the shorter the thickness of lamellar crystals. In fact, the lamellar thickness is 6-7nm for the samples RDG-1-13, RDG-1-26, RDG-1-20, RDG-1-29, RDG-1-36 with molecular mass of the PE blocks comprised between 40 and 164Kg/mol, and drops to ≈4nm for the sample RDG-1-15, with the highest molecular mass of the PE blocks (369Kg/mol). We speculate that this is due to the different morphology occurring in the melt, and therefore to the different geometry of the crystallisable PE domains. Namely, for the samples RDG-1-13, RDG-1-26, characterized by a volume fraction of PE blocks of 0.26 and 0.34, respectively, the PE blocks represent the minority phase and PE crystallization is expected to be initiated within spherical, or cylindrical domains (Figure 1.16 A). In the case of the samples RDG-1-20 and RDG-1-29 with volume fraction of the PE blocks of 0.42 and 0.69, respectively, the blocks have nearly identical length, and PE crystallization is expected to be initiated within phase separated lamellar domains (Figure 1.16 B). Finally, in the case of the sample RDG-1-15, the volume fraction of PE block is 0.78 and PE crystallization is expected to be initiated in a continuous matrix surrounding the PHD cylindrical domains, which easily act as hurdles preventing the development of well-formed stacks including thick lamellar crystals (Figure 1.16 C).

1.1.4 Mechanical characterization

The stress-stain curves measured by stretching films of the PE-*b*-PHD BCPs obtained from the melt, by compression molding are reported in Figure 1.17.

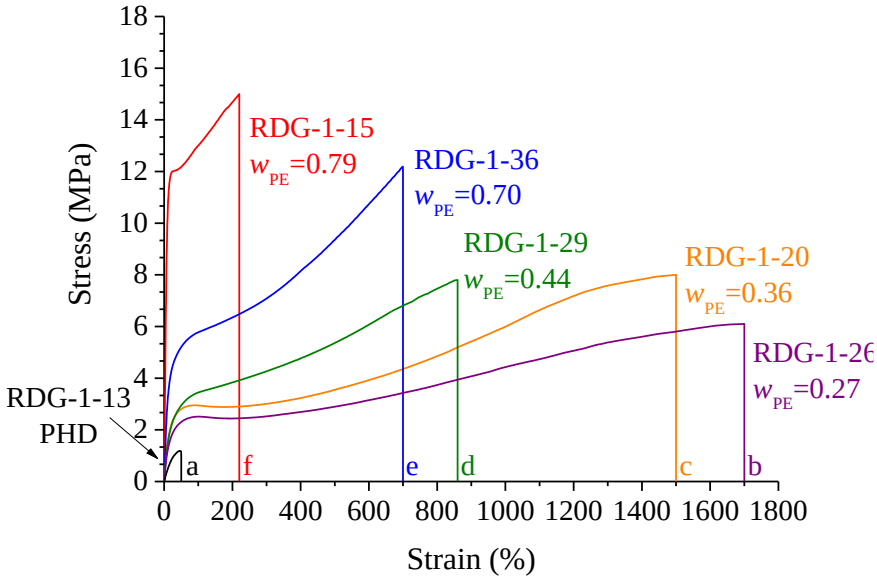

Figure 1.17 Stress-strain curves of the compression-molded samples of the PHD homopolymer (a) and of the PE-*b*-PHD BCPs (b-f).

The stress-strain curves reveal that the mechanical properties of PE-*b*-PHD BCPs depend on the relative block length. In particular, decreasing the mass fraction of the crystalline PE blocks (w_{PE}), ductility increases, while the Young's modulus, the stress at the yield and at break decrease. The mechanical behavior of the PHD homopolymer is not comparable to that of the PE-*b*-PHD BCPs since it is dictated by its low molecular mass. The values of the mechanical parameters obtained from stress-strain curves are reported in Table 1.7 and are shown in Figure 1.18 as a function of the mass fraction of the PE block (w_E).

Table 1.7 Total molecular mass ($M_{n\ TOT}$), molecular mass ($M_{n\ PE}$) and mass fraction (w_{PE}) of the PE block, Young's modulus (E), elongation at the yield point (ε_y), stress at the yield point (σ_y), elongation at break (ε_b), stress at break (σ_b) and tension set at break (t_b) of the PE-*b*-PHD BCPs.

SAMPLE	$M_{n\ TOT}$ (Kg/mol)	$M_{n\ PE}$ (Kg/mol)	w_{PE}	E (MPa)	ε_y (%)	σ_y (MPa)	ε_b (%)	σ_b (MPa)	t_b (%)
RDG-1-13	78.4	-	0	-	-	-	-	-	
RDG-1-26	146.4	39.7	0.27	10.2±0.6	93±6	2.5±0.1	1700±300	6.1±0.5	390±70
RDG-1-20	175.7	62.3	0.36	13.7±0.2	81±8	3.0±0.2	1500±200	8±1	400±30
RDG-1-29	203.5	89.2	0.44	13.5±0.8	90±10	2.9±0.1	900±200	8.0±0.5	220±30
RDG-1-36	232.6	163.8	0.70	32±1	120±30	5.7±0.3	700±200	12±3	220±70
RDG-1-15	466.4	368.8	0.79	92±5	24±2	12±1	220±30	15±1	27±2

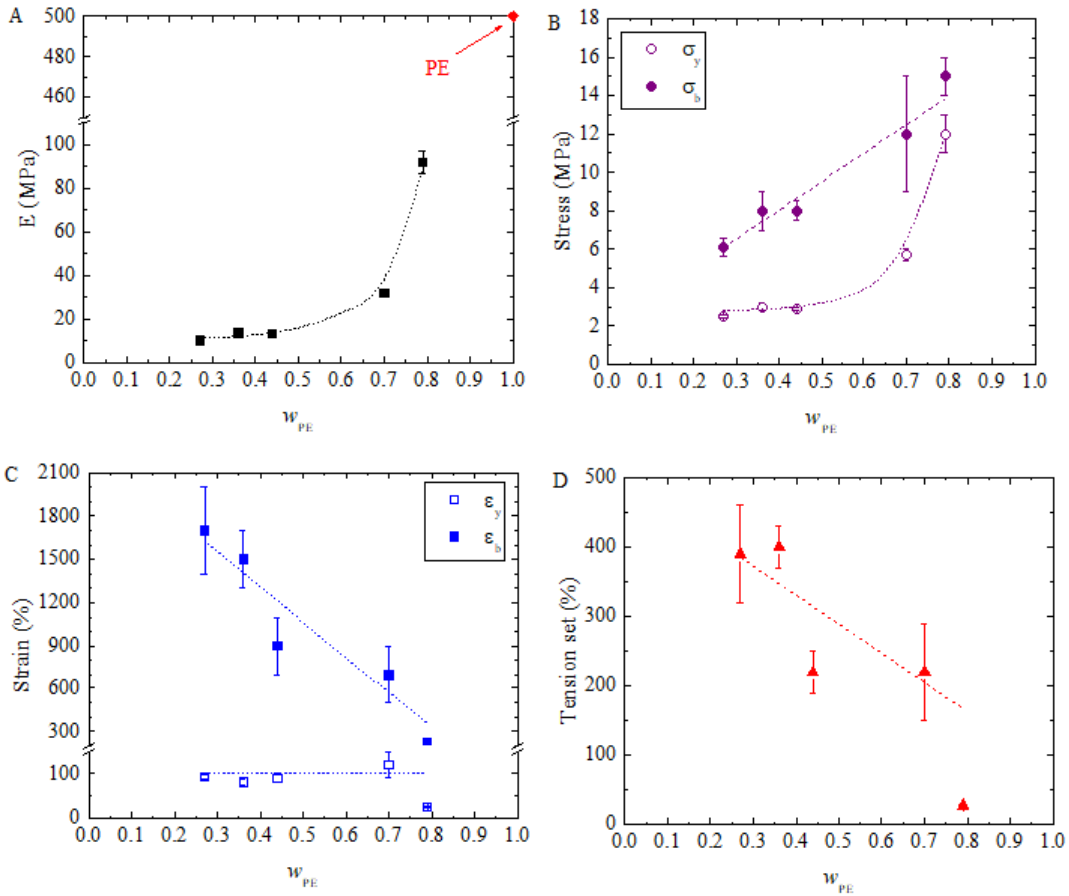

Figure 1.18 Values of the Young's modulus (A), stress at yield (○) and at break (●) (B), elongation at yield (□) and at break (■) (C) and tension set at break (▲) (D), evaluated from the stress-strain curves shown in Figure 1.17, as a function of the mass fraction of the PE blocks.

As shown in Figure 1.18 A, the presence of a rubbery amorphous block linked to a crystalline PE block results in a drastic decrease in the value of the Young's modulus. In particular, the value of the Young's modulus of a PE homopolymer synthesized by means of a catalyst similar to that shown in Scheme 1.1, is around 500MPa, and decreases to 100MPa in the sample RDG-1-15, with PE mass fraction of 0.79 and the smallest content of PHD (w_{PHD}=0.21). With further decrease of PE mass fraction, the Young's modulus decreases up to reach a value of 10MPa.

The stress at the yield and at break of PE-*b*-PHD BCPs decrease with decreasing w_{PE}. The values of the stress at the yield point vary in the range 12MPa-2MPa, while those of the stress at break vary in the range 15MPa-6MPa according to a nearly linear trend. The decrease of the Young's modulus and of the stress at the yield point and at break are closely-related to the decrease of crystallinity observed with the decrease of w_{PE} (Table 1.2).

From Figure 1.18 C it is apparent that the strain at break increases linearly with decreasing w_{PE}, with values varying in the range 200-1800%, while the strain at the yield is approximately constant around a value of 100%. The tension set at break (Figure 1.18 D) slightly increases with decreasing w_{PE}. The difference between the values of the strain at break and the tension set at break increases with the decrease of w_{PE}, indicating that the samples with a high mass fraction of the amorphous block show higher elastomeric properties.

The mechanical characterization performed on the PE-*b*-PHD samples shows extremely interesting results: PE-*b*-PHD BCPs span different mechanical behaviors depending on the relative block length of PE and PHD. Therefore, by changing the sole mass fraction of one of the two blocks, it is possible to design materials with tailored properties ranging from those of stiff plastomers (similar to PE) at high w_{PE} values, to those of materials with high flexibility and ductility with partial elastomeric properties at lower w_{PE} values. In addition, it is worth mentioning that regardless of the mechanical properties, these BCPs also show a good thermal resistance due to the presence of the crystalline PE blocks having a melting temperature of ≈110°C.

1.1.5 Structural characterization of oriented fibers

The structural changes occurring in PE-*b*-PHD BCPs during tensile deformation have been studied by X-ray fiber diffraction analysis. Compression moulded samples of the BCPs have been stretched at room temperature at different strain (ε) values up to the break. For each sample, the X-ray fiber diffraction patterns, the corresponding intensity profiles read along the equatorial line and the azimuthal profiles relative to the 110 PE reflection, are shown in Figure 1.19-1.22. For the stretched samples RDG-1-20 (w_{PE}=0.36), RDG-1-29 (w_{PE}=0.44) and RDG-1-36 (w_{PE}=0.70), X-ray fiber diffraction patterns have been also acquired after release of the tension and successive aging for ≈1month. The sample RDG-1-15 (w_{PE}=0.79), instead, has not been analyzed because of its low ductility; in fact, stretching, even at low values of deformations, has not been achieved.

The X-ray fiber diffraction patterns of the BCP samples (Figure 1.19-1.22) show the gradual orientation of PE crystals in the stretching direction and at high deformation, also partial polarization of the amorphous halo on the equator. The orientation of the crystals is marked by the gradual arcing on the equator of the 110 and 200 reflections of the orthorhombic form of PE, at 2θ≈21° and 23° respectively. The orientation of the crystals is also evidenced by the gradual sharpening of the peaks in the azimuthal profiles relative to the 110 reflection (2θ≈21°) and by the corresponding decrease in the value of the full width at half maximum (Δχ) of the same peaks.

In the case of the sample RDG-1-26 (w_{PE}=0.27), with the shortest relative length of the PE block, only a low degree of orientation of the crystals is achieved at 500% deformation (Figure 1.19 C and curve b in D). Higher values of deformation have not been achieved. Instead, for the BCP samples with relative length of the PE blocks longer than that of the sample RDG-1-26, a good degree of orientation is achieved already at 300-400% deformation (Figure 1.20-1.22). In particular, comparing the polarization of the 110 reflection on the equator at 600% deformation for the samples of Figure 1.20-1.22, it appears that the longer the relative length of PE blocks, the higher the degree of orientation achieved by PE crystals.

This effect may be better observed in Figure 1.23, wherein the values of Δχ evaluated from the azimuthal profiles of Figures 1.19-1.22 have been reported as a function of the strain, for the different PE-*b*-PHD samples. It is apparent that at a certain value of the deformation, the degree of orientation achieved

by the PE crystals increases (lower $\Delta\chi$ value) on increasing the mass fraction of the PE block. In fact, it corresponds to the shortening of the relative length of PHD amorphous block which generates a compliant matrix meandering the PE crystalline domains. The higher the volume fraction of PHD amorphous blocks, the higher is the damping effect, so that the stress is transmitted to the crystals less efficiently. Whether the efficiency of stress transmitters is also a function of geometry of phase separated domain is an open question, deserving more detailed and complementary analysis. It is worth noting that in the case of the sample RDG-1-36 with w_{PE}=0.70, at 600% deformation, the 200 reflection disappears, and only a broad halo centered at $2\theta\approx21°$ is apparent (Figure 1.22 C). We argue that since the relative length of PHD blocks is short, the stress transmitted to the crystals is so high that produces lamellar fragmentation, up to achieve mechanical melting, followed by re-crystallization of PE chains in a disordered pseudo-hexagonal form.[26] In the case of the samples RDG-1-20 (w_{PE}=0.36) (Figure 1.20 G), RDG-1-29 (w_{PE}=0.44) (Figure 1.21 E) and RDG-1-36 (w_{PE}=0.70) (Figure 1.22 D) the diffraction patterns of fiber specimens stretched up to 1000%, 600% and 600% deformation, respectively, and then relaxed and aged for ≈1 month show partial loss of orientation and partial elastic recovery.

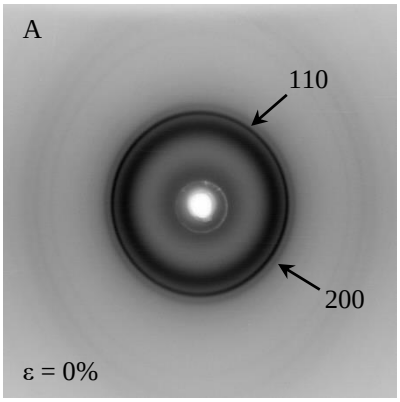

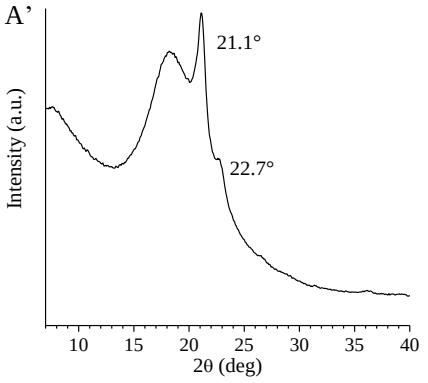

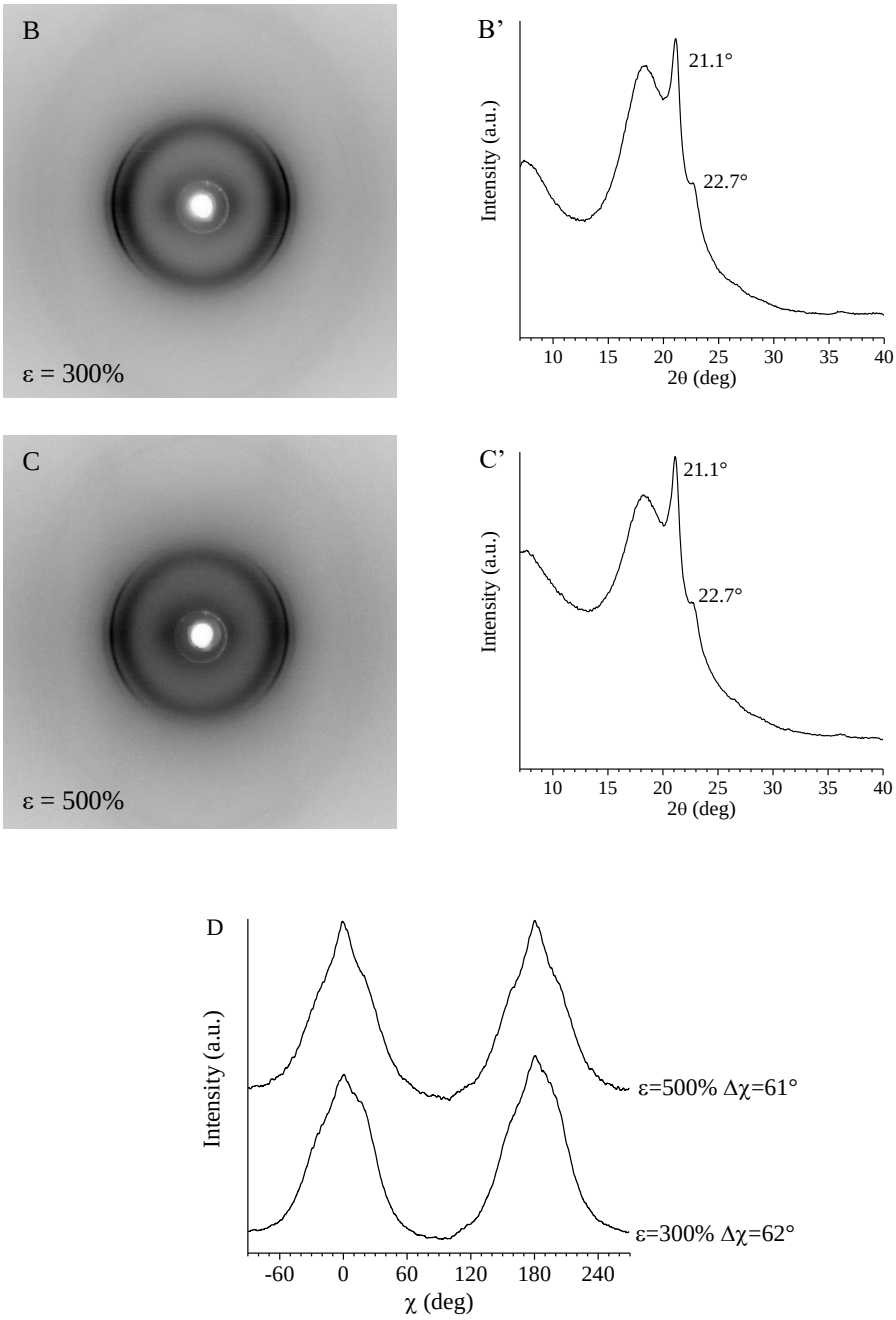

Figure 1.19 X-ray fiber diffraction patterns of the sample RDG-1-26 (w_{PE}=0.27) stretched at 0% (A), 300% (B) and 500% (C) deformation and corresponding equatorial profiles (A', B' and C'). (D) Azimuthal profiles relative to the 110 reflection, obtained from the X-ray fiber diffraction patterns recorded at the indicated values of deformation (ε). For each profile, the full width at half maximum (Δχ) of the peaks is also reported.

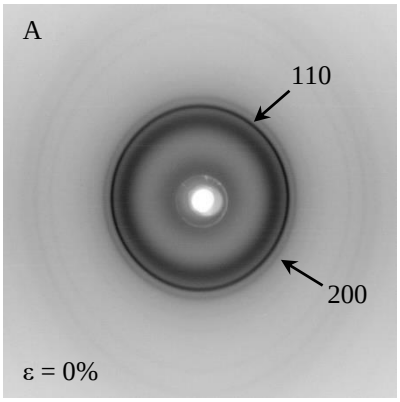
A
110
200
ε = 0%

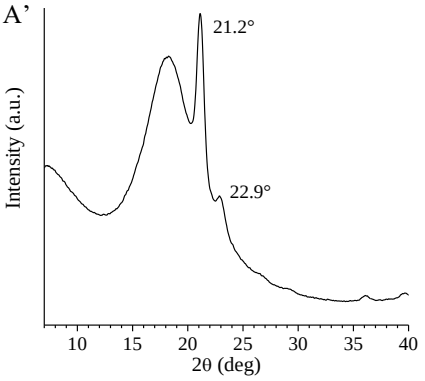
A'
21.2°
22.9°
Intensity (a.u.)
10 15 20 25 30 35 40
2θ (deg)

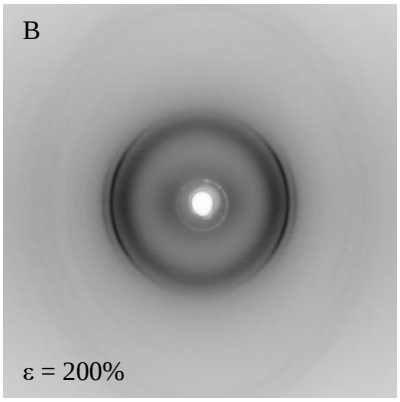
B
ε = 200%

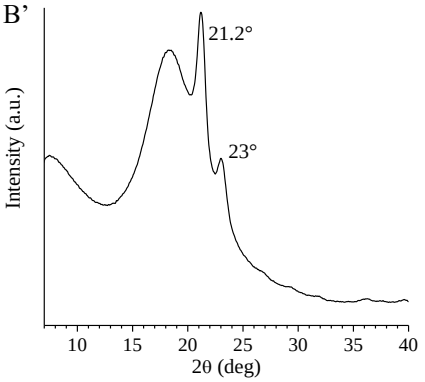
B'
21.2°
23°
Intensity (a.u.)
10 15 20 25 30 35 40
2θ (deg)

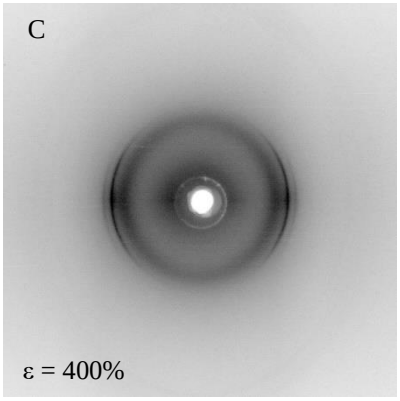
C
ε = 400%

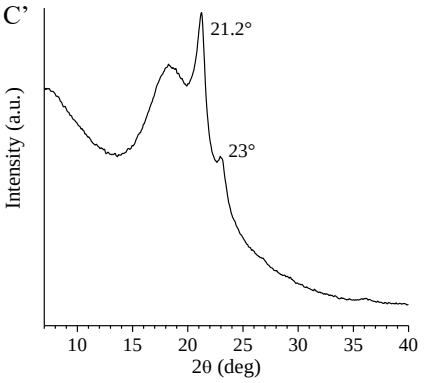
C'
21.2°
23°
Intensity (a.u.)
10 15 20 25 30 35 40
2θ (deg)

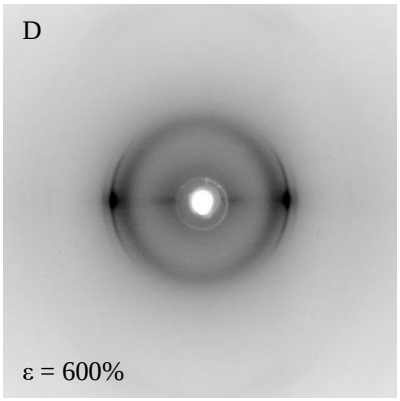
D
ε = 600%

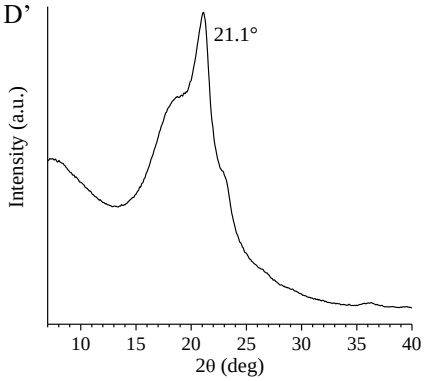
D'
21.1°
Intensity (a.u.)
10
15
20
25
30
35
40
2θ (deg)

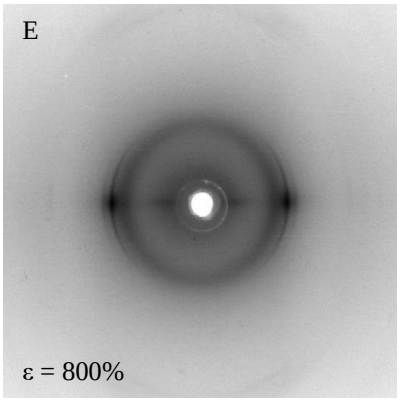
E
ε = 800%

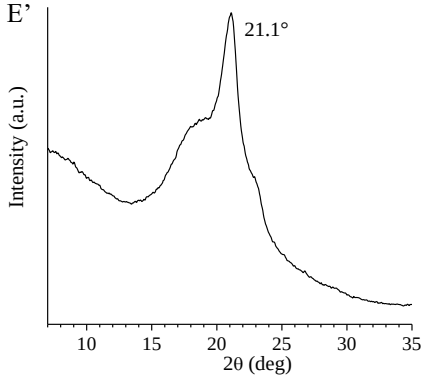
E'
21.1°
Intensity (a.u.)
10
15
20
25
30
35
2θ (deg)

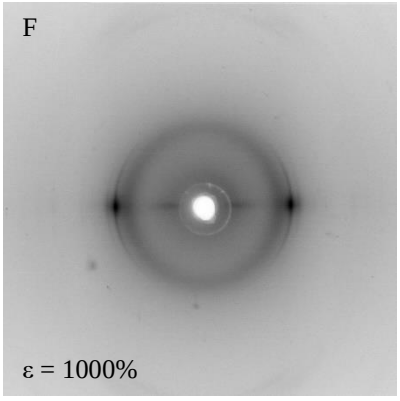
F
ε = 1000%

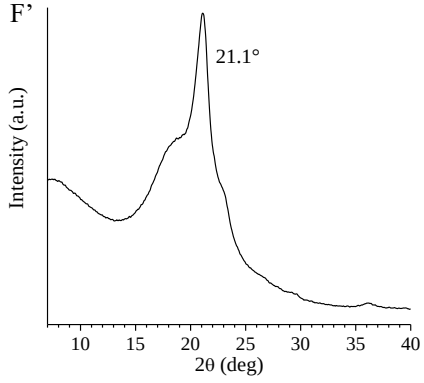
F'
21.1°
Intensity (a.u.)
10
15
20
25
30
35
40
2θ (deg)

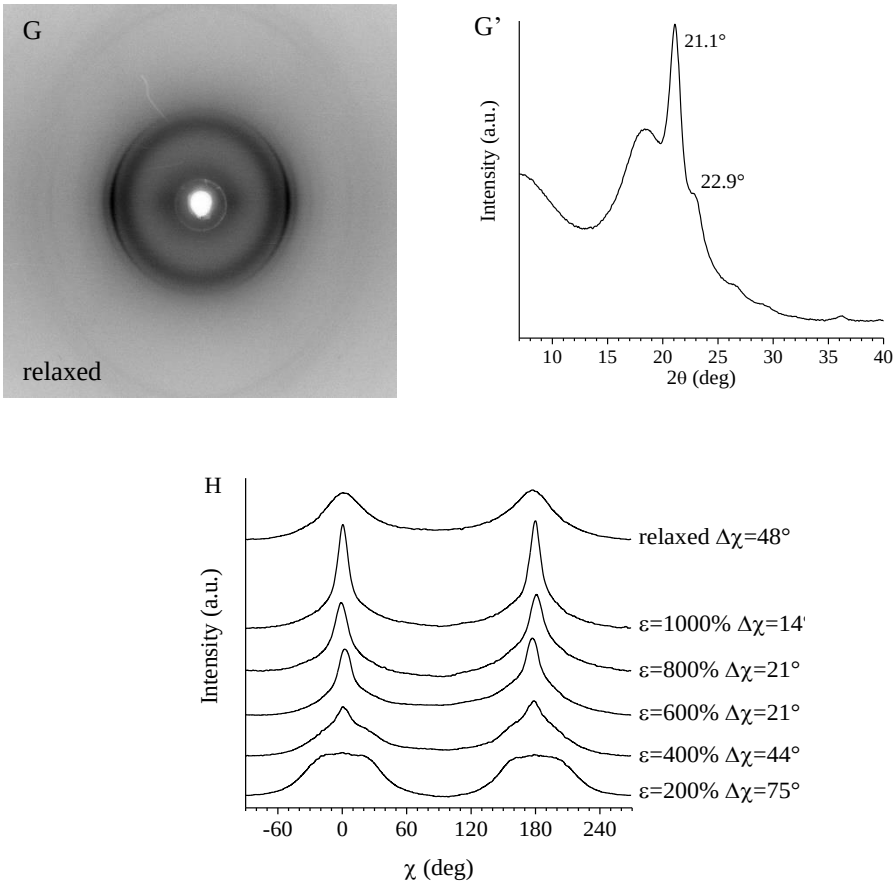

Figure 1.20 X-ray fiber diffraction patterns of the sample RDG-1-20 (w_{PE}=0.36) stretched at 0% (A), 200% (B), 400% (C), 600% (D), 800% (E), 1000% (F) deformation, and of the sample stress-relaxed from 1000% deformation and successively aged for 1 month at room temperature (G) and corresponding equatorial profiles (A'-G'). (H) Azimuthal profiles relative to the 110 reflection, obtained from the X-ray fiber diffraction patterns recorded at the indicated values of deformation (ε). For each profile, the full width at half maximum (Δχ) of the peaks is also reported.

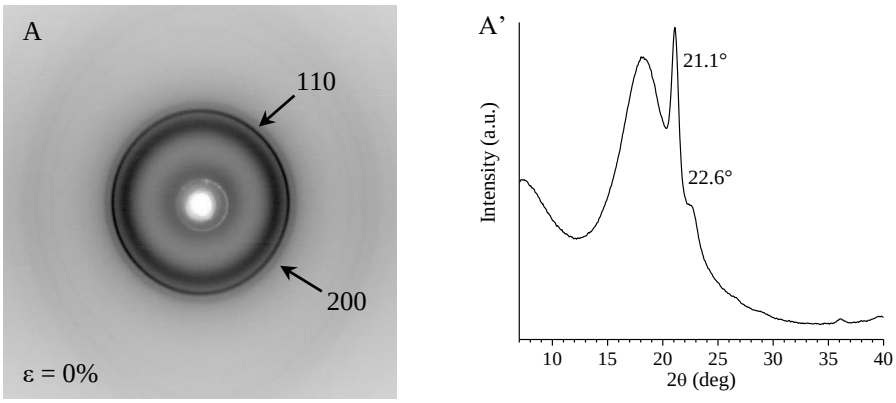

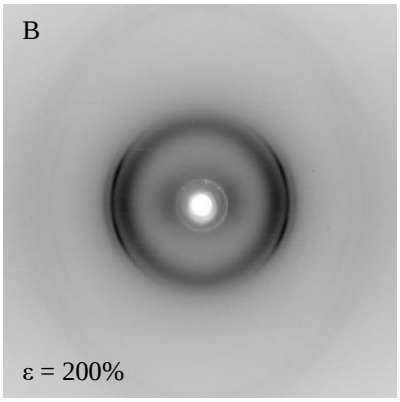
B
ε = 200%

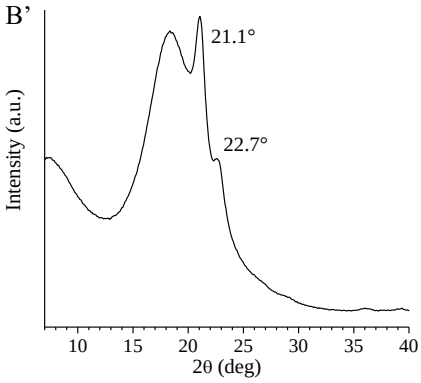
B'
21.1°
22.7°
Intensity (a.u.)
10
15
20
25
30
35
40
2θ (deg)

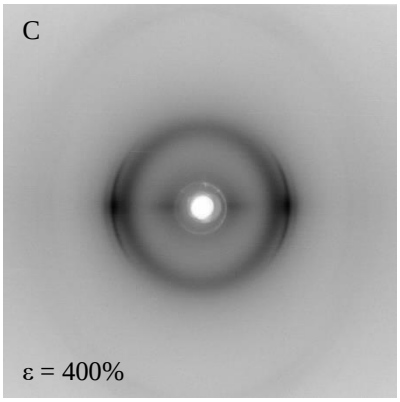
C
ε = 400%

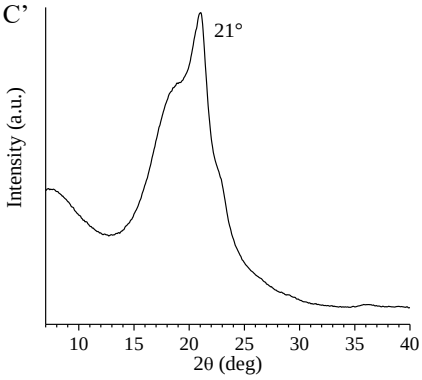
C'
21°
Intensity (a.u.)
10
15
20
25
30
35
40
2θ (deg)

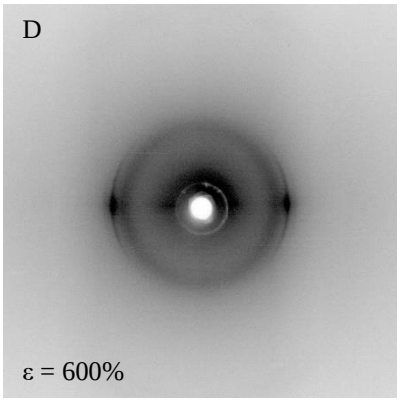
D
ε = 600%

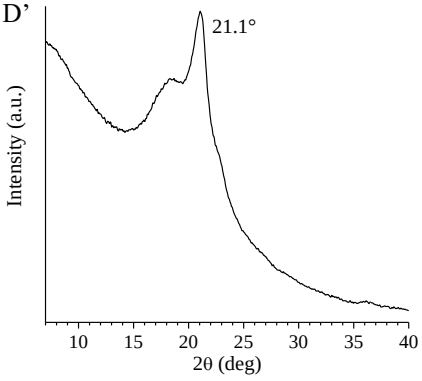
D'
21.1°
Intensity (a.u.)
10
15
20
25
30
35
40
2θ (deg)

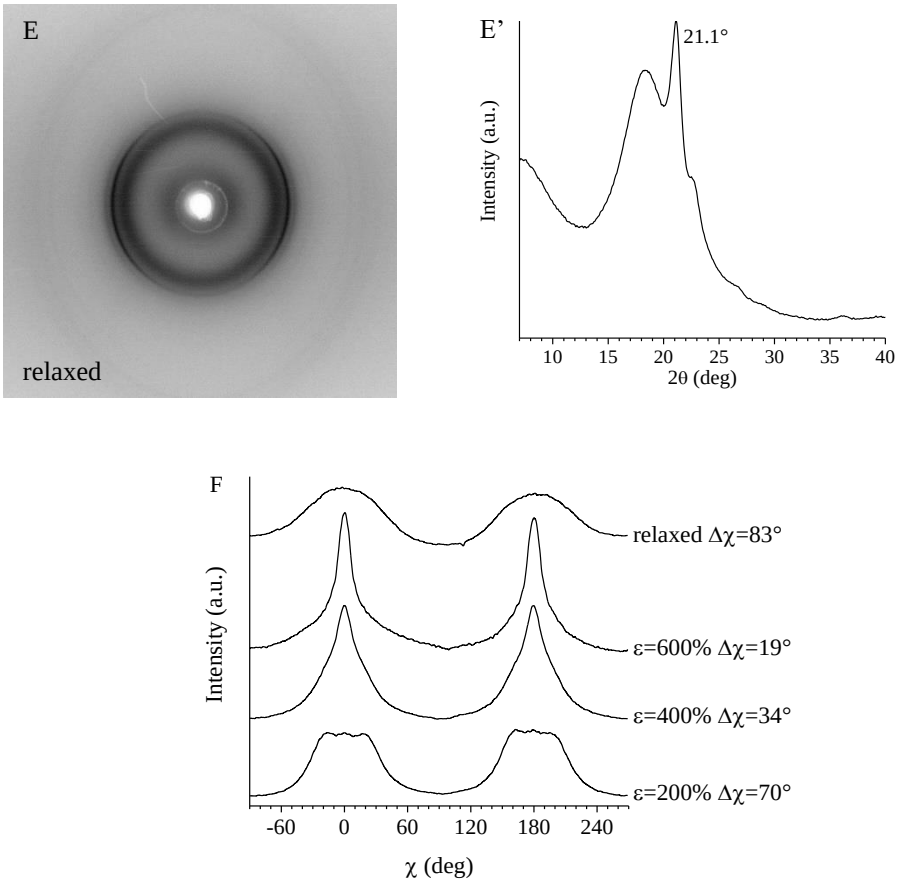

Figure 1.21 X-ray fiber diffraction patterns of the sample RDG-1-29 (w_{PE}=0.44) stretched at 0% (A), 200% (B), 400% (C), 600% (D) deformation, and of the sample stress-relaxed from 600% deformation and successively aged for 1 month at room temperature (E) and corresponding equatorial profiles (A'-E'). (F) Azimuthal profiles relative to the 110 reflection, obtained from the X-ray fiber diffraction patterns recorded at the indicated values of deformation (ε). For each profile, the full width at half maximum (Δχ) of the peaks is also reported.

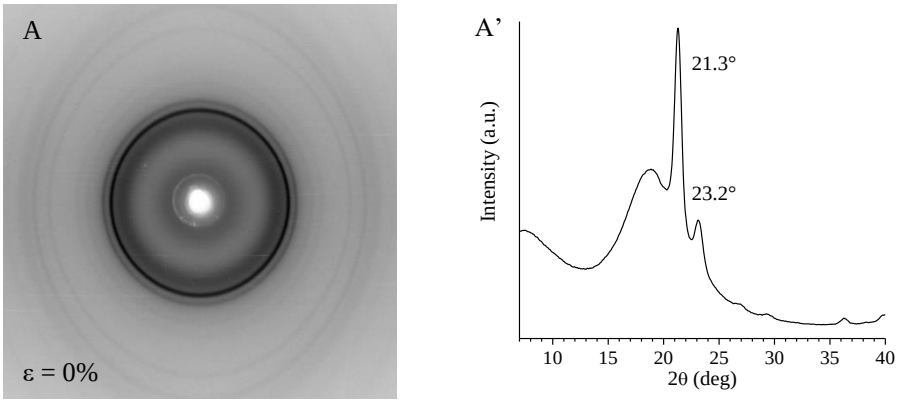

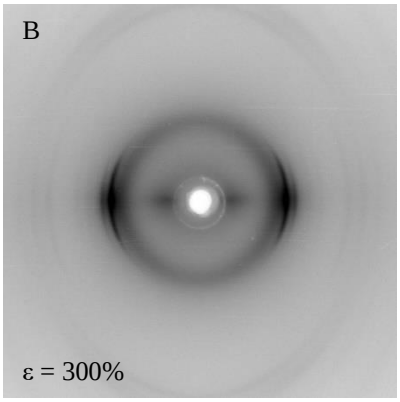
B
ε = 300%

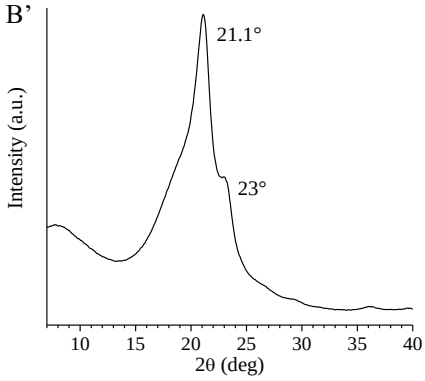
B'
21.1°
23°
Intensity (a.u.)
10
15
20
25
30
35
40
2θ (deg)

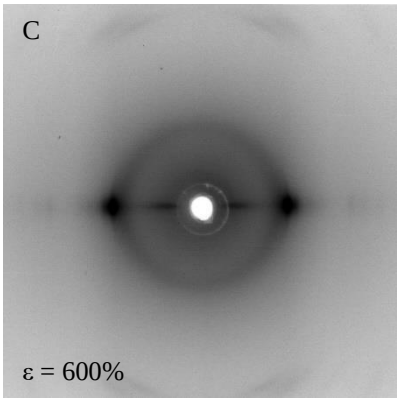
C
ε = 600%

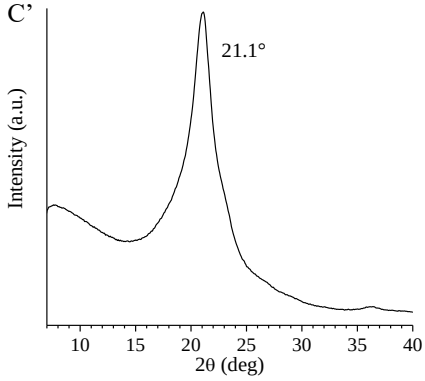
C'
21.1°
Intensity (a.u.)
10
15
20
25
30
35
40
2θ (deg)

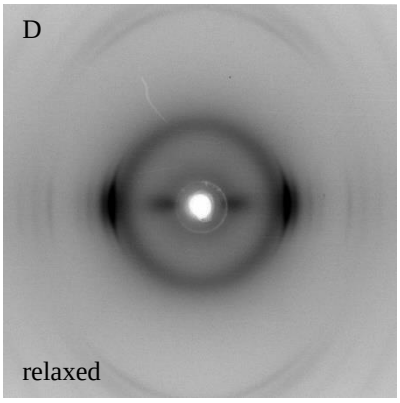
D
relaxed

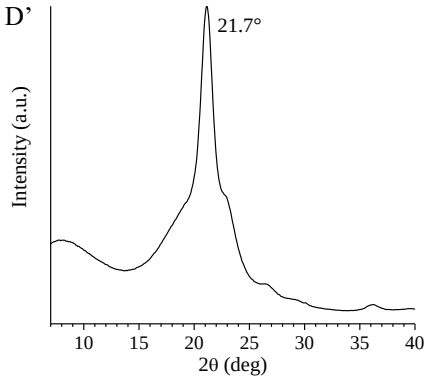
D'
21.7°
Intensity (a.u.)
10
15
20
25
30
35
40
2θ (deg)

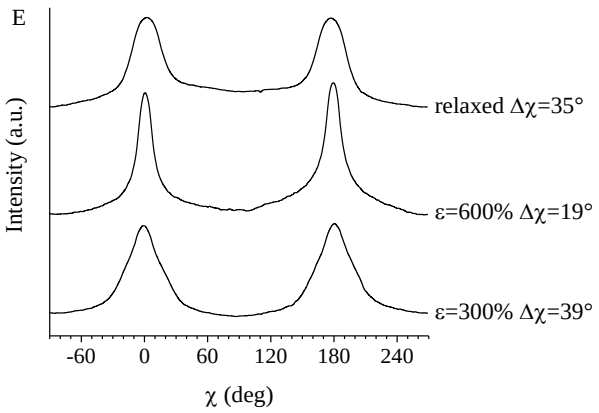

Figure 1.22 X-ray fiber diffraction patterns of the sample RDG-1-36 (w_{PE}=0.70) stretched at 0% (A), 300% (B), 600% (C) deformation, and of the sample stress-relaxed from 600% deformation and successively aged for 1 month at room temperature (D) and corresponding equatorial profiles (A'-D'). (E) Azimuthal profiles relative to the 110 reflection, obtained from the X-ray fiber diffraction patterns recorded at the indicated values of deformation (ε). For each profile, the full width at half maximum (Δχ) of the peaks is also reported.

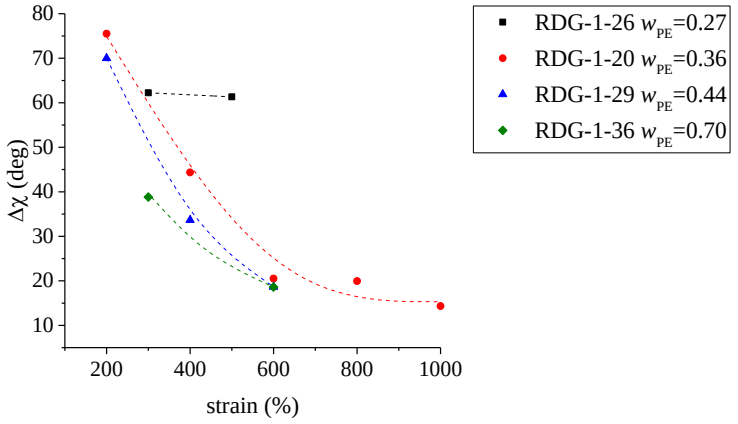

Figure 1.23 Values of the full width at half maximum (Δχ) of the 110 reflection of the orthorhombic form of PE, evaluated from the azimuthal profiles shown in Figures 1.19-1.22, as a function of the strain, for the PE-*b*-PHD BCPs.

1.1.6 Morphological characterization

A preliminary analysis of morphology of PE-*b*-PHD BCPs by Transmission Electron Microscopy was also performed, in the case of the sample RDG-1-29 (w_{PE}=0.44). A thin film of the sample (thickness<100nm) has been deposited on a copper grid by casting from a diluted solution (0.5%wt) of the BCP in p-xylene. The thin polymer film thus obtained is then subjected to melting at a temperature of 180°C, maintained at this temperature for 36 hours (in an oven at reduced pressure), and then quenched by putting it in contact with a metallic panel immersed in liquid N_2. The temperature of the metallic panel is around -20°C. This particular thermal treatment has been selected in order to induce the crystallization of the PE blocks at low temperatures, and possibly prevent disruption of the nanostructure established in the melt, through vitrification of the amorphous matrix. On the basis of the value of the volume fraction of the blocks, a lamellar morphology developing in the melt is expected for this sample.

In Figure 1.24 the TEM images obtained for the so prepared sample, at different magnifications, are shown. TEM images where collected over RuO_4 stained samples. RuO_4 staining should allow distinguishing lamellar features from the surrounding amorphous environment. However, the TEM images of Figure 1.24 show no features. This indicates that the technique used for preparing and staining the BCP does not allow to mark the morphology developing in the solid state. TEM analysis deserves a more in depth and accurate investigation.

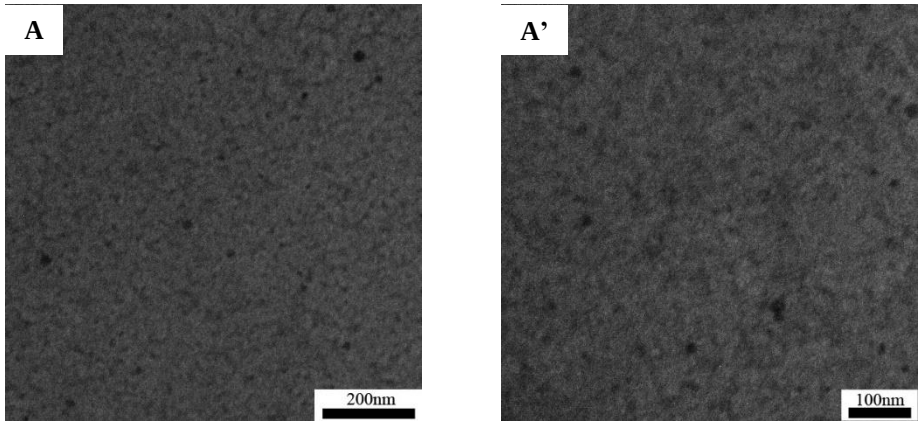

Figure 1.24 TEM images at different magnifications collected over RuO4 stained samples of RDG-1-29 (w_{PE}=0.44) quenched from the melt at ≈ -20°C.

1.2 Polyethylene-*b*-poly(ethylene-*co*-vinyl cyclohexene) di-block copolymers PE-*b*-P(E-*co*-VCH)

In this paragraph, the structural characterization of semicrystalline di-block copolymers having a crystalline block made of polyethylene (PE) and an amorphous block made of a random copolymer of ethylene and vinyl cyclohexene (P(E-*co*-VCH)) is reported (Figure 1.25).

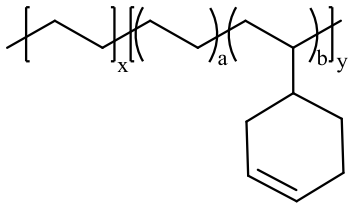

Figure 1.25 Structure of the polyethylene-*block*-poly(ethylene-*co*-vinyl cyclohexene) di-block copolymers.

These BCPs are extremely interesting materials since they may be used as precursors of novel functional thermoplastic materials with high thermal and mechanical resistance. In fact, the VCH units in the amorphous block bear pendant reactive moieties that provide easy access to a wide range of functionalities.[27] By combining the high melting temperature crystalline PE block with a functionalized P(E-*co*-VCH) block, thermoplastic materials for advanced applications may be obtained. Moreover, the mechanical properties of these BCPs having a rigid crystalline block linked to an amorphous rubbery block may be of interest for uses which require advanced function in robust materials.

1.2.1 Materials and methods

A sample of PE-*b*-P(E-*co*-VCH) BCP having a mass fraction of the PE block (w_{PE}) equal to 0.59 was synthesized by living polymerization with a C_s-symmetric pyridylamidohafnium dimethyl complex activated with $B(C_6F_5)_3$. The synthetic procedure, consisting in the sequential synthesis of the PE and P(E-*co*-VCH) blocks, is shown in Scheme 1.2.

A sample of P(E-*co*-VCH) random copolymer was also synthesized by means of the same catalyst and in the same reaction conditions used for the synthesis of the PE-*b*-P(E-*co*-VCH) BCP.

The P(E-*co*-VCH) random copolymer was synthesizes by the following procedure: in the glovebox, a 200mL Lab-Crest® pressure reaction vessel (Andrews Glass) was charged with toluene, diisobutylaluminumphenolate (DIBAP) scavenger and vinyl cyclohexene. The glass reactor was sealed and saturated with ethylene under a constant feed. The solution was allowed to stir in a 20°C water bath for 15min prior to inject the Hf precatalyst solution containing the catalyst (see scheme 1.2), $B(C_6F_5)_3$ and toluene. Ethylene feed was interrupted right before the catalyst injection. The polymerization was allowed to proceed for 30min and then quenched by addition of a methanol/HCl solution with simultaneous venting of the reactor. The polymer was precipitated in copious methanol, stirred overnight, and then collected via filtration. The polymer was dried to constant weight in vacuo at 25°C.

The PE-*b*-P(E-*co*-VCH) BCP was synthesized by a similar procedure: a 200mL glass reactor (Andrews Glass) was charged under nitrogen with dry toluene and diisobutylaluminumphenolate (DIBAP) scavanger, thermostated at 20°C under stirring, and saturated with ethylene. Polymerization was initiated by injection of the precatalyst solution (Hf precatalyst and $B(C_6F_5)_3$ in toluene) under constant ethylene feed. The polymerization was allowed to proceed for the desired period of time (10min), then an aliquot of the polymerization medium (PE block) was removed for GPC analysis and vinyl cyclohexene was injected in the reactor. The second stage of the polymerization (P(E-*co*-VCH) block) was allowed to proceed under a constant feed of ethylene for 30min. The polymerization was terminated by injecting a methanol/HCl solution. The polymer was precipitated into copious methanol and allowed to stir overnight. It was then collected via filtration and dried in vacuo to constant weight at 25°C.

The molecular characteristics of these samples are shown in Table 1.8.

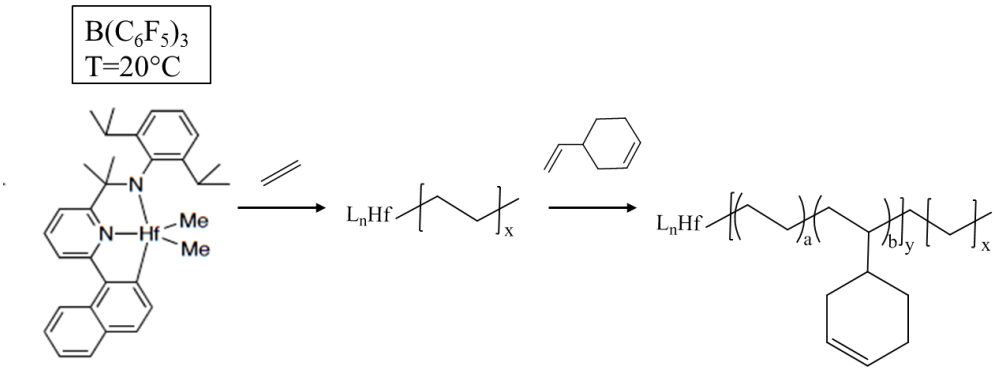

Scheme 1.2 Structure of pyridylamidohafnium dimethyl complex activated with $B(C_6F_5)_3$ used as catalyst for the preparation of the PE-*b*-P(E-*co*-VCH) BCP and scheme of the sequential polymerization procedure.

Table 1.8 Total molecular mass ($M_{n\ TOT}$), molecular mass of the PE block ($M_{n\ PE}$) and P(E-*co*-VCH) block ($M_{n\ PEVCH}$), polydispersity index (M_w/M_n), mass (w_{PE}) and volume (f_{PE}) fractions of the PE block, content of vinyl cyclohexene monomer in the P(E-*co*-VCH) block.

SAMPLE	M_n[a] TOT (Kg/mol)	M_n[a] PE (Kg/mol)	M_n[b] PEVCH (Kg/mol)	$\frac{M_w}{M_n}$[a]	w_{PE}[c]	f_{PE}[d]	VCH[e] (mol%)
RDG-1-126	113.8	-	-	1.23	1	1	27
RDG-1-130	121.3	71.6	49.7	1.28	0.59	0.55[d]	27

a evaluated from GPC analysis; **b** calculated from $M_{n\ TOT}$ and $M_{n\ PE}$ as $M_{n\ PEVCH}=M_{n\ TOT}-M_{n\ PE}$; **c** calculated as $M_{n\ PE}/M_{n\ TOT}$; **d** calculated from the molecular masses $M_{n\ PE}$ and $M_{n\ TOT}$ and the densities of PE (0.996 g/cm^3) and of the PE-*b*-P(E-*co*-VCH) BCP (0.929 g/cm^3) as $f_{PE}=(M_{n\ PE}/0.996)/(M_{n\ TOT}/0.929)$. The density of PE is the theoretical value for a sample having 100% crystallinity, the density of the PE-*b*-P(E-*co*-VCH) BCP has been experimentally determined by flotation as described in Appendix 3. **e** evaluated from ^{13}C-NMR as described in Appendix 1 section 2.

The composition of the P(E-*co*-VCH) random copolymer has been determined by ^{13}C-NMR analysis as described in Appendix 1 section 2. Since the P(E-*co*-VCH) random copolymer has been synthesized with the same catalyst as the PE-*b*-P(E-*co*-VCH) BCP and, in particular, in the same reaction conditions as the P(E-*co*-VCH) block, we assume that the concentration of VCH (mol%) determined for the random copolymer is equal to that of the P(E-*co*-VCH) block of the BCP. ^{13}C-NMR spectra were obtained with a Bruker Advance spectrometer (400 MHz) equipped with a 5 mm high temperature cryoprobe operating on 50mg/mL solutions in 1,1,2,2-tetrachloroethane-d2 at 120°C.

The thermal characterization of the samples has been carried out by calorimetric measurements performed with a differential scanning calorimeter (DSC-822 by Mettler Toledo) in a flowing N_2 atmosphere and at a scanning rate of 10°C/min.

The structural characterization has been carried out by X-ray scattering technique using a Ni-filtered CuKα radiation. Wide angle X-ray scattering (WAXS) analysis has been performed on powder and fiber samples using an automatic diffractometer (Philips) and a cylindrical camera equipped with a MS (MultiSensitive) phosphor storage imaging plate (Fujifilm) respectively. Small angle X-ray scattering (SAXS) analysis has been performed with a Kratky compact camera diffractometer working in line collimation geometry (SAXSess by Anton Paar) equipped with a MS phosphor storage imaging plate (Fujifilm), in a configuration that allows collecting simultaneously SAXS and WAXS patterns. The SAXS/WAXS data recorded on MS imaging plates have been read with a digital imaging reader Cyclone Plus (Perkin Elmer) and then processed with SAXSquant2D and SAXSquant1D software by Anton Paar to obtain the calculated (desmeared) SAXS profiles in point collimation geometry.

Mechanical characterization has been performed at room temperature with a universal mechanical tester (Zwicky by Zwick Roell) following the standard test method for tensile properties of thin plastic sheets, ASTM D882-83. The mechanical parameters reported for each sample are averaged results from at least five independent experiments.

1.2.2 WAXS and thermal analyses of as prepared and compression moulded samples

X-ray powder diffraction profiles of as prepared samples (A) and of compression moulded samples (A') of the PE-*b*-P(E-*co*-VCH) BCP and of the P(E-*co*-VCH) random copolymer are shown in Figure 1.26. The X-ray powder diffraction profiles of the P(E-*co*-VCH) random copolymer, RDG-1-126, (curves a of Figure 1.26 A and A'), show an halo centered at 2θ=18.6°, indicating that the sample is amorphous. The X-ray powder diffraction profiles of the PE-*b*-P(E-*co*-VCH) BCP, RDG-1-130 (w_{PE}=0.59) (curves b of Figure 1.26 A and A') show two Bragg peaks at 2θ≈21° and 2θ≈24°, overlaying an amorphous halo, due to the 110 and 200 reflections, respectively, of the orthorhombic form of PE.

The degree of crystallinity calculated for the PE-*b*-P(E-*co*-VCH) BCP is reported in Table 1.9.

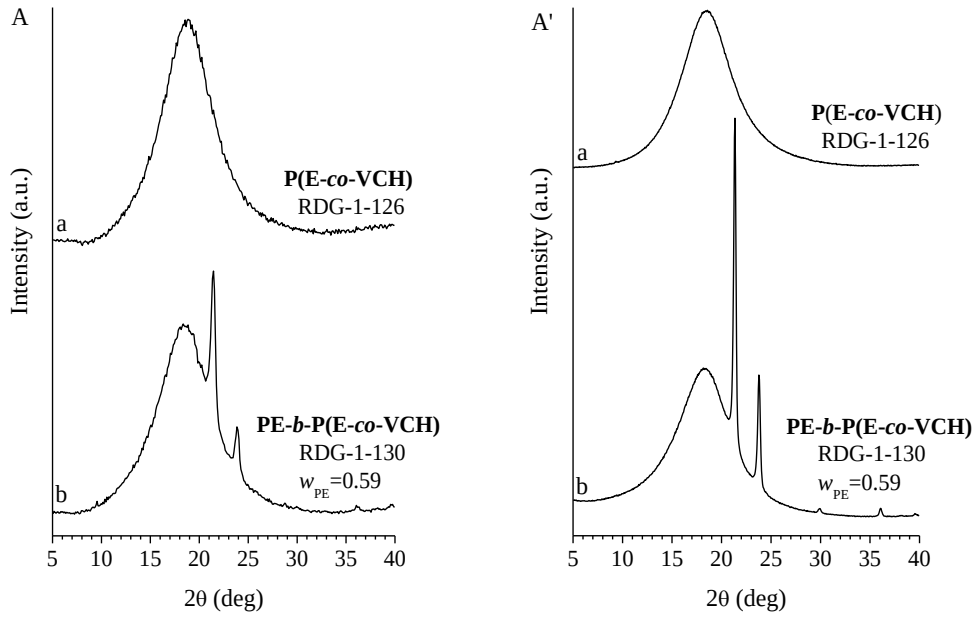

Figure 1.26 X-ray powder diffraction profiles of as prepared (A) and compression moulded (A') samples of the P(E-*co*-VCH) random copolymer (a) and PE-*b*-P(E-*co*-VCH) BCP (b).

DSC thermograms of the as prepared and compression molded samples of the PE-*b*-P(E-*co*-VCH) BCP and of the P(E-*co*-VCH) random copolymer are shown in Figure 1.27 and Figure 1.28.

The DSC heating and cooling thermograms of the P(E-*co*-VCH) random copolymer (curves a of Figure 1.27 and 1.28), show a glass transition at $T_g \approx$ -20°C. A small melting peak at T=51°C is also present in the first heating scan of the as prepared sample of the random copolymer (curve a Figure 1.27 A), indicating the presence of short crystallizable ethylene sequences along the chain. However, these sequences are not able to crystallize in the successive cooling step (curve a in Figure 1.27 B) and or form the melt (curves a of Figure 1.27 C and 1.28).

The DSC heating thermograms of the PE-*b*-P(E-*co*-VCH) BCP show an endothermic peak at T=133°C which is relative to the melting of the crystalline PE block (curves b of Figure 1.27 A, C and 1.28 A, C). The crystallization temperature of PE blocks is ≈120°C (curves b of Figure 1.27 B and 1.28 B). However, in the DSC cooling scans of the BCP sample, a small exothermic peak at $T \approx$78°C is also present (curves b of Figure 1.27 B and 1.28 B), probably related to the crystallization of short ethylene sequences in the P(E-*co*-VCH) block. These crystals probably melt at the same temperature as the crystals in the PE block, since no additional exothermic peaks besides

the main peak at 133°C are observed in the heating thermograms (curves b of Figure 1.27 A, C and 1.28 A, C). Therefore, contrary to the random copolymer sample, short ethylene sequences belonging to the random copolymer block in the BCP show some crystallization from melt, probably favored by epitaxy, on the crystals of the PE block which form during the cooling at higher temperature.

The values of the melting temperature and enthalpy recorded during the first (T_m^I, ΔH_m^I) and second heating (T_m^{II}, ΔH_m^{II}), crystallization temperature and enthalpy (T_c, ΔH_c) and glass transition temperature (T_g) for both the as prepared and compression moulded samples of the P(E-*co*-VCH) random copolymer and PE-*b*-P(E-*co*-VCH) BCP are reported in Table 1.9.

Table 1.9 Mass fraction of the PE block (w_{PE}), values of the degree of crystallinity referred to the whole sample (x_c) and to the PE block ($x_{c\ PE}$), of the melting temperature and enthalpy recorded during the first (T_m^I, ΔH_m^I) and second (T_m^{II}, ΔH_m^{II}) heating, of the crystallization temperature and enthalpy (T_c, ΔH_c) and of the glass transition temperature (T_g) of as prepared and compression molded samples of the P(E-*co*-VCH) random copolymer and of the PE-*b*-P(E-*co*-VCH) BCP.

SAMPLE	w_{PE}	x_c **(%)**	$x_{c\ PE}$ **(%)**	T_m^I **(°C)**	ΔH_m^I **(J/g)**	T_m^{II} **(°C)**	ΔH_m^{II} **(J/g)**	T_c **(°C)**	ΔH_c **(J/g)**	T_g **(°C)**
As prepared samples										
RDG-1-126	-	0	0	50	-1.2	-	-	-	-	-21
RDG-1-130	0.59	8	13	138	-35.2	134	-26.6	78;120	3.4;23.5	-21
Compression molded samples										
RDG-1-126	-	0	0	-	-	-	-	-	-	-21
RDG-1-130	0.59	14	24	133	-31.6	135	-28.4	79;121	4.3;33.2	-20

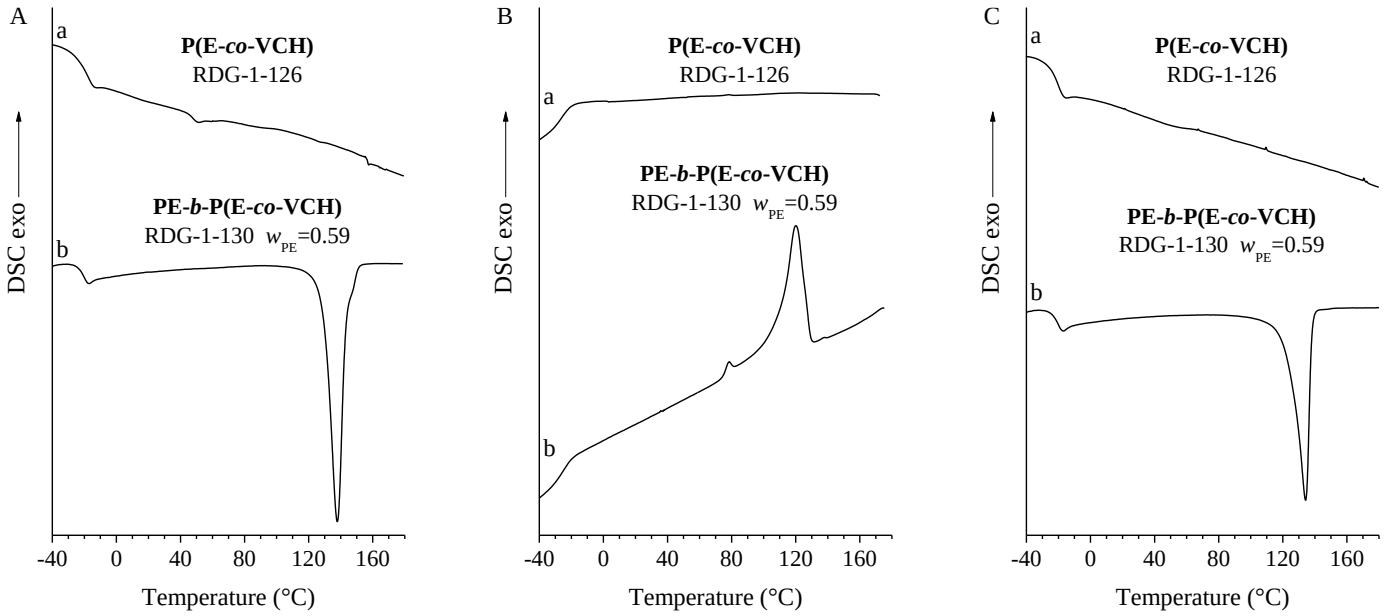

Figure 1.27 DSC thermograms recorded during heating (A), successive cooling (B) and second heating (C) of as prepared samples of the P(E-*co*-VCH) random copolymer (a) and of the PE-*b*-P(E-*co*-VCH) BCP (b).

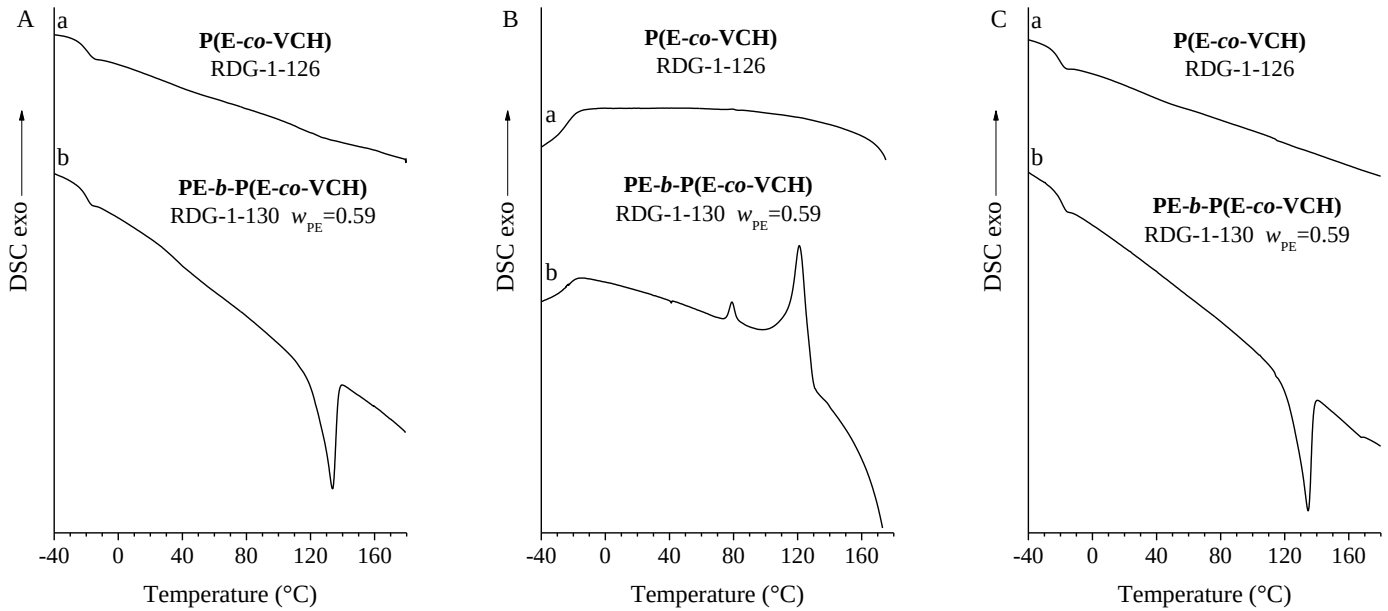

Figure 1.28 DSC thermograms recorded during heating (A), successive cooling (B) and second heating (C) of compression molded samples of the P(E-*co*-VCH) random copolymer (a) and of the PE-*b*-P(E-*co*-VCH) BCP (b).

1.2.3 SAXS/WAXS analysis as a function of temperature

WAXS and SAXS data of a film of the BCP sample PE-*b*-P(E-*co*-VCH) were measured step-wise in the temperature range 25-180°C in a heating/cooling run. Data were collected simultaneously on melt cooled samples obtained by compression molding. Room temperature measurements were also performed on the P(E-*co*-VCH) random copolymer. Results are shown in Figure 1.29 and 1.30. For the BCP sample, the SAXS intensity profiles corrected for the Lorentz factor are also reported.

The SAXS profile of the random copolymer recorded at 25°C (Figure 1.29) shows deviation from a q^{-4} dependence in the sampled q range, probably due to the presence of isolated lamellae with low contrast embedded in the amorphous matrix.

The SAXS pattern of the sample RDG-1-130 (w_{PE}=0.59) recorded at 25°C before heating (curve a of Figure 1.30 A) shows a faint correlation peak of low intensity at $q^*\approx0.1nm^{-1}$, corresponding to a correlation distance $L_B\approx63nm$. The position of the correlation peak is confirmed in the Lorentz corrected intensity profile (curve a of Figure 1.30 C) which shows a peak at $q^*=0.105nm^{-1}$ (L_B=59nm). The correlation peak is relative to the presence of crystalline lamellar aggregates of the PE block, as confirmed by the SAXS patterns of the melt (recorded at 180°C and 150°C), wherein the correlation peak disappears (curves b, c of Figure 1.30 A). Moreover, the absence of any feature in the SAXS profile of the melt indicates that for this sample, either crystallization occurs from a homogeneous melt, or that heterogeneity occurs at higher length scales than those accessible in our measurements. Finally, by cooling the melt, the correlation peak due to lamellar stacking reappears $q^*=0.091nm^{-1}$ (L_B=69nm) (curves d-g in Figure 1.30 A).

The correlation function of PE-*b*-P(E-*co*-VCH) BCP calculated from the SAXS profile recorded at 25°C is shown in Figure 1.31. The shape of the correlation function obtained for this sample corresponds to that expected for a biphasic lamellar morphology. The value of P (64nm) evaluated from the abscissa of the secondary maximum of $p(r)$ is similar to the value of L_B evaluated from the position of the correlation peak in the SAXS profile recorded at 25°C. The minimum layer thickness corresponds to l_c ($x_{c\,PE}$<50%) and is equal to 8.2nm.

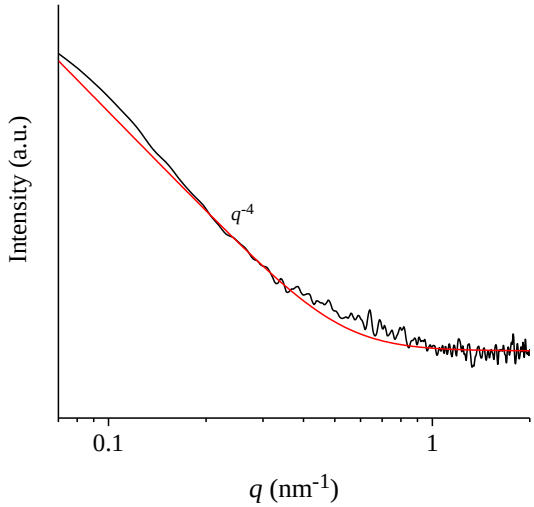

Figure 1.29 SAXS intensity profile of the P(E-*co*-VCH) random copolymer RDG-1-126, recorded at 25°C.

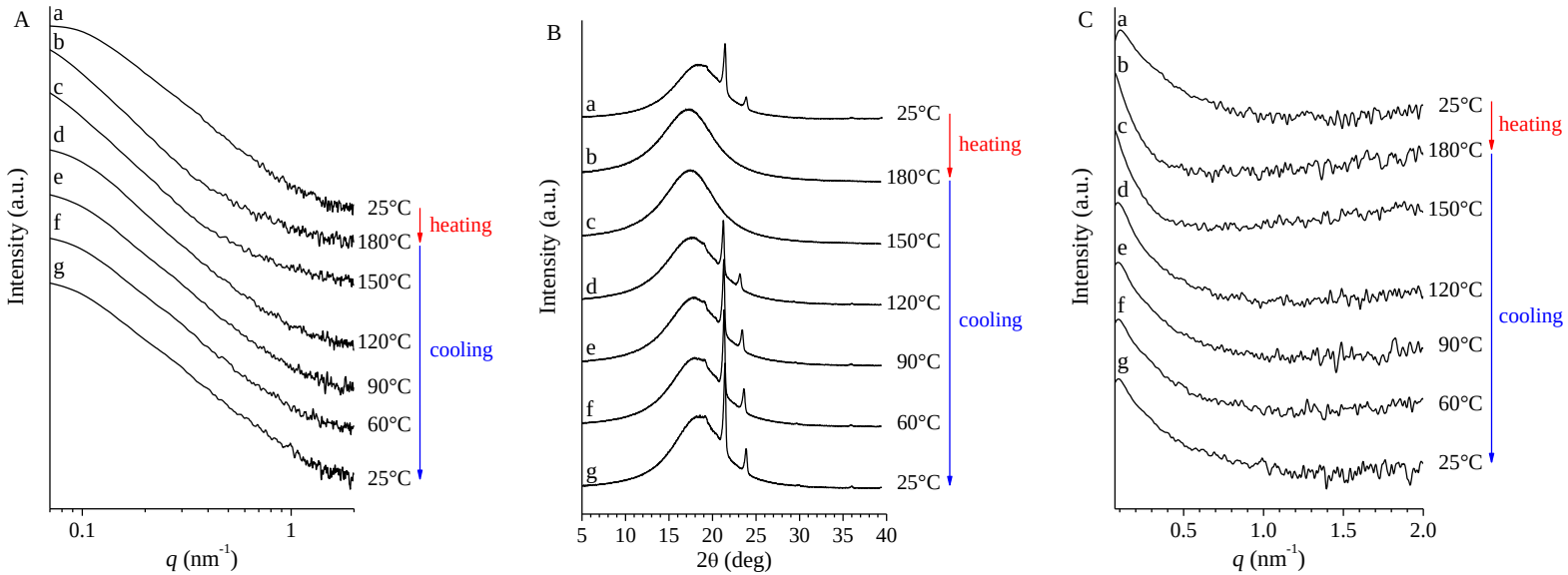

Figure 1.30 SAXS (A), WAXS (B) and Lorentz corrected (C) intensity profiles recorded at the indicated temperatures during heating and successive cooling of the PE-*b*-P(E-*co*-VCH) sample RDG-1-130 (w_{PE}=0.59).

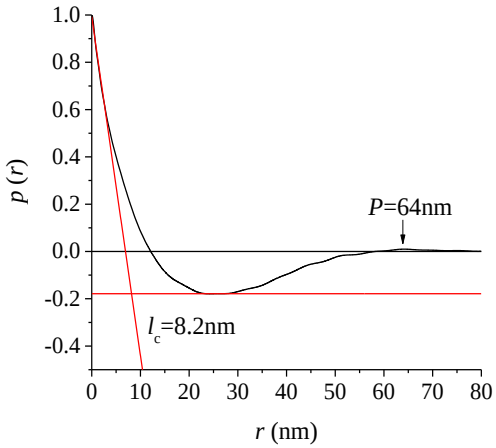

Figure 1.31 Normalized correlation function obtained for the PE-*b*-P(E-*co*-VCH) sample RDG-1-130 (w_{PE}=0.59) from the experimental SAXS profile recorded at 25°C.

Table 1.10 Molecular mass ($M_{n\ PE}$), mass fraction (w_{PE}) and degree of crystallinity ($x_{c\ PE}$) of the PE block. Position of the correlation peak (q^*), value of the Bragg distance (L_B), periodicity of the lamellar stack (P), crystalline (l_c) and amorphous (l_a) layers thickness of the crystalline PE block in PE-*b*-P(E-*co*-VCH) BCP.

SAMPLE	$M_{n\ PE}$ (Kg/mol)	w_{PE}	$x_{c\ PE}$ (%)	q^* (nm^{-1})	L_B (nm)	P (nm)	l_c (nm)	l_a (nm)
RDG-1-130	71.6	0.59	25	0.091	69	64	8.2	55.8

1.2.4 Mechanical characterization

The mechanical characterization of the compression molded samples of the P(E-*co*-VCH) random copolymer and of the PE-*b*-P(E-*co*-VCH) BCP has been performed by means of tensile tests. The stress-strain curves obtained for these samples are shown in Figure 1.32. The mechanical parameters obtained from these curves are reported in Table 1.11.

The stress-strain curves show that the P(E-*co*-VCH) random copolymer behaves like a typical amorphous, rubbery material with low value of the Young's modulus, no yield point and high deformation at break. The very small or absent crystallinity and the relatively low molecular mass produce a region of cold drawing, at constant stress up to breaking, with no strain hardening. When the same amorphous block is linked to a crystalline PE block the mechanical behavior changes to that of a more rigid material with a higher value of the Young's modulus, lower value of the deformation at break and high strain hardening.

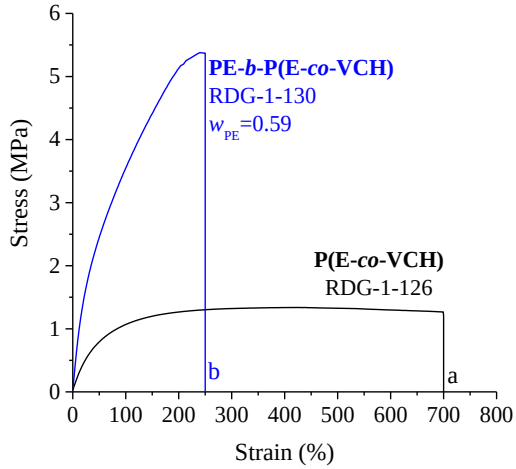

Figure 1.32 Stress-strain curves of the compression-molded samples of the P(E-*co*-VCH) random copolymer (a) and of the PE-*b*-P(E-*co*-VCH) BCP (b).

Table 1.11 Total molecular mass ($M_{n\ TOT}$), molecular mass ($M_{n\ PE}$) and mass fraction (w_{PE}) of the PE block, Young's modulus (E), elongation at break (ε_b) and stress at break (σ_b) of the P(E-*co*-VCH) random copolymer and of the PE-*b*-P(E-*co*-VCH) BCP.

SAMPLE	$M_{n\ TOT}$ (Kg/mol)	$M_{n\ PE}$ (Kg/mol)	w_{PE}	E (MPa)	ε_b (%)	σ_b (MPa)
RDG-1-126	113.8	-	1	2.2±0.4	700±200	1.2±0.2
RDG-1-130	121.3	71.6	0.59	7.3±0.9	250±40	5±1

CHAPTER 2

Isotactic polypropylene-based semicrystalline di-block copolymers

2.1 Isotactic polypropylene-*b*-poly(propylene-*co*-vinyl cyclohexene) di-block copolymers iPP-*b*-P(P-*co*-VCH)

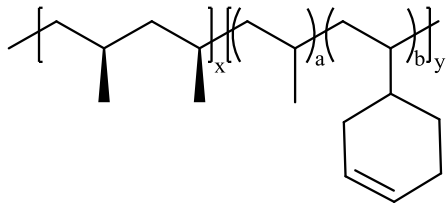

Figure 2.1 Structure of the isotactic polypropylene-*block*-poly(propylene-*co*-vinyl cyclohexene) di-block copolymers.

Semicrystalline di-block copolymers having a crystalline block made of isotactic polypropylene (iPP) and an amorphous block made of a random copolymer of propene and vinyl cyclohexene (P(P-*co*-VCH)) (Figure 2.1) have been studied.

The interest for these BCPs arises from the presence of a double bond in the VCH units and the consequent possibility to add functionalities and access new properties. In the present contest, the main interest stems from the intrinsic polymorphism of the iPP blocks. In fact, iPP homopolymer shows a complex polymorphic behavior due to the existence of three different crystalline forms (α, β and γ) and of a mesomorphic form. They are obtained from the melt under different crystallization conditions[28] and show different physical and mechanical properties. By linking an iPP block with a chemically different block it is possible to combine the wide range of morphologies developing in crystalline BCPs with the polymorphism of iPP and, by selecting the proper crystallization conditions, it is possible to tailor the properties of this class of materials.

2.1.1 Materials and methods

Samples of iPP-*b*-P(P-*co*-VCH) BCPs were synthesized by living polymerization with a C_s-symmetric pyridylamidohafnium dimethyl complex activated with $B(C_6F_5)_3$. The synthetic procedure, consisting in the sequential synthesis of the iPP and P(P-*co*-VCH) blocks, is shown in Scheme 2.1.

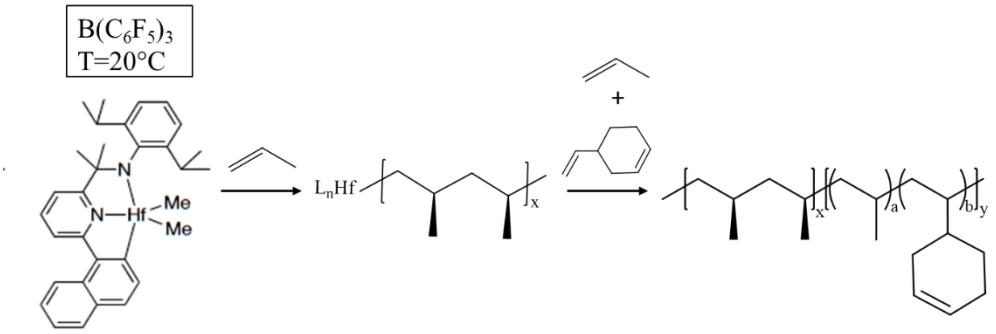

Scheme 2.1 Structure of pyridylamidohafnium dimethyl complex activated with $B(C_6F_5)_3$ used as catalyst for the preparation of the iPP-*b*-P(P-*co*-VCH) BCPs and scheme of the sequential polymerization procedure.

Two samples of iPP-*b*-P(P-*co*-VCH) with different mass fractions of the iPP block (w_{iPP}), were synthesized. A sample of P(P-*co*-VCH) random copolymer and a sample of iPP homopolymer were also synthesized by means of the same catalyst and in the same reaction conditions used for the synthesis of the iPP-*b*-P(P-*co*-VCH) BCPs.

In particular, the P(P-*co*-VCH) random copolymer was synthesizes by the following procedure: a 200mL Lab-Crest® pressure reaction vessel was charged with toluene, diisobutylaluminumphenolate (DIBAP) scavanger and vinyl cyclohexene. The glass reactor was sealed and saturated with propylene under a constant feed. The solution was allowed to stir in a 20°C water bath for 20 minutes prior to injection of the Hf precatalyst solution containing the pyridylamidohafnium catalyst, $B(C_6F_5)_3$ and toluene. Propylene feed was interrupted right before catalyst injection. The polymerization was allowed to proceed for 30min and then quenched by addition of a methanol/HCl solution with simultaneous venting of the reactor. The polymer was precipitated in copious methanol, stirred overnight, and then collected via filtration. The polymer was dried to constant weight in vacuo at 25 °C.

The iPP-*b*-P(P-*co*-VCH) BCPs were synthesized by a similar procedure: a 200mL glass reactor (Andrews Glass) was charged in a nitrogen-filled glove box with toluene and DIBAP scavanger. The reaction vessel was sealed and

charged with propylene gas and stirred for 1h at room temperature in a water bath. In the glovebox, a vial was charged with pyridylamidohafnium catalyst along with $B(C_6F_5)_3$. This co-catalyst mixture was then dissolved in toluene and transferred via a gas-tight syringe to the glass reactor. The polymerization was allowed to proceed for 20-25min (depending on the desired block length) under constant propylene feed to produce the iPP block. Thereafter, an aliquot of the polymerization medium was removed for GPC analysis, and vinyl cyclohexene was injected in the reactor. The second block polymerization P(P-*co*-VCH) was allowed to proceed for the desired amount of time (40-70min depending on the desired block length) and then quenched by addition of a methanol/HCl solution with simultaneous venting of the reactor. The polymer was precipitated in copious methanol, stirred overnight, and then collected via filtration. The polymer was dried to constant weight in vacuo at 25 °C.

The molecular characteristics of samples are shown in Table 2.1.

Table 2.1 Total molecular mass ($M_{n\ TOT}$), molecular mass of the iPP block ($M_{n\ iPP}$) and of the P(P-*co*-VCH) block ($M_{n\ PPVCH}$), polydispersity index (M_w/M_n), mass fraction (w_{iPP}) and volume fraction (f_{iPP}) of the iPP block, concentration of the vinylcyclohexene units in the P(P-*co*-VCH) block (VCH).

SAMPLE	$M_{n\ TOT}$[a] (Kg/mol)	$M_{n\ iPP}$[a] (Kg/mol)	$M_{n\ PPVCH}$[b] (Kg/mol)	$\frac{M_w}{M_n}$[a]	w_{iPP}[c]	f_{iPP}[d]	VCH[e] (mol%)
RDG-1-142	45	-	-	1.31	-	-	3
RDG-1-41	139.8	-	-	1.29	1	1	-
RDG-1-143	55.9	43.5	12.4	1.36	0.78	0.75	7
RDG-1-145	80.5	54.2	26.3	1.39	0.67	0.65	7

a evaluated from GPC analysis; **b** calculated from $M_{n\ TOT}$ and $M_{n\ iPP}$ as $M_{n\ PPVCH}=M_{n\ TOT}-M_{n\ iPP}$; **c** calculated as $M_{n\ iPP}/M_{n\ TOT}$; **d** calculated from the molecular masses $M_{n\ iPP}$ and $M_{n\ TOT}$ and the densities of iPP (ρ_{iPP}=0.936 g/cm^3) and of the iPP-*b*-P(P-*co*-VCH) BCPs ($\rho_{iPP\text{-}b\text{-}P(P\text{-}co\text{-}VCH)}$) as $f_{iPP}=(M_{n\ iPP}/\rho_{iPP})/(M_{n\ TOT}/\rho_{iPP\text{-}b\text{-}P(P\text{-}co\text{-}VCH)})$. The density of iPP is the theoretical value for a sample having 100% crystallinity, the densities of the iPP-*b*-P(P-*co*-VCH) BCPs have been experimentally as described in Appendix 3.; **e** evaluated from ^{13}C-NMR as described in Appendix 1 section 3.

The VCH content in the P(P-*co*-VCH) random copolymer and in the iPP-*b*-P(P-*co*-VCH) BCPs has been determined by ^{13}C-NMR analysis as described in Appendix 1 section 3. Since the two iPP-*b*-P(P-*co*-VCH) BCPs have been synthesized with the same catalyst we have assumed that the VCH content determined for the P(P-*co*-VCH) block in the sample RDG-1-143

(w_{iPP}=0.78) is identical to that of the P(P-*co*-VCH) block in the sample RDG-1-145 (w_{iPP}=0.67).

The characterization has been performed on as prepared samples and/or on compression molded samples. Compression molded samples have been prepared by heating the as prepared sample at ≈160°C under a press at very low pressure, keeping it at this temperature for 5min, and cooling it down to room temperature at a cooling rate of about 15°C/min.

The thermal characterization of the samples has been carried out by calorimetric measurements performed with a differential scanning calorimeter (DSC-822 by Mettler Toledo) in a flowing N_2 atmosphere and at a scanning rate of 10°C/min.

The structural characterization has been carried out by X-ray scattering technique using a Ni-filtered CuKα radiation. Wide angle X-ray scattering (WAXS) analysis has been performed on unoriented (powder) and oriented (fiber) samples using an automatic diffractometer (Philips) and a cylindrical camera equipped with a MS (MultiSensitive) phosphor storage imaging plate (Fujifilm), respectively. Small angle X-ray scattering (SAXS) analysis has been performed with a Kratky compact camera working in line collimation geometry (SAXSess by Anton Paar) equipped with a MS imaging plate (Fujifilm) and conventional X-ray source. The apparatus allows collecting simultaneously WAXS and SAXS data. The WAXS/SAXS data recorded on MS imaging plates have been read with a digital imaging reader Cyclone Plus (Perkin Elmer) and then processed with SAXSquant2D and SAXSquant1D software by Anton Paar to obtain the calculated (desmeared) SAXS profiles in point collimation geometry.

Time/temperature resolved SAXS/WAXS analysis has been carried out on BM26B (DUBBLE) station at the European Synchrotron Radiation Facility (ESRF) in Grenoble, France. A modified DSC Linkam hot stage permitting the transmission of the X-rays through the sample has been employed for the in situ thermal treatment of the samples. The data have been acquired during the heating/cooling of the sample at a rate of 10°C/min or 30°C/min, with an acquisition time of 6 s, a delay time of 6 s and a wavelength of 1.0402 Å.

Mechanical characterization has been performed at room temperature with a universal mechanical tester (Zwicky by Zwick Roell) following the standard test method for tensile properties of thin plastic sheets, ASTM D882-83. The mechanical parameters reported for each sample are averaged results from at least five independent experiments.

Morphological characterization has been performed by using an optical miscroscope (Zeiss Axioskop 40) working in polarized light (POM), a Transmission Electron Microscope (TEM) (Philips EM 208S) operating at 100kV and an atomic force microscope (AFM) (Veeco Caliber microscope) working in tapping mode.

2.1.2 WAXS and thermal analyses of as prepared and compression molded samples

X-ray powder diffraction profiles of as prepared samples (A) and of compression molded samples (A') of the iPP-*b*-P(P-*co*-VCH) BCPs and of the iPP homopolymer and P(P-*co*-VCH) random copolymer are shown in Figure 2.2. The X-ray powder diffraction profile of the as prepared P(P-*co*-VCH) random copolymer (curve a in Figure 2.2 A) mainly shows an amorphous halo, centered at 2θ≈15-17°, and two low-intensity crystalline reflections at 2θ ≈14° and 17°. In the X-ray powder diffraction profile of the compression molded sample (curve a in Figure 2.2 A') the low-intensity crystalline reflections are barely visible. These two profiles indicate that in the P(P-*co*-VCH) random copolymer slight iPP crystallinity is observed, in agreement with the low concentration of VCH units (3mol%). The X-ray powder diffraction profiles of as prepared and compression molded iPP homopolymer, (curve b in Figure 2.2 A and A' respectively), show that iPP mainly crystallizes in the α form, as indicated by the presence of the $(130)_\alpha$ reflection at 2θ=18.3°. In the X-ray diffraction profile of the compression molded sample, a low-intensity crystalline reflection at 2θ=20° is also present. It corresponds to the $(117)_\gamma$ reflection of the γ form of iPP (see Appendix 2), indicating that in the compression molded sample, a small amount of γ form is also present. The X-ray powder diffraction profiles of the as prepared and compression molded samples of the iPP-*b*-P(P-*co*-VCH) BCPs (curves c-d in Figure 2.2 A and A' respectively) show the same crystalline reflections as iPP homopolymer, due to the crystallization of the iPP block. The iPP block mainly crystallizes in the α form, as indicated by the $(130)_\alpha$ reflection at 2θ=18.6°. Only in the case of the sample RDG-1-145 (w_{iPP}=0.68), a low-intensity $(117)_\gamma$ reflection at 2θ=20° also appears, indicating that small amounts of γ form crystallites are also present (curve d of Figure 1.2 A'). Moreover, the X-ray diffraction profile of the compression molded sample of RDG-1-145 (w_{iPP}=0.68) reveals that

compression molding induces partial orientation of the crystals, as indicated by the high intensity of the (040) reflection at 2θ=17.1°.

The degree of crystallinity calculated for the iPP homopolymer and for the iPP-*b*-P(P-*co*-VCH) BCPs is reported in Table 2.2 for the as prepared samples and in Table 2.3 for the compression molded samples.

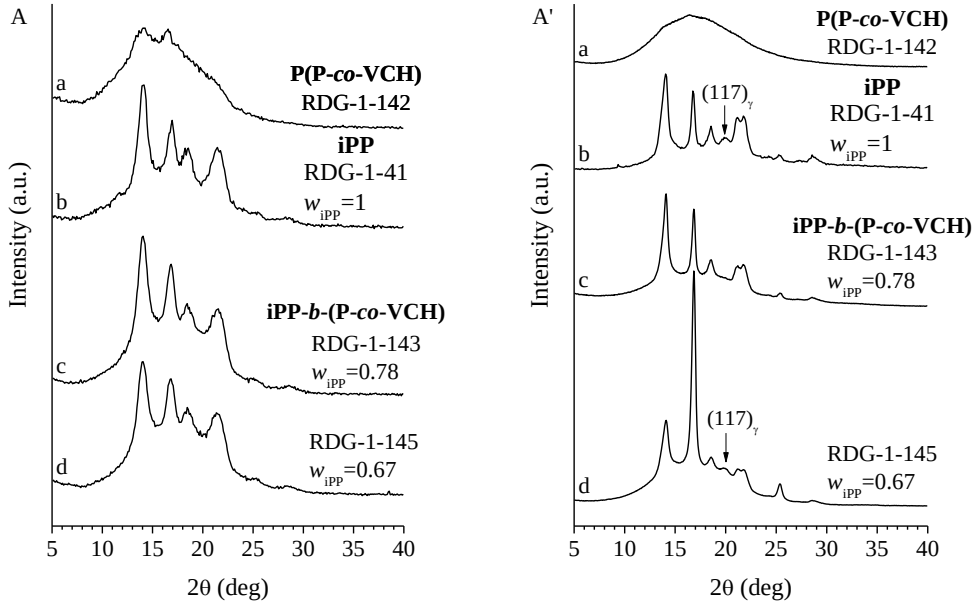

Figure 2.2 X-ray powder diffraction profiles of as prepared (A) and compression molded (A') samples of P(P-*co*-VCH) random copolymer (a), iPP homopolymer (b) and of iPP-*b*- P(P-*co*-VCH) BCPs (c-d).

DSC thermograms of the as prepared and compression molded samples of the P(P-*co*-VCH) random copolymer, iPP homopolymer and iPP-*b*-P(P-*co*-VCH) BCPs are shown in Figure 2.3 and Figure 2.4, respectively. The thermograms are recorded during the first heating from -40°C to 180°C (A), successive cooling from 180°C to -40°C (B) and second heating from -40°C to 180°C (C).

The DSC thermogram of the as prepared sample of the P(P-*co*-VCH) random copolymer recorded during the first heating (curve a in Figure 2.3 A), shows the inflection point relative to the glass transition at 3°C (T_g) and multiple endothermic peaks in the range 50-90°C relative to the melting of the small and defective crystals of iPP observed in WAXS analysis. At T>120°C, oxidation or degradation phenomena of the sample are observed. The cooling thermogram (curve a in Figure 2.3 B) and the second heating thermogram (curve a in Figure 2.3 C) only show the inflection point relative to the T_g at

3°C, indicating that no crystallinity develops upon cooling the sample from the melt, and that the extend of oxidation/degradation reactions occurring by effect of heating up to 160°C, may be neglected.

The DSC thermograms of the as prepared sample of the iPP homopolymer, recorded during the heating and cooling of the sample, show that the crystals in the α form melt at ≈134-135°C (curve b in Figure 2.3 A and C) and crystallize at T=102°C (curve b in Figure 2.3 B).

The DSC thermograms of the as prepared samples of iPP-*b*-P(P-*co*-VCH) BCPs recorded during the first heating (curves c-d in Figure 2.3 A) show a main endothermic peak at T=127°C relative to the melting of the crystalline iPP block, and low temperatures (in the range 7-20°C) small endothermic and exothermic phenomena probably due to the melting and recrystallization of the small and defective crystallites in the P(P-*co*-VCH) block. In the DSC thermograms recorded during the cooling and second heating step of the as prepared samples of iPP-*b*-P(P-*co*-VCH) BCPs, no significant low temperatures endothermic/exothermic peaks are apparent, only an exothermic peak at ≈85-90°C in the cooling step (curves c-d in Figure 2.3 B) and an endothermic peak at ≈133°C in the second heating step are observed, respectively due to the crystallization and successive melting of crystals in α form in the iPP block. This indicates that the P(P-*co*-VCH) block does not crystallizes upon cooling from the melt, in agreement with what observed for the P(P-*co*-VCH) random copolymer. On the other hand, the inflection point observed in the DSC thermograms of iPP-*b*-P(P-*co*-VCH) BCPs at ≈ -1°C, is probably due to the glass transition of the iPP blocks, since the P(P-*co*-VCH) block constitute only the minor component (20-30%wt).

The DSC thermograms of the compression molded sample of the P(P-*co*-VCH) random copolymer (curves a in Figure 2.4 A, B, and C) only show the T_g at 3°C. The DSC thermograms of the compression molded sample of the iPP homopolymer show a melting temperature (T_m) at 134°C (curves b in Figure 2.4 A and C) and a crystallization temperature (T_c) at 102°C (curve b in Figure 2.4 B). Finally, the thermal behaviour of the compression molded samples of the iPP-*b*-P(P-*co*-VCH) BCPs is similar to that of the as prepared samples, with melting and crystallization of the iPP block at ≈133°C and ≈95°C, respectively and a glass transition of ≈0°C, similar to iPP.

The values of the melting temperature and enthalpy recorded during the first (T_m^I, ΔH_m^I) and second heating (T_m^{II}, ΔH_m^I), crystallization temperature and enthalpy (T_c, ΔH_c) and glass transition temperature (T_g) are reported in Table

2.2 for the as prepared samples and in Table 2.3 for the compression molded samples.

All in all, the thermal data of the compression molded samples confirm that the P(P-*co*-VCH) copolymer does not crystallize by cooling the melt in the adopted conditions, neither when it is covalently linked to an iPP block, nor when it is not part of a BCP. The most remarkable result consists in having evidenced that, compared with iPP homopolymer, the iPP blocks in the BCPs melt at about the same temperature, but crystallize at a temperature which is 6-9°C lower. This can be the result of some kind of confinement of iPP blocks in the BCPs, due to the low chemical affinity of iPP with the the P(P-*co*-VCH) block.[29]

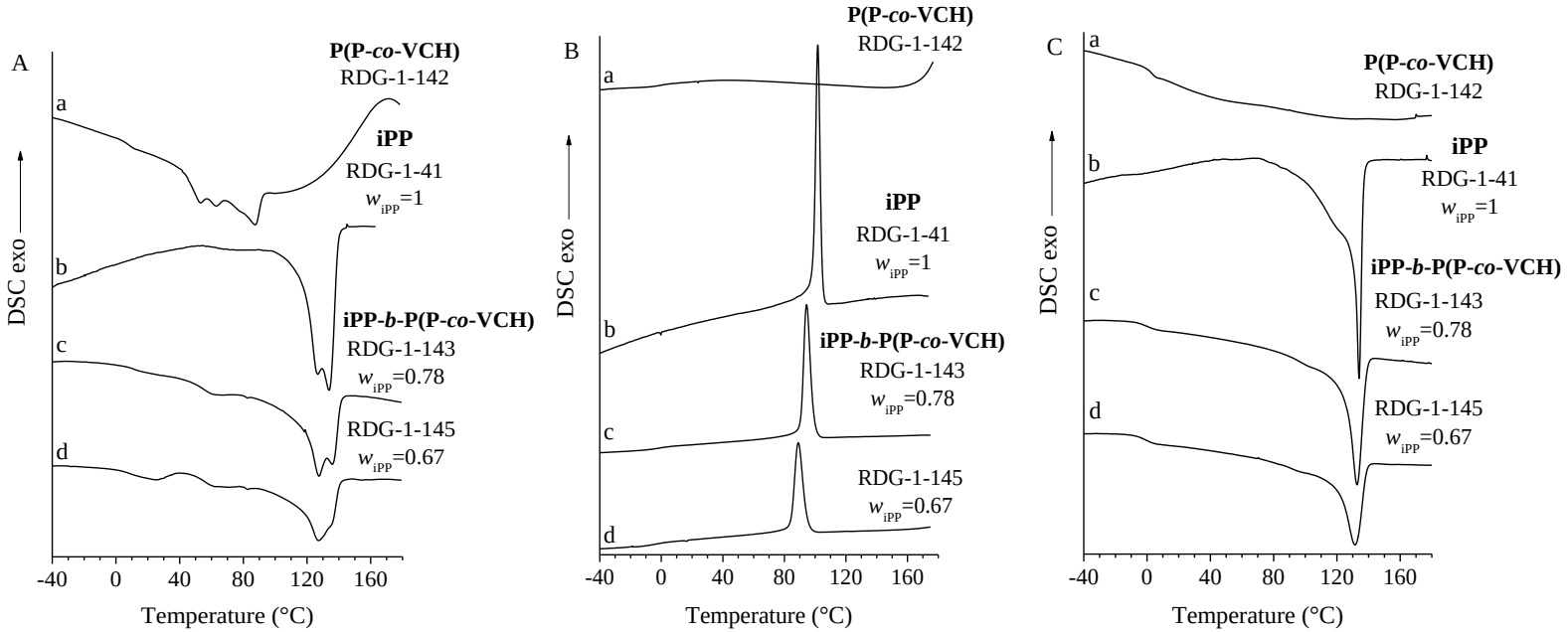

Figure 2.3 DSC thermograms recorded during heating (A), successive cooling (B) and second heating (C) of the as prepared samples of the P(P-*co*-VCH) random copolymer (a), iPP homopolymer (b) and of iPP-*b*- P(P-*co*-VCH) BCPs (c-d).

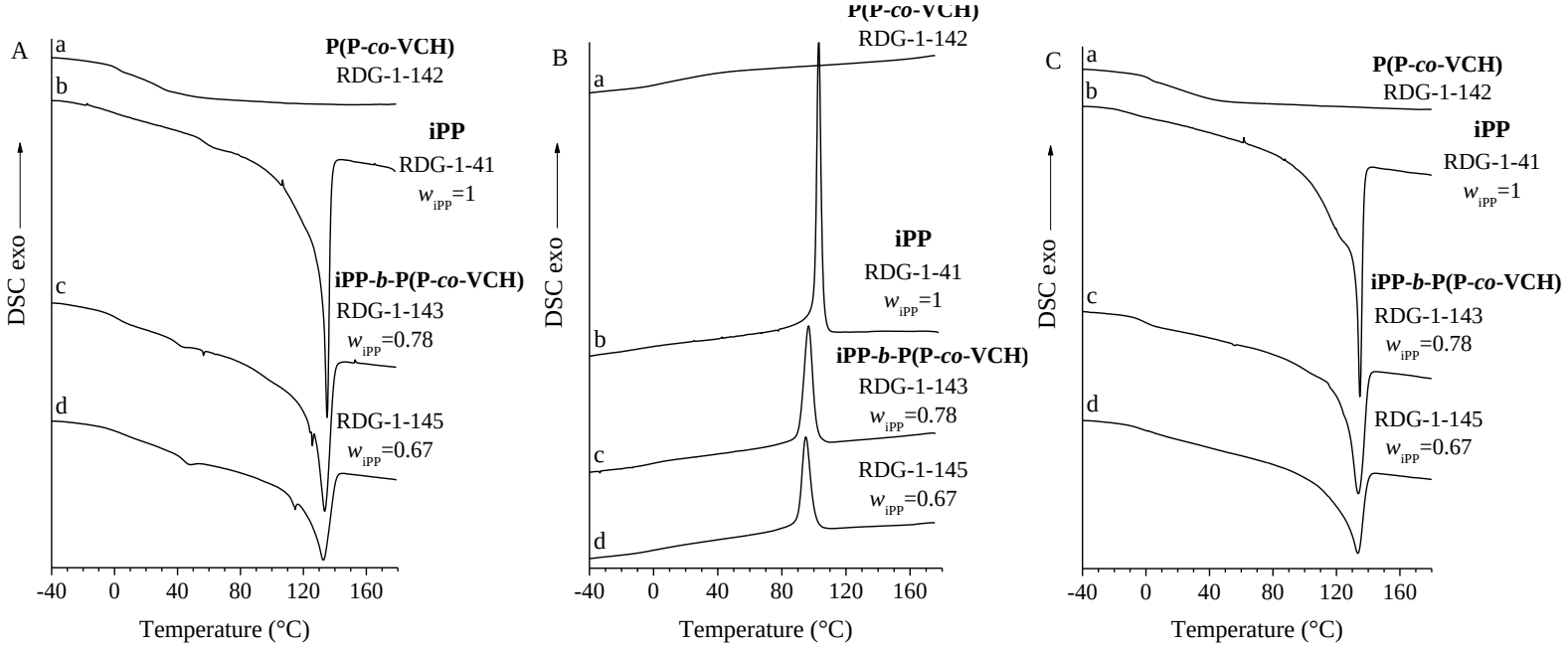

Figure 2.4 DSC thermograms recorded during heating (A), successive cooling (B) and second heating (C) of the compression molded samples of the P(P-*co*-VCH) random copolymer (a), iPP homopolymer (b) and of the iPP-*b*- P(P-*co*-VCH) BCPs (c-d).

Table 2.2 Mass fraction of the iPP block (w_{iPP}), degree of crystallinity relative to the whole sample (x_c) and to the iPP block ($x_{c\,iPP}$), melting temperature and enthalpy recorded during the first (T_m^I, ΔH_m^I) and second (T_m^{II}, ΔH_m^{II}) heating, crystallization temperature and enthalpy (T_c, ΔH_c) and glass transition temperature (T_g) of the as prepared samples of the P(P-*co*-VCH) random copolymer, iPP homopolymer, iPP-*b*-P(P-*co*-VCH) BCPs.

SAMPLE	w_{iPP}	x_c (%)	$x_{c\,iPP}$ (%)	T_m^I (°C)	ΔH_m^I (J/g)	T_m^{II} (°C)	ΔH_m^{II} (J/g)	T_c (°C)	ΔH_c (J/g)	T_g (°C)
RDG-1-142	-	-	-	62; 86	-31.8	-	-	-	-	3
RDG-1-41	1	46	46	134	-67.6	134	-62.3	102	68.8	-
RDG-1-143	0.78	30	38	127; 135	-43.3	132	-44.8	94	46.2	-1
RDG-1-145	0.67	30	45	127	-36.6	131	-40.7	89	40.5	-1

Table 2.3 Mass fraction of the iPP block (w_{iPP}), degree of crystallinity relative to the whole sample (x_c) and to the iPP block ($x_{c\,iPP}$), melting temperature and enthalpy recorded during the first (T_m^I, ΔH_m^I) and second (T_m^{II}, ΔH_m^{II}) heating, crystallization temperature and enthalpy (T_c, ΔH_c) and glass transition temperature (T_g) of the compression molded samples of the P(P-*co*-VCH) random copolymer, iPP homopolymer, iPP-*b*-P(P-*co*-VCH) BCPs.

SAMPLE	w_{iPP}	x_c (%)	$x_{c\,iPP}$ (%)	T_m^I (°C)	ΔH_m^I (J/g)	T_m^{II} (°C)	ΔH_m^{II} (J/g)	T_c (°C)	ΔH_c (J/g)	T_g (°C)
RDG-1-142	-	-	-	-	-	-	-	-	-	3
RDG-1-41	1	51	51	135	-65.8	135	-66.6	103	72.4	-
RDG-1-143	0.78	38	49	133	-64.4	133	-50.6	96	53.1	0
RDG-1-145	0.67	33	49	132	-41.2	133	-40.8	95	41.1	0

2.1.3 SAXS/WAXS analysis as a function of temperature

The study of the structural organization as a function of temperature and at lamellar length scales of the crystalline iPP-*b*-P(P-*co*-VCH) BCPs, has been performed through SAXS/WAXS experiments at different temperatures.
The compression molded samples have been heated up to 180°C and then cooled to room temperature. The SAXS/WAXS patterns (recorded step-by-step on a MS imaging, with an acquisition time of 1h) have been acquired at 25°C before heating (25°C start), at 180°C and at selected temperatures (150°C, 120°C, 90°C, 60°C) during the cooling down to 25°C (25°C end). During the cooling, the temperature decreased with an average rate of 10°C/min in the range 180-90°C and with an average rate of 2°C/min in the range 90-25°C. For comparison, the SAXS/WAXS patterns of the iPP homopolymer have been also recorded.
For each sample, the SAXS and WAXS patterns and the SAXS intensity profiles corrected for the Lorentz factor (Iq^2 vs q) are shown.

The SAXS profile of the iPP homopolymer recorded at 25°C (curve a in Figure 2.5 B) shows a correlation peak at q^*=0.54nm^{-1} which disappears when the sample is melt at 180°C and 150°C (curves b, c in Figure 2.5 B). According to the Bragg law, the periodicity of the lamellar stacks in the sample at 25°C is L_B=11.6nm. After the slow crystallization of the sample from the melt (curves d-g in Figure 2.5 B), according to the thermal treatment used in this experiment, the correlation peak appears at lower q values, e.g. q^*=0.34nm^{-1} at 120°C and q^*=0.46nm^{-1} at 25°C, thus indicating that lamellar stacks with higher periodicity are formed, with respect to those in the same sample at 25°C before the thermal treatment. It is also apparent that the position of the correlation peak moves towards higher q values on decreasing the temperature from 120°C to 25°C, which corresponds to a decrease of the periodicity L_B of the lamellar stacks. This is probably due to insertion of new crystalline lamellae in between the pristine lamellae formed at 120°C by effect of cooling. As new lamellar crystals are formed through an insertion mechanism, the mean distance between the lamellae L_B decreases from ≈18nm (at 120°C) to ≈14nm (at 25°C) (Figure 2.5 A, A'). Simultaneously, the scattering invariant (Q), proportional to the area subtended by the Lorentz corrected SAXS curves, decreases (Figure 2.5 D). The values of q^*, L_B and Q at the temperatures at which crystallinity is observed, after cooling from the melt, are reported in Table 2.4.

The WAXS profiles show that in these crystallization conditions, the iPP homopolymer almost entirely crystallizes in the γ form, as indicated by the presence of the $(117)_\gamma$ reflection at $2\theta=20°$ (curves d-g in Figure 2.5 C). Very small amounts of α form crystals are present (Table 2.4).

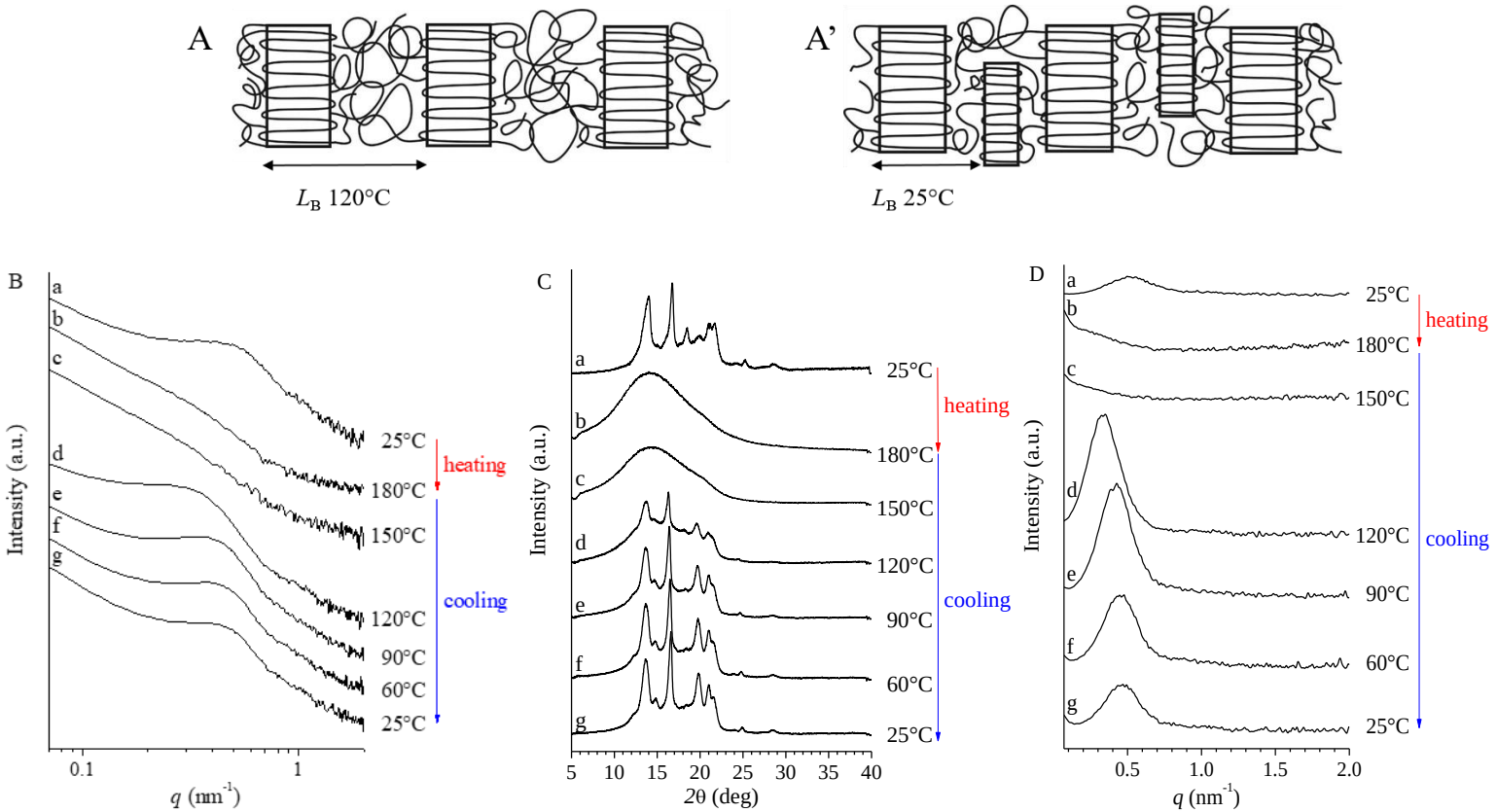

Figure 2.5 Scheme of the lamellar stacks developing in iPP homopolymer at 120°C (A) and 25°C (A') after cooling from the melt. (B) SAXS, (C) WAXS and (D) Lorentz corrected intensity profiles recorded at the indicated temperatures during heating and successive cooling of the sample iPP homopolymer, RDG-1-41.

The SAXS profile of the sample RDG-1-143 (w_{iPP}=0.78) recorded at 25°C, before heating (curve a in Figure 2.6 A), shows a correlation peak at q^*=0.49nm^{-1} which is similar to that of iPP homopolymer. Therefore, lamellar stacking of iPP crystals with periodicity L_B=12.8nm occurs also in the BCP. The correlation peak at q^*=0.49nm^{-1} disappears upon melting, as observed in the SAXS profiles recorded at 180°C in the heating step and at 150°C in the successive cooling step (curves b, c in Figure 2.6 A). The absence of any feature in the SAXS profiles of the melt indicates that for this sample, either that the melt is not phase separated at these temperatures or that phase separation is not detectable. In turn, phase separation is not detectable either because of the low contrast, or because the size of domains is bigger than the maximum correlation distance that can be probed by our experimental set-up (80nm). The SAXS profiles of the sample crystallized from the melt, recorded at the indicated temperature during the cooling from 180°C to 25°C (curves d-g in Figure 2.6 A), show that the correlation peak relative to the lamellar stacking of iPP crystals reappears already at 120°C. With decrease of the temperature, the correlation peak shifts toward higher q values, from 0.32nm^{-1} at 120°C to 0.45nm^{-1} at 25°C, indicating a decrease of the periodicity (L_B). As previously observed for iPP homopolymer, this may be due to the insertion of new crystalline lamellae in between the pristine lamellae formed at 120°C by effect of cooling. With the insertion of the new lamellae, the mean distance between the lamellae, L_B, decreases from ≈20nm to ≈14nm. Simultaneously, the scattering invariant, proportional to the area subtended by the Lorentz corrected SAXS curves, decreases (Figure 2.6 C).

The simultaneous recording of WAXS profiles confirms that the sample is in the melt state at 180° and 150°C (curves b, c of Figure 2.6 B). Moreover, the WAXS profiles of the sample recorded upon crystallization at lower temperature (curves d-g in Figure 2.6 B) indicate that the iPP block crystallizes as a mixture of α and γ form, as indicated by the presence of the reflections $(130)_\alpha$ at 2θ=18.6° of α and $(117)_\gamma$ at 2θ=20° of γ forms.

The SAXS profile of the sample RDG-1-145 (w_{iPP}=0.67) recorded at 25°C (curve a in Figure 2.7 A) does not show any correlation peak even though the WAXS data indicate that the sample is crystalline. Indeed, crystals of α form and a little amount of crystals of γ form are present, as indicated by the $(130)_\alpha$ and $(117)_\gamma$ reflections in the corresponding WAXS profile (curve a in Figure 2.7 B). Upon melting the original crystals and successive cooling, the newly formed crystals (curves d-g in Figure 2.7 B) appear organized in well-

defined stacks as indicated by the appearance of a well-defined correlation peak in the SAXS patterns recorded at 120°, 90°, 60° and 25°C (curves d-g in Figure 2.7 A). As already observed for iPP homopolymer and for the BCP sample RDG-1-143 (w_{iPP}=0.78), the correlation peak shifts toward higher q values, from 0.37nm^{-1} at 120°C to 0.45nm^{-1} at 25°C during the cooling. Therefore, also in this case, during cooling, new lamellar crystals are formed in between the pristine lamellae formed at 120°C, leading to a decrease of L_B from ≈17nm to ≈14nm. Simultaneously, also the scattering invariant, proportional to the area subtended by the Lorentz corrected SAXS curves, decreases (Figure 2.7 C).

The corresponding WAXS profiles (curves d-g in Figure 2.7 B) indicate that the iPP block crystallizes as a mixture of α and γ form. At 120°C the relative amount of α form is prevalent (curve d of Figure 2.7 B) as indicated by the high intensity $(130)_\alpha$ reflection of α form at 2θ=18.6°. With decrease of temperature, the relative intensity of $(117)_\gamma$ reflection at 2θ=20° of the γ form increases, and at 25°C the relative amount of α and γ form are nearly similar (curve g of Figure 2.7 B).

The position of the correlation peak observed in the SAXS patterns recorded at different temperatures during the heating and cooling steps, the corresponding Bragg distance, the SAXS scattering invariant, the degree of crystallinity and the relative amount of α and γ forms for the iPP homopolymer and for the iPP-*b*-P(P-*co*-VCH) BCPs, are reported in Table 2.4.

It is worth noting that the values of lamellar periodicity for both BCP samples are similar to those of the iPP homopolymer. This suggest that regardless of the state of the melt, whether homogeneous, or already separated in two phases, crystallization marks phase separation, that is crystallization occurs in iPP separated domains where the lamellar crystals are organized in stacks with little or no inclusion of the P(P-*co*-VCH) blocks.

In the hypothesis that the SAXS intensity in the sampled q region probes the lamellar organization occurring in the phase separated domains of iPP blocks, only two phases contribute to the value of the SAXS invariant, that is the iPP lamellar crystals and the interlamellar amorphous phase. Since the invariant for a biphasic system is proportional to the product of the volume fraction of the amorphous (φ_a) and crystalline (φ_c) phases (φ_a φ_c), the decrease of the invariant suggests that the proposed mechanism of insertion induces an increase of crystallinity in the iPP block domains from values close to 50% to values higher than 50%.

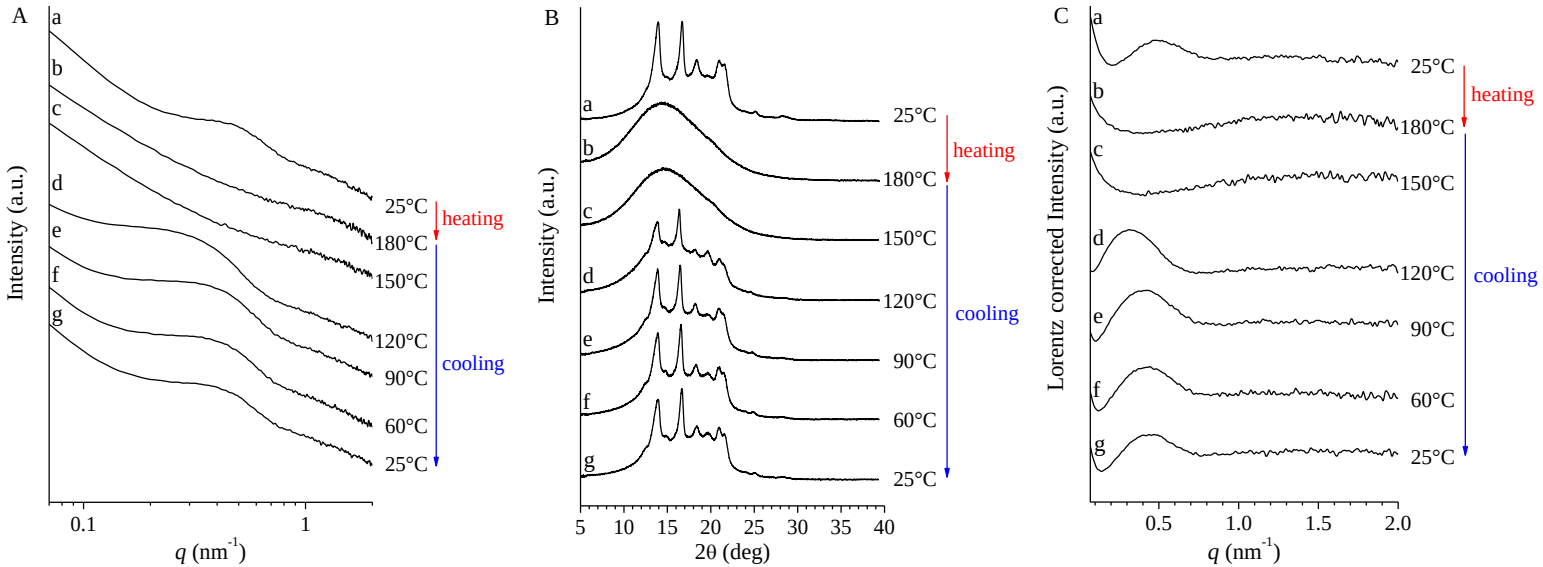

Figure 2.6 SAXS (A), WAXS (B) and Lorentz corrected (C) intensity profiles recorded at the indicated temperatures during heating and successive cooling of the sample RDG-1-143 (w_{iPP}=0.78).

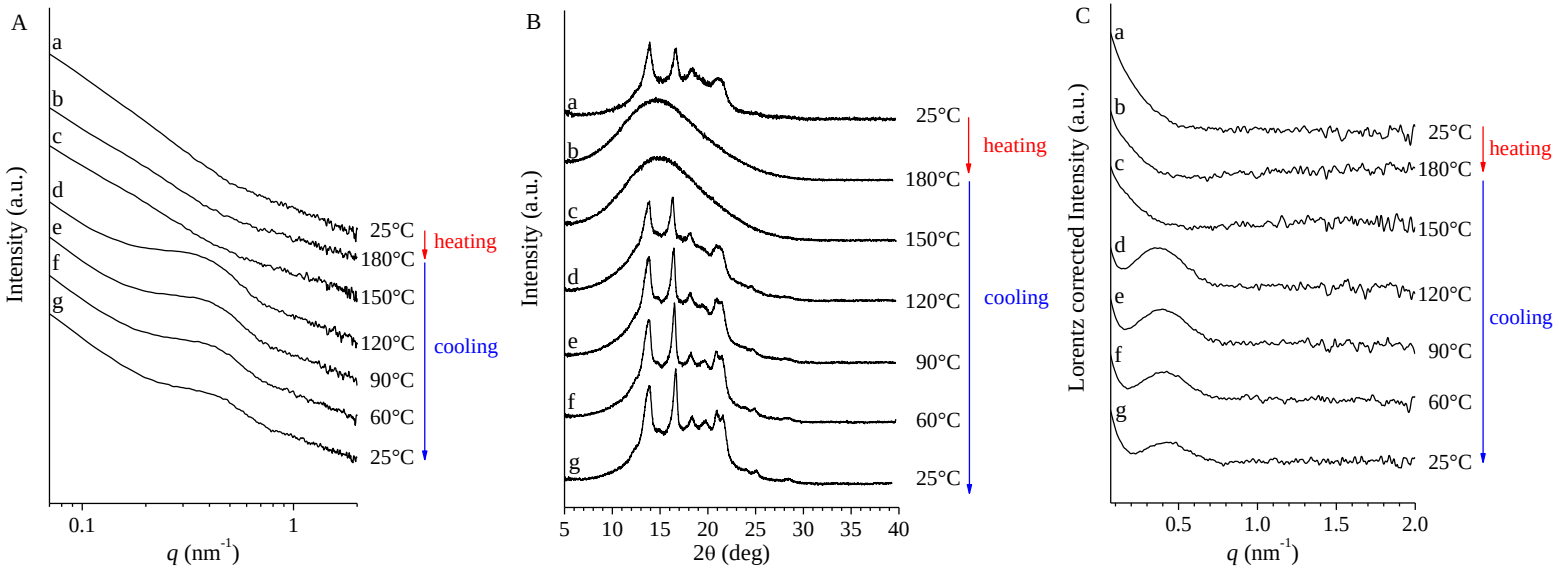

Figure 2.7 SAXS (A), WAXS (B) and Lorentz corrected (C) intensity profiles recorded at the indicated temperatures during heating and successive cooling of the sample RDG-1-145 (w_{iPP}=0.67).

Table 2.4 Mass fraction of the iPP block (w_{iPP}), scattering invariant (Q), position of the correlation peak read in the SAXS profiles (q^*) and corresponding value of the Bragg distance (L_B), degree of crystallinity relative to the whole BCP molecule (x_c) and amount of α and γ form of iPP (α/γ), at the indicated temperatures, for iPP homopolymer and for iPP-*b*-P(P-*co*-VCH) BCPs.

		RDG-1-41	**RDG-1-143**	**RDG-1-145**
w_{iPP}		1	0.78	0.67
$Q \cdot 10^3$ (nm)	120°C	31.1	27.0	18.9
	90°C	28.5	22.4	15.2
	60°C	21.5	16.6	13.7
	25°C	19.7	12.6	10.4
q^* (nm^{-1})	120°C	0.34	0.32	0.37
	90°C	0.42	0.41	0.41
	60°C	0.45	0.43	0.42
	25°C	0.46	0.45	0.45
L_B (nm)	120°C	18.5	19.6	17.0
	90°C	15.0	15.3	15.3
	60°C	14.0	14.6	15.0
	25°C	13.6	14.0	14.0
x_c (%)	120°C	33	21	24
	90°C	45	26	27
	60°C	55	36	34
	25°C	60	40	39
α / γ (%)	120°C	10 / 90	32 / 68	-
	90°C	5 / 95	80 / 20	70 / 30
	60°C	4 / 96	66 / 34	64 / 36
	25°C	2 / 98	67 / 33	61 / 39

From the SAXS profiles of the iPP homopolymer and iPP-*b*-P(P-*co*-VCH) BCP samples recorded during the cooling, at the temperatures of 120°C, marking the onset of crystallization, and 25°C, marking the end of cooling step, we have calculated the self-correlation function of electron density fluctuations (correlation function). The so obtained correlation functions are reported in Figure 2.8-2.10.

From the self-correlation function, the value of the periodicity (P) of the lamellar stacks and the value of the minimum layer thickness in the stacks may be obtained. For the iPP-*b*-P(P-*co*-VCH) BCPs, the degree of crystallinity of the iPP block, calculated as the degree of crystallinity of the di-block copolymer experimentally determined from the WAXS profile recorded at 25°C after cooling from the melt, divided by the mass fraction of the iPP block (w_{iPP}), is higher than 50%, therefore the minimum layer thickness obtained from the self-correlation function corresponds to that of the amorphous layer (l_a). Also in the case of iPP homopolymer, the minimum layer thickness calculated from the self-correlation function relative to the SAXS profile recorded at 25°C, corresponds to that of the amorphous phase (l_a). We make the same assumption even in the case of the self-correlation function calculated from the SAXS profiles recorded at 120°C. This entails that the minimum layer thickness corresponds to that of the amorphous layers placed in between the lamellae within the stacks, even though the degree of crystallinity of the iPP blocks at 120°C, calculated from WAXS data for both RDG-1-143 (w_{iPP}=0.78) and RDG-1-145 (w_{iPP}=0.67), is around 20-25%. The values of $x_{c\ iPP}$, L_B, P, l_a, l_c at 25°C and 120°C, obtained for the iPP-*b*-P(P-*co*-VCH) BCPs and for iPP homopolymer are reported in Table 2.5.

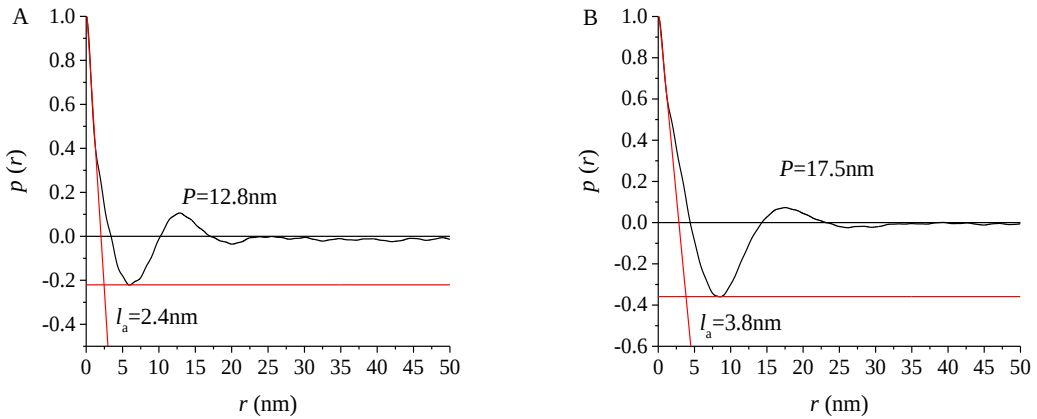

Figure 2.8 Normalized correlation function obtained for the iPP homopolymer RDG-1-41 from the experimental SAXS profile recorded at 25°C (A) and 120°C (B).

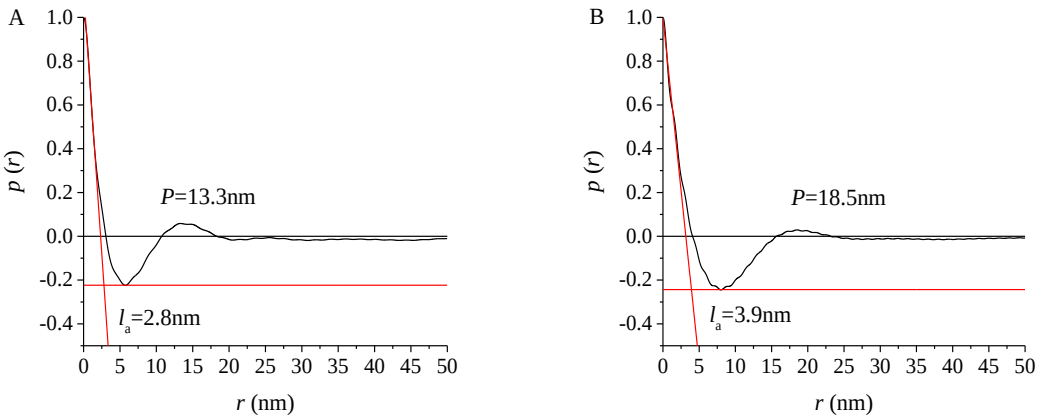

Figure 2.9 Normalized correlation function obtained for the sample RDG-1-143 (w_{iPP}=0.78) from the experimental SAXS profile recorded at 25°C (A) and 120°C (B).

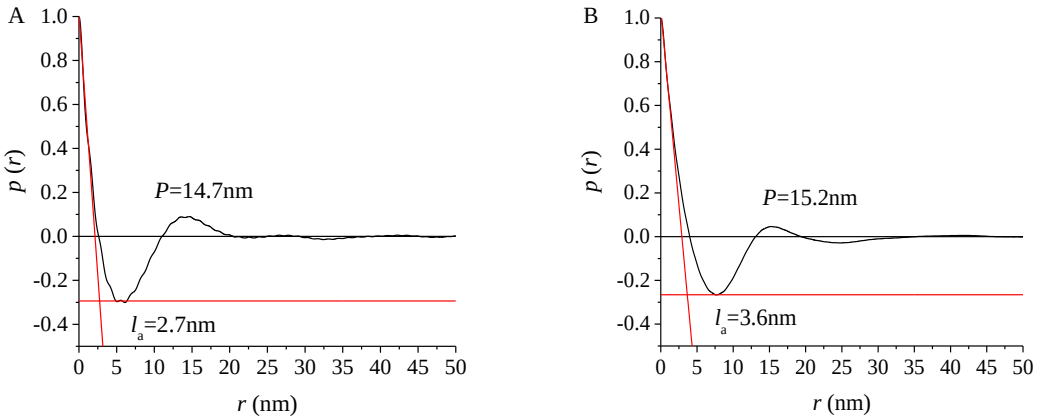

Figure 2.10 Normalized correlation function obtained for the sample RDG-1-145 (w_{iPP}=0.67) from the experimental SAXS profile recorded at 25°C(A) and 120°C (B).

Table 2.5 Molecular mass ($M_{n\ iPP}$) and mass fraction (w_{iPP}) of the iPP block. Degree of crystallinity ($x_{c\ iPP}$), Bragg distance (L_B), periodicity of the lamellar stacks (P), thickness of the crystalline (l_c) and amorphous layers (l_a) of the crystalline iPP block in iPP-*b*-P(P-*co*-VCH) BCPs calculated at 25°C and 120°C.

SAMPLE	$M_{n\ iPP}$ (kg/mol)	w_{iPP}	25°C					120°C				
			$x_{c\ iPP}$ (%)	L_B (nm)	P (nm)	l_c (nm)	l_a (nm)	$x_{c\ iPP}$ (%)	L_B (nm)	P (nm)	l_c (nm)	l_a (nm)
RDG-1-41	139.8	1	60	13.6	12.8	10.4	2.4	33	18.5	17.5	13.7	3.8
RDG-1-143	43.5	0.78	51	14.0	13.3	10.5	2.8	27	19.6	18.5	14.6	3.9
RDG-1-145	54.2	0.67	58	14.0	14.7	12.0	2.7	36	17.0	15.2	11.6	3.6

The values of *P* evaluated from the self-correlation functions are similar to the L_B values evaluated from the corresponding experimental SAXS profiles, both in the case of iPP homopolymer and iPP-*b*-P(P-*co*-VCH) BCPs. In particular, $L_B \approx$13-14nm at 25°C and $L_B \approx$15-20nm at 120°C.

The decrease of lamellar periodicity indicates that during the stepwise decrease of temperature, the crystallization at 120°C is not complete. With decrease of temperature, new lamellae are formed in the iPP domains, leading to a decrease of the average long period, even though the average lamellar thickness decreases only slightly.

In an alternative hypothesis, for the BCPs at 120°C, crystallization occurs from a homogeneous melt. This implies that part of P(P-*co*-VCH) blocks are included in the interlamellar amorphous layers. With decrease of temperature, the mobility of chains is still high enough to trigger phase separation, and consequent ejection of P(P-*co*-VCH) blocks outside the inter-lamellar amorphous layers and formation of more compact stacks of iPP lamellae in the separated domains.

However, this second hypothesis is ruled out by the fact that the values of *P*, l_c and l_a calculated at 25°C and 120°C for the iPP block of the iPP-*b*-P(P-*co*-VCH) BCPs are similar to the values obtained for iPP homopolymer, thus indicating that the structural organization of the crystalline iPP block is the same as in iPP homopolymer. This suggests that crystallization of iPP blocks takes place in the BCPs from a phase separated melt, rather than from a homogeneous melt.

2.1.4 Structural and thermal characterization of iPP-*b*-P(P-*co*-VCH) BCPs quenched from the melt

It is well known that iPP, by effect of fast cooling of the melt (*quench*) to low temperatures (generally 0°C), crystallizes in a mesomorphic form.[30] In fact, in these conditions, the crystallization kinetics of the monoclinic α form is slowed down, and iPP crystallizes in the more kinetically favored mesomorphic form.[31] The resulting mesomorphic form is characterized by a degree of order intermediate between that of the crystals and the disorder of the amorphous phase. The mesomorphic form is metastable and upon heating reorganizes into the stable monoclinic α form around a temperature of 70-80°C.

The ability of iPP-based BCPs to undergo the same structural change observed for iPP homopolymer quenched from the melt, has been studied. In particular, the sample RDG-1-143 (w_{iPP}=0.78), with the highest mass fraction of the iPP block, has been selected for this kind of analysis. For comparison, the same analysis has been carried out also on the iPP homopolymer RDG-1-41 synthesized with the same catalysts and in the same reaction conditions as iPP-*b*-P(P-*co*-VCH) BCPs.

Powder samples have been heated at temperatures 30-40°C higher than the respective melting temperatures, kept at this temperature for 5min, and then cooled by quenching in an ethyl alcohol bath at 0°C. The X-ray powder diffraction profiles of the iPP homopolymer RDG-1-41 and of the iPP-*b*-P(P-*co*-VCH) BCP RDG-1-143 (w_{iPP}=0.78) quenched from the melt are shown in Figure 2.11 A. In Figure 2.11 A', the X-ray powder diffraction profiles of the same samples slowly crystallized from the melt (already discussed in section 2.1.2) are also shown.

The X-ray powder diffraction profile of the iPP homopolymer quenched from the melt (curve a in Figure 2.11 A) confirms the crystallization in the mesomorphic form under these conditions, as indicated by the two typical haloes at 2θ=15° and 2θ=21.3°. Also the iPP block of the iPP-*b*-P(P-*co*-VCH) BCP RDG-1-143 (curve b of Figure 2.11 A) crystallizes in the mesomorphic form of iPP by effect of fast cooling of the melt to 0°C. On the contrary the iPP homopolymer sample and the iPP block of the BCP crystallize in the normal α form with low or no amounts of γ forms by effect of slow cooling of the melt (curves a and b in Figure 2.11 A').

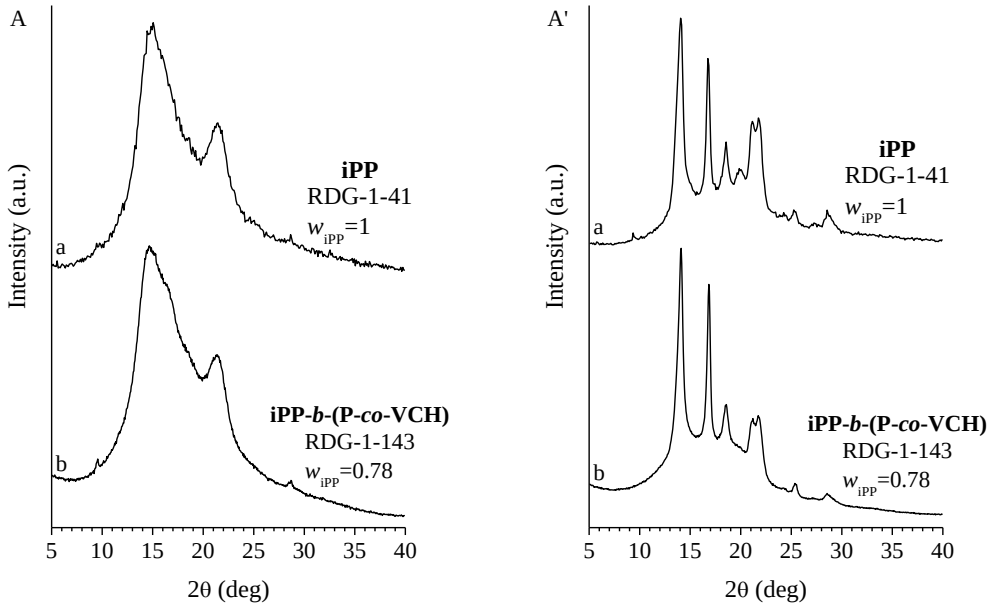

Figure 2.11 X-ray powder diffraction profiles of the samples of iPP homopolymer RDG-1-41 (a) and of the iPP-*b*- P(P-*co*-VCH) BCP RDG-1-143 (w_{iPP}=0.78) (b), crystallized by fast cooling the melt to 0°C (A) and by slow cooling the melt to 25°C (A').

The DSC thermograms of the BCP sample with the iPP block crystallized in the mesophase are shown in Figure 2.12 A. The thermograms are recorded during the heating from -40°C to 180°C (curve h1) and successive cooling from 180°C to -40°C (curve c1).

The DSC thermogram recorded during the heating shows a low intensity endothermic peak at 50°C corresponding to the typical "annealing peak" of the iPP mesophase, which is relative to relaxation phenomena and/or phenomena associated to transitions that precede the melting of the mesophase and the successive recrystallization.[30] At higher temperatures, i.e. 132°C, a high intensity endothermic peak is also evident. This corresponds to the melting of the α form crystals formed from the transformation of the mesophase in the range 70-80°C.

The DSC cooling thermogram (curve c1) shows an exothermic peak at 97°C which is relative to the crystallization of the iPP block.

The structural transformations occurring in the sample upon heating have been monitored by time/temperature-resolved WAXS/SAXS measurements using synchrotron radiation at ESRF in Grenoble. The radiation wavelength used for this experiment is 1.0402 Å. WAXS and SAXS data have been collected while heating/cooling the sample at 10°C/min and 30°C/min respectively, at a rate of 0.071frame/s, for an exposure time of 6s.

The WAXS and SAXS data recorded during the heating and the successive cooling step are shown in Figure 2.12 B and C. Only the scattering data (curves a-h) collected at the relevant temperatures marked by the vertical segments in the DSC thermograms of Figure 2.12 A are reported in Figure 2.12 B and C.

WAXS analysis (Figure 2.12 B) reveals that the mesophase developing in the iPP block upon quenching of the sample from the melt is stable up to a temperature of nearly 60°C (curves a-c). At higher temperatures, the mesomorphic form transforms into α form as indicated by the appearance of the typical reflections $(110)_\alpha$, $(040)_\alpha$ and $(130)_\alpha$ (curves d-f). The intensity of the reflections of α form gradually increases with increasing the temperature, up to disappear at the melting (curve g). By effect of heating, the mesophase does not transform into the γ form, as instead observed by slow cooling the melt to room temperature. Indeed, the corresponding X-ray powder diffraction profile of the melt crystallized sample (curve h of Figure 2.12 B) shows not only the reflections of α form, but also a low-intensity $(117)_\gamma$ reflection typical of γ form. The transformation of the mesophase into the sole α form by effect of heating is typical of iPP, regardless of the degree stereoregularity. Indeed, even in the case of iPP samples with a high concentration of stereodefects that crystallize from the melt into the pure γ form, the mesophase transforms into the α form with no trace of γ form during heating.[30]

The SAXS profiles recorded during the heating of the BCP sample initially crystallized in the mesophase do not show any correlation peak up to ≈70°C, (curves a-c of Figure 2.12 C). Only at temperatures higher than 70°C, that is in correspondence of the transformation of the mesomorphic form into the α form, a correlation peak becomes apparent (curves d-f), up to disappear again once the sample is melt (curve g). With increasing the temperature, the degree of transformation of the mesophase into the α form increases. Simultaneously, the maximum intensity of the correlation peak I_{max} increases, whereas the position of the maximum q_{max} decreases. In particular, the value of q_{max} is 0.64nm^{-1} at 74°C (curve d of Figure 2.12 C) and 0.45nm^{-1} at 116°C (curve f of Figure 2.12 C). The SAXS profile recorded at 25°C after cooling from the melt shows a well-defined correlation peak at 0.49nm^{-1}, corresponding to L_B=13nm, which is in agreement with the results of the SAXS analysis discussed in section 2.1.3.

The absence of any relevant correlation peak in the SAXS profiles of the BCP sample with the iPP block crystallized in the mesophase is mostly due to the low contrast between the mesomorphic domains and the surrounding amorphous matrix. In the case of iPP homopolymer, instead, the mesophase shows a broad correlation peak in the SAXS pattern, even though the intensity of this peak is weak.[32] In particular it has been shown that for iPP homopolymer, with increasing the temperature, the maximum intensity I_{max} of the correlation peak and the peak position q_{max} remain almost constant, up to the temperature marking the onset of transformation into the α form. However, with further increase of the degree of transformation of mesophase into the α form, a simultaneous increase of I_{max} and decrease of q_{max} is observed. Therefore, the behavior of the BCP at nanometric length scale is similar to that of iPP homopolymer.

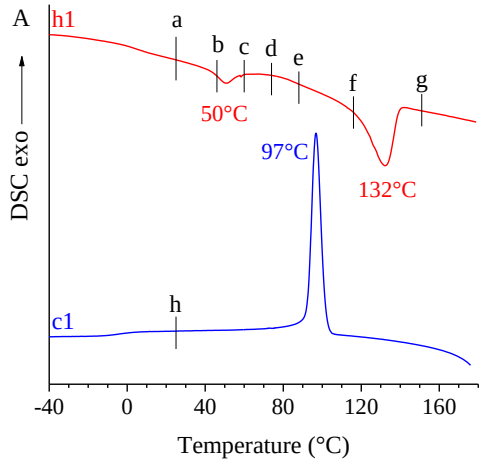

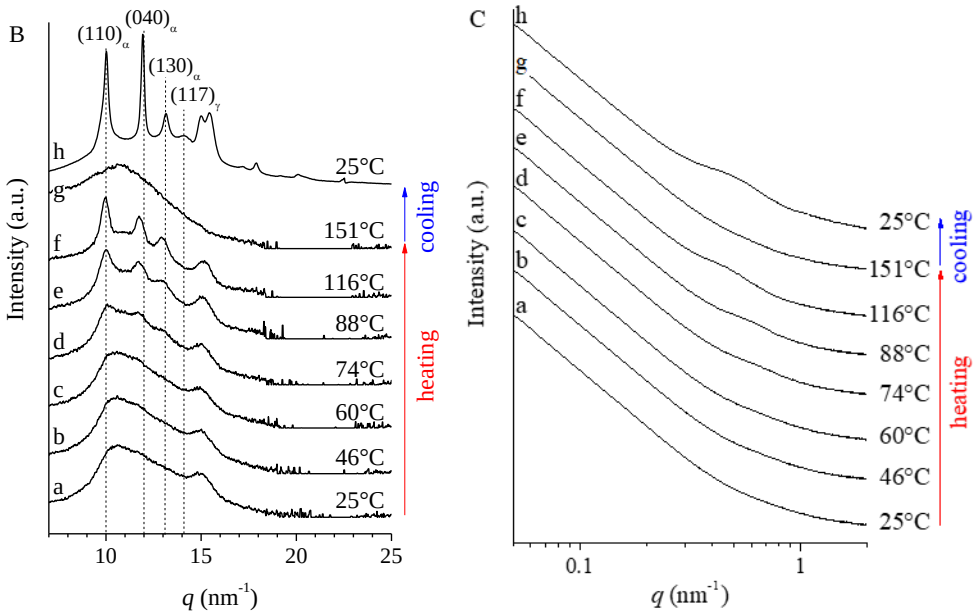

Figure 2.12 (A) DSC thermograms of the sample RDG-1-143 quenched from the melt, recorded during the heating at a rate of 10°C/min from -40°C to 180°C (h1) and the successive cooling at a rate of 10°C/min from 180°C to -40°C (h2). (B) WAXS and (C) SAXS profiles of the sample RDG-1-143 quenched from the melt, recorded at the indicated temperatures during the heating of the sample at a rate of 10°C/min (a-g) and after the successive cooling at a rate of 10°C/min (h).

2.1.5 Mechanical characterization

The mechanical characterization of the compression molded samples of the P(P-*co*-VCH) random copolymer, iPP homopolymer and of the iPP-*b*-P(P-*co*-VCH) BCPs has been performed by means of tensile tests. The stress-strain curves obtained for these samples are shown in Figure 2.13. The mechanical parameters obtained from these curves, i.e. Young's modulus, (*E*), stress and elongation at the yield point (σ_y and ε_y respectively) and stress and elongation at break (σ_b and ε_b respectively) are reported in Table 2.6.

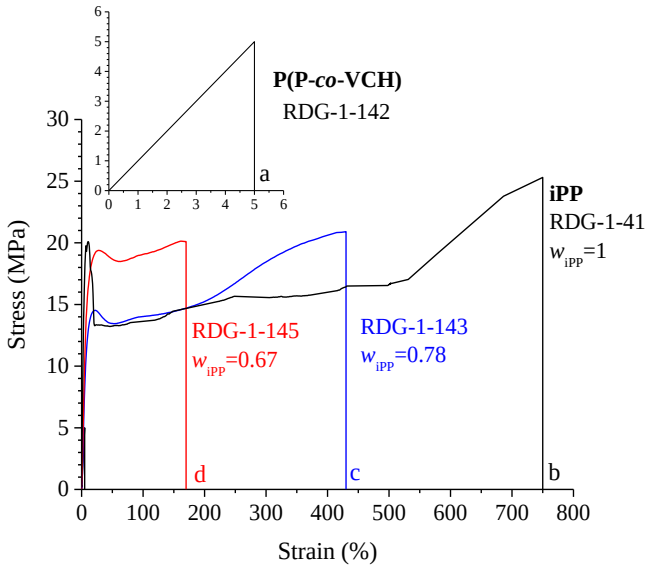

Figure 2.13 Stress-strain curves of the compression-molded samples of the P(P-*co*-VCH) random copolymer (a), iPP homopolymer (b) and of the iPP-*b*-P(P-*co*-VCH) BCPs, RDG-1-145 (w_{iPP}=0.67) and RDG-1-143 (w_{iPP}=0.78) (c, d).

The stress-strain curve recorded for the P(P-*co*-VCH) random copolymer (curve a) indicates a fragile mechanical behavior, with no yield, and a deformation at break of only 5% due to the low molecular mass of the sample. The iPP homopolymer and the BCP samples, instead, show ductile behavior, with sharp yield and strain hardening at high deformation.

In particular, the deformation at break of the iPP homopolymer (curve b) reaches a value of ≈750%, whereas in the case of the BCPs, values in the range 150-450% are observed, in agreement with the fact that the values of the molecular mass of the BCPs are lower than that of iPP.

The values of the Youngγ's modulus of the iPP-*b*-P(P-*co*-VCH) BCPs (≈190MPa) are in between those of the P(P-*co*-VCH) random copolymer (≈100MPa) and of the iPP homopolymer (≈420MPa). The stress at the yield point of the BCP sample RDG-1-143 (w_{iPP}=0.78) (≈15MPa) is lower than that of the iPP homopolymer, while the stress at the yield of the BCP sample RDG-1-145 (w_{iPP}=0.67), having a lower mass fraction of the iPP block, is comparable to that of the iPP homopolymer (≈20MPa). This is probably due to the partial orientation of the crystals in the compression molded film of this sample, as shown by the corresponding X-ray diffraction pattern (curve d of Figure 2.2 A').

Table 2.6 Total molecular mass ($M_{n\ TOT}$), molecular mass of the iPP block ($M_{n\ iPP}$), molecular mass of the P(P-*co*-VCH) block ($M_{n\ PPVCH}$), mass fraction of the iPP block (w_{iPP}), Young's modulus (E), elongation at the yield point (ε_y), stress at the yield point (σ_y), elongation at break (ε_b) and stress at break (σ_b) of the P(P-*co*-VCH) random copolymer, of the iPP homopolymer and of the iPP-*b*-P(P-*co*-VCH) BCPs.

SAMPLE	$M_{n\ TOT}$ **(Kg/mol)**	$M_{n\ iPP}$ **(Kg/mol)**	$M_{n\ PPVCH}$ **(Kg/mol)**	w_{iPP}	E **(MPa)**	ε_y **(%)**	σ_y **(MPa)**	ε_b **(%)**	σ_b **(MPa)**
RDG-1-142	45	-	-	-	100±10	-	-	<10	5±1
RDG-1-41	139.8	-	-	1	420±40	10±1	20.0±0.2	750±70	25±2
RDG-1-143	55.9	43.5	12.4	0.78	190±20	22±2	14.6±0.8	430±40	20±2
RDG-1-145	80.5	54.2	26.3	0.67	190±20	27.6±0.4	19.4±0.1	170±10	20.1±0.1

2.1.6 Structural characterization of oriented fibers

The structural changes occurring in the samples RDG-1-41 (w_{iPP}=1) and in the BCP sample RDG-1-143 (w_{iPP}=0.78) during tensile deformation have been studied by X-ray fiber diffraction analysis.

In Figure 2.14, the X-ray diffraction patterns and the corresponding equatorial profiles of the iPP homopolymer are shown. As already observed in section 2.1.2, the unoriented sample (ε=0%, Figure 2.14 A and A') mainly crystallizes in the α form of iPP, as indicated by the $(130)_\alpha$ reflection at 2θ≈18.6°. Small amounts of γ form crystallites are also present, as indicated by the low intensity $(117)_\gamma$ reflection at 2θ≈20° (see Appendix 2). Already at low deformation, the γ form transforms into the α form, as indicated by the absence of the $(117)_\gamma$ reflection (2θ≈20°) in the diffraction pattern recorded at ε=100%, (Figure 2.14 B and B'), while the $(130)_\alpha$ reflection (2θ≈18.6°) is still present. Moreover, at this deformation value, partial orientation of the α form crystals with the chain axes parallel to the stretching direction (fiber axes) is also observed, as indicated by the slightly polarization of the $(110)_\alpha$ and $(040)_\alpha$ reflections on the equator and the $(111)_\alpha$ and $(\bar{1}31)_\alpha$+$(041)_\alpha$ reflections at 2θ≈21° on the first layer line (Figure 2.14 B). The broad halo in the range of 2θ=14-18° on the equator indicates that even at low deformation values, partial transition of the α form crystals into the mesomorphic form of iPP occurs. At higher deformations, ε=500%, the α form completely transforms into the mesomorphic form, as indicated by the absence of reflections of α form and the presence of the two haloes on the equator and first layer line (Figure 2.14 C) typical of the oriented mesomorphic form of iPP.[33,34]

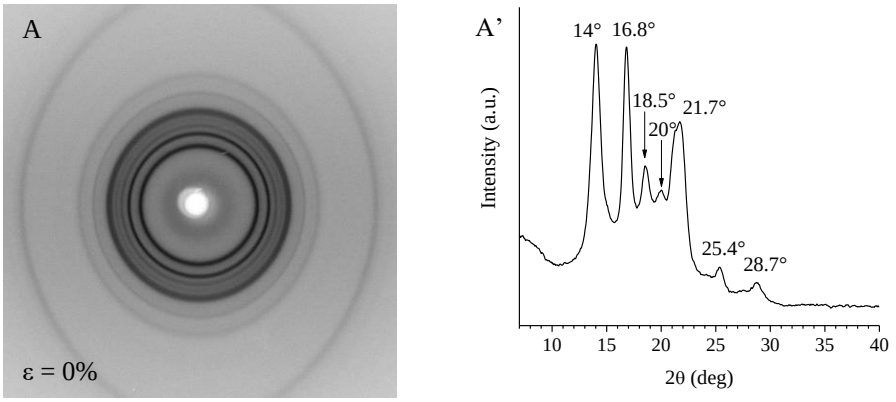

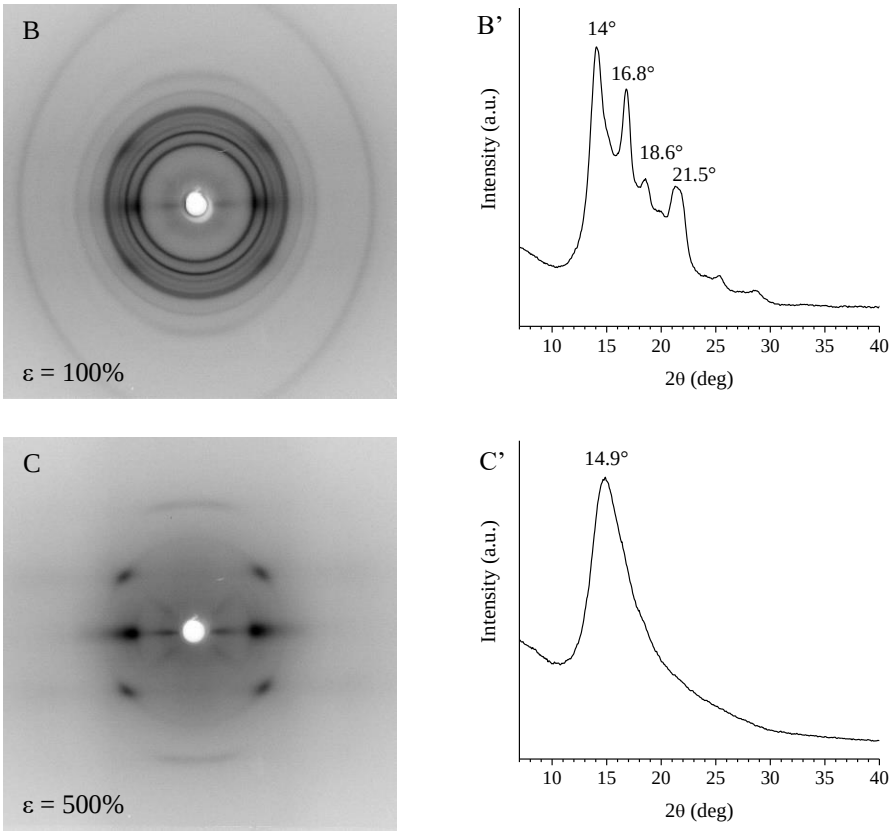

Figure 2.14 X-ray fiber diffraction patterns of the sample RDG-1-41 (w_{iPP}=1) stretched at 0% (A), 100% (B), 500% (C) deformation and corresponding equatorial profiles (A'-C').

In Figure 2.15 the X-ray diffraction patterns and the corresponding equatorial profiles of the iPP-*b*-P(P-*co*-VCH) BCP RDG-1-143 (w_{iPP}=0.78) are shown. The X-ray diffraction pattern of the unoriented sample (ε=0%, Figure 2.15 A) shows that the iPP block mainly crystallizes in the α form of iPP ($(130)_\alpha$ reflection at 2θ≈18.6°) in agreement with the powder diffraction data shown in section 2.1.2. At a deformation ε=150%, slight polarization of the $(110)_\alpha$ reflection (2θ≈14°) on the equator and of the $(040)_\alpha$ reflection (2θ≈17°) near the meridian is observed (Figure 2.15 B). At higher deformation, ε=450%, the α form transforms almost completely into the mesomorphic form of iPP as indicated by the presence of the two typical haloes on the equator (2θ=14.5°) and first layer line (2θ=21°) (Figure 2.15 C). However, small amounts of α form crystals are still present. The X-ray diffraction pattern of the stress-relaxed from 450% deformation and ≈1 month aged sample (Figure 2.15 D) shows that parts of the crystals remain in the

mesomorphic form, as indicated by the presence of the two haloes on the equator (2θ=14.5°) and first layer line (2θ=21°), while parts of the crystals transform back into the α form, as indicated by the presence of the typical reflections of α form.

It is worth mentioning that the stretching of iPP samples crystallized in α form, generally induces a preferential orientation of the crystals with chain axes directed parallel to the stretching direction (c_α-axis orientation), like in a standard fiber morphology. X-ray diffraction patterns of crystals of α form in the normal c_α-axis orientation show the $(110)_\alpha$, $(040)_\alpha$, and $(130)_\alpha$ reflections polarized on the equator (2θ=14°, 17°, and 18.6°, respectively) and the $(111)_\alpha$ and $(\bar{1}31)_\alpha$+$(041)_\alpha$ reflections polarized on the first layer line (2θ=21°).[27]

The stretching of the iPP samples crystallized in γ form induces a preferred orientation wherein half of the chain axes are parallel to the stretching direction and half are tilted at an angle of ≈81° with respect to the fiber axis. This preferential orientation is defined *parallel chain axis orientation*.[28] The corresponding X-ray diffraction patterns show the $(111)_\gamma$ and $(117)_\gamma$ reflections (2θ=14° and 20°, respectively) polarized both on the equator and on the first layer line, the $(008)_\gamma$ reflection (2θ=17°) polarized on the equator, the $(202)_\gamma$ and $(026)_\gamma$ reflections (2θ=21°) polarized on the first layer line.[27]

However, at low deformations, crystals of the γ form may assume a different kind of preferred orientation with the c_γ-axis parallel to the stretching direction and, therefore, with the two sets of chain axes directed along directions nearly normal to the stretching direction. This preferential orientation is defined *perpendicular chain axis orientation* (or *cross-β*).[26,27,30] The resulting diffraction patterns are characterized by the presence of a strong meridional spot at 2θ≈17°, corresponding to the $(008)_\gamma$ reflection.

Analogous patterns can be obtained in the case of crystals of α form or in α/γ disordered modifications oriented in the perpendicular chain axis orientation.[27] Also in these cases, indeed, the diffraction patterns would present a strong meridional reflection corresponding to the $(040)_\alpha$ reflection of the α form and the $(008)_\gamma$ reflection of the γ form.

Therefore, in an experimental X-ray fiber diffraction pattern of the BCP sample stretched at 150% deformation (Figure 2.15 B), the presence at 2θ≈17° of a reflection polarized on the meridian or in a nearly meridional position indicates the presence of crystalline domains (in the α or γ form or in their

disordered modifications) oriented according to the perpendicular or nearly perpendicular chain axis orientation (cross-β).

The X-ray diffraction patterns of the iPP homopolymer shown in Figure 2.14, indicate that upon stretching the sample, the standard fibrillar morphology develops, i.e. the chain axes of the crystalline lamellae are oriented only parallel to the stretching direction. On the contrary, the X-ray diffraction patterns of the iPP-*b*-P(P-*co*-VCH) sample RDG-1-143 (w_{iPP}=0.78) shown in Figure 2.15, indicate that upon stretching at low deformations, the α form crystals undergo a cross-*β* orientation with the chain axes nearly perpendicular to the stretching direction, as indicated by the polarization of the $(040)_\alpha$ reflection on the meridian. At higher deformation, the transition into the mesomorphic form occurs. After tension removal and aging of the sample for ≈ 1month, parts of the crystals remain in the mesomorphic form, while parts of the crystals crystallize again in the α form.

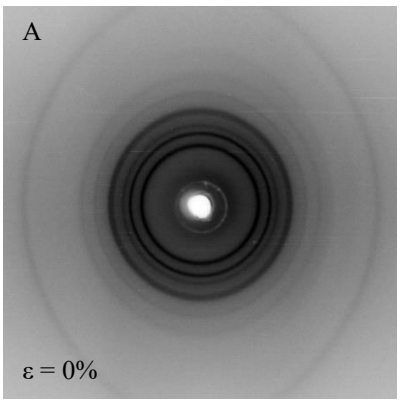

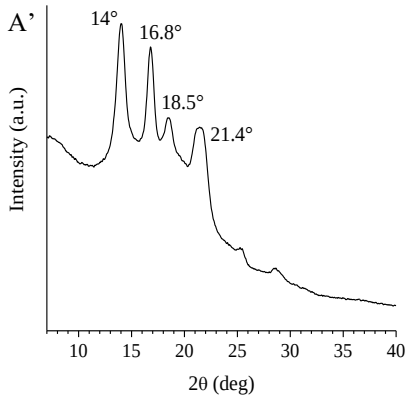

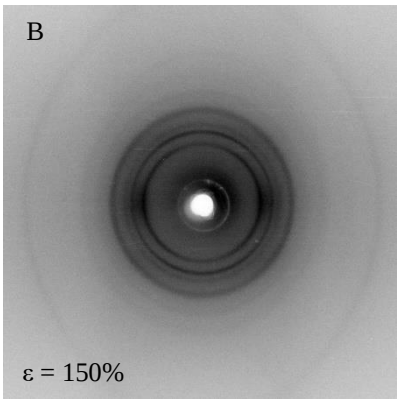

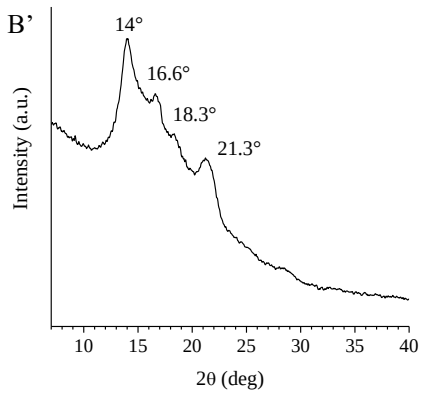

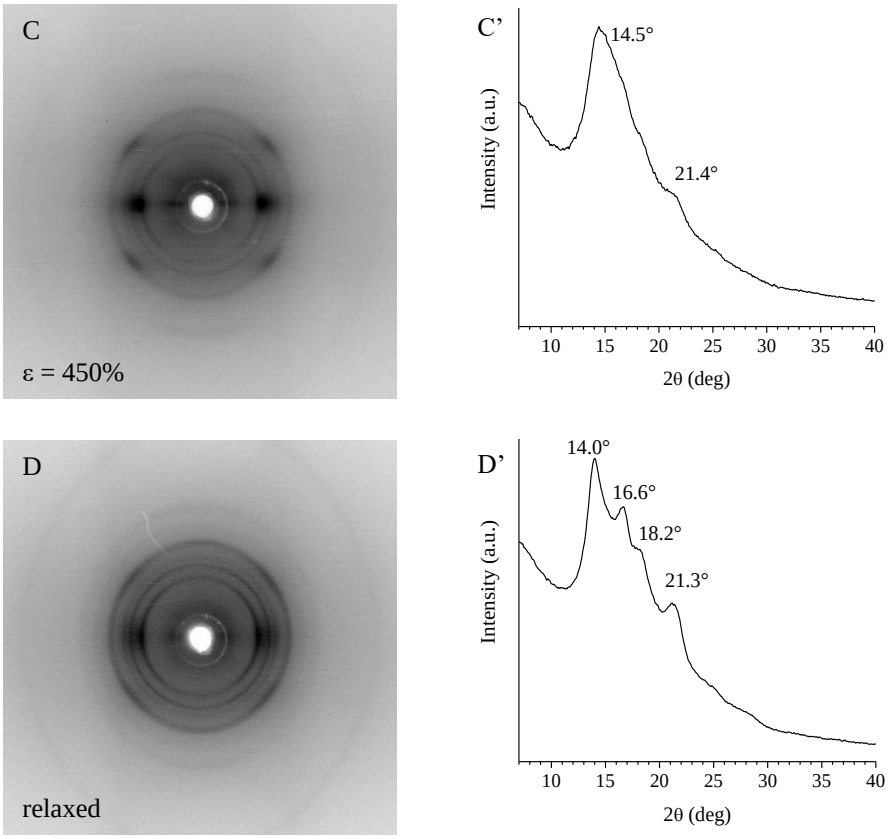

Figure 2.15 X-ray fiber diffraction patterns of the sample RDG-1-143 (w_{iPP}=0.78) stretched at 0% (A), 150% (B), 450% (C) deformation and of the sample stress-relaxed from 450% deformation and successively aged for 1 month at room temperature (D) and corresponding equatorial profiles (A'-D').

2.1.7 Morphological characterization

The morphological characterization of the iPP-*b*-P(P-*co*-VCH) BCPs at micrometer length scale has been carried out by polarized light optical microscopy (POM). The samples have been crystallized by cooling the melt at a rate of 10°C/min. The thickness of the polymer films is ≈100μm. For comparison, POM analysis of the iPP homopolymer has also been carried out. The POM images of the analyzed samples are shown in Figure 2.16.

The image of the iPP homopolymer RDG-1-41 shows the presence of bundle-like entities organized in a nearly 90° texture[35] that are typical of iPP samples in which both α and γ forms crystals are present. The POM images of the iPP-*b*-P(P-*co*-VCH) BCPs (B for RDG-1-143 (w_{iPP}=0.78) and C for

RDG-1-145 (w_{iPP}=0.67)), on the contrary, show disordered lamellar aggregates of dimensions of 5-10μm, thus indicating that the presence of the amorphous block linked to the crystalline iPP block somewhat influences the morphology of the crystalline phase at micrometer length scales.

A) RDG-1-41 (w_{iPP}=1)

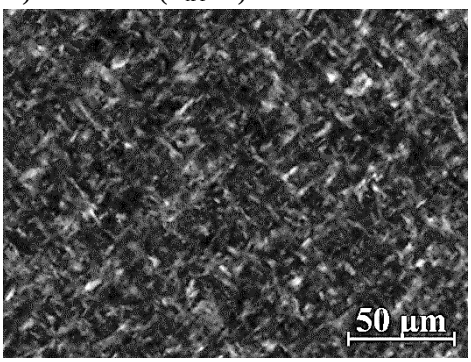

B) RDG-1-143 (w_{iPP}=0.78)

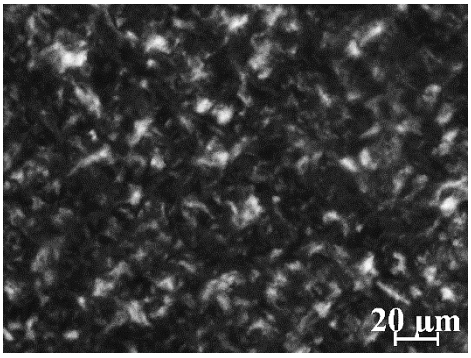

C) RDG-1-145 (w_{iPP}=0.67)

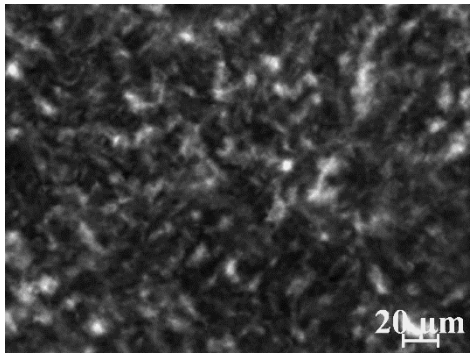

Figure 2.16 POM images of samples crystallized from the melt at a cooling rate of 10°C/min of the iPP homopolymer RDG-1-41 (A) and of the iPP-*b*-P(P-*co*-VCH) BCP samples RDG-1-143 (w_{iPP}=0.78) (B) and RDG-1-145 (w_{iPP}=0.67) (C).

The morphology investigation at nanometer length scale has been performed by Transmission Electron Microscopy. A thin film of the sample (thickness<100nm) has been deposited on a copper grid by casting from a diluted solution (0.5%wt) of the BCP in p-xylene. The so obtained thin film is then subjected to melting, maintained in the molten state for 5min and then rapidly cooled to ≈ -20°C (quenching), by putting it in contact with a metallic panel immersed in liquid N_2, in order to inhibit the crystallization of the iPP block and, at the same time, obtain the vitrification of the possible nanostructure developing in the melt.

The sample RDG-1-143 (w_{iPP}=0.78) having a volume fraction of the iPP block (f_{iPP}) equal to 0.75 has been selected for the morphological analysis. On the basis of the value of f_{iPP}, the possible nanostructure developing in the melt may have a cylindrical morphology, with cylinders of the P(P-*co*-VCH) block embedded in a crystalline matrix of the iPP block. The TEM image of the RDG-1-143 sample (Figure 2.17 A) has been obtained after staining of the thin polymer film with RuO_4. It shows lamellar entities ≈10-15nm thick which correspond to crystalline lamellae of the iPP block, thus indicating that the quenching has not been efficient in inhibiting iPP crystallization. A second quenching attempt has thus been performed, however in this case the thin film obtained by casting has been maintained at the temperature of 180°C for 3 days (in an oven at reduced pressure) in order to eliminate the crystalline memory of the melt. The TEM image of the sample stained with RuO_4 (Figure 2.17 B) shows that in this case crystallinity development has been inhibited, since only small crystalline aggregates are observed (inset). However, the resultant morphology is highly disordered.

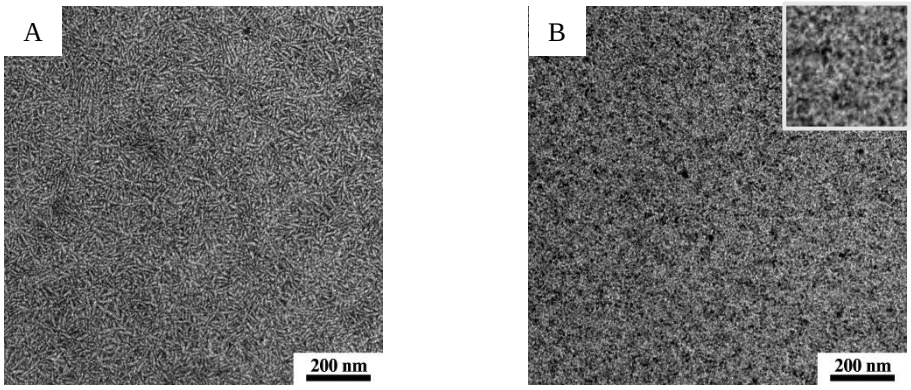

Figure 2.17 TEM images of the sample RDG-1-143 (w_{iPP}=0.78) quenched from the melt after 5min at 180°C (A) and after 3 days at 180°C (B). Contrast is generated by staining with RuO_4.

In section 2.1.4, the possibility of the iPP block of the iPP-*b*-P(P-*co*-VCH) BCPs to undergo mesophase crystallization upon quenching of the sample from the melt has been studied. In particular, the study has been carried out on the sample RDG-1-143 (w_{iPP}=0.78) showing the highest mass fraction of the iPP block. For this sample crystallizing in iPP mesophase upon quenching from the melt (curve b in Figure 2.11 section 2.1.4), the morphological characterization has also been carried out. In Figure 2.18, the POM and AFM (Atomic Force Microscopy) images are shown. For

comparison, the AFM images obtained for the iPP homopolymer RDG-1-41 subjected to quenching from the melt are also shown (Figure 2.19).

The POM image of the sample RDG-1-143 quenched from the melt (Figure 2.18 A) shows that upon quenching, no birefringence is observed, in agreement with what expected for the iPP mesophase. Only small and isolated birefringent aggregates are present. The AFM images (Figure 2.18 B and B') show that the mesophase developing in the iPP block of the iPP-*b*-P(P-*co*-VCH) BCP is characterized by a nodular morphology, similar to iPP homopolymer. These data indicate that in iPP-*b*-(P-*co*-VCH) BCPs, the presence of the random copolymer (P-*co*-VCH) block covalently linked to the iPP block does not affect the nodular morphology of the iPP mesophase (Figure 2.19).

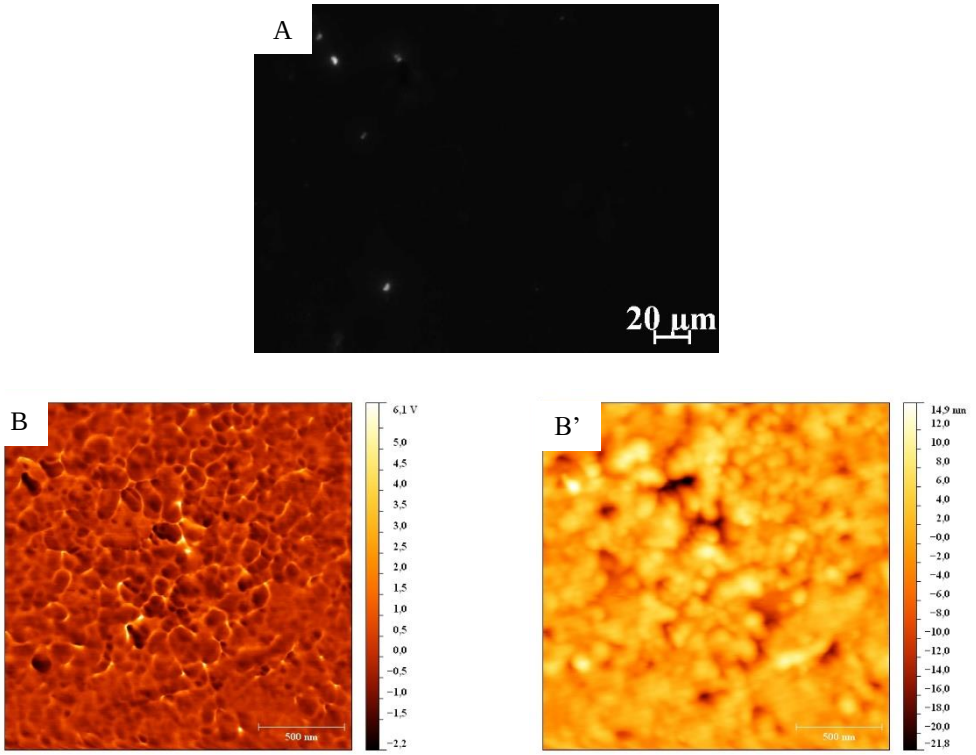

Figure 2.18 Optical microscopy images acquired in polarized light (cross polars) (A) and AFM phase (B) and height (B') images of the iPP-*b*-P(P-*co*-VCH) BCP RDG-1-143 (w_{iPP}=0.78).

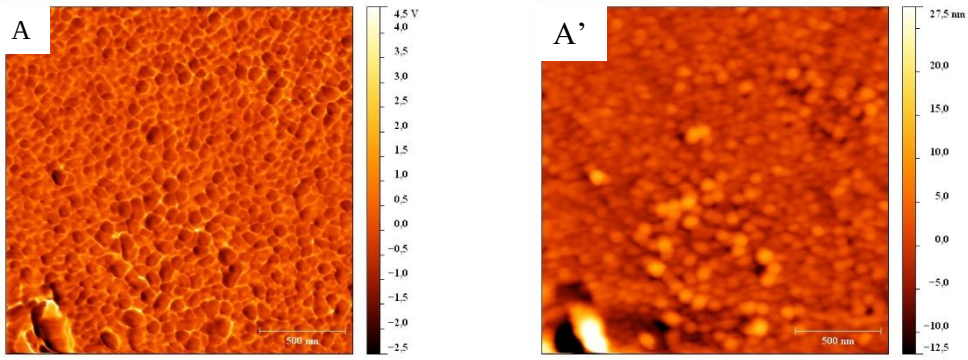

Figure 2.19 AFM phase (A) and height (A’) images of the iPP homopolymer RDG-1-41(w_{iPP}=1).

2.2 Isotactic polypropylene-*b*-poly(propylene-*co*-1-octadecene) di-block copolymers iPP-*b*-P(P-*co*-C18)

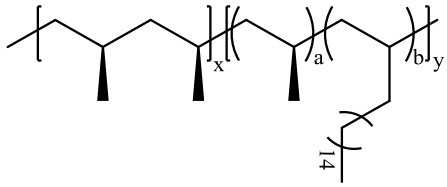

Figure 2.20 Structure of the isotactic polypropylene-*block*-poly(propene-*co*-1-octadecene) di-block copolymers.

Semicrystalline di-block copolymers having a crystalline block made of isotactic polypropylene (iPP) and an amorphous block made of a random copolymer of propene and 1-octadecene (P(P-*co*-C18)) have been studied.
The interest towards this class of materials arises from the possibility to combine the peculiar structural and thermal properties of the iPP and P(P-*co*-C18) blocks: on one hand the iPP block that can possibly crystallize in three different crystalline forms (α, β and γ) or in the mesomorphic form depending on the crystallization conditions, on the other hand the P(P-*co*-C18) block that whilst amorphous at room temperature, can possibly develop crystallinity when cooled below room temperature due to the crystallization of the side chains of the 1-octadecene (C18) units. Therefore, by linking the two different blocks, and by selecting the proper crystallization conditions, it is possible to tailor the properties of this class of materials.

2.2.1 Materials and methods

Samples of iPP-*b*-P(P-*co*-C18) BCPs were synthesized by living polymerization with a C_s-symmetric pyridylamidohafnium dimethyl complex activated with $B(C_6F_5)_3$. The synthetic procedure, consisting in the sequential synthesis of the iPP and P(P-*co*-C18) blocks, is shown in Scheme 2.2.

Different samples of iPP-*b*-P(P-*co*-C18) with different mass fractions of the iPP block (w_{iPP}), were synthesized. A sample of P(P-*co*-C18) random copolymer and a sample of iPP homopolymer (the same analyzed in section 2.1) were also synthesized by means of the same catalyst and in the same reaction conditions used for the synthesis of the iPP-*b*-P(P-*co*-C18) BCPs.

The P(P-*co*-C18) random copolymer was synthesized by the following procedure: a 200mL glass reactor (Andrews Glass) was charged in a nitrogen-filled glove box with toluene, DIBAP scavenger and 1-octadecene. The reaction vessel was sealed and charged with propylene gas and stirred for 1h at room temperature in a water bath. In the glovebox, a vial was charged with pyridylamidohafnium catalyst (see scheme 2.2) along with $B(C_6F_5)_3$. This co-catalyst mixture was then dissolved in toluene and transferred via a gas-tight syringe to the glass reactor. The polymerization was allowed to proceed for 20min under constant propylene feed, and then quenched by addition of a methanol/HCl solution with simultaneous venting of the reactor. The polymer was precipitated in copious methanol, stirred overnight, and then collected via filtration. The polymer was dried to constant weight in vacuo at 25 °C.
For the synthesis of the iPP-*b*-P(P-*co*-C18) BCPs a similar procedure was followed: a 200mL glass reactor (Andrews Glass) was charged in a nitrogen-filled glove box with toluene and DIBAP scavenger. The reaction vessel was sealed and charged with propylene gas and stirred for 1h at room temperature in a water bath. In the glovebox, a vial was charged with pyridylamidohafnium catalyst along with $B(C_6F_5)_3$. This co-catalyst mixture was then dissolved in toluene and transferred via a gas-tight syringe to the glass reactor. The polymerization was allowed to proceed for 5-10min (depending on the desired block length) under constant propylene feed, to produce the iPP block. Then an aliquot of the polymerization medium was removed for GPC analysis and 1-octadecene (in amounts depending on the desired composition) was injected in the reactor. The second block polymerization (P(P-*co*-C18)) was allowed to proceed under a constant propylene pressure for the desired amount of time and then quenched by addition of a methanol/HCl solution with simultaneous venting of the reactor. The polymer was precipitated in copious methanol, stirred overnight, and then collected via filtration. The polymer was dried to constant weight in vacuo at 25 °C.

The molecular characteristics of these samples are shown in Table 2.7.

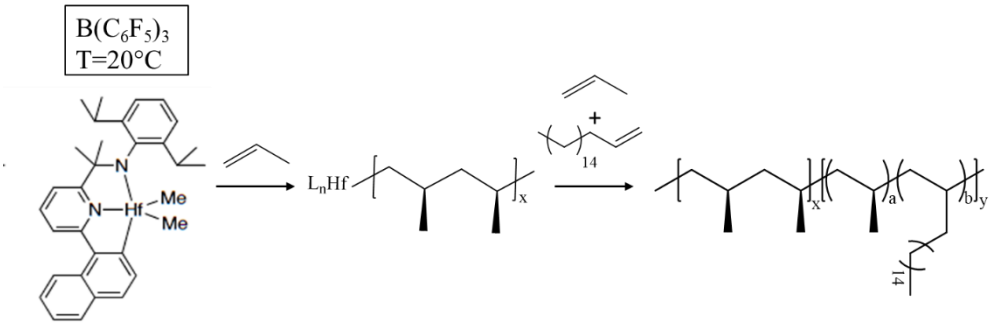

Scheme 2.2 Structure of pyridylamidohafnium dimethyl complex activated with $B(C_6F_5)_3$ used as catalyst for the preparation of the iPP-*b*-P(P-*co*-C18) BCPs and scheme of the sequential polymerization procedure.

Table 2.7 Total molecular mass ($M_{n\ TOT}$), molecular mass of the iPP block ($M_{n\ iPP}$) and of the P(P-*co*-C18) block ($M_{n\ PPC18}$), polydispersity index (M_w/M_n), mass fraction (w_{iPP}) and volume fraction (f_{iPP}) of the iPP block, concentration of the 1-octadecene units in the P(P-*co*-C18) random copolymer block (C18).

SAMPLE	M_n[a] TOT (kg/mol)	M_n[a] iPP (kg/mol)	M_n[b] PPC18 (kg/mol)	$\frac{M_w}{M_n}$[a]	w_{iPP}[c]	f_{iPP}[d]	C18[e] (mol%)
RDG-1-133P	250.1	-	-	1.39	-	-	18
RDG-1-41	139.8	-	-	1.29	1	1	-
RDG-1-148P	135	66.8	68.2	1.30	0.49	0.47	24
RDG-1-135P	114.4	50.3	64.1	1.27	0.44	0.41	13
RDG-1-139P	124.9	38.3	86.6	1.30	0.31	0.28	≈24

a evaluated from GPC analysis; **b** calculated from $M_{n\ TOT}$ and $M_{n\ iPP}$ as $M_{n\ PPC18}=M_{n\ TOT}-M_{n\ iPP}$; **c** calculated as $M_{n\ iPP}/M_{n\ TOT}$; **d** calculated from the molecular masses $M_{n\ iPP}$ and $M_{n\ TOT}$ and the densities of iPP (ρ_{iPP}=0.936 g/cm^3) and of the iPP-*b*-P(P-*co*-C18) BCPs ($\rho_{iPP\text{-}b\text{-}P(P\text{-}co\text{-}C18)}$) as $f_{iPP}=(M_{n\ iPP}/\rho_{iPP})/(M_{n\ TOT}/\rho_{iPP\text{-}b\text{-}P(P\text{-}co\text{-}C18)})$. The density of iPP is the theoretical value for a sample having 100% crystallinity, the densities of the iPP-*b*-P(P-*co*-C18) BCPs have been experimentally determined by flotation (see Appendix 3); **e** evaluated from ^{13}C-NMR as described in Appendix 1 section 4.

The composition of the P(P-*co*-C18) random copolymer and of the iPP-*b*-P(P-*co*-C18) BCPs has been determined by ^{13}C-NMR analysis as described in Appendix 1 section 4.

The characterization has been performed on as prepared samples and/or on compression molded samples. The compression molded samples have been prepared by heating the as prepared samples at ≈160 °C under a press at very low pressure, keeping it at this temperature for 5min, and cooling it down to room temperature at a cooling rate of about 15°C/min.

The thermal characterization of the samples has been carried out by calorimetric measurements performed with a differential scanning calorimeter

(DSC-822 by Mettler Toledo) in a flowing N_2 atmosphere and at a scanning rate of 10°C/min.

The structural characterization at different length scales has been carried out by X-ray scattering techniques. Wide angle X-ray scattering (WAXS) analysis has been performed on unoriented (powder) and oriented (fiber) samples using an automatic diffractometer (Philips) and a cylindrical camera equipped with a MS (MultiSensitive) phosphor storage imaging plate (Fujifilm) respectively. The low-temperature structural characterization of oriented fibers has been performed by using Bruker-Nonius Kappa CCD diffractometer equipped with Oxford-Cryostream 700 apparatus, using graphite monochromatized Mo-Kα radiation (0.71073Å). Time/temperature resolved Small and Wide angle (SAXS/WAXS) X-ray scattering analysis has been performed on BM26B (DUBBLE) station at the European Synchrotron Radiation Facility (ESRF) in Grenoble, France. A modified DSC Linkam hot stage permitting the transmission of the X-rays through the sample has been employed for the in situ thermal treatment of the samples. The data have been acquired during the heating/cooling of the sample at a rate of 10°C/min or 40°C/min, with an acquisition time of 6s, a delay time of 6s and a wavelength of 1.0402Å.

Mechanical characterization has been performed at room temperature with a universal mechanical tester (Zwicky by Zwick Roell) following the standard test methods for tensile properties of thin plastic sheets, ASTM D882-83. The mechanical parameters reported for each sample are averaged results from at least five independent experiments.

Morphological characterization at different length scales has been performed by using an optical miscroscope (Zeiss Axioskop 40) working in polarized light (POM), a Transmission Electron Microscope (TEM) (Philips EM 208S) operating at 100kV and an atomic force microscope (AFM) (Veeco Caliber microscope) working in tapping mode.

2.2.2 WAXS and thermal analyses of as prepared and compression molded samples

X-ray powder diffraction profiles of as prepared samples (A) and of compression molded samples (A') of the iPP-*b*-P(P-*co*-C18) BCPs and of the iPP homopolymer and P(P-*co*-C18) random copolymer are shown in Figure 2.21.

The X-ray diffraction profile of the as prepared sample of the P(P-*co*-C18) random copolymer (curve a in Figure 2.21 A) shows an amorphous halo centered at 2θ=18.8°. This sample is sticky, and subjected to flow during the compression molding protocol at relatively high temperatures (≈100°C), therefore the WAXD data of the compression-molded sample has not been acquired.

As stated in section 2.1.2, the X-ray powder diffraction profiles of the as prepared and compression molded iPP homopolymer (curves b in Figure 2.21 A and A' respectively), show the typical reflections of α form. The presence of the $(117)_\gamma$ reflection at 2θ=20° of low intensity indicates that this sample crystallizes in the α form, with small amounts of γ form.

The X-ray diffraction profile of the as prepared sample of the iPP-*b*-P(P-*co*-C18) BCP RDG-1-148P (w_{iPP}=0.49) (curves c in Figure 2.21 A) shows the typical reflections of the α form of iPP. The $(130)_\alpha$ reflection at 2θ≈18° shows a small shoulder at 2θ≈20° corresponding to the of $(117)_\gamma$ reflection of γ form. This indicates that the iPP block crystallizes in the α form with small amounts of γ form or α/γ disordered modifications.

The X-ray diffraction profile of the as prepared sample of the iPP-*b*-P(P-*co*-C18) BCP RDG-1-135P (w_{iPP}=0.44) shows only faint reflections overlaying the amorphous halo (curve d in Figure 2.21 A), while the X-ray diffraction profile of the as prepared sample of the BCP RDG-1-139P (w_{iPP}=0.31) (curve e in Figure 2.21 A) shows no crystalline reflections. Only two haloes centered at 2θ≈15° and ≈20° are present. The absence of narrow Bragg peaks for the sample RDG-1-139P is due to the low fraction of iPP block (w_{iPP}=0.31) which is unable to crystallize in the powder obtained from the reaction medium. The absence of crystallinity in this BCP indicates that the P(P-*co*-C18) block is amorphous, and is in agreement with the fact that also the P(P-*co*-C18) random copolymer synthesized with the same catalyst and in the same reaction conditions as the iPP-*b*-P(P-*co*-C18) BCPs, is amorphous, as indicated by the corresponding X-ray powder diffraction profile (curve a in Figure 2.21 A).

The X-ray powder diffraction profiles of the compression moulded samples of the iPP-*b*-P(P-*co*-C18) BCPs (curves c-e in Figure 2.21 A') show the typical reflections of the α form of iPP. The presence of small amounts γ form and/or α/γ disordered modifications is indicated by the shoulder at 2θ ≈20° relative to the $(117)_\gamma$ reflection of γ form.

The degree of crystallinity (x_c) of as prepared and compression molded samples of the iPP-*b*-P(P-*co*-C18) BCPs decreases by decreasing the mass fraction of the iPP block (w_{iPP}). The values of x_c calculated from the experimental WAXS profiles of the iPP-*b*-P(P-*co*-C18) BCPs as well as iPP homopolymer, are reported in Table 2.8 in the case of the as prepared samples and in Table 2.9 in the case of the compression molded samples.

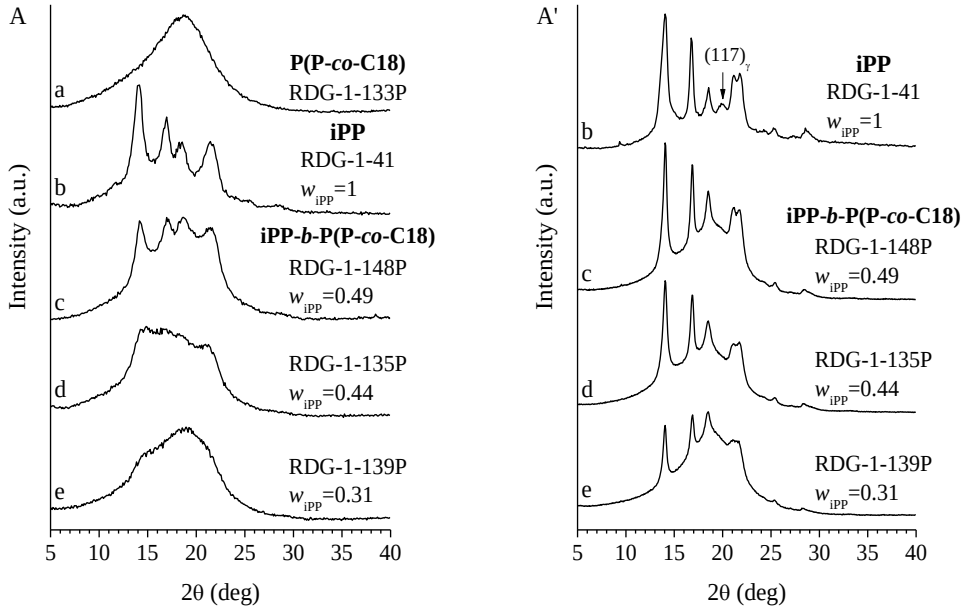

Figure 2.21 X-ray powder diffraction profiles of the as prepared (A) and compression molded samples (B) of the P(P-*co*-C18) random copolymer (a), iPP homopolymer (b) and iPP-*b*- P(P-*co*-C18) BCPs (c-e).

DSC thermograms of the as prepared and compression molded samples of the P(P-*co*-C18) random copolymer, iPP homopolymer and iPP-*b*-P(P-*co*-C18) BCPs are shown in Figure 2.22 and Figure 2.23, respectively.

The DSC thermograms of the as prepared sample of the P(P-*co*-C18) random copolymer only show an endothermic peak in the heating scans (Figures 2.22 A and C) and an exothermic peak in the cooling scan (Figure 2.22 B), both below room temperature, which are relative to melting and crystallization of the side chain of the 1-octadecene (C18) units. This confirms that at room temperature the sample is amorphous, as observed from WAXS analysis.

As shown in section 2.1.2, the DSC thermograms of the as prepared sample of the iPP homopolymer show the melting of the crystals in the α form

at *T*=134°C (curve b in Figure 2.22 A), the crystallization of the α and γ forms crystals at *T*=102°C during the cooling (curve b in Figure 2.22 B), and successive melting, during the second heating, at *T*=135°C (curve b in Figure 2.22 C).

The DSC heating thermograms recorded during the first heating of the as prepared samples of the iPP-*b*-P(P-*co*-C18) BCPs (curves c-e in Figure 2.22 A) show two main endothermic peaks. The low temperature peak, in the temperature range 9-20°, is relative to the melting of the side chains of the C18 units in the P(P-*co*-C18) blocks, whereas the peak at higher temperature, ≈136°C, is relative to the melting of the iPP blocks. Broad endothermic peaks of low area are also evident in the range 40-80°C. These are probably due to the melting of thin and defective iPP crystals formed by the longest propene sequences belonging to the P(P-*co*-C18) blocks and/or to the melting/relaxation/re-organization phenomena of the mesomorphic aggregates formed in the P(P-*co*-C18) block domains, characterized by inclusion of the long side chains of the C18 units in between the chains in 3/1 helical conformation ("new mesophase" vide infra).[43] The DSC thermograms recorded during the cooling and successive heating of the as prepared samples of the iPP-*b*-P(P-*co*-C18) BCPs (curves c-e in Figure 2.22 B and C, respectively) show a low temperature peak due to the crystallization/melting of the side chains of the C18 units in the P(P-*co*-C18) blocks, and a high temperature peak due to the crystallization/melting of the iPP blocks.

The DSC thermograms of the compression molded samples (Figure 2.23 A-C) are similar to those of the as prepared samples. The most remarkable difference consists in the fact that during the first heating scan, the melting peak of the side chains belonging to the C18 units in the P(P-*co*-C18) blocks results double (curves c-e in Figure 2.23 A).

The values of the melting/crystallization temperatures relative to the side chains of the C18 units and to the iPP block, and the corresponding enthalpies, are reported in Table 2.8 for the as prepared samples and in Table 2.9 for the compression molded samples.

It is apparent that for all the iPP-*b*-P(P-*co*-C18) BCPs within the series, the melting temperature of the iPP block is 133°C, while the melting temperature of the crystals formed by the side chains of the C18 units in the P(P-*co*-C18) block depends on the concentration of the C18 units and varies in the range 10-25°C. The higher the concentration of the C18 units, the higher the melting temperature of the crystals.

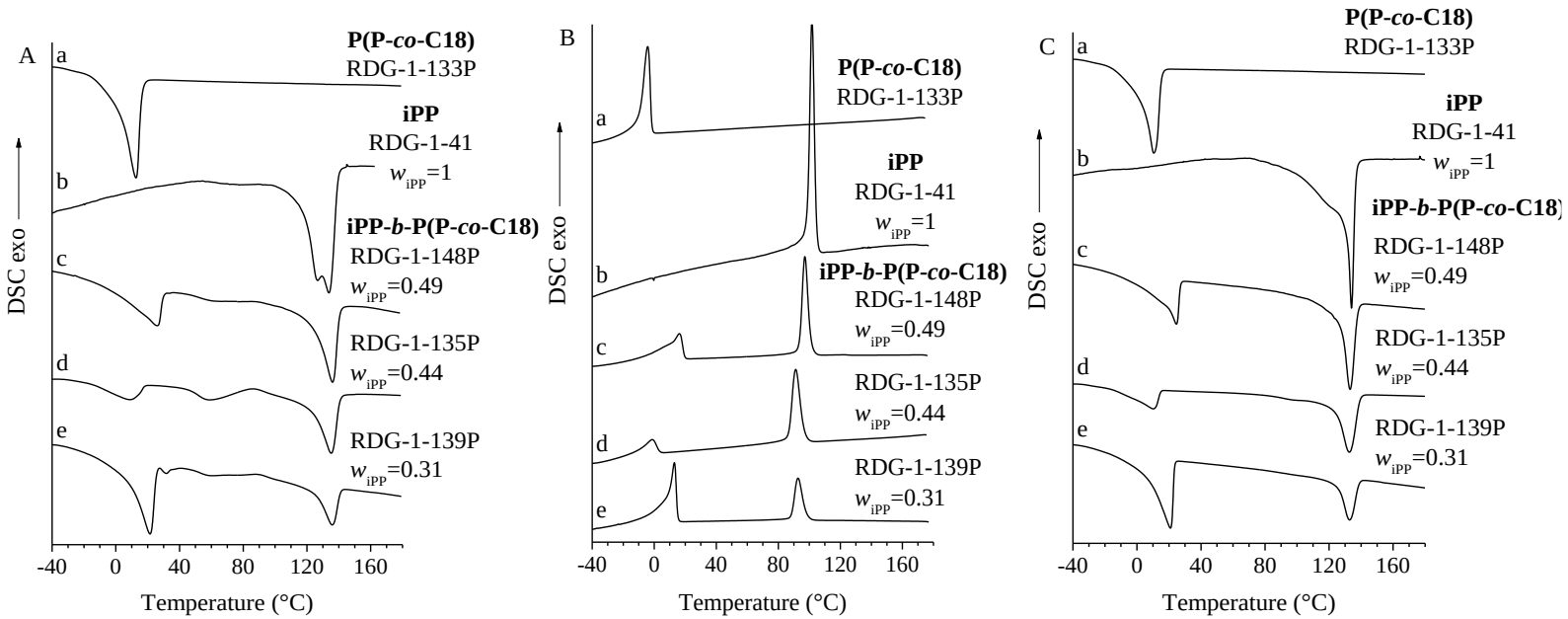

Figure 2.22 DSC thermograms recorded during heating (A), successive cooling (B) and second heating (C) of the as prepared samples of the P(P-*co*-C18) random copolymer (a), iPP homopolymer (b) and of the iPP-*b*- P(P-*co*-C18) BCPs (c-e).

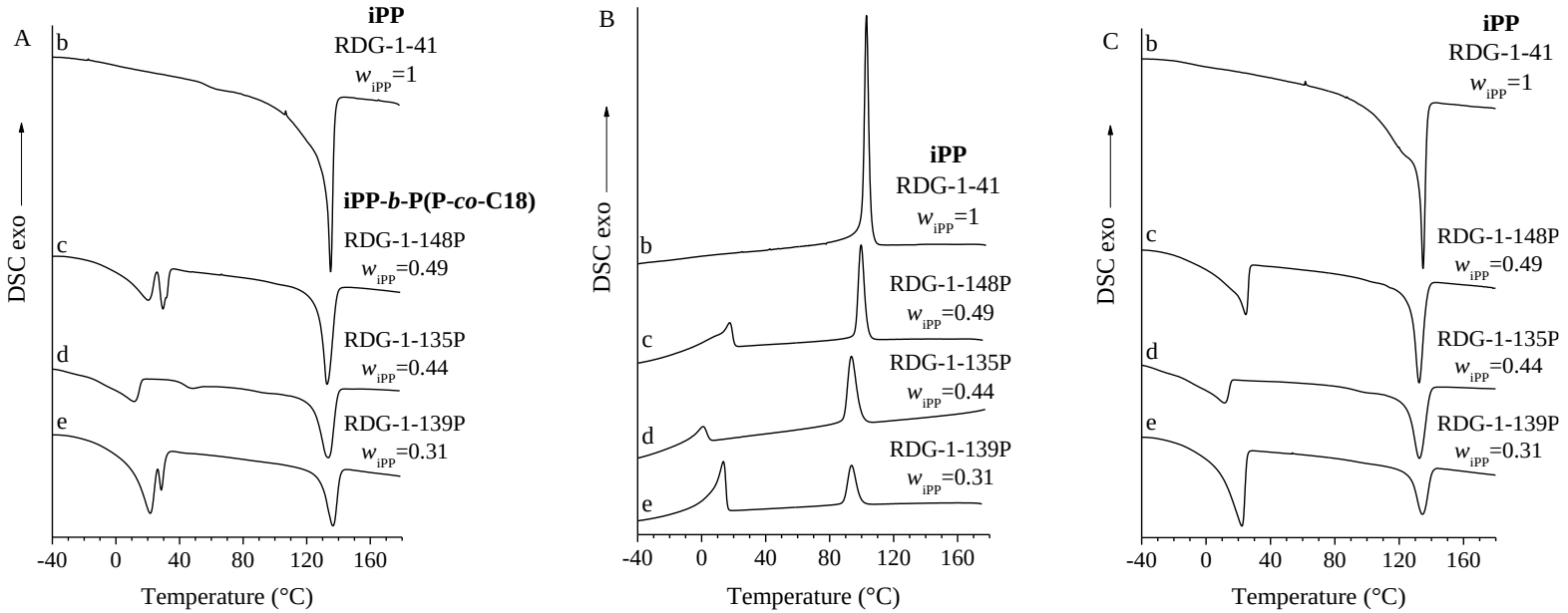

Figure 2.23 DSC thermograms recorded during heating (A), successive cooling (B) and second heating (C) of the compression molded samples of the P(P-*co*-C18) random copolymer (a), iPP homopolymer (b) and of the iPP-*b*- P(P-*co*-C18) BCPs (c-e).

Table 2.8 Mass fraction of the iPP block (w_{iPP}), degree of crystallinity of the whole sample (x_c) and of the iPP block ($x_{c\,iPP}$), melting temperature and enthalpy relative to the C18 units recorded during the first ($T_m^{I}{}_{C18}$, $\Delta H_m^{I}{}_{C18}$) and second ($T_m^{II}{}_{C18}$, $\Delta H_m^{II}{}_{C18}$) heating, melting temperature and enthalpy of the iPP block recorded during the first ($T_m^{I}{}_{iPP}$, $\Delta H_m^{I}{}_{iPP}$) and second ($T_m^{II}{}_{iPP}$, $\Delta H_m^{II}{}_{iPP}$) heating, crystallization temperature and enthalpy relative to the C18 units ($T_{c\,C18}$, $\Delta H_{c\,C18}$) and to the iPP block ($T_{c\,iPP}$, $\Delta H_{c\,iPP}$) recorded during the cooling, for the as prepared sample of the P(P-*co*-C18) random copolymer, iPP homopolymer and iPP-*b*-P(P-*co*-C18) BCPs.

SAMPLE	w_{iPP}	x_c (%)	x_c iPP (%)	T_m^{I} C18 (°C)	ΔH_m^{I} C18 (J/g)	T_m^{II} C18 (°C)	ΔH_m^{II} C18 (J/g)	T_m^{I} iPP (°C)	ΔH_m^{I} iPP (J/g)	T_m^{II} iPP (°C)	ΔH_m^{II} iPP (J/g)	T_c C18 (°C)	ΔH_c C18 (J/g)	T_c iPP (°C)	ΔH_c iPP (J/g)
RDG-1-133P	-	-	-	12	-43.3	10	-43.8	-	-	-	-	-4	40.4	-	
RDG-1-41	1	46	46	-	-	-	-	134	-67.6	134	-62.3	-	-	102	68.8
RDG-1-148P	0.49	17	35	26	-27.1	24	-27.6	136	-26.3	133	-29.1	16	28.4	97	33.9
RDG-1-135P	0.44	17	39	9	-10.5	11	-14.0	134	-30.8	133	-32.7	-1.5	13.4	92	34.1
RDG-1-139P	0.31	-	-	21	-36.5	21	-39.8	135	-16.4	133	-15.1	13	39.2	93	17.4

Table 2.9 Mass fraction of the iPP block (w_{iPP}), degree of crystallinity of the whole sample (x_c) and of the iPP block ($x_{c\ iPP}$), melting temperature and enthalpy relative to the C18 units recorded during the first ($T_m^{I}{}_{C18}$, $\Delta H_m^{I}{}_{C18}$) and second ($T_m^{II}{}_{C18}$, $\Delta H_m^{II}{}_{C18}$) heating, melting temperature and enthalpy of the iPP block recorded during the first ($T_m^{I}{}_{iPP}$, $\Delta H_m^{I}{}_{iPP}$) and second ($T_m^{II}{}_{iPP}$, $\Delta H_m^{II}{}_{iPP}$) heating, crystallization temperature and enthalpy relative to the C18 units ($T_{c\ C18}$, $\Delta H_{c\ C18}$) and to the iPP block ($T_{c\ iPP}$, $\Delta H_{c\ iPP}$) recorded during the cooling, for the compression molded sample of the iPP homopolymer and iPP-*b*-P(P-*co*-C18) BCPs.

SAMPLE	w_{iPP}	x_c (%)	x_c iPP (%)	T_m^{I} C18 (°C)	ΔH_m^{I} C18 (J/g)	T_m^{II} C18 (°C)	ΔH_m^{II} C18 (J/g)	T_m^{I} iPP (°C)	ΔH_m^{I} iPP (J/g)	T_m^{II} iPP (°C)	ΔH_m^{II} iPP (J/g)	T_c C18 (°C)	ΔH_c C18 (J/g)	T_c iPP (°C)	ΔH_c iPP (J/g)
RDG-1-41	1	51	51	-	-	-	-	135	-65.8	135	-66	-	-	103	72.4
RDG-1-148P	0.49	28	57	20	-27.1	25	-27.8	133	-29.8	132	-29.8	17	28.8	100	34.4
RDG-1-135P	0.44	27	61	12	-6.2	12	-14.9	133	-31.3	132	-27.8	0.5	15.1	93	36.3
RDG-1-139P	0.31	20	65	21	-40.1	22	-42.0	136	-18.4	134	-16.6	13	40.0	94	19.6

The crystallization of the side chains of the C18 units in the P(P-*co*-C18) random copolymer and in the P(P-*co*-C18) block of the iPP-*b*- P(P-*co*-C18) BCPs observed through thermal analysis has been confirmed by performing WAXS analysis at low temperatures. The X-ray diffraction analysis has been conducted for the P(P-*co*-C18) random copolymer, RDG-1-133P, and for the iPP-*b*-P(P-*co*-C18) BCP RDG-1-148P (w_{iPP}=0.49) (Figure 2.24).

The X-ray diffraction profiles recorded for the P(P-*co*-C18) random copolymer, RDG-1-133P, (Figure 2.24 A) show that the sample, that at T≥25°C is amorphous (curve a), undergoes crystallization when cooled below room temperature. In fact, the X-ray diffraction patterns recorded at 0°C (curve b) and -40°C (curve c) show a reflection at 2θ≈21°, due to the presence of polyethylene-like crystals formed by the side chains of the C18 units. The reflection at 2θ≈21° corresponds to the (110) reflection of the orthorhombic form of PE.

The X-ray diffraction profiles recorded for the iPP-*b*-P(P-*co*-C18) BCP RDG-1-148P (w_{iPP}=0.49) (Figure 2.24 B) show that the sample, that at room temperature exhibits crystallinity deriving from the sole iPP block, undergoes further crystallization when cooled below room temperature. In fact, the X-ray diffraction profiles recorded at 0°C (curve b) and -40°C (curve c) show increased intensity at 2θ≈21°, because of the overlapping of the $(110)_{PE}$ reflection, relative to the PE-like crystals formed by the side chains of the C18 units in the P(P-*co*-C18) blocks, with the $(111)_\alpha$, $(\bar{1}31)_\alpha$ +$(041)_\alpha$ reflections of the α form crystals formed by the iPP blocks.

Therefore, in iPP-*b*-P(P-*co*-C18) BCPs, different types of crystallinity may co-exist as a function of the temperature, which may be exploited in applications requiring heat release/absorption at fast rate, depending on the temperature.

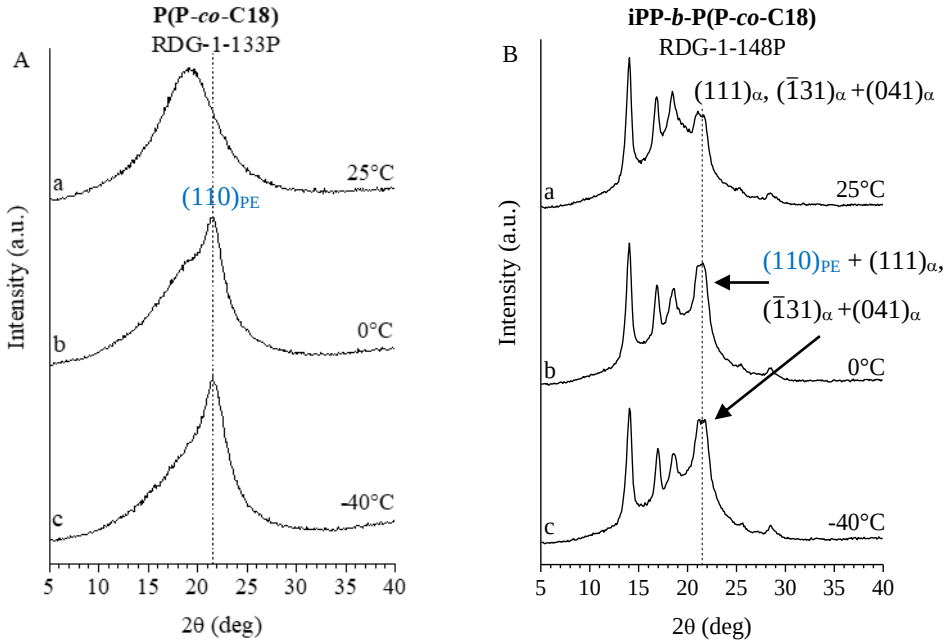

Figure 2.24 WAXS profiles of the P(P-*co*-C18) random copolymer RDG-1-133P (A) and of the iPP-*b*-P(P-*co*-C18) BCP RDG-1-148P (w_{iPP}=0.49) (B) recorded at the indicated temperatures.

2.2.3 Time/temperature resolved SAXS/WAXS analysis

The study of the structural organization of the crystalline iPP-*b*-P(P-*co*-C18) BCPs, at different length scales and as a function of temperature, has been performed through SAXS/WAXS analysis by using synchrotron radiation at ESRF.

For each BCP, a small piece of the compression molded sample has been enclosed between two kapton sheets and subjected to the following thermal treatment: rapid heating, at a rate of 40°C/min, up to 180°C, isotherm at 180°C for 1 minute, cooling down to -40°C at a rate of 10°C/min and heating up to 180°C at a rate of 10°C/min. An acquisition time of 6s and a delay time of 6s have been used, at a collection rate of 0.071frames/s. Selected SAXS/WAXS patterns recorded during three consecutive thermal ramps (heating-cooling-heating) and Lorentz corrected SAXS intensity profiles are shown for each sample in Figures 2.25-2.27.

The SAXS/WAXS profiles of a poly(1-octadecene) homopolymer (P(C18)) (see Appendix 4) have also been recorded at T=25°C and are shown in Figure 2.28.

In the case of the sample RDG-1-148P (w_{iPP}=0.49) (Figure 2.25), the SAXS patterns recorded during the first heating at 40°C/min up to the melting show no correlation peak in the temperature range T=38-70°C, even though the sample is crystallized in the α form, as indicated by the WAXS profiles a-b in A'. At 102°C a correlation peak appears (curve c in A) at $q^*\approx0.4nm^{-1}$ ($L_B\approx16nm$), which is relative to the crystalline lamellar stacks in the iPP block. With further increase of the temperature (142°C), the intensity of the correlation peak increases, whereas the position of the maximum shifts toward lower q values. In particular, at 142°C we have $q^*\approx0.26nm^{-1}$ corresponding to $L_B\approx24nm$ (curve d of Figure 2.25 A). The corresponding WAXS profiles (curves c, d of Figure 2.25 A') show a decrease of the intensity of Bragg peaks due to the incipient melting of the sample. Therefore, the decrease of q^* may be due to the incipient melting that leads to an increase of the mean distance between the crystalline lamellae L_B. Upon melting, at temperatures higher than 150°C, no features are observed in the corresponding SAXS profiles (curves e, f of Figure 2.25 A). Therefore, for this sample, the possible phase separation in the melt between iPP and the P(P-*co*-C18) blocks may not be established based on SAXS analysis, probably because of the too low contrast.

The SAXS/WAXS patterns recorded during the cooling of the sample from the melt at a rate of 10°C/min (Figure 2.25 B and B'), show that at 101.5°C the crystallization of the iPP block starts developing as indicated by the appearance of low intensity signals both in the SAXS and WAXS patterns (curve d in B and B' respectively). At lower temperatures, i.e. 71-55°C, once the crystallization is complete, a well-defined correlation peak at $q\approx0.46nm^{-1}$ ($L_B\approx14nm$) is observed in the SAXS patterns (curves e-f in B). In the corresponding WAXS profiles (curves e-f in B'), the typical reflections of the α form of iPP appear. At T≤0°C, the crystallization of the side chains of the C18 units in the P(P-*co*-C18) blocks occurs. In fact, the SAXS patterns show a second weak correlation peak at higher q values, $q\approx1nm^{-1}$ ($L_B\approx6nm$), that partly overlaps with the correlation peak at $q\approx0.49nm^{-1}$ relative to the lamellar stacking of the iPP blocks (curves g-h in B). The corresponding WAXS profiles, indeed, show an increase of the intensity at q=15nm^{-1} due to the superimposition of the (110) reflection of the PE-like crystallites with the $(111)_\alpha$ and $(\bar{1}31)_\alpha$ + $(041)_\alpha$ reflections of the α form crystals in the iPP block (curves g-h in B').

The SAXS/WAXS patterns recorded during the successive heating of the sample at a rate of 10°C/min (Figure 2.25 C and C') show the melting of the

side chains of the C18 units at $T \approx 0.5$°C, as indicated by the disappearance of the correlation peak at $q \approx 1 nm^{-1}$ in the SAXS patterns and the decrease of the intensity at $q = 15 nm^{-1}$ in the WAXS patterns. At higher temperatures, 26-110°C, the intensity of the correlation peak relative to the crystalline iPP block at $q \approx 0.45 nm^{-1}$ increases (curves c-f in C), probably due to an increase of the electron density contrast between the amorphous and crystalline phases. At $T > 134$°C, once the melting of the sample occurs, the correlation peak disappears and no other features are visible in the SAXS profile (curve h in C).

The emergence/disappearance of correlation peaks in the SAXS profiles during the heating/cooling runs is confirmed by the presence of maxima in the SAXS profiles corrected for the Lorentz factor (Figure 2.25 A'', B'' and C''). The position of these maxima (q^*) as a function of the temperature are collected in Table 2.10. The corresponding correlation distance (L_B), calculated using the Bragg law, is also reported.

Table 2.10 Values of the position of the correlation peak (q^*) and of the corresponding Bragg distance (L_B) at the indicated temperatures (T) obtained from the Lorentz corrected intensity profiles recorded during the first heating (*heating 40°C/min*), cooling (*cooling 10°C/min*) and successive heating (*heating 10°C/min*) of the iPP-*b*-P(P-*co*-C18) BCP sample RDG-1-148P (w_{iPP}=0.49).

heating 40°C/min			***cooling 10°C/min***			***heating 10°C/min***		
T **(°C)**	***q**** **(nm^{-1})**	***L*B** **(nm)**	***T*** **(°C)**	***q**** **(nm^{-1})**	***L*B** **(nm)**	***T*** **(°C)**	***q**** **(nm^{-1})**	***L*B** **(nm)**
38	-	-	180	-	-	-40	0.50/1[a]	12.6/6.3[a]
70	-	-	125.5	-	-	0.5	0.49/1[a]	12.8/6.3[a]
102	0.38		103.5	0.36	17.4	26.5	0.42	14.9
142	0.26	24	101.5	0.37	17.0	50.5	0.39	16.1
150	-		71.5	0.38	16.5	80.5	0.38	16.5
180	-	-	55.5	0.47	13.4	110.5	0.36	17.4
			-0.5	0.49/1[a]	12.8/6.3[a]	134.5	0.31	20.6
			-40	0.50/1[a]	12.6/6.3[a]	140.5	-	-

a) value relative to the PE-like crystallites formed by the side chains of the C18 units in the P(P-*co*-C18) blocks.

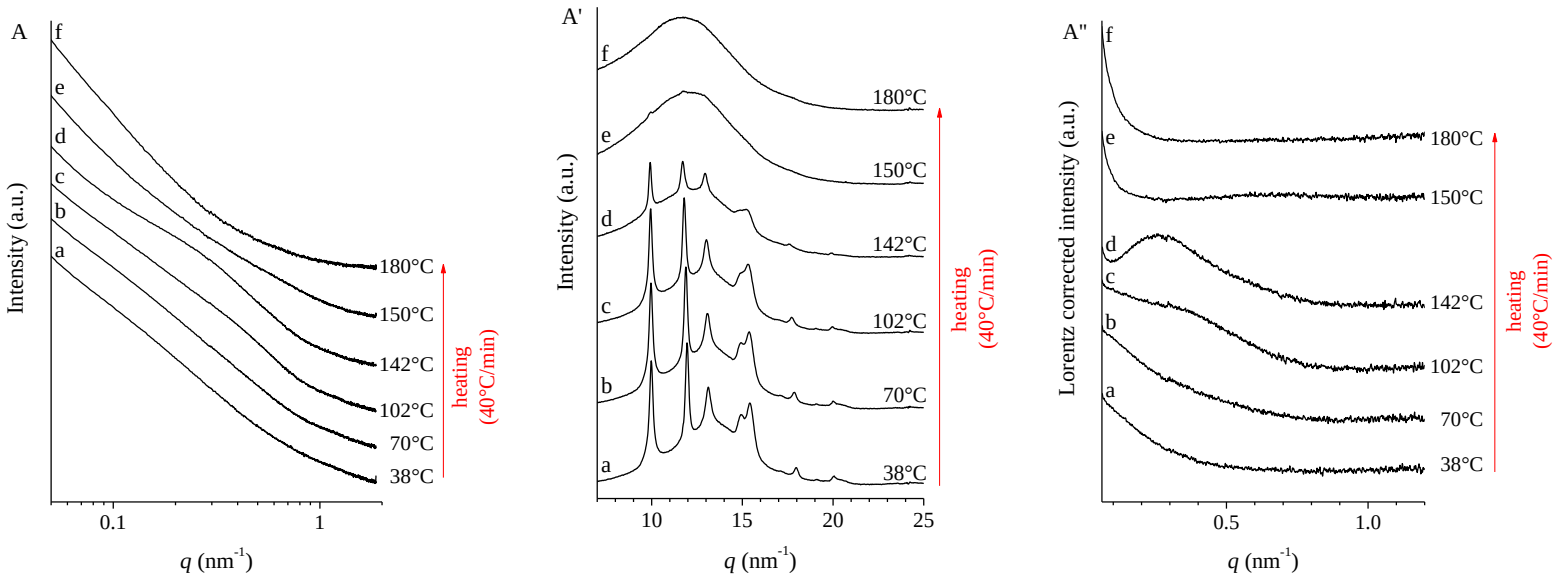
A
Intensity (a.u.)
f
e
d
c
b
a
180°C
150°C
142°C
102°C
70°C
38°C
heating
(40°C/min)
0.1
1
q (nm-1)
A'
Intensity (a.u.)
10
15
20
25
q (nm-1)
A"
Lorentz corrected intensity (a.u.)
0.5
1.0
q (nm-1)

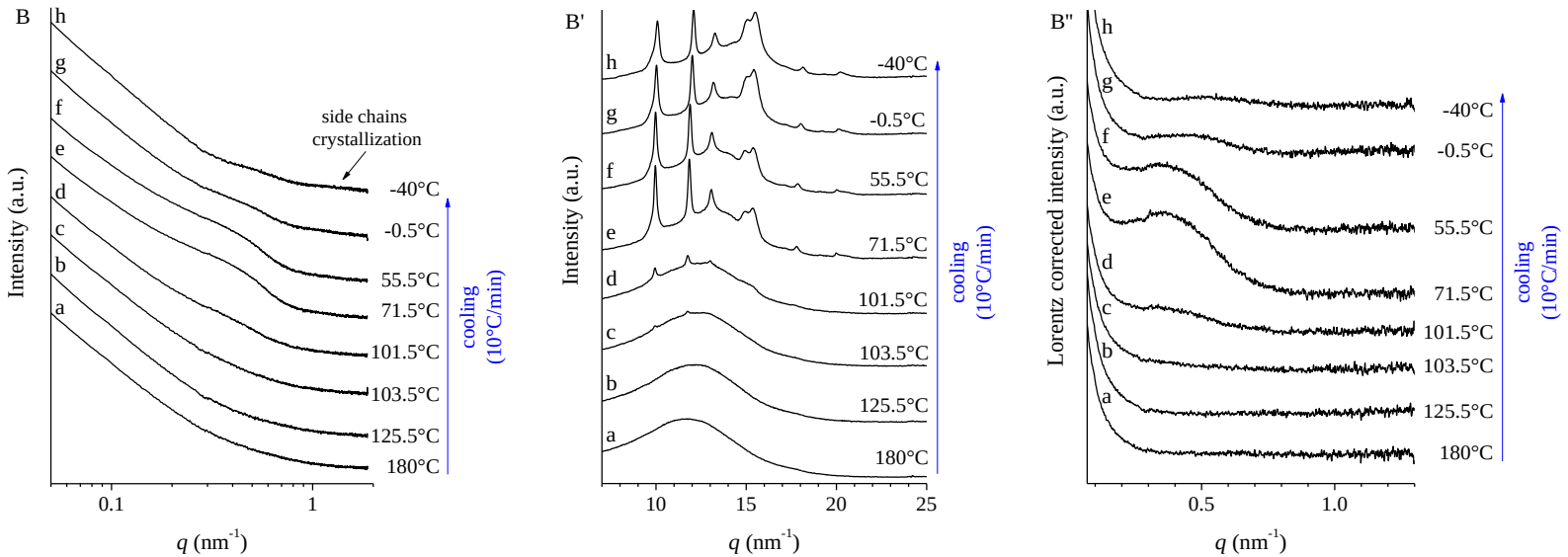
B
h
g
f
e
d
c
b
a
side chains
crystallization
-40°C
-0.5°C
55.5°C
71.5°C
101.5°C
103.5°C
125.5°C
180°C
cooling
(10°C/min)
Intensity (a.u.)
0.1
1
q (nm-1)
B'
-40°C
-0.5°C
55.5°C
71.5°C
101.5°C
103.5°C
125.5°C
180°C
cooling
(10°C/min)
Intensity (a.u.)
10
15
20
25
q (nm-1)
B"
Lorentz corrected intensity (a.u.)
0.5
1.0
q (nm-1)

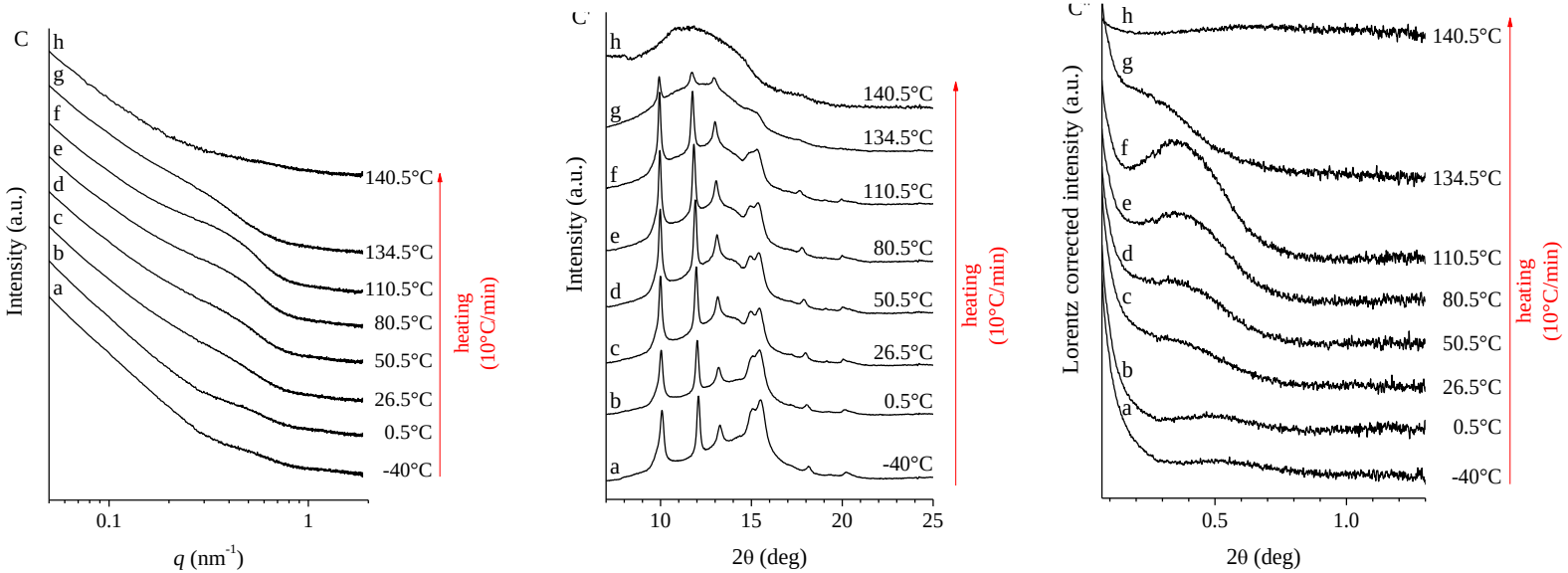

Figure 2.25 SAXS (A, B, C), WAXS (A', B', C') and Lorentz corrected (A'', B'', C'') intensity profiles of the sample RDG-1-148P (w_{iPP}=0.49) recorded at the indicated temperatures during heating at a rate of 40°C/min (A, A', A''), cooling at a rate of 10°C/min (B, B', B'') and successive heating at a rate of 10°C/min (C, C', C'').

The SAXS/WAXS profiles recorded at different temperatures for the sample RDG-1-135P (w_{iPP}=0.44) are shown in Figure 2.26. The patterns recorded during the heating at 40°C/min up to the melting (Figure 2.26 A and A') show that the sample is crystalline up to 142°C. In fact, a correlation peak in the SAXS profiles (curves a-d in A) and crystalline reflections of the α form in the corresponding WAXS profiles (curves a-d in A') are observed. The correlation peak increases in intensity during the heating and, at the same time, shifts to lower q values (from q≈0.57nm^{-1} to q≈0.48nm^{-1}). This indicates that, similar to the sample RDG-1-148P, higher L_B values are reached. At T≥150°C the sample is in the melt state and the correlation peak in the SAXS profile is undetectable (curves e-f in A). Therefore, also for this sample, the possible phase separation in the melt may not be established based on SAXS analysis.
The SAXS/WAXS profiles recorded during the cooling at a rate of 10°C/min (Figure 2.26 B and B' respectively), show that at 97°C the crystallization of the iPP blocks starts occurring, as indicated by the appearance of reflections of low intensity in the corresponding WAXS pattern (curve c in B'). At lower temperatures, 80-3°C, when a higher amount of crystals has developed, the intensity of the crystalline reflections in the WAXS patterns increases (curves d-g in B') and a correlation peak of low intensity also appears in the corresponding SAXS profiles at q≈0.5nm^{-1} (indicated by the arrows in curves d-g in B). By further cooling the sample to T≤0°C, the crystallization of the side chains of the C18 units in the P(P-*co*-C18) blocks occurs. In the SAXS pattern recorded at -40°C (curve h in B), the correlation peak at q^*≈1nm^{-1} relative to the crystallization of the side chains of the C18 units is barely visible. Only a change in the slope of the curve is observed. Similarly, the corresponding WAXS pattern shows only a small increase of the intensity at q=15nm^{-1} (curve h in B') due to the formation of the PE-like crystals. This is due to the fact that for this sample, the concentration of the C18 units in the P(P-*co*-C18) block is lower than that observed in the P(P-*co*-C18) block of the sample RDG-1-148P, therefore smaller quantities of PE-like crystallites develop.
The SAXS/WAXS profiles recorded during the successive heating at a rate of 10°C/min (Figure 2.26 C and C') show the melting of the side chains of the C18 units at T>0°C as indicated by the change in the slope of the SAXS profile at q≈1nm^{-1} and by the decrease of the intensity at q=15nm^{-1} in the corresponding WAXS profile. In the range of T=20-134°C a low intensity correlation peak at q≈0.5nm^{-1} relative to the iPP block is observed. The

position of the correlation peak shifts towards lower q values during the heating of the sample (curves d-g in C), up to disappear at T>134°C, because of the melting of the sample (curve h in C).

The emergence/disappearance of correlation peaks in the SAXS profiles during the heating/cooling runs is confirmed by the presence of maxima in the Lorentz corrected intensity profiles (Figure 2.26 A'', B'' and C'').

The position of these maxima (q*) as a function of the temperature are collected in Table 2.11. The corresponding correlation distance (L_B), calculated using the Bragg law, is also reported.

Table 2.11 Values of the position of the correlation peak (q*) and of the corresponding Bragg distance (L_B) at the indicated temperatures (T) obtained from the Lorentz corrected intensity profiles recorded during the first heating (*heating 40°C/min*), cooling (*cooling 10°C/min*) and successive heating (*heating 10°C/min*) of the iPP-*b*-P(P-*co*-C18) BCP sample RDG-1-135P (w_{iPP}=0.44).

heating 40°C/min			***cooling 10°C/min***			***heating 10°C/min***		
T **(°C)**	***q**** **(nm^{-1})**	***L*$_B$** **(nm)**	***T*** **(°C)**	***q**** **(nm^{-1})**	***L*$_B$** **(nm)**	***T*** **(°C)**	***q**** **(nm^{-1})**	***L*$_B$** **(nm)**
38	0.57	11.0	180	-	-	-40	0.48	13.1
70	0.52	12.0	125	-	-	0	0.48	13.1
102	0.49	12.8	97	-	-	20	0.47	13.4
142	-	-	80	0.47	13.4	50	0.47	13.4
150	-	-	50	0.47	13.4	80	0.46	13.6
180	-	-	20	0.47	13.4	120	0.45	14.0
			3	0.48	13.1	134	-	-
			-40	0.48	13.1	180	-	-

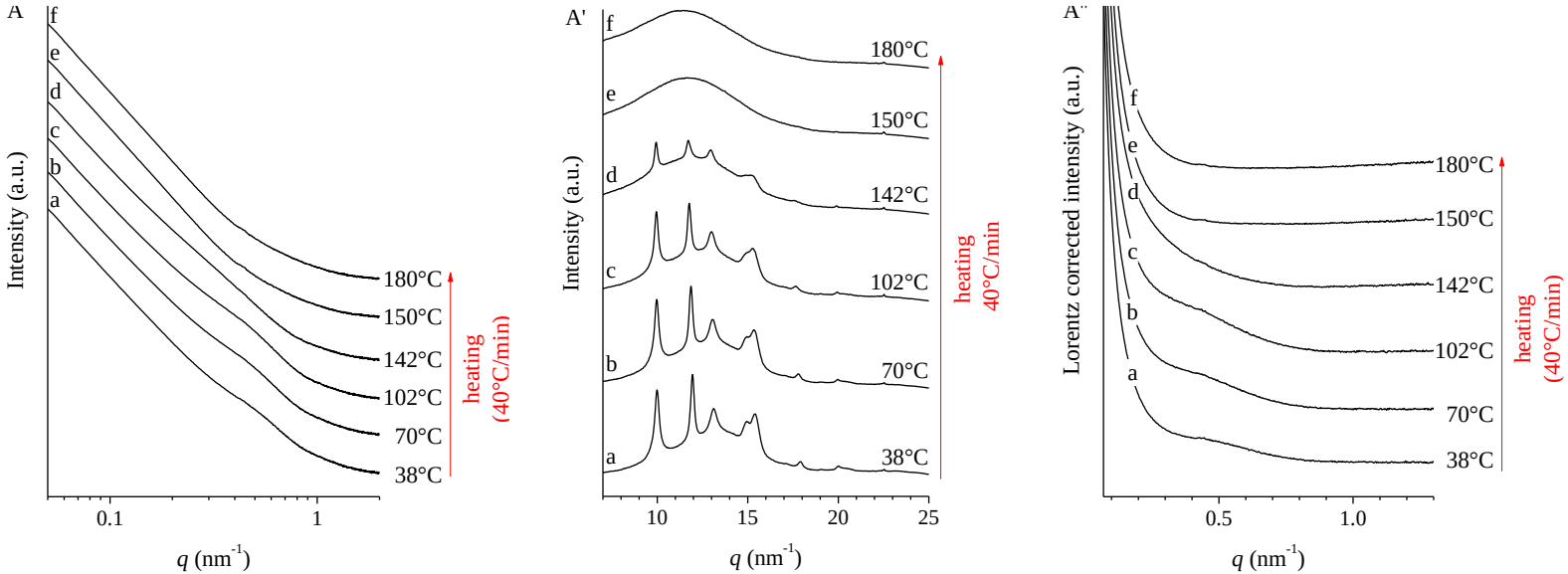
A
Intensity (a.u.)
f
e
d
c
b
a
180°C
150°C
142°C
102°C
70°C
38°C
heating
(40°C/min)
0.1
1
q (nm-1)
A'
Intensity (a.u.)
f
e
d
c
b
a
180°C
150°C
142°C
102°C
70°C
38°C
heating
40°C/min
10
15
20
25
q (nm-1)
A''
Lorentz corrected intensity (a.u.)
f
e
d
c
b
a
180°C
150°C
142°C
102°C
70°C
38°C
heating
(40°C/min)
0.5
1.0
q (nm-1)

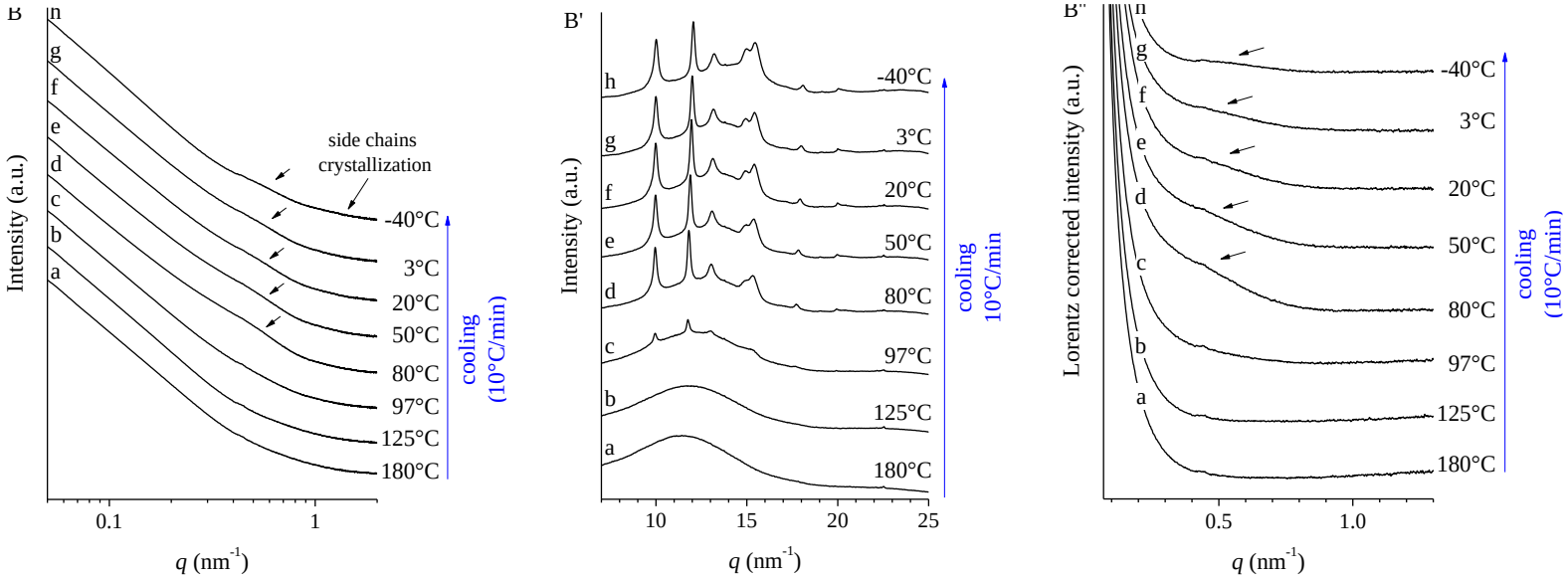
B
Intensity (a.u.)
side chains
crystallization
-40°C
3°C
20°C
50°C
80°C
97°C
125°C
180°C
cooling
(10°C/min)
0.1
1
q (nm-1)
B'
Intensity (a.u.)
-40°C
3°C
20°C
50°C
80°C
97°C
125°C
180°C
cooling
10°C/min
10
15
20
25
q (nm-1)
B''
Lorentz corrected intensity (a.u.)
-40°C
3°C
20°C
50°C
80°C
97°C
125°C
180°C
cooling
(10°C/min)
0.5
1.0
q (nm-1)

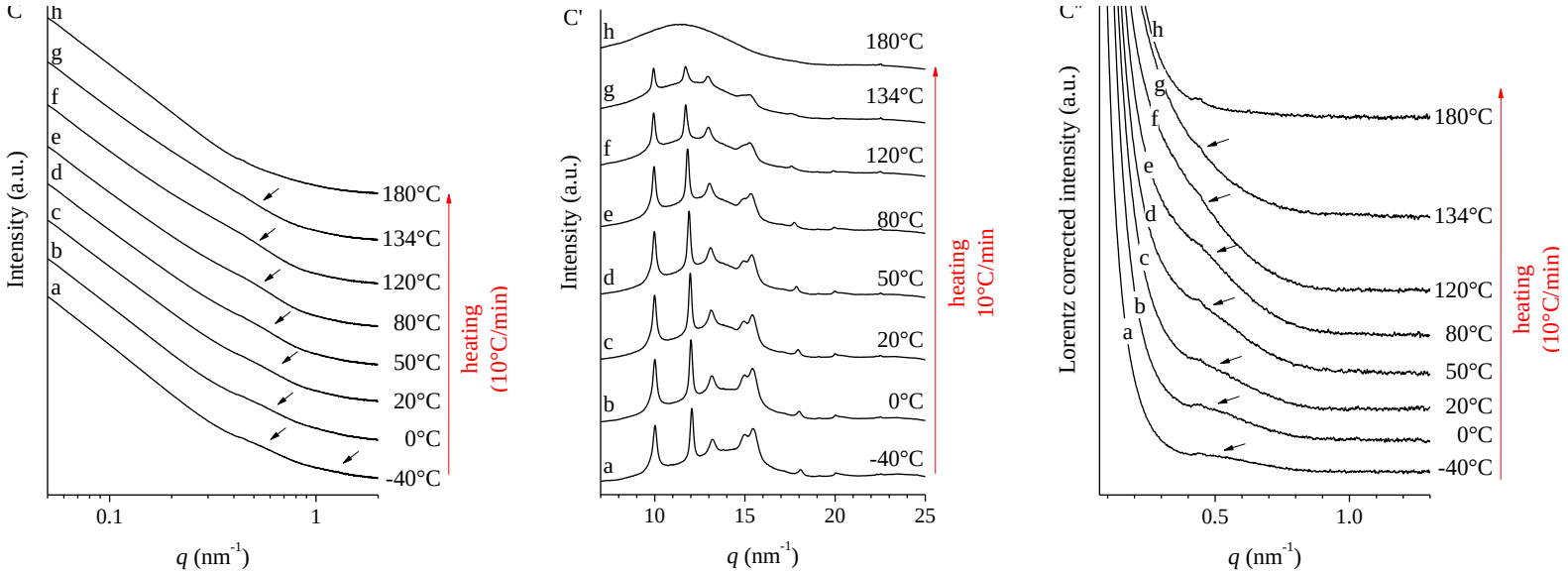

Figure 2.26 SAXS (A, B, C), WAXS (A', B', C') and Lorentz corrected (A'', B'', C'') intensity profiles of the sample RDG-1-135P (w_{iPP}=0.44) recorded at the indicated temperatures during heating at a rate of 40°C/min (A, A', A''), cooling at a rate of 10°C/min (B, B', B'') and successive heating at a rate of 10°C/min (C, C', C'')

The SAXS/WAXS profiles recorded as a function of the temperature for the sample RDG-1-139P (w_{iPP}=0.31) are shown in Figure 2.27.

The WAXS profiles recorded during the heating of the sample at 40°C/min show that initially, only slight crystallinity is present. In fact, the crystalline reflections relative to the iPP blocks are not visible (curves a-b in Figure 2.27 A'). With increasing the temperature, the annealing of the crystalline phase occurs, with the formation of higher amounts and/or less defective crystals in the iPP blocks. In fact, in the corresponding WAXS profiles (curves c-d in A'), the appearance of crystalline reflections superimposed to the amorphous halo of the P(P-*co*-C18) block is observed. At $T \geq 150$°C, the sample is in the melt state, and a single amorphous halo is observed in the corresponding WAXS profiles (curves e-f in A').

The corresponding SAXS patterns, as well as the Lorentz corrected intensity profiles, recorded during the heating at 40°C/min, show two correlation peaks, at q^*=0.15nm^{-1} ($L_B \approx$40nm) and q^*=0.62nm^{-1} ($L_B \approx$10nm). The intensities of these peaks increases with increasing the temperature (curves a-c in Figure 2.27 A and A''). At T=102°C, a shift of the two correlation peaks toward lower q values at ≈0.13 and ≈0.54nm^{-1} is observed, thus indicating increase of the correlation distance within the system. A possible model emerging from these data is shown in Figure 2.27 D. According to this model, the correlation distance $L_B \approx$40nm possibly corresponds to the average interdomain distance due to a phase separated morphology of the different blocks, whereas the correlation distance $L_B \approx$10nm, probably corresponds to intradomain periodicity due to lamellar stacking occurring within the iPP block domains. At higher temperatures, i.e. 142°C, the two correlation peaks merge in a single broad signal centered at $q \approx$0.3nm^{-1} (curve d in A and A''), which disappears at T≥150°C, due to the sample melting. Therefore, also in this case, the possible phase separation in the melt of the block domains may not be established based on SAXS data, probably because of the too low contrast in electron density between the iPP and P(P-*co*-C18) blocks. Only when the iPP block is in a crystalline state, the electron density contrast between the two block domains becomes high enough, as indicated by the small but significant correlation peak at q=0.15nm^{-1} in the SAXS profiles recorded in the range 38-102°C.

The patterns recorded during the cooling of the sample at a rate of 10°C/min, show that at 97.5°C, the crystallization of the iPP starts developing, as indicated by a change in the slope of the SAXS profile (curves a-c of Figure

2.27 B) and by the appearance of the crystalline reflections of low intensity in the corresponding WAXS profile (curve c in Figure 2.27 B'). At T<97.5°C, when higher amounts of crystals are formed in the iPP block domains, a broad signal appears in the SAXS profiles (curves d-g in B). This may be due to the overlapping of two different signals, one at lower *q* values due to the phase separated morphology of the two different block domains, and one at higher *q* values due to the lamellar stacking occurring within the iPP domains (Figure 2.27 D). This is better observed in the Lorentz corrected intensity profiles (curves d-g in B'') wherein a well-defined peak at q^*=0.1nm^{-1} and a broad signal at q≈0.4nm^{-1} are evident. At low temperatures, i.e. -40°C, upon crystallization of the side chains of the C18 units in the P(P-*co*-C18) blocks, two distinct correlation peaks in the SAXS profile are visible at q=0.53nm^{-1} (L_B≈12nm) and q=1.2nm^{-1} (L_B≈5nm) (curve h in B). The correlation peak at q=1.2nm^{-1} (L_B≈5nm) may arise from crystallization of the side chains belonging to the C18 units, occurring in the phase separated P(P-*co*-C18) block domains. The composite architecture of the copolymer sample RDG-1-139P which is established at low temperatures is shown in Figure 2.27 D. The resultant model includes phase separated domains populated by iPP and P(P-*co*-C18) blocks, lamellar stacking within the iPP domains, and presence of PE-like crystals within the P(P-*co*-C18) domains.

The WAXS profiles recorded during the cooling of the sample at a rate of 10°C/min show well-defined crystalline reflections, typical of the α form of iPP. The intensity of these reflections increases with decrease of the temperature (curves d-h in B'). At T= -40°C, the relative intensity of the reflection at q≈15nm^{-1} increases, due to the crystallization of the side chains belonging to the C18 units, in PE-like crystals. Indeed, the reflection at q≈15nm^{-1} increases by effect of the overlap of the $(111)_\alpha$ and $(\bar{1}31)_\alpha$ + $(041)_\alpha$ reflections of iPP-α form, with the $(110)_{PE}$ reflection relative to the PE-like crystals.

The position of the maxima (q^*) in the Lorentz corrected intensity profiles as a function of the temperature are collected in Table 2.12. The corresponding correlation distance (L_B), calculated using the Bragg law is also reported.

Table 2.12 Values of the position of the correlation peak (q^*) and of the corresponding Bragg distance (L_B) at the indicated temperatures (T) extracted from the Lorentz corrected intensity profiles recorded during the heating (*heating 40°C/min*) and successive cooling (*cooling 10°C/min*) of the iPP-*b*-P(P-*co*-C18) BCP sample RDG-1-139P (w_{iPP}=0.31).

heating 40°C/min			***cooling 10°C/min***		
T **(°C)**	***q**** **(nm^{-1})**	***L*B** **(nm)**	***T*** **(°C)**	***q**** **(nm^{-1})**	***L*B** **(nm)**
38	0.15[a]/0.62	41.9[a]/10.1	180	-	-
70	0.15[a]/0.62	41.9[a]/10.1	125.5	-	-
102	0.14[a]/0.52	44.9[a]/12.1	97.5	-	-
142	0.32	19.6	93.5	≈0.40	≈15.7
150	-	-	65.5	≈0.40	≈15.7
180	-	-	35.5	≈0.40	≈15.7
			7.5	≈0.3	≈21
			-40	0.53/1.1[b]	11.8/5.7[b]

a) value relative to the possible phase separated morphology.
b) value relative to the PE-like crystallites formed by the side chains of the C18 units in the P(P-*co*-C18) blocks.

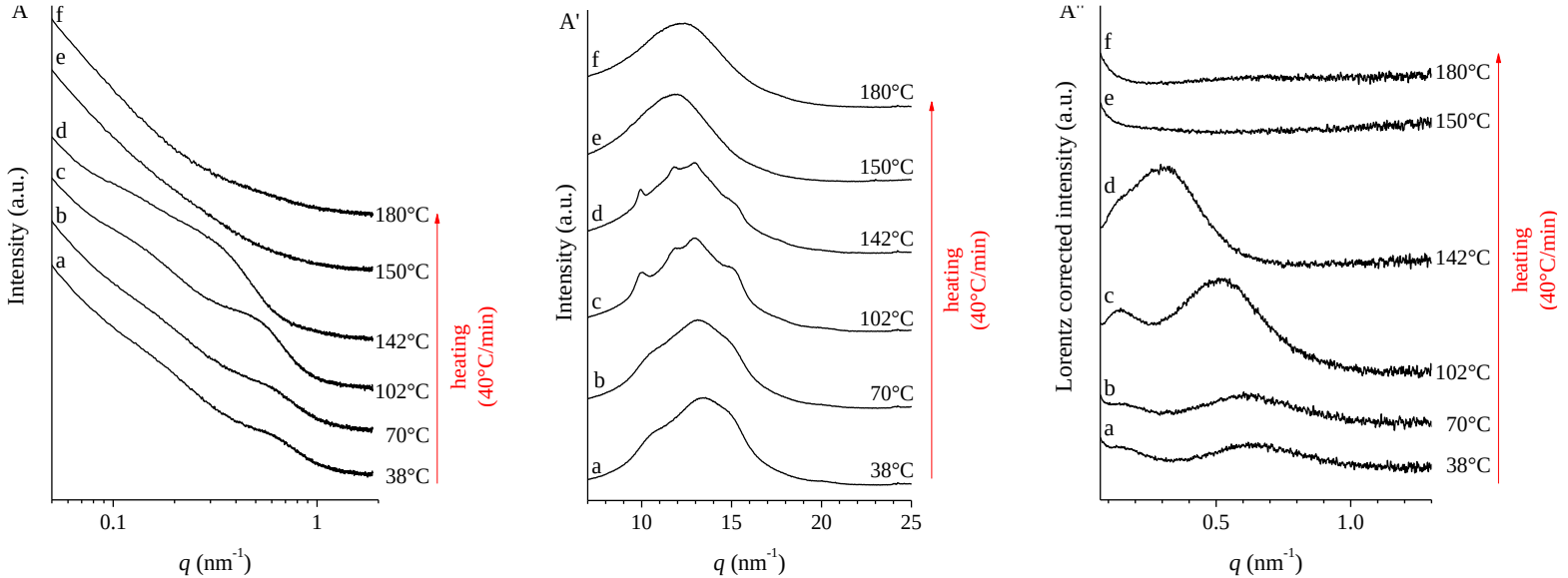
A
f
e
d
c
b
a
180°C
150°C
142°C
102°C
70°C
38°C
heating
(40°C/min)
Intensity (a.u.)
0.1
1
q (nm-1)
A'
f
e
d
c
b
a
180°C
150°C
142°C
102°C
70°C
38°C
heating
(40°C/min)
Intensity (a.u.)
10
15
20
25
q (nm-1)
A''
f
e
d
c
b
a
180°C
150°C
142°C
102°C
70°C
38°C
heating
(40°C/min)
Lorentz corrected intensity (a.u.)
0.5
1.0
q (nm-1)

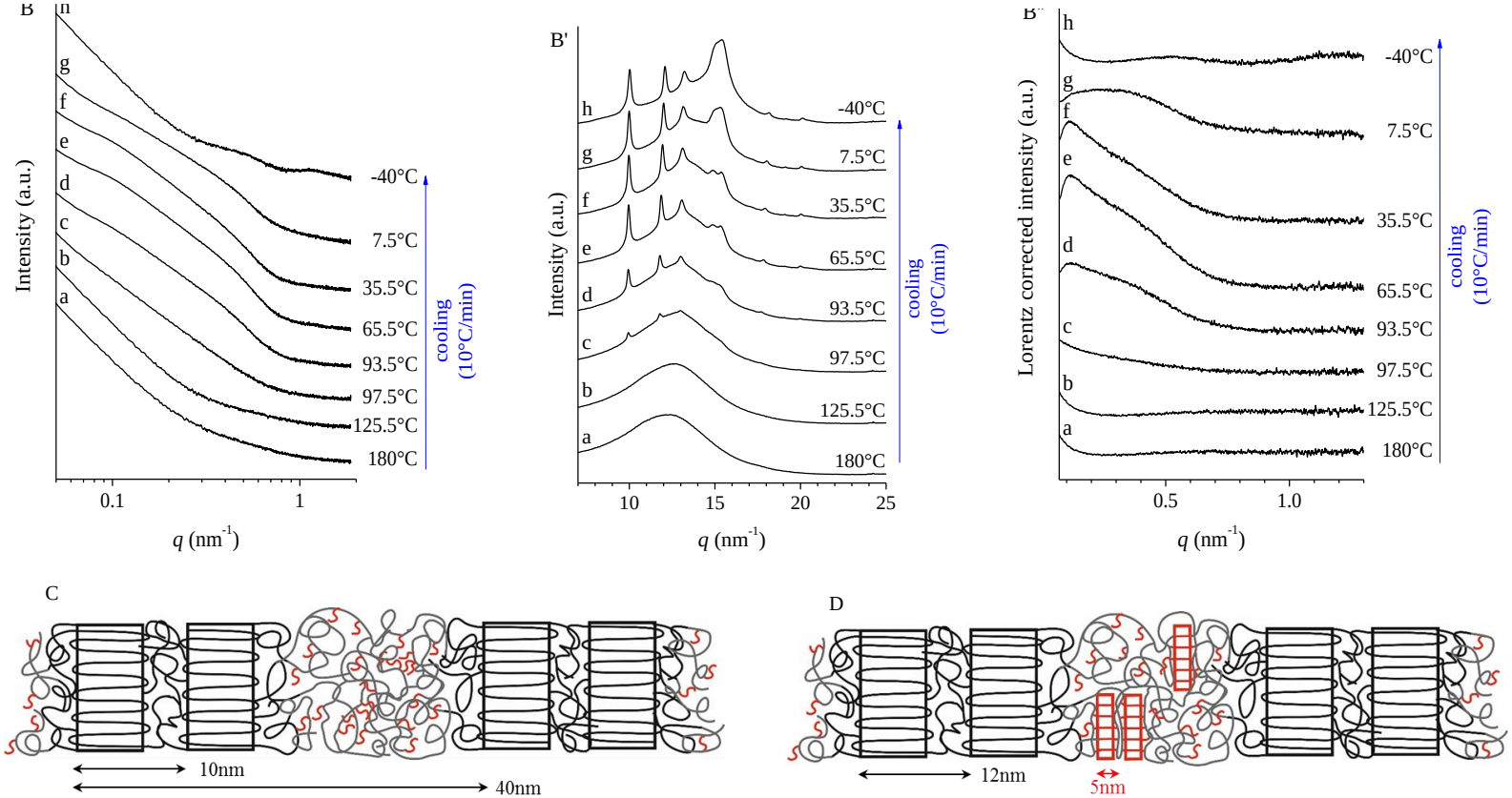

Figure 2.27 SAXS (A, B), WAXS (A', B') and Lorentz corrected (A'', B'') intensity profiles of the sample RDG-1-139P (w_{iPP}=0.31) recorded at the indicated temperatures during heating at a rate of 40°C/min (A, A', A'') and cooling at a rate of 10°C/min (B, B', B''). Scheme of the solid state organization of the iPP-*b*-P(P-*co*-C18) block copolymers above (C) and below (D) the melting temperature of the PE-like crystals formed by effect of crystallization of the side chains of the C18 units.

In Figure 2.28, the SAXS/WAXS patterns recorded at 25°C for a poly(1-octadecene) homopolymer (P(C18)), RDG-1-71P, are reported. This sample has been synthesized in an independent work (Appendix 4) with an octahedral group IV bis(phenolate) catalyst (different from that used for the synthesis of the BCP samples). In this sample, the crystallinity due to the organization of the methylene sequences of the side chains of C18 units into PE-like crystals is observed already at room temperature. The melting of these crystals, indeed, occurs in the range 40-60°C (Figure A4.3 in Appendix 4). It is apparent that the WAXS profile (A') of the homopolymer sample P(C18), recorded at 25°C, shows a sharp reflection at q=15nm^{-1}, corresponding to a Bragg distance d=4.1Å, which is similar to the Bragg distance relative to the (110) planes of the orthorhombic form of PE. The corresponding SAXS profile (A) shows a well-defined correlation peak at q=0.88nm^{-1}, corresponding to a periodicity L_B=7nm. This confirms that in the case of iPP-*b*-P(P-*co*-C18) BCPs, the concomitant increase of the WAXS intensity at q=15nm^{-1} and the emergence of a SAXS peak at $q \geq 1$nm^{-1} occurring at sub-zero temperatures, corresponds to the crystallization of the side chains of the C18 units belonging to the P(P-*co*-C18) blocks, which form PE-like crystals. It is worth noting that in the case of the BCPs the correlation distance between the PE-like crystals, L_B, of 5-6nm is lower than that of P(C18) homopolymer, in agreement with the fact the crystals formed at sub-zero temperature are expected to have lower thickness.

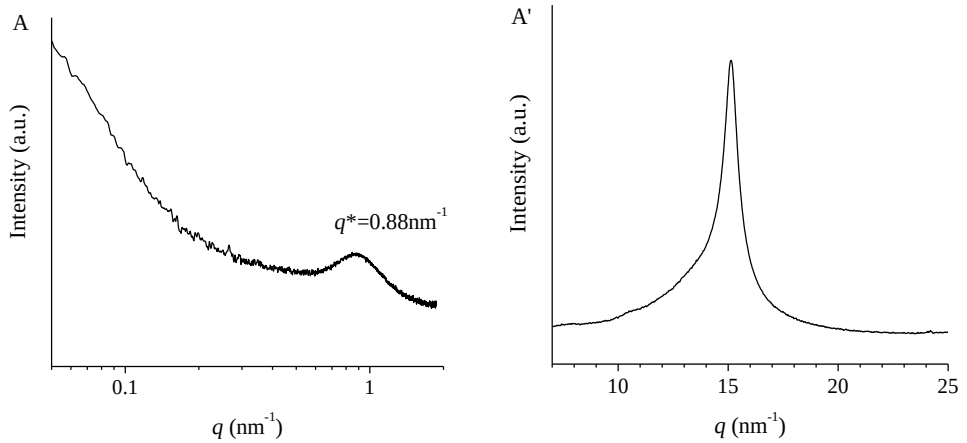

Figure 2.28 SAXS (A) and WAXS (A') intensity profiles of a poly(1-octadecene) homopolymer (P(C18)), RDG-1-71P, recorded at 25°C.

2.2.4 Structural and thermal characterization of the samples quenched from the melt

The ability of the iPP block in the iPP-*b*-P(P-*co*-C18) BCPs to crystallize in a mesomorphic form similar to that observed for iPP homopolymer, by effect of quenching procedures of the melt,[30] has been studied.

Powder samples of the iPP-*b*-P(P-*co*-C18) BCPs have been heated at temperatures 30-40°C higher than the respective melting temperatures, kept at this temperature for 5min, and then cooled by quenching in an ethyl alcohol bath at 0°C. The X-ray powder diffraction profiles of the iPP homopolymer RDG-1-41 and of the iPP-*b*-P(P-*co*-C18) BCPs quenched from the melt are shown in Figure 2.29 A. For comparison, in Figure 2.29 A', the X-ray powder diffraction profiles of the same samples slowly crystallized from the melt (discussed in section 2.2.2) are also shown.

The X-ray powder diffraction profile of the iPP homopolymer quenched from the melt (curve a in Figure 2.29 A) confirms that upon quenching, the sample crystallizes in the mesomorphic form, as indicated by the two typical broad haloes at $2\theta=15°$ and $2\theta=21.3°$. We recall that this sample crystallizes from the melt in a mixture of α and γ forms by slow cooling procedures, as shown by the X-ray diffraction profile reported in Figure 2.29 A' (curve a). The X-ray powder diffraction profiles of the iPP-*b*-P(P-*co*-C18) BCPs (curves b-d in Figure 2.29 A) show that upon quenching, the crystallization of the iPP block in the α form, normally obtained by slow cooling from the melt (curves b-d in A'), is inhibited. In fact, in the WAXS profiles obtained for the samples quenched from the melt, no crystalline reflections are present. Only two broad haloes are present, at $2\theta\approx15°$ and $2\theta\approx21°$, indicating that the iPP block crystallizes in the mesomorphic form, similarly to iPP homopolymer. In the case of the sample RDG-1-139P ($w_{iPP}=0.31$) with the lowest fraction of the iPP blocks, the two haloes of the mesophase at $2\theta=15°$ and $2\theta=21.3°$ are less resolved, because they are largely concealed by the overlaid halo of the amorphous P(P-*co*-C18) block.

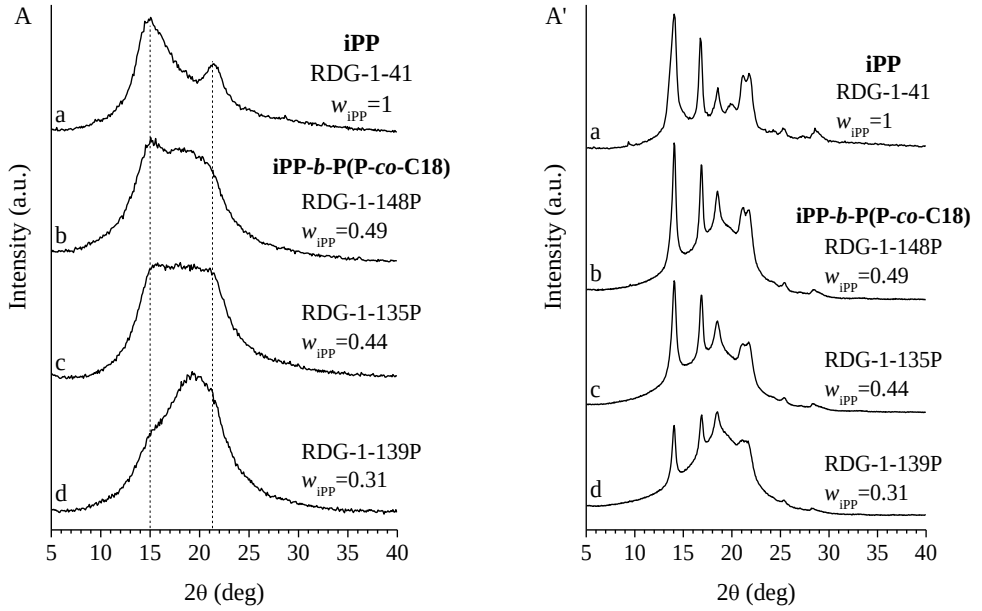

Figure 2.29 X-ray powder diffraction profiles of the melt-quenched (A) and slowly crystallized from the melt (A') samples of iPP homopolymer RDG-1-41 (a) and of the iPP-*b*-P(P-*co*-C18) BCPs (b-d).

The DSC thermograms of the iPP-*b*-P(P-*co*-C18) BCPs quenched from the melt are shown in Figure 2.30. The thermograms are recorded during the heating from -40°C to 180°C (A) and successive cooling from 180°C to -40°C (B).

The DSC thermograms recorded during the heating show a first strong endothermic peak, in the range 10-25°C, which is relative to the melting of the PE-like crystallites formed by the side chains of the C18 units in the P(P-*co*-C18) blocks. At ≈50°C, a small endothermic peak is also evident (black arrows in Figure 2.30 A). It corresponds to the typical "annealing peak" of the iPP mesophase, which is relative to the relaxation phenomena occurring before the melting of the mesophase and the successive recrystallization into the α form.[30] At higher temperatures, 70-80°C, an exothermic peak due to the transformation of the mesomorphic form into α form is observed (red arrows in Figure 2.30 A). Finally, at 133°C, the high-intensity endothermic peak relative to the melting of the α form crystals is observed.

The DSC cooling thermograms (B) show two strong exothermic peaks, at ≈95°C and in the range -2° to 16°C, which correspond to the crystallization of the iPP blocks and of the side chains of the C18 units in the P(P-*co*-C18) blocks, respectively.

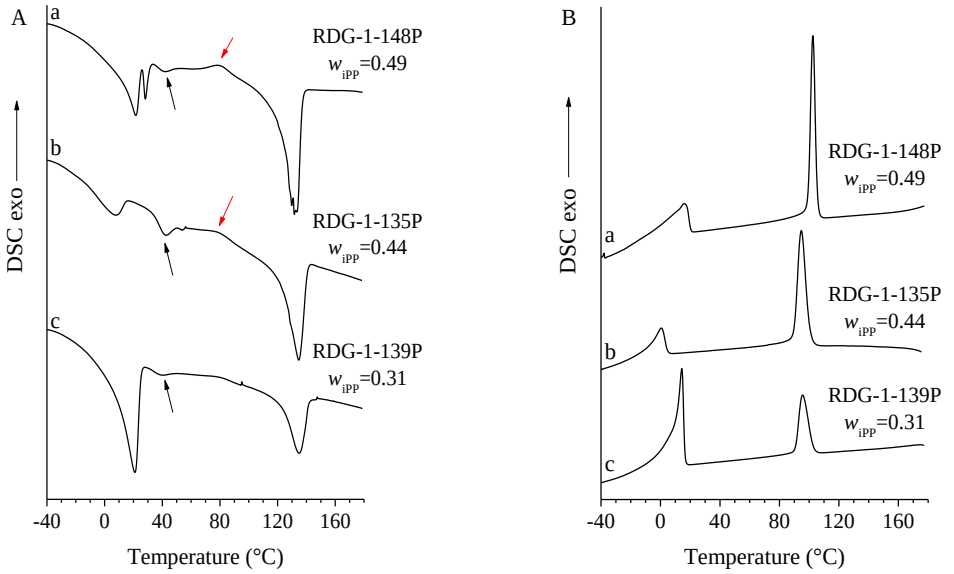

Figure 2.30 DSC thermograms recorded during heating at a rate of 10°C/min (A) and successive cooling at a rate of 10°C/min (B) of the iPP-*b*- P(P-*co*-C18) BCPs quenched from the melt.

The structural transformations occurring in the samples upon heating have been monitored by time/temperature-resolved WAXS/SAXS measurements using synchrotron radiation at ESRF in Grenoble. All the samples within the series have been first cooled from 25°C to -40°C at a rate of 10°C/min in order to induce the crystallization of the side chains of the C18 units in the P(P-*co*-C18) blocks; then a heating from -40°C to 180°C at a rate of 10°C/min has been performed. The data have been collected for 6s, with a delay time of 6s, at a collection rate of 0.071frames/s. The wavelength of radiation is 1.0402Å. Selected WAXS and SAXS patterns of the samples are displayed in Figure 2.31.

The WAXS profiles recorded for the sample RDG-1-148P quenched from the melt (w_{iPP}=0.49) (Figure 2.31 A) show that during cooling from 25°C to -40°C, the intensity of the reflection at q=15nm^{-1} increases due to the crystallization of the side chains of the C18 units in PE-like crystals (curve b). During the successive heating, the PE-like crystals in the P(P-*co*-C18) block domains melt (curve d), while the mesophase in the iPP block is stable up to a temperature of nearly 60°C (curves c-f). At higher temperatures, the mesomorphic form gradually transforms into α form as indicated by the appearance of the typical reflections $(110)_\alpha$, $(040)_\alpha$ and $(130)_\alpha$ at $q\approx$10nm^{-1}, ≈12nm^{-1} and ≈13nm^{-1}, respectively (curves g-l,), and the gradual increase of

intensity of these reflections, up to the melting (curve m). The γ form is not obtained by heating the mesophase, as indicated by the absence of the $(117)_\gamma$ reflection, even though this sample crystallize from the melt in the α form with a small fraction of crystals in the γ form, at the common cooling rates. As already discussed in section 2.2.2, it is known that the mesomorphic form of iPP always transforms into the α form regardless of the stereoregularity of iPP, even for samples with high concentration of stereodefects that in normal conditions of slow cooling of the melt crystallize in the γ form.[30]

The SAXS and the Lorentz corrected intensity profiles of the sample RDG-1-148P (w_{iPP}=0.49) (Figure 2.31 A' and A'' respectively) crystallized in the mesophase show a correlation peak at q=0.75nm^{-1} (L_B=8.3nm) (curve a). By cooling the sample, the crystallization of the side chains of the C18 units occurs, and a change in the slope of the curve at q>1nm^{-1} is observed (curve b). This indicates that crystalline entities with dimensions <6nm are formed in the amorphous domains of the P(P-*co*-C18) blocks. During the successive heating and after the melting of the side chains of the C18 units, the correlation peak q=0.75nm^{-1} relative to the mesophase appears again (curves c-e). At T≈75°C, corresponding to the onset of transformation of the mesophase into the α form (curve g of Figure 2.31 A), the correlation peak in the SAXS profile becomes more evident, due to increase of the contrast. During the heating up to the melting, the intensity of this correlation peak increases, whereas the q position of the maximum gradually shifts from q=0.67nm^{-1} (L_B=9.4nm) at 55°C to lower q values, e.g. q=0.57nm^{-1} at 135°C (L_B=11nm) (curves g-i). This indicates that the average periodicity of the α form crystals increases. The correlation peak disappears at T>135°C because of the melting of the sample (curves m-n).

The behavior of the other two iPP-*b*-P(P-*co*-C18) BCPs, RDG-1-135P (w_{iPP}=0.44) and RDG-1-139P (w_{iPP}=0.31), is similar to that observed for the sample RDG-1-148P. Also in these cases, the samples with the iPP blocks initially crystallized in the mesomorphic form, show the crystallization of the side chains of the C18 units confined in the P(P-*co*-C18) domains and the transformation of the mesomorphic form into α form during heating, starting at temperatures T>70°C.

The change of the typical periodicities as a function of the temperature, extracted from SAXS data of Figure 2.31, are shown in Table 2.13.

Table 2.13 Values of the position of the correlation peak (q^*) and of the corresponding Bragg distance (L_B) at the indicated temperatures (T) extracted from the SAXS data recorded for the iPP-*b*-P(P-*co*-C18) BCP samples RDG-1-148P (w_{iPP}=0.49), RDG-1-135P (w_{iPP}=0.44), RDG-1-139P (w_{iPP}=0.31) during the cooling from 25°C to -40°C and the successive heating from -40°C to 180°C at a rate of 10°C/min.

RDG-1-148P (w_{iPP}=0.49)			**RDG-1-135P (w_{iPP}=0.44)**			**RDG-1-139P (w_{iPP}=0.31)**		
T **(°C)**	***q**** **(nm^{-1})**	L_B **(nm)**	***T*** **(°C)**	***q**** **(nm^{-1})**	L_B **(nm)**	***T*** **(°C)**	***q**** **(nm^{-1})**	L_B **(nm)**
25	0.73	8.6	25	0.76	8.3	25	0.70	9.0
-40	0.73/1.5[a]	8.6/4.2[a]	-40	0.76	8.3	-40	0.70/1.5[a]	9.0/4.2[a]
0	0.73	8.6	0	0.72	8.7	10	0.70	9.0
21	0.72	8.7	25	0.72	8.7	25	0.67	9.3
34	0.72	8.7	40	0.71	8.8	40	0.67	9.3
55	0.69	9.1	55	0.70	9.0	55	0.65	9.7
75	0.66	9.5	70	0.62	10.1	75	0.62	10.1
85	0.62	10.1	85	0.58	10.8	85	0.58	10.8
100	0.56	11.2	100	0.51	12.3	100	0.54	11.6
135	0.30	20.9	135	0.33	19.0	135	0.34	18.5
150	-	-	150	-	-	150	-	-
180	-	-	180	-	-	180	-	-

a) value relative to the PE-like crystallites formed by the side chains of the C18 units in the P(P-*co*-C18) blocks.

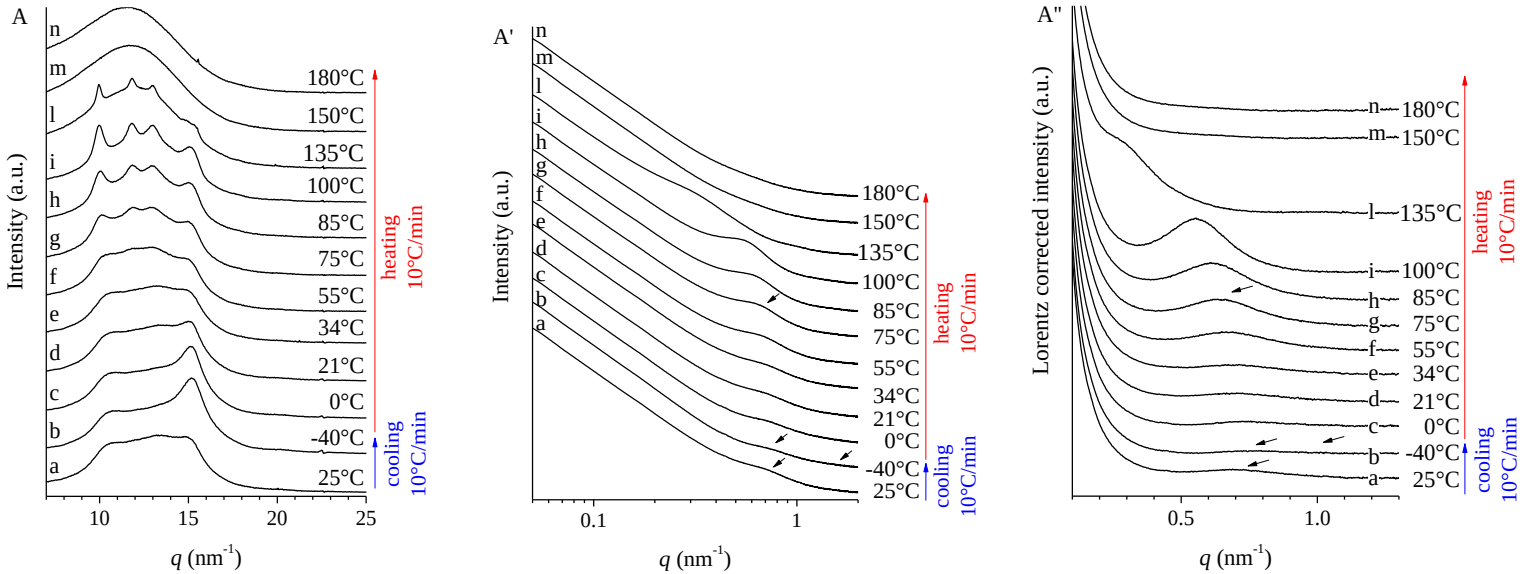
A
Intensity (a.u.)
n
m
l
i
h
g
f
e
d
c
b
a
180°C
150°C
135°C
100°C
85°C
75°C
55°C
34°C
21°C
0°C
-40°C
25°C
heating
10°C/min
cooling
10°C/min
10
15
20
25
q (nm-1)
A'
Intensity (a.u.)
0.1
1
q (nm-1)
A"
Lorentz corrected intensity (a.u.)
0.5
1.0
q (nm-1)

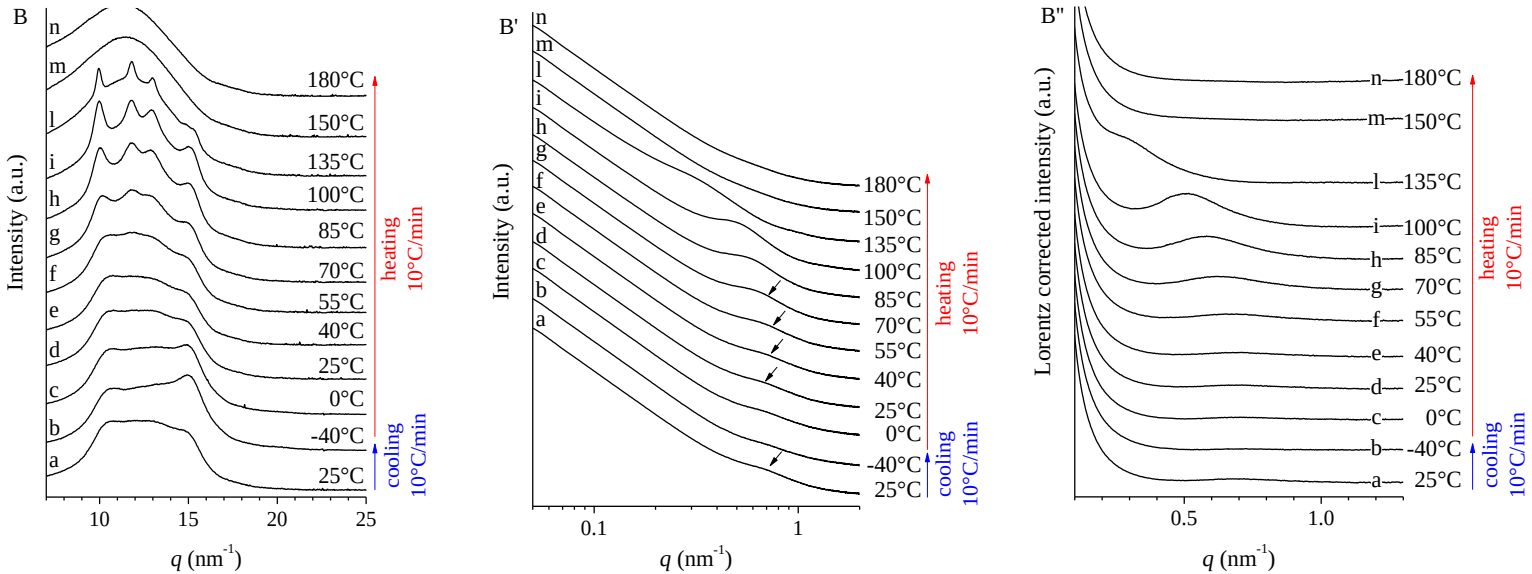
B
Intensity (a.u.)
n
m
l
i
h
g
f
e
d
c
b
a
180°C
150°C
135°C
100°C
85°C
70°C
55°C
40°C
25°C
0°C
-40°C
25°C
heating
10°C/min
cooling
10°C/min
10
15
20
25
q (nm-1)
B'
Intensity (a.u.)
0.1
1
q (nm-1)
B"
Lorentz corrected intensity (a.u.)
0.5
1.0
q (nm-1)

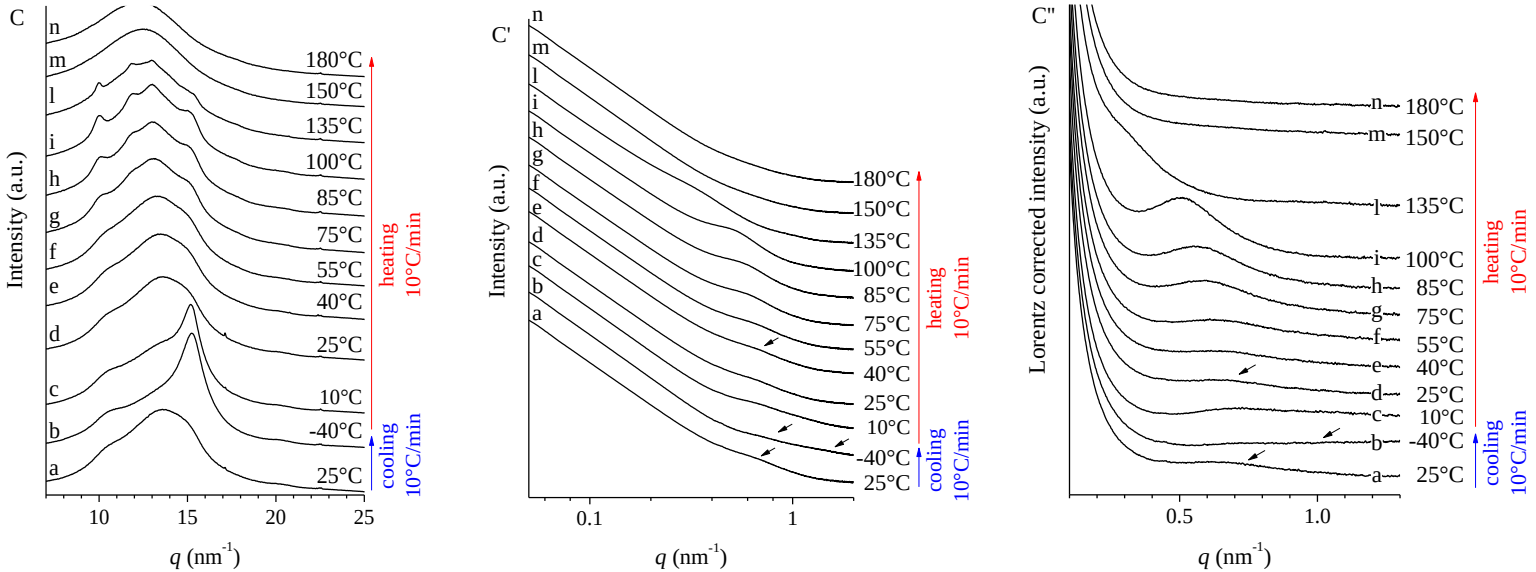

Figure 2.31 WAXS (A, B, C), SAXS (A', B', C') and Lorentz corrected (A'', B'', C'') intensity profiles of the iPP-*b*-P(P-*co*-C18) BCPs RDG-1-148P (w_{iPP}=0.49) (A, A', A''), RDG-1-135P (w_{iPP}=0.44) (B, B', B''), RDG-1-139P (w_{iPP}=0.31) (C, C', C'') quenched from the melt, recorded at the indicated temperatures during the cooling of the sample from 25°C to -40°C (a-b) and successive heating from -40°C to 180°C (c-n) at a rate of 10°C/min.

2.2.5 Mechanical characterization of the melt crystallized samples at slow and fast (quench) cooling rates

It is well known that the mesomorphic form of iPP homopolymer, developing by effect of quenching procedures of the melt at 0°C, shows peculiar mechanical properties different from that of the stable crystalline α form. In fact, while iPP samples crystallized in the stable α form are rigid and strong materials, samples of iPP crystallized in the mesophase by quenching of the melt to low temperature, are a ductile and flexible material with greatly enhanced deformability.[36]

In the previous sections, the ability of the iPP block of the iPP-*b*-(P-*co*-C18) BCPs to undergo crystallization in a mesomorphic form when quenched from the melt, has been studied. For this reason, the mechanical characterization of the iPP-*b*-(P-*co*-C18) BCPs has been carried out not only on samples slowly crystallized from the melt, but also on samples quenched at 0°C.

The stress-strain curves of the iPP-*b*-P(P-*co*-C18) BCPs slowly crystallized from the melt in the α form are shown in Figure 2.32. For comparison, the stress-strain curve obtained for the iPP homopolymer is also shown. The mechanical parameters obtained from these curves, i.e. Young's modulus, (*E*), stress and elongation at the yield point (σ_y and ε_y respectively) and stress and elongation at break (σ_b and ε_b respectively) are reported in Table 2.14.

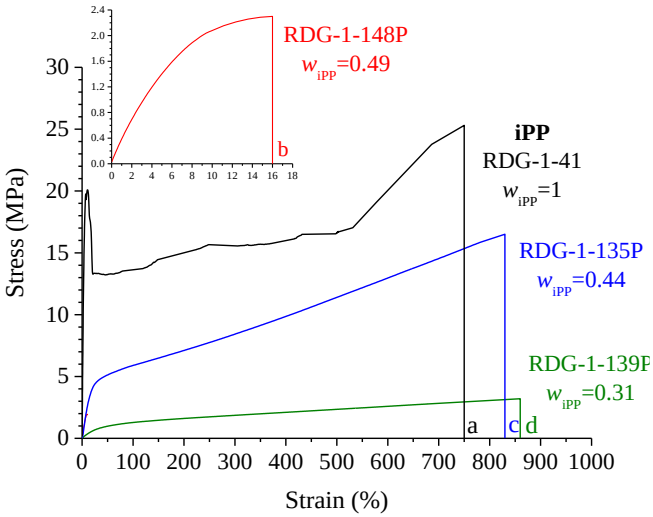

Figure 2.32 Stress-strain curves of the melt crystallized samples in the α form by slow cooling of the iPP homopolymer (a) and the iPP-*b*-P(P-*co*-C18) BCPs, RDG-1-148P (w_{iPP}=0.49) (b), RDG-1-135P (w_{iPP}=0.44) (c) and RDG-1-139P (w_{iPP}=0.31) (d).

Except for the sample RDG-1-148P (w_{iPP}=0.49) which breaks at low deformation (≈16%, Figure 2.32, inset), the iPP-*b*-(P-*co*-C18) BCPs slowly crystallized from the melt show good ductility, with similar values of the deformation at break around 850% (curves c, d). The iPP homopolymer (curve a), also shows similar ductility. The stress at the break and the stress at the yield of the iPP-*b*-P(P-*co*-C18) BCPs are lower than that of the iPP homopolymer, due to the presence of the amorphous P(P-*co*-C18) blocks linked to the crystalline iPP blocks. In addition, the sample RDG-1-135P which has a higher value of w_{iPP} and hence a higher crystallinity, shows higher values of the stress at the yield and at break than the sample RDG-1-139P (w_{iPP}=0.31).

The stress-strain curves of the iPP-*b*-P(P-*co*-C18) BCPs quenched from the melt are shown in Figure 2.33. The mechanical parameters obtained from these curves, i.e. Young's modulus, (*E*), stress and elongation at the yield point (σ_y and ε_y respectively) and stress and elongation at break (σ_b and ε_b respectively) are reported in Table 2.15. The iPP-*b*-(P-*co*-C18) BCPs quenched from the melt at 0°C show, in general, good ductility. The samples RDG-1-148P (curve a) and RDG-1-139P (curve c) having w_{iPP}=0.49 and w_{iPP}=0.31, respectively, and also having almost the same content of C18 units in the P(P-*co*-C18) block (24mol%), show a similar mechanical behavior, with similar values of the elongation and stress at break, around 600% and 5MPa respectively. On the contrary, the sample RDG-1-135P (curve b) having an intermediate value of w_{iPP}, i.e. 0.44, and a lower content of C18 in the P(P-*co*-C18) block (13mol%) with respect to the other two samples, shows a more ductile mechanical behavior, with higher values of the elongation and stress at break.

In Figure 2.34, the stress-strain curves obtained for the samples slowly crystallized from the melt and quenched from the melt are compared. It is worth noting that whereas the sample RDG-1-148P (curves a, a') crystallized in the α form shows a fragile behavior, it has a much higher ductility by effect of crystallization at high cooling rate due to the crystallization of the iPP blocks in the mesomorphic form.

In the case of the samples RDG-1-139P and RDG-1-135P, the values of the elongation at break are similar to those observed for the same samples slowly crystallized from the melt (curves b, b', c, c'). In all cases, the values of the stress at break of the quenched samples are higher than the values observed for the respective samples slowly crystallized from the melt.

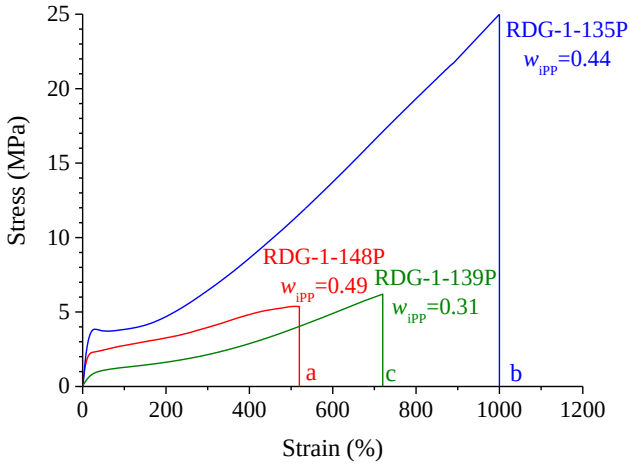

Figure 2.33 Stress-strain curves of the iPP-*b*-P(P-*co*-C18) BCPs RDG-1-148P (w_{iPP}=0.49) (a), RDG-1-135P (w_{iPP}=0.44) (b) and RDG-1-139P (w_{iPP}=0.31) (c) crystallized by quenching the melt in the mesomorphic form.

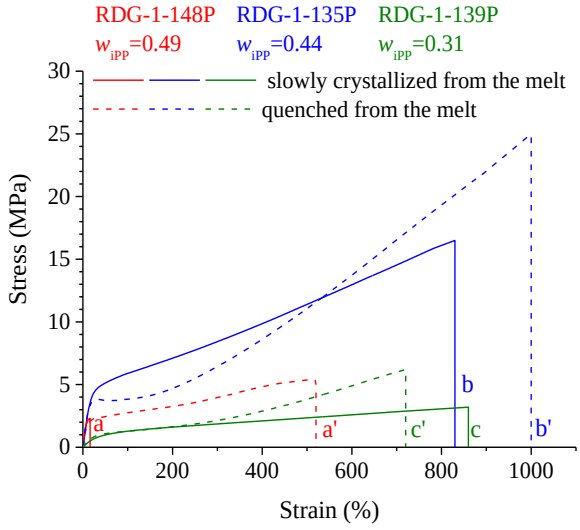

Figure 2.34 Stress-strain curves of the iPP-*b*-P(P-*co*-C18) BCPs which have been crystallized from the melt in the α form by slow cooling rate (continuous line) and in the mesomorphic form by effect of fast cooling rates (dashed line).

Table 2.14 Total molecular mass ($M_{n\ TOT}$), molecular mass of the iPP block ($M_{n\ iPP}$), molecular mass of the P(P-*co*-C18) block ($M_{n\ PPC18}$), mass fraction of the iPP block (w_{iPP}), Young's modulus (E), elongation (ε_y) and stress at the yield point (σ_y), elongation (ε_b) and stress at break (σ_b) of the iPP homopolymer and of the iPP-*b*-P(P-*co*-C18) BCPs slowly crystallized from the melt in the α form.

SAMPLE	$M_{n\ TOT}$ (kg/mol)	$M_{n\ iPP}$ (kg/mol)	$M_{n\ PPC18}$ (kg/mol)	w_{iPP}	E (MPa)	ε_y (%)	σ_y (MPa)	ε_b (%)	σ_b (MPa)
RDG-1-41	139.8	-	-	1	420±40	10±1	20.0±0.2	750±70	25±2
RDG-1-148P	135	66.8	68.2	0.49	27±6	-	-	16±5	2.3±0.4
RDG-1-135P	114.4	50.3	64.1	0.44	35±3	18±4	4.8±0.3	830±60	16±1
RDG-1-139P	124.9	38.3	86.6	0.31	2.2±0.2	-	-	900±200	3.2±0.7

Table 2.15 Total molecular mass ($M_{n\ TOT}$), molecular mass of the iPP block ($M_{n\ iPP}$), molecular mass of the P(P-*co*-C18) block ($M_{n\ PPC18}$), mass fraction of the iPP block (w_{iPP}), Young's modulus (E), elongation (ε_y) and stress at the yield point (σ_y), elongation (ε_b) and stress at break (σ_b) of the iPP-*b*-P(P-*co*-C18) BCPs quenched from the melt and crystallized in the mesomorphic form.

SAMPLE	$M_{n\ TOT}$ (kg/mol)	$M_{n\ iPP}$ (kg/mol)	$M_{n\ PPC18}$ (kg/mol)	w_{iPP}	E (MPa)	ε_y (%)	σ_y (MPa)	ε_b (%)	σ_b (MPa)
RDG-1-148P	135	66.8	68.2	0.49	22±4	30±10	2.3±0.3	520±90	5.4±0.9
RDG-1-135P	114.4	50.3	64.1	0.44	26±3	31±1	3.8±0.2	1000±200	25±3
RDG-1-139P	124.9	38.3	86.6	0.31	3.2±0.2	24±2	1.0±0.1	720±40	6.2±0.3

2.2.6 Structural characterization of oriented fibers

The structural changes occurring in the samples slowly crystallized or quenched from the melt, during tensile deformation, have been studied by X-ray fiber diffraction analysis. The compression molded samples have been stretched at room temperature at different strain (ε) values up to the break. For the iPP-*b*-P(P-*co*-C18) BCP RDG-1-148P (w_{iPP}=0.49) slowly crystallized from the melt, the structural analysis has not been performed because of its fragile behavior.

The X-ray fiber diffraction patterns and the corresponding intensity profiles read along the equatorial line of the stretched sample are shown in Figure 2.35-2.40. The X-ray diffraction pattern of the samples relaxed after tension release, and aged for ≈1 month, have been also acquired.

The study of the oriented fibers of iPP homopolymer has already been discussed in section 2.1.6.

The X-ray diffraction patterns and the corresponding equatorial profiles of the sample RDG-1-135P (w_{iPP}=0.44) (Figure 2.35) show that the unoriented sample (ε=0%, Figure 2.35 A and A') mainly crystallizes in the α form of iPP, as indicated by the presence of the $(130)_\alpha$ reflection at 2θ≈18°, in agreement with the results of section 2.2.2. Upon stretching the sample at deformation of 350%, parts of the α form crystals of the iPP block transform into the mesomorphic form, as indicated by the presence of two low-intensity halos polarized on the equator (2θ≈15°) and on the first layer line (2θ=21°) in addition to the typical reflections of the α form (B). By increasing the degree of deformation up to 700%, the degree of transformation of the initial α form into the mesophase increases and also the degree of orientation of the crystals with chain axes parallel to the stretching direction increases. Small amounts of crystals in the α form are still present (C and C'), as indicated by the emergence of the $(110)_\alpha$, $(040)_\alpha$ and $(130)_\alpha$ reflections of α form of small intensity overlaying the amorphous halo. It is worth reminding that in the case of the iPP homopolymer, the complete transformation of the α and γ form into the mesomorphic form is observed already at a deformation of 500% (see Figure 2.14 C and C'). In the case of the BCP RDG-1-135P, instead, the presence of residual amounts of α form in the sample stretched at 700% deformation may be due to the fact that the nanometric dispersion of the iPP block domains with the amorphous domains of the P(P-*co*-C18) blocks having

high compliance, makes the stress transmission mechanism less efficient than in the iPP homopolymer.

The X-ray diffraction pattern of the sample RDG-1-135P recorded after removing the tension from 700% deformation and ≈1 month aging (Figure 2.35 D) shows partial transformation of the mesophase into the α form.

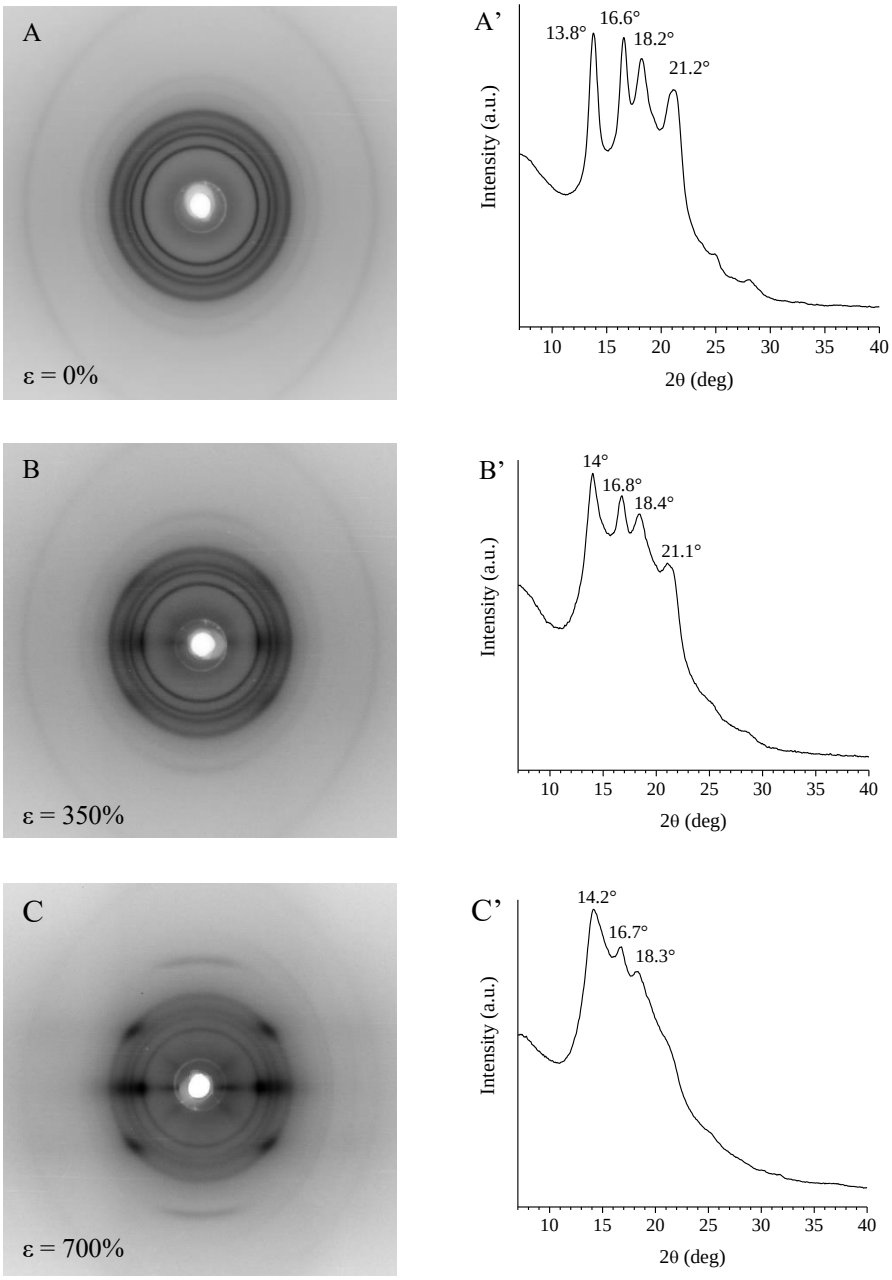

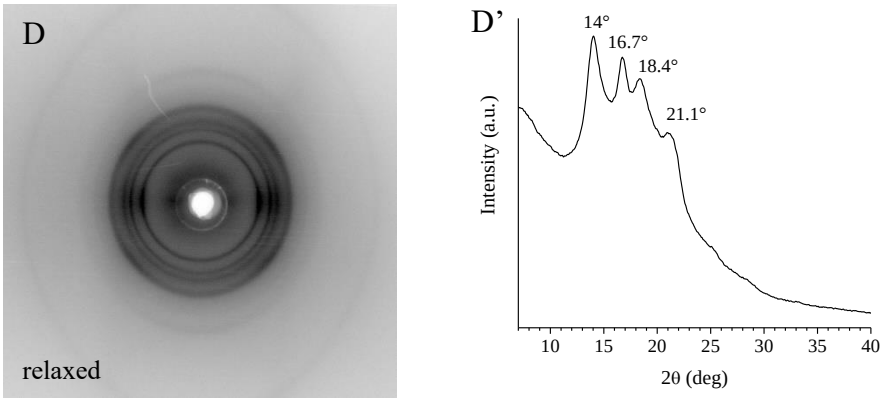

Figure 2.35 X-ray fiber diffraction patterns of the sample RDG-1-135P (w_{iPP}=0.44) at deformation of 0% (A), 350% (B) and 700% (C), and of the sample relaxed from 700% deformation and then aged for about 1 month (D) and corresponding equatorial profiles (A'-D').

The X-ray diffraction patterns and the corresponding equatorial profiles of the sample RDG-1-139P (w_{iPP}=0.31) shown in Figure 2.36 confirm that the unoriented sample mainly crystallizes in the α form of iPP as indicated by the presence of $(130)_\alpha$ reflection at 2θ=18.6° (A and A'). The deformation of the sample at 300% induces partial polarization of the $(110)_\alpha$ and $(040)_\alpha$ reflections on the meridian and on the equator (B), respectively. Further stretching, up to 600% deformation also induces partial polarization of the $(111)_\alpha$ and $(\bar{1}31)_\alpha$ + $(041)_\alpha$ reflections on the first layer line (C).

As described in section 2.1.6, the stretching of iPP samples in the α form generally induces preferential orientation of crystals with chain axes directed parallel to the stretching direction (c_α-axis orientation), like for a standard fiber morphology. However, in samples drawn at high temperature, lamellar branching may also occur.[37-40] Daughter lamellae grow on mother lamellae with the chain axes tilted ≈81° with respect to the chain axis of mother lamellae. The origin of this lamellar branching is purely crystallographic and corresponds to a case of self-epitaxy that results from the near-identity of the a_α- and the c_α-axes dimensions.[41] Therefore, while the mother lamellae are in the normal c_α-axis orientation, daughter lamellae present the a_α-axes directed parallel to the fiber axis (a_α-axis orientation), leading to a crosshatched morphology. The X-ray fiber diffraction patter of the α form in the normal c_α-axis orientation shows the $(110)_\alpha$, $(040)_\alpha$ and $(130)_\alpha$ reflections on the equator and the $(111)_\alpha$, $(\bar{1}31)_\alpha$ + $(041)_\alpha$ reflections on the first layer line. In the case

of tilted crystals of the α form in the a_α-axis orientation the $(110)_\alpha$ and $(130)_\alpha$ reflections disappear from the equator and appear on the first layer line, the $(041)_\alpha$ reflection becomes equatorial, whereas the positions of the $(040)_\alpha$, $(111)_\alpha$ and $(\bar{1}31)_\alpha$ reflections are left unaltered in the same positions as those relative to the crystals of the α form with the normal c_α-axis orientation.
Uniaxially drawn iPP samples in the α form containing a non-negligible fraction of tilted (daughter) lamellae aside mother lamellae with normal c_α-axis orientation, present X-ray diffraction patterns having features intermediate between those of the samples in a_α- and c_α-axis orientation. In particular, the $(110)_\alpha$, $(130)_\alpha$ and $(041)_\alpha$ reflections appear both on the equator and on the first layer line, the $(040)_\alpha$ lays on the equator and the $(111)_\alpha$ and $(\bar{1}31)_\alpha$ reflections are placed on the first layer line.[42]

In the X-ray diffraction pattern of the sample RDG-1-139P stretched at ε=600% (Figure 2.36 C), the partial polarization of the $(110)_\alpha$ reflection both on the first layer line (appearing as meridional reflection) and on the equator, as well as the partial polarization of the $(130)_\alpha$ and $(040)_\alpha$ reflections on the equator and of the $(041)_\alpha$, $(111)_\alpha$ and $(\bar{1}31)_\alpha$ reflections on the first layer line indicate that in this sample partial orientation of the α form crystals with a_α- and c_α-axes parallel to the fiber axis is obtained. For this sample, no transformation of the α form crystals into the mesophase is observed.
Upon removing the tension from 600% deformation and successive ageing for ≈1 month, the orientation of the crystals is almost entirely lost (D).

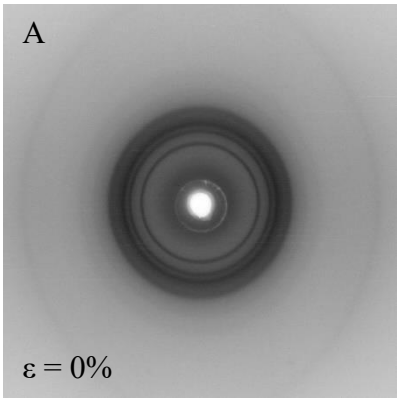

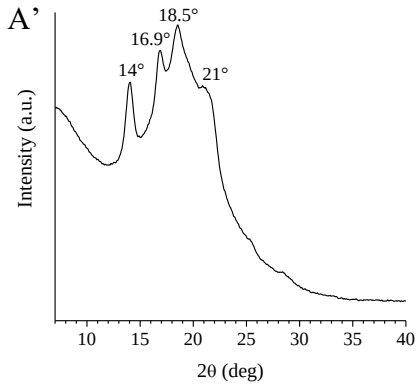

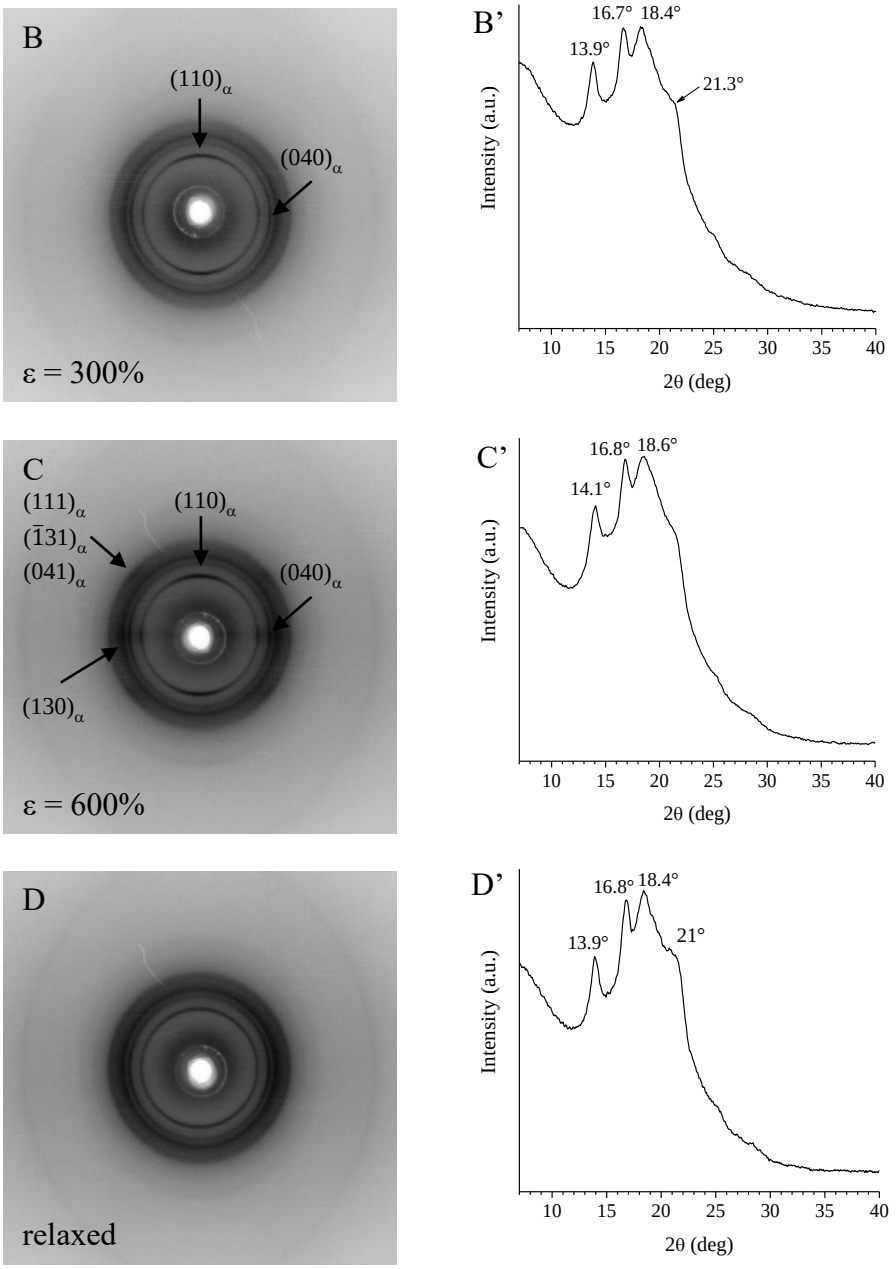

Figure 2.36 X-ray fiber diffraction patterns of the sample RDG-1-139P (w_{iPP}=0.44) at 0% (A), 300% (B), 600% (C) deformation, of the sample relaxed from 600% deformation and then aged for ≈ 1 month (D) and corresponding equatorial profiles (A'-D').

It is worth noting that the behaviour of the iPP-*b*-P(P-*co*-C18) BCPs upon stretching is different from that observed for the iPP homopolymer RDG-1-41 (Figure 2.14) where the complete transformation of the α form into

mesophase is observed. This may be due to the high compliance of the amorphous P(P-*co*-C18) blocks that does not provide an efficient transfer of the stress between the amorphous and the crystalline iPP block, which is necessary to induce the complete transition of the α form into the mesomorphic form.

The structural characterization of the oriented fibers has been carried out also on the samples crystallized in the mesophase, obtained by quenching the melt.

In this case, also the sample RDG-1-148P (w_{iPP}=0.49), has been analyzed, since the mesophase shows higher ductility than the α form. The X-ray diffraction patterns and the corresponding equatorial profiles are shown in Figure 2.37. The X-ray diffraction pattern of the unoriented sample (A) confirms that upon quenching, the crystallization of the α form of the iPP block is inhibited (section 2.2.4). In fact, the corresponding equatorial profile (A') shows a low-intensity peak at 2θ=15° and a peak appearing as a shoulder at 2θ≈21°, indicating that the iPP blocks are in the mesomorphic form of iPP. The X-ray diffraction patterns and the corresponding equatorial profiles of the sample stretched at 200% (B and B'), 300% (C and C') and 400% (D and D') deformation, show a peak polarized on the equator at 2θ≈15° characterized by a small shoulder at 2θ=18-19°, and a peak polarized on the first layer line at 2θ≈21°, typical of oriented crystals of iPP mesomorphic form. These data indicate that by drawing the sample, only a high degree of orientation of the mesophase in the iPP block is achieved and that no structural transformations occur. The X-ray diffraction pattern recorded after removing the tension and aging for ≈1 month (E) shows that two low-intensity crystalline reflections appear at 2θ=16° and 18°, thus indicating that part of the mesomorphic form transforms into the α form of iPP.

It is worth noting that the shoulder at 2θ=18-19° observed in the equatorial profiles B', C' and D' may be related to the orientation of a mesomorphic form, different from that observed in iPP samples quenched from the melt, which has been defined *new mesophase*,[43] and has been firstly observed in random copolymers of propylene with long branched comonomers (e.g. 1-octadecene).[43,44]

In particular, in the case of random copolymers of propene with 1-octadecene (iPPC18), the new mesophase has been observed in as prepared samples having a concentration of C18 units higher than 2-3mol%. As already mentioned, the new mesophase that crystallizes in these long-branched

copolymers is different from the classic mesophase of the iPP homopolymer that normally is obtained by quenching the melt or by stretching at high deformations. In fact, the new mesophase crystallizes already in the powder samples without quenching and stretching. Moreover, the diffraction patterns of the stretched samples of the iPPC18 copolymers crystallized in the new mesophase present two strong reflections at 2θ=14° and 20° (*d*=6.33 and 4.44Å, respectively) polarized on the equator and a reflection at 2θ=20° polarized on the first layer line (the equatorial reflection at 2θ=20° is absent in the diffraction pattern of the mesophase of iPP). The position of these reflections indicates that the structure of the mesomorphic aggregates is characterized by parallel chains in 3/1 helical conformation packed at average interchain distances of about 6Å, defined by the self-organization of the flexible side groups, which, in turn, produces the equatorial reflection at 2θ=20° (*d*=4.44Å) (see Figure 2.38). This reflection is, indeed, at nearly the same 2θ position as that of the maximum of the diffuse halo observed in the X-ray diffraction profiles of amorphous iPPC18 copolymer samples having high concentration of 1-octadecene and probably reflects the average distance of about 4.4Å between the disordered branches or between the main chains and the branches.[43]

In the case iPP-*b*-P(P-*co*-C18) BCPs, the crystallization of the P(P-*co*-C18) block in the new mesophase may also be hypothesized. In particular, for the sample RDG-1-148P quenched from the melt, the second equatorial reflection appears as a shoulder at 2θ=18° (*d*=4.93Å), at nearly the same 2θ position as that of the maximum of the diffuse halo observed in the X-ray diffraction profile of the amorphous P(P-*co*-C18) random copolymer (curve a in Figure 2.21 A), thus indicating that in this case the average distance between the disordered branches or between the main chains and the branches is around 4.9Å.

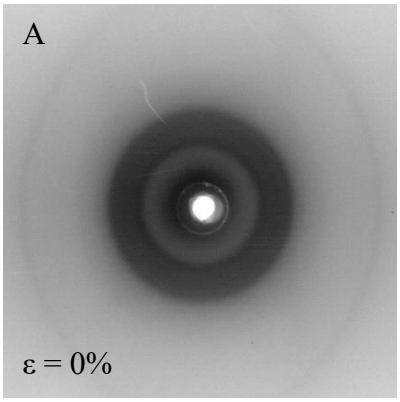
A
ε = 0%

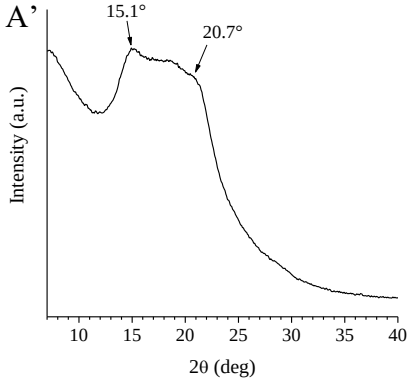
A'
15.1°
20.7°
Intensity (a.u.)
10
15
20
25
30
35
40
2θ (deg)

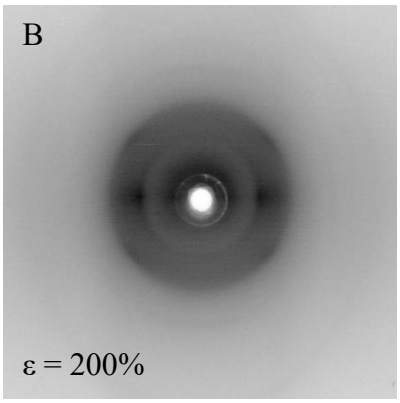
B
ε = 200%

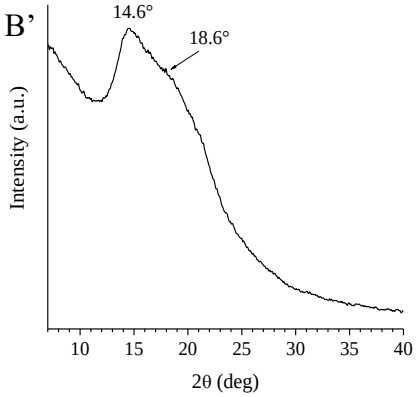
B'
14.6°
18.6°
Intensity (a.u.)
10
15
20
25
30
35
40
2θ (deg)

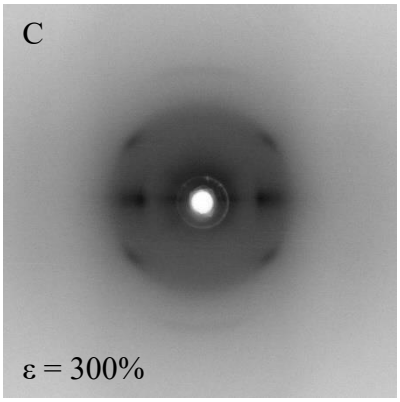
C
ε = 300%

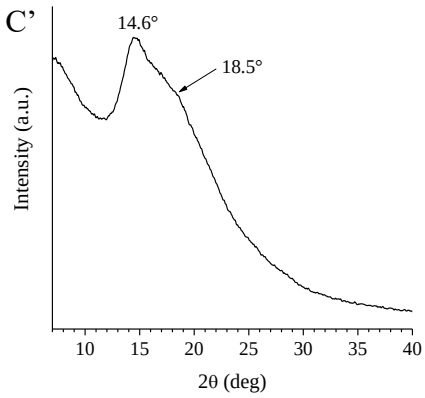
C'
14.6°
18.5°
Intensity (a.u.)
10
15
20
25
30
35
40
2θ (deg)

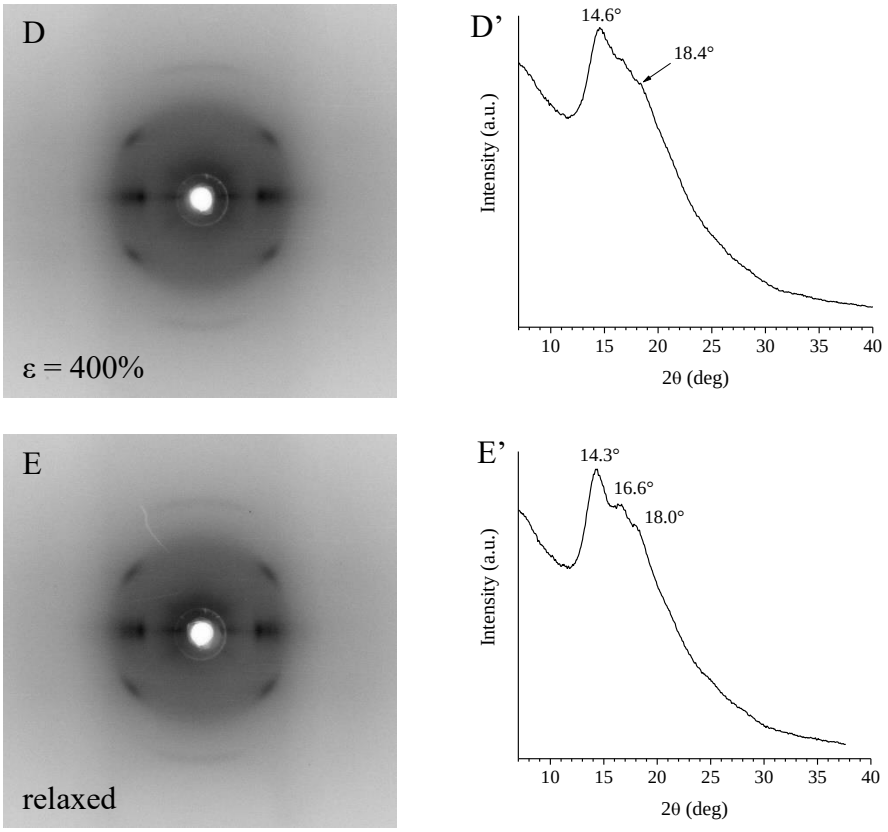

Figure 2.37 X-ray fiber diffraction patterns of the sample RDG-1-148P (w_{iPP}=0.49) at 0% (A), 200% (B), 300% (C), 400% (D) deformation, after release of the tension from 400% deformation and then aged for ≈1 month (E) and corresponding equatorial profiles (A'-E').

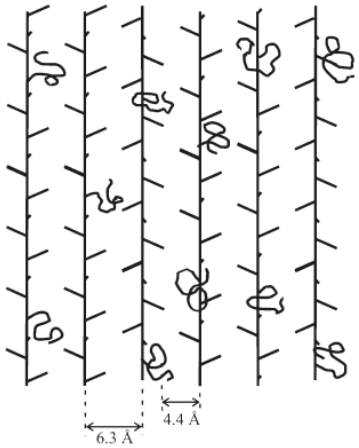

Figure 2.38 Schematic model of the organization of chains of iPPC18 copolymers in the new mesophase.

A similar behavior is observed for the sample RDG-1-135P (w_{iPP}=0.44) quenched from the melt (Figure 2.39). In fact, the X- ray diffraction pattern and the corresponding equatorial profile of the unoriented sample (A and A') show that the quenching of the sample from the melt induces the crystallization of the iPP blocks in the mesomorphic form (section 2.2.4), indicated by the two low-intensity reflections at 2θ=15° and ≈21°. By stretching the sample at 350% (B and B'), 500% (C and C') and 700% (D and D') deformation, the orientation of the mesomorphic form of the iPP blocks with chain axes parallel to the stretching direction is observed, as indicated by the polarization of the two reflections at 2θ=15° and 21° on the equator and on the first layer line, respectively. The equatorial reflection at 2θ=15° shows a shoulder at 2θ≈18-19° which can be attributed to the crystallization of the P(P-*co*-C18) blocks in the new mesophase of iPP, as previously supposed also for the sample RDG-1-148P quenched from the melt. The X-ray diffraction pattern and the corresponding equatorial profile acquired after removing the tension from 700% deformation and successive aging for ≈1 month show that the broad equatorial halo transforms into a well-defined reflection at 2θ=14.5° and a broad halo at 2θ=18°, probably indicating an incipient crystallization of α form crystals during aging, as also observed for the sample RDG-1-148P.

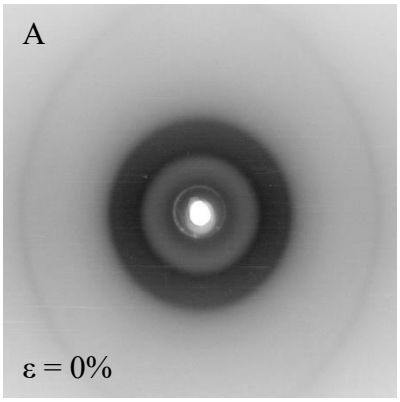

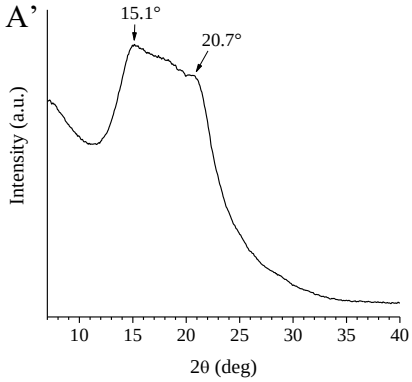

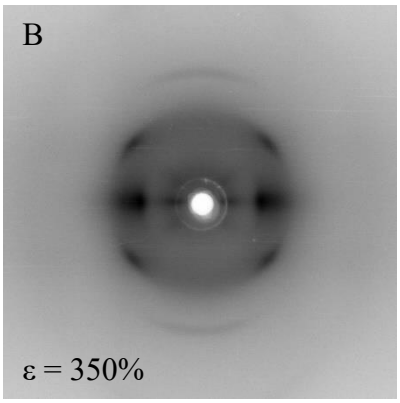
B
ε = 350%

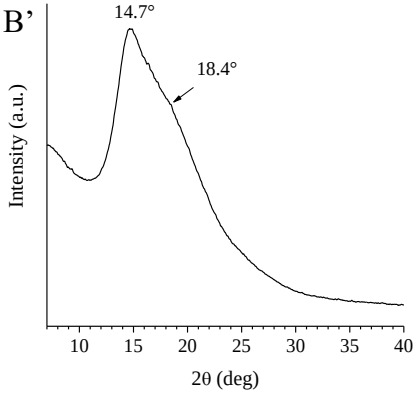
B'
14.7°
18.4°
Intensity (a.u.)
10
15
20
25
30
35
40
2θ (deg)

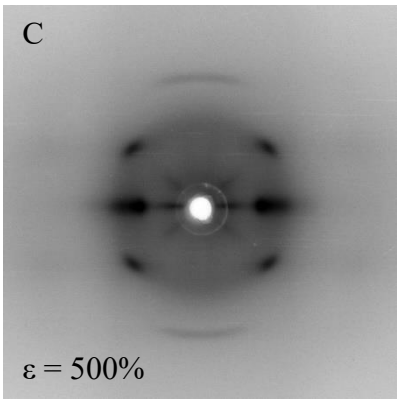
C
ε = 500%

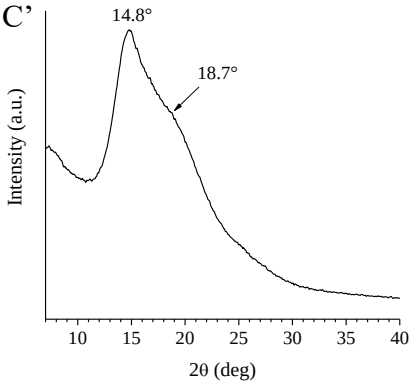
C'
14.8°
18.7°
Intensity (a.u.)
10
15
20
25
30
35
40
2θ (deg)

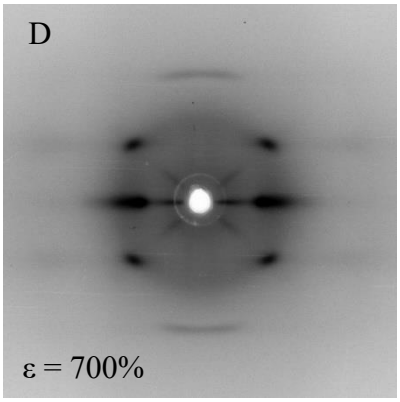
D
ε = 700%

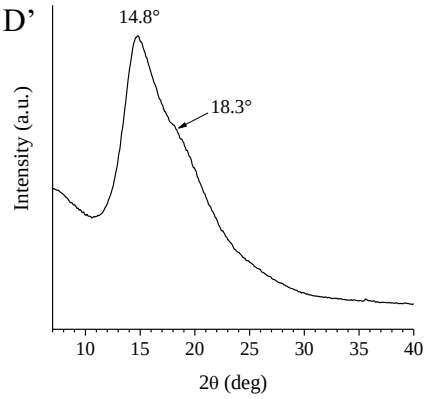
D'
14.8°
18.3°
Intensity (a.u.)
10
15
20
25
30
35
40
2θ (deg)

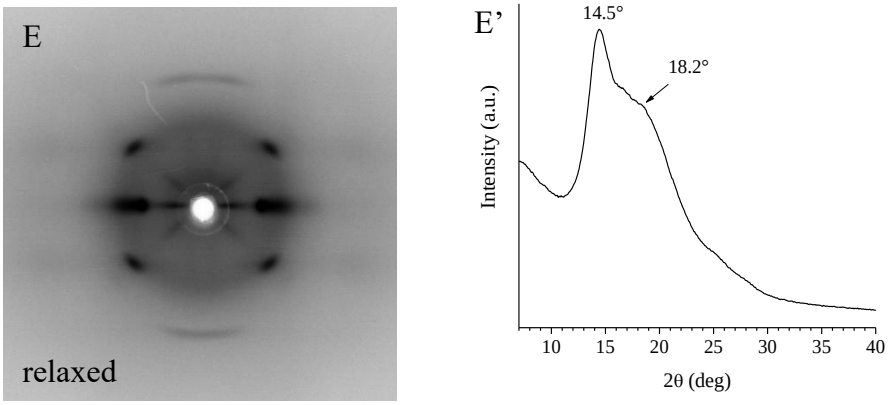

Figure 2.39 X-ray fiber diffraction patterns of the sample RDG-1-135P (w_{iPP}=0.44) at 0% (A), 350% (B), 500% (C), 700% (D) deformation, after release of the tension from 700% deformation and successive aging for ≈1 month (E) and corresponding equatorial profiles (A'-E').

The X-ray diffraction patterns of the sample RDG-1-139P (w_{iPP}=0.31) quenched from the melt are shown in Figure 2.40. The X-ray diffraction pattern of the unoriented sample (ε=0%) and the corresponding equatorial profile (A and A') show that the quenching of the sample from the melt inhibits the crystallization of the iPP block in the α form, as already observed in section 2.2.4. A broad halo centered at 2θ=18.8° characterized by a shoulder at 2θ≈15° is observed in the equatorial profile (A'). In this sample, the characteristic reflections of the mesomorphic form at 2θ=15° and 21° are concealed by the amorphous halo centered at 2θ=18° relative to the P(P-*co*-C18) block (see curve a in Figure 2.21 A), due to the low mass fraction of the iPP blocks. By stretching the sample at 250% (B and B') and 450% (C and C') deformation, the typical polarization of the two reflections of the mesomorphic form at 2θ=15° and 21° on the equator and first layer line, respectively, is observed. For this sample, a well-defined second reflection polarized on the equator at 2θ≈18° is also observed. As hypothesized also for the other two BCPs within the series, this may be relative to the crystallization of the P(P-*co*-C18) block in the new mesophase of iPP. The X-ray diffraction pattern acquired after removing the tension and successive aging for ≈1 month shows that the orientation of the iPP mesophase is partly lost.

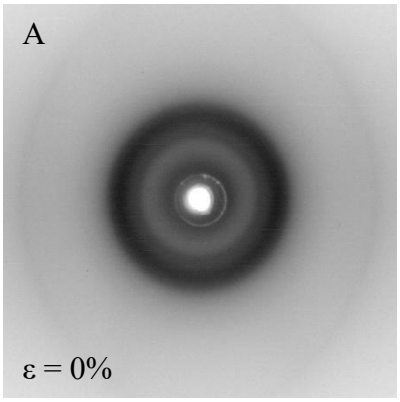
A
ε = 0%

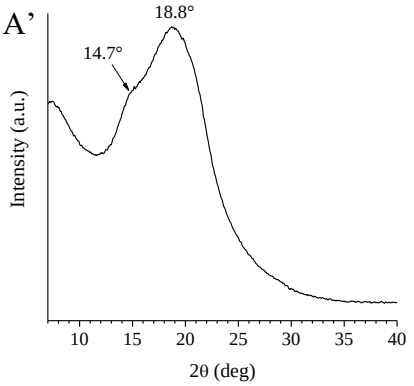
A'
18.8°
14.7°
Intensity (a.u.)
10
15
20
25
30
35
40
2θ (deg)

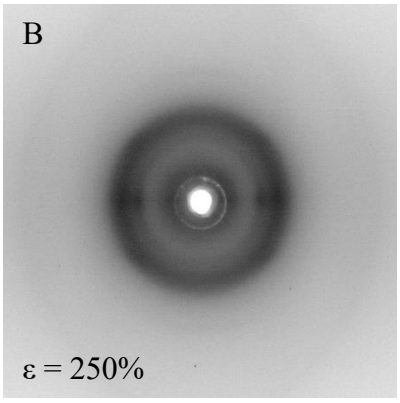
B
ε = 250%

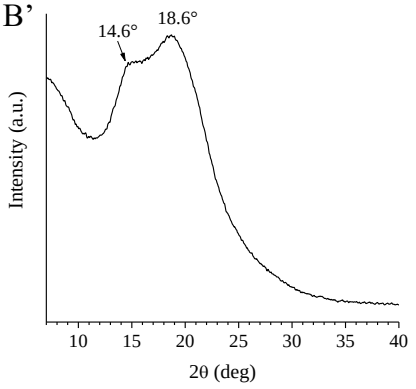
B'
14.6°
18.6°
Intensity (a.u.)
10
15
20
25
30
35
40
2θ (deg)

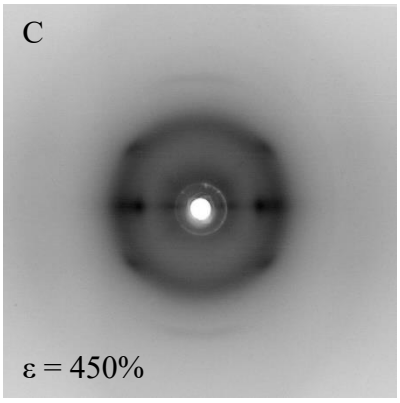
C
ε = 450%

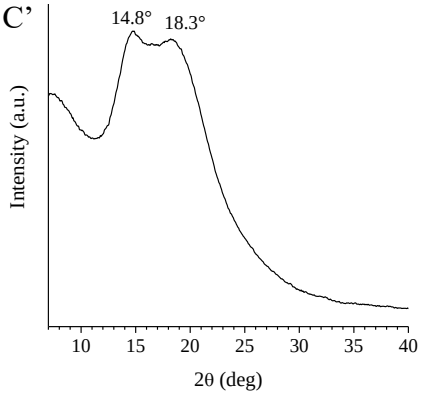
C'
14.8°
18.3°
Intensity (a.u.)
10
15
20
25
30
35
40
2θ (deg)

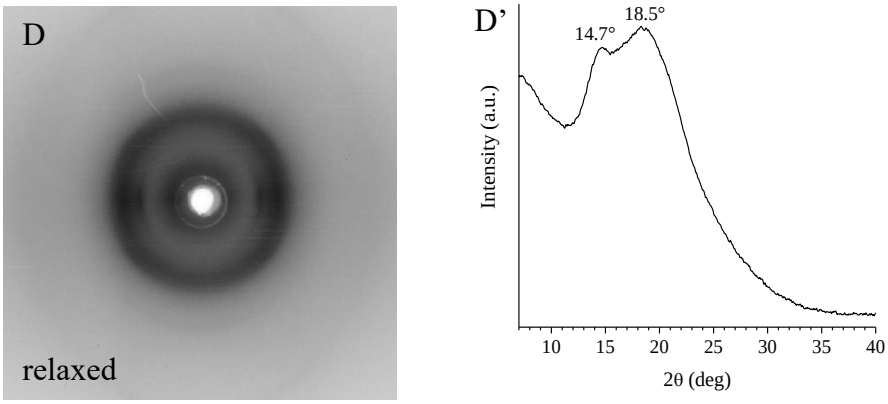

Figure 2.40 X-ray fiber diffraction patterns of the sample RDG-1-139P (w_{iPP}=0.31) at 0% (A), 250% (B), 450% (C) deformation, and after release of the tension from 450% deformation followed by aging for ≈1 month (D) and respective equatorial profiles (A'-D').

In conclusion, the structural characterization of the oriented fibers of the samples quenched from the melt shows that upon stretching, no structural changes occur. The orientation of the mesophase of the iPP block and that of the new mesophase of the P(P-*co*-C18) block are observed. By release of the tension of the oriented mesophase, the high degree of orientation of the crystals with chain axes parallel to the stretching direction is not lost for the BCP samples RDG-1-148P (w_{iPP}=0.49) and RDG-1-135P (w_{iPP}=0.44), with the highest fraction of the iPP blocks, and in the case of the sample RDG-1-148P (w_{iPP}=0.49) a slight crystallization of the mesophase in the α form is observed at room temperature, probably by effect of ≈1 month aging. In the case of the sample RDG-1-139P (w_{iPP}=0.31), instead, by effect of release of the tension of the stretched fiber and ≈1 month aging, the mesophase does not transform in α form, but part of orientation is lost. Simultaneously a partial recovery of the initial dimensions of the sample is observed (tension set=170%).

It is worth noting that, as discussed above, the crystallization of the random copolymers of propene with 1-octadecene comonomer in the new mesophase is observed already in powder samples, without resorting to quenching of the sample from the melt. Therefore, the presence of the new mesophase in the P(P-*co*-C18) block domains cannot be excluded also for the samples slowly crystallized from the melt. However, in that case, direct detection of the new mesophase is not easy, since the typical reflection at 2θ≈18° of the mesophase coincides with the 2θ position of the amorphous halo of the P(P-*co*-C18) copolymer (curve a of Figure 2.21 A), and of $(130)_\alpha$ reflection of α form. Even

in the stretched BCP samples crystallized in the α form, detection of the new mesophase is ambiguous, because complete transformation of the α form crystals of the iPP blocks into the iPP mesophase has not been achieved, even at the highest deformation reached in our experiments, before breaking.

2.2.7 Structural characterization of oriented fibers at low-temperatures

The structural characterization of the oriented fibers of the iPP-*b*-P(P-*co*-C18) BCPs has been performed also at low-temperatures, since in these samples additional crystallization of the side chains is observed when cooling below 0°C. Compression molded samples have been stretched at room temperature at different strains (ε) and then cooled below the crystallization temperature of the side chains of the C18 units in the P(P-*co*-C18) blocks.

For each sample, the X-ray fiber diffraction patterns and the corresponding intensity profiles read along the equatorial line are shown at the different values of deformation and at the indicated temperatures. The X-ray diffraction pattern have been recorded by using MoKα radiation (λ=0.71073Å). The corresponding equatorial profiles are shown as a function of the scattering angle, 2θ, calculated for the CuKα radiation (λ=1.5418Å). Diffraction data have been collected with an area detector XYZ, using an exposition time of 240s/frame. Each image is the sum of at least 6 frames, collected consecutively, for each deformation, at the different temperatures.

The structural analysis at low temperature and as a function of temperature has been carried out to probe the crystallization of the side chains in the amorphous P(P-*co*-C18) blocks, in samples crystallized from the melt at slow and fast cooling rate, wherein the iPP blocks crystallize in the α and mesomorphic forms, respectively. Therefore, the possible oriented crystallization of the PE-like crystals is investigated.

In Figure 2.41, the X-ray diffraction patterns and the corresponding equatorial profiles of the sample RDG-1-135P (w_{iPP}=0.44), recorded at the indicated values of deformation and at the indicated temperatures, are reported. The X-ray diffraction patterns of the unoriented sample recorded at *T*=25°C (A) and *T*= -25°C (B) confirm that upon cooling of the sample, additional crystallization in the sample is observed, as already observed in the previous section. The crystallization of the PE-like crystals formed by the side chains of the C18 units is indicated by the presence of the $(110)_{PE}$ reflection

of the orthorhombic form of PE in Figure 2.41 B and by the corresponding increase in intensity at 2θ=21° in Figure 2.41 B'. The X-ray diffraction profile of the sample stretched at 400% (C) shows that upon stretching the sample and cooling it at -25°C, the crystallization of the C18 units still occurs, but no orientation of the PE-like crystallites is observed. In fact, at *T*= -25°C (C) the intensity of the $(110)_{PE}$ reflection is uniformly distributed along the corresponding Debye-Scherrer ring, and only the crystals of α form result oriented. At 25 °C, instead, the crystallization of the PE-like crystals is not observed (D, D'). This is also observed in the azimuthal profiles extracted from the bidimensional diffraction patterns (C) and (D), at 2θ=21°, (curves a and b in Figure 2.41 E). χ is the azimuthal angle assuming a value of 0° on the equator and ±90° on the meridian. In the profile at *T*= -25°C (curve a) no additional peaks are observed with respect to that at *T*= 25°C, thus indicating that no other orientation, in addition to that of the α form crystals in the iPP blocks, is achieved.

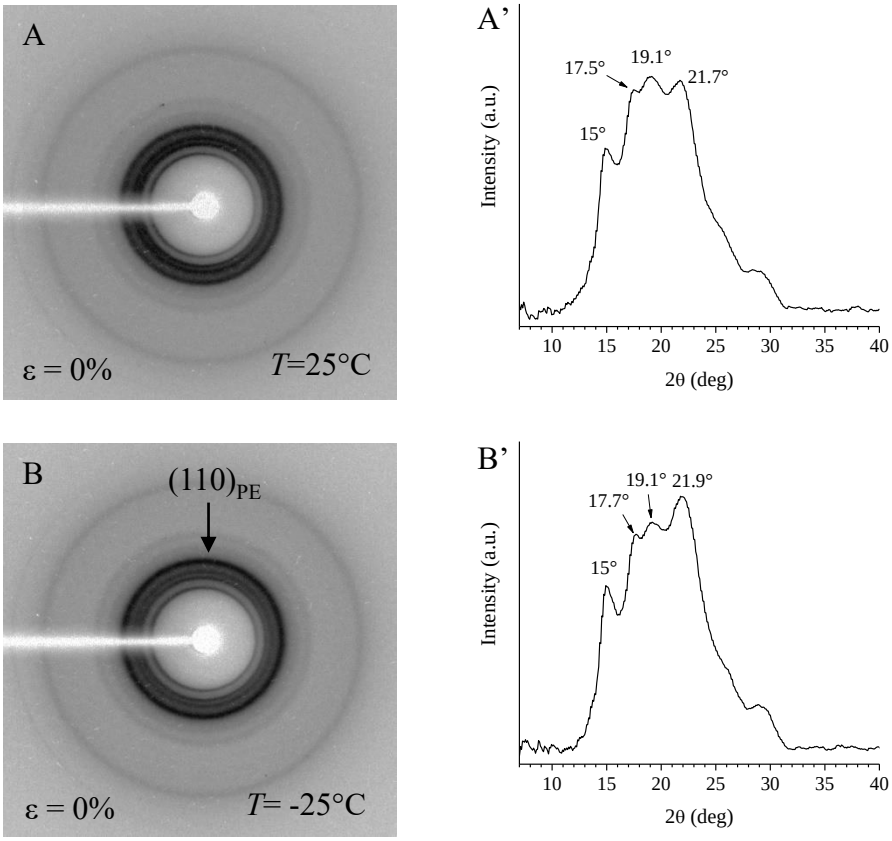

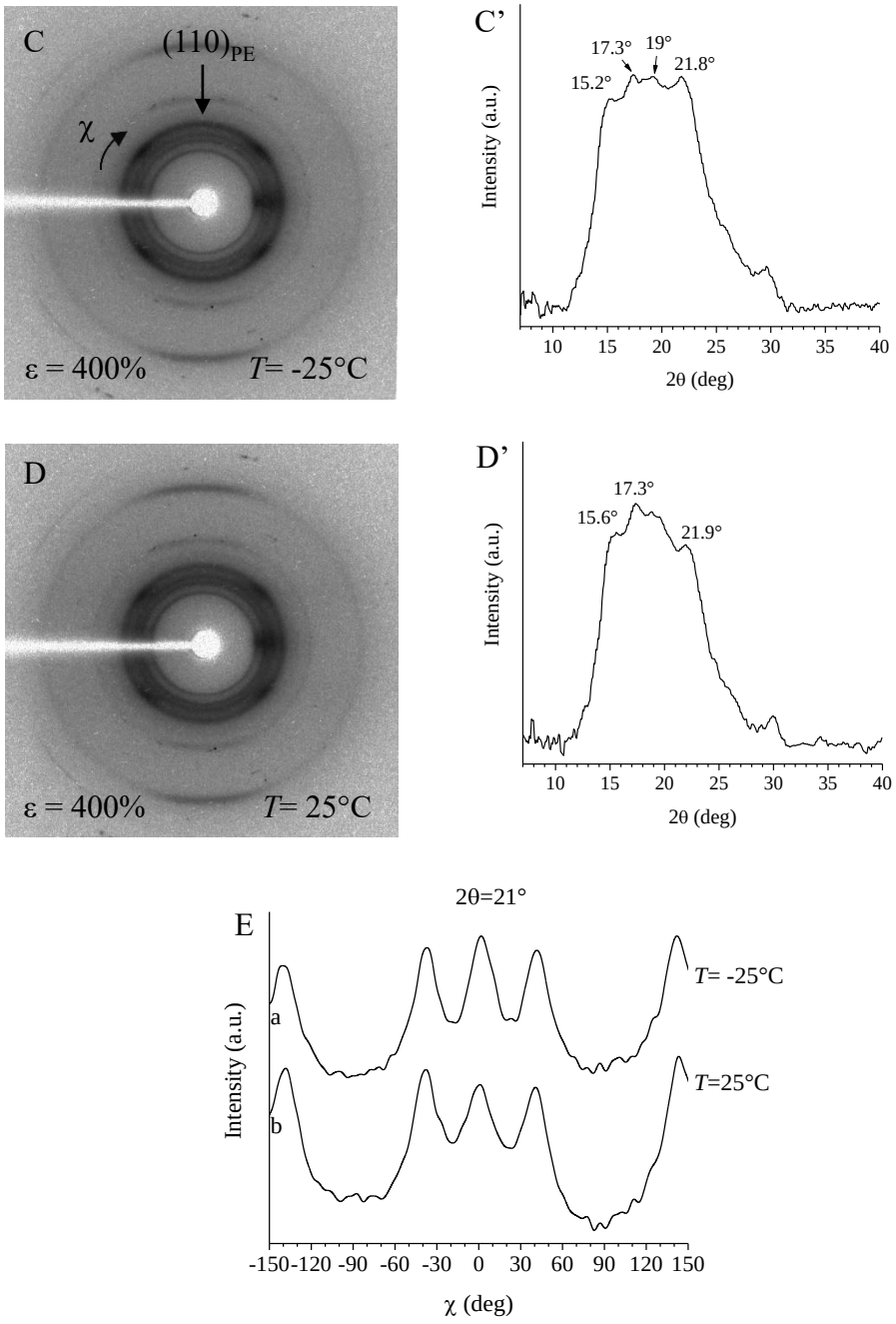

Figure 2.41 X-ray fiber diffraction patterns of the sample RDG-1-135P (w_{iPP}=0.44) collected at the indicated temperatures at 0% (A, B) and 400% (C, D) deformation and corresponding equatorial profiles (A'-D'). The equator is horizontal in A-D. (E) Azimuthal profiles at 2θ=21° obtained from the X-ray diffraction patterns recorded at -25°C (a) and 25°C (b). The azimuthal angle χ is defined in C. χ = 0° on the equator and χ = ±90°on the meridian.

In Figure 2.42, the X-ray diffraction patterns and the corresponding equatorial profiles of the sample RDG-1-139P (w_{iPP}=0.31), recorded at a value of deformation of 600% and at the indicated temperatures, are reported. In this case it is apparent that upon stretching the sample at 600%, the successive cooling at -15°C induces the oriented crystallization of the side chains of the C18 units. In fact, at variance with Figure 2.41 C, the intensity of $(110)_{PE}$ reflection at -15°C (Figure 2.42 B) appears polarized in a nearly meridional position, even though the crystals of α form achieve only slight degree of orientation. The oriented crystallization of the PE-like crystals may be better appreciated in Figure 2.42 C by comparing the azimuthal intensity profiles of the reflections at 2θ=21° extracted from the diffraction images collected at -15°C (curve a) and 25°C (curve b). It is apparent that at -15°C, the additional intensity emerging at 2θ=21° is mainly polarized at $\chi \approx \pm 90°$, wherein χ is the azimuthal angle assuming a value of 0° on the equator and ±90° on the meridian. The polarization of the $(110)_{PE}$ reflection on the meridian indicates that the PE crystallites are preferentially oriented with their *c*-axes perpendicular to the fiber axis. It is worth reminding that for this sample, the partial polarization of the $(110)_{\alpha}$ reflection both on the first layer line (appearing as meridional reflection) and on the equator, indicate that in this sample the α form is oriented with the parent lamellae in the c_{α}-axis orientation (the chains are parallel to the fiber axis) and daughter lamellae (cross-hatches) in the a_{α}-axis orientation (the chains are parallel to the fiber axis).

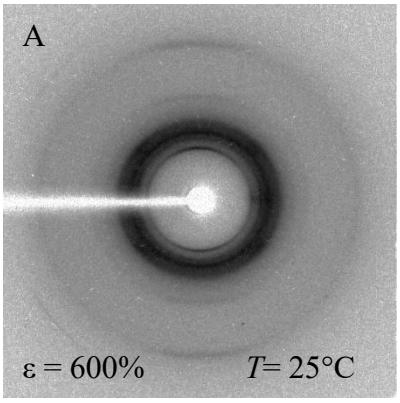

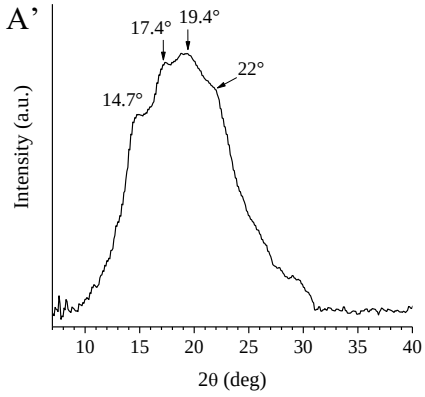

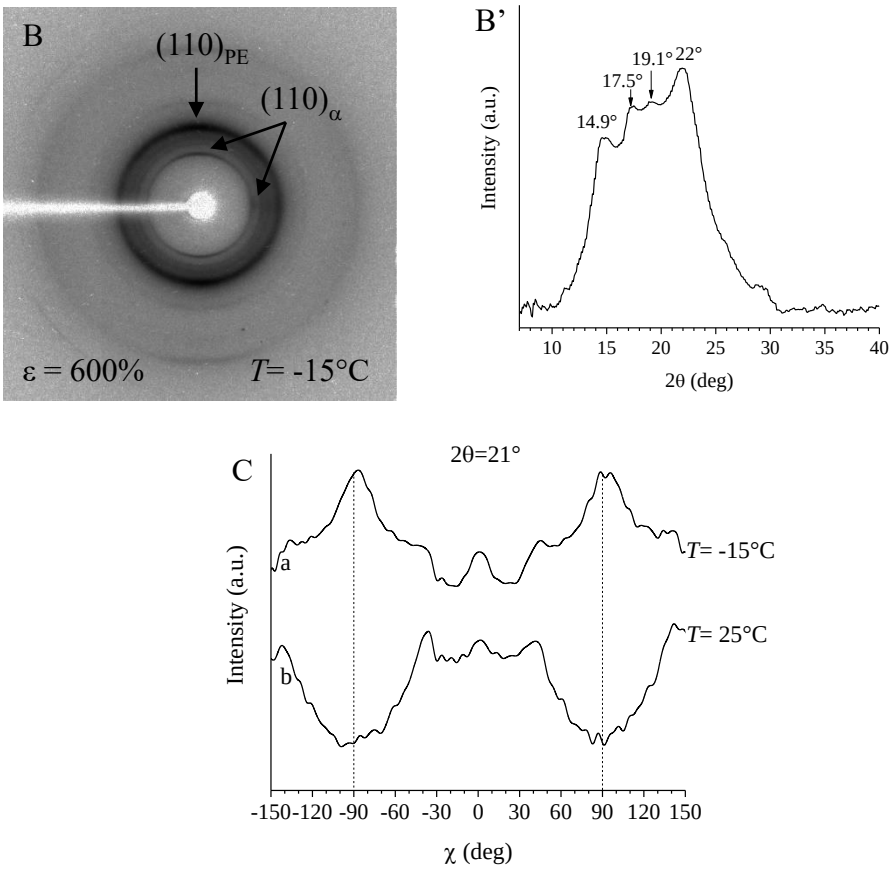

Figure 2.42 X-ray fiber diffraction patterns of the sample RDG-1-139P (w_{iPP}=0.31) acquired at the indicated temperatures, stretched at 600% (A, B) deformation and corresponding equatorial profiles (A'-B'). (C) Azimuthal profiles at 2θ=21° obtained from the X-ray diffraction patterns recorded at -15°C (a) and 25°C (b).

In Figure 2.43 the X-ray diffraction patterns and the corresponding equatorial profiles of the sample RDG-1-148P (w_{iPP}=0.49) crystallized from the melt in mixtures of iPP mesophase (for the iPP blocks) and new mesophase (for the amorphous block of the P(P-*co*-C18) copolymer) at fast cooling rate, are reported. The X-ray diffraction patterns of the unoriented sample recorded at 20°C (A) and -20°C (B) confirm that upon cooling, additional crystallization in the sample is observed. The crystallization of the PE-like crystallites formed by the side chains of the C18 units is indicated by the presence of the $(110)_{PE}$ reflection of the orthorhombic form of PE in Figure 2.43 B and by the corresponding increase in intensity at 2θ=21° in Figure 2.43 B'. The X-ray diffraction profile of the sample stretched at 400% and cooled at -20°C (C) shows that the crystallization of the C18 units still occurs, but no orientation of the PE-like crystals is observed. In fact, at -20°C (C) the

intensity of the $(110)_{PE}$ reflection is uniformly distributed along the corresponding Debye-Scherrer ring, and only the iPP mesophase and the new mesophase result oriented. This is also observed in the azimuthal profiles extracted from the bidimensional diffraction patterns (C) and (D), at 2θ=21°, (curves a and b in Figure 2.43 E).

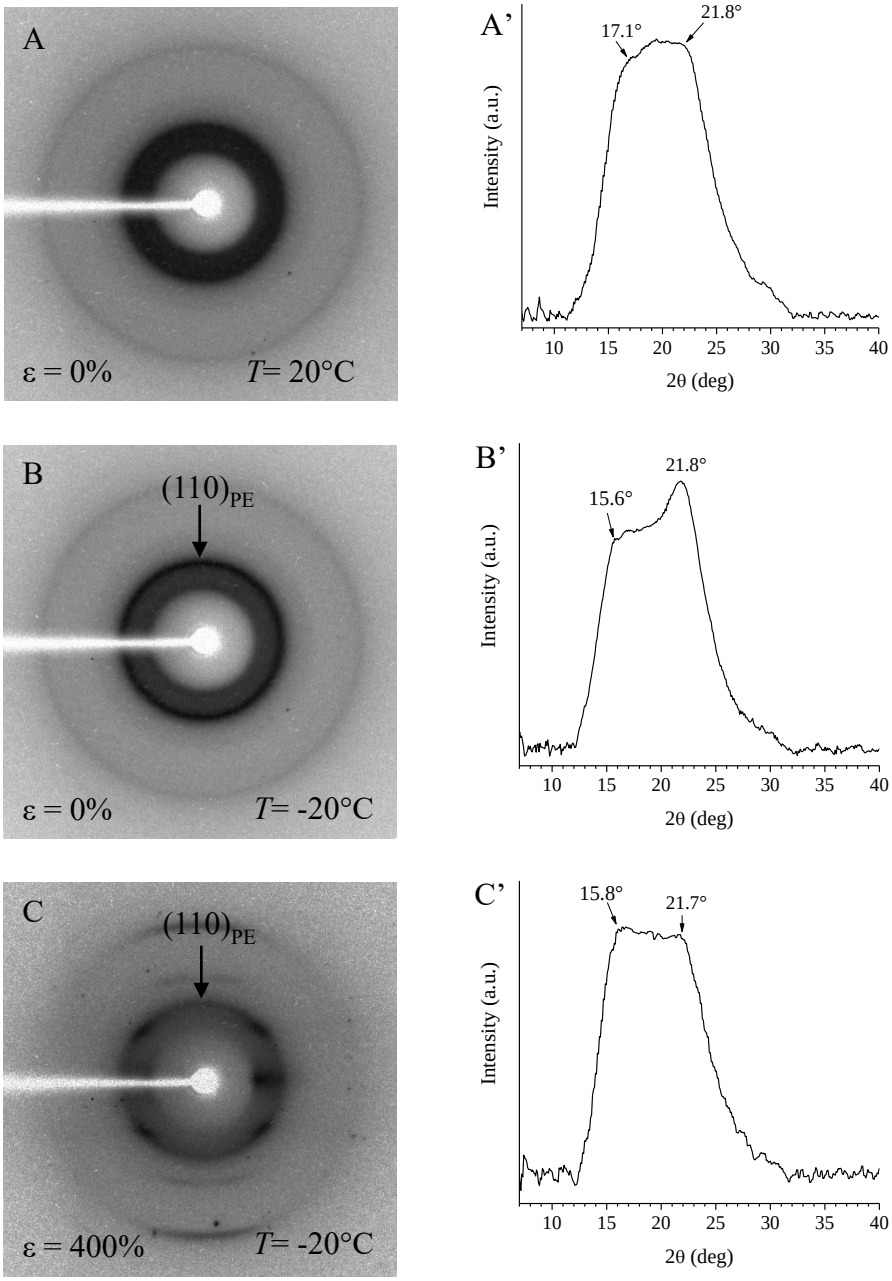

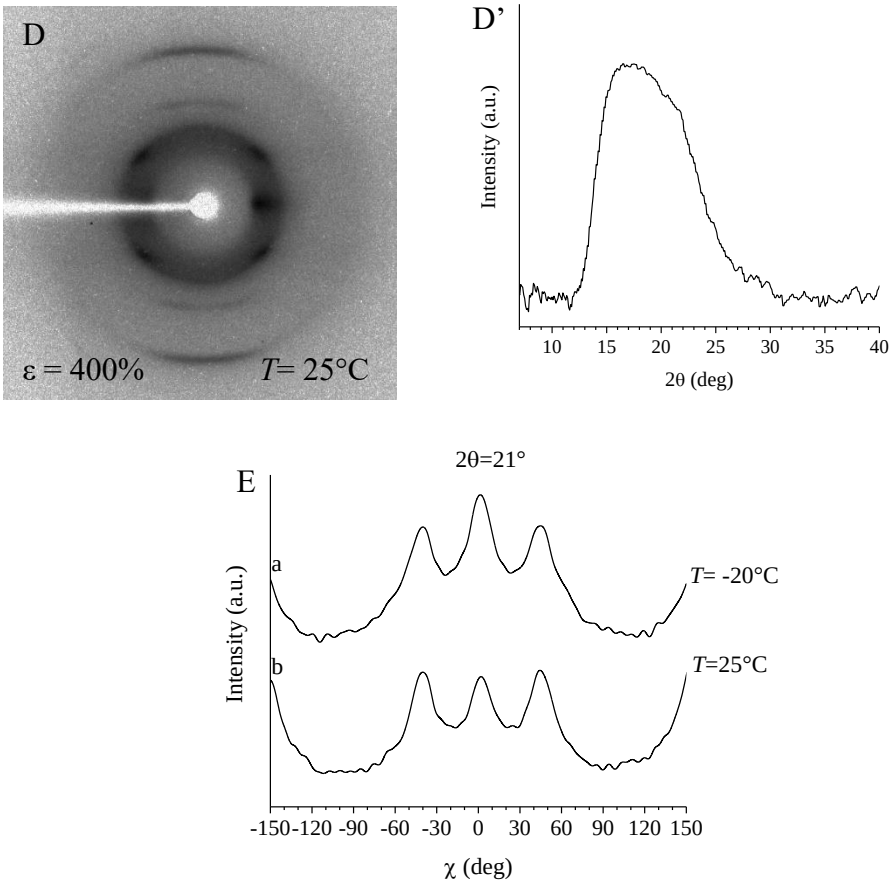

Figure 2.43 X-ray fiber diffraction patterns of the quenched sample of RDG-1-148P (w_{iPP}=0.49) collected at the indicated temperatures at 0% (A, B) and 600% (C, D) deformation and corresponding equatorial profiles (A'-D'). (E) Azimuthal profiles at 2θ=21° obtained from the X-ray diffraction patterns recorded at -20°C (a) and 25°C (b).

In Figure 2.44 the X-ray diffraction patterns and the corresponding equatorial profiles of the sample RDG-1-135P (w_{iPP}=0.44) quenched from the melt are reported. The X-ray diffraction patterns of the unoriented sample recorded at 25°C (A) and -20°C (B) confirm that upon cooling, the crystallization of the PE-like crystals occurs, as indicated by the presence of the $(110)_{PE}$ reflection at -20°C (B) and its absence at 25°C (A). By stretching the sample at a value of deformation of 450%, the cooling at -20°C does not induce any relevant crystallization of the C18 units, as indicated by the absence of the $(110)_{PE}$ reflection in the X-ray diffraction pattern in Figure 2.44 C. Only the orientation of the iPP mesophase and new mesophase is observed. It may be due to the fact that since the concentration of C18 units belonging to the P(P-*co*-C18) blocks is lower (13mol%) than that in the other BCPs (24

mol%), by effect of deformation, the average distance between the side chains of the C18 units increases, preventing their organization in PE-like crystals, and only when the sample is in the unstretched state the side chains are able to crystallize.

On the other hand, the fact that in the case of the sample RDG-1-135P (w_{iPP}=0.44) slowly crystallized from the melt, the side chains are able to crystallize at low temperatures even in the stretched state (400% deformation, -25°C, Figure 2.41 C), may indicate that the formation of PE-crystals is critically dependent on the state of organization of the main chains of the P(P-*co*-C18) blocks. In other terms, the absence of any relevant crystallization of the side chains in the stretched sample crystallized by fast cooling may be due to the fact that the crystallization of the P(P-*co*-C18) blocks in the new mesophase prevents any efficient packing of the side chains, and only if the P(P-*co*-C18) blocks are less organized, as in the sample crystallized at low cooling rate, PE-like crystals may be formed at low temperatures even in the stretched samples.

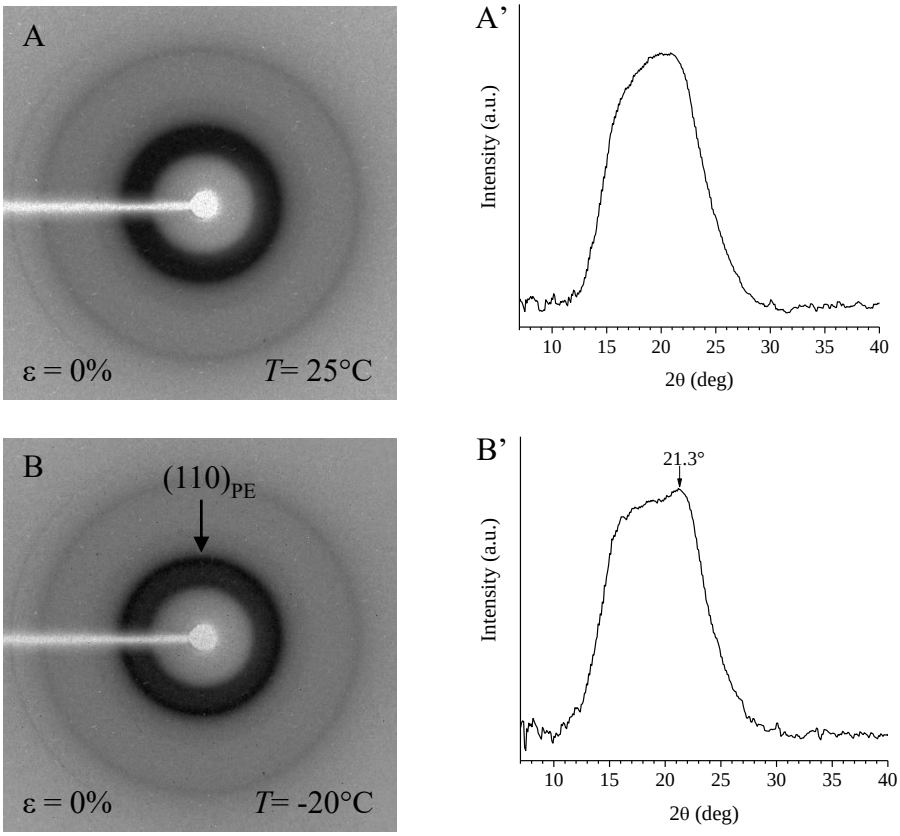

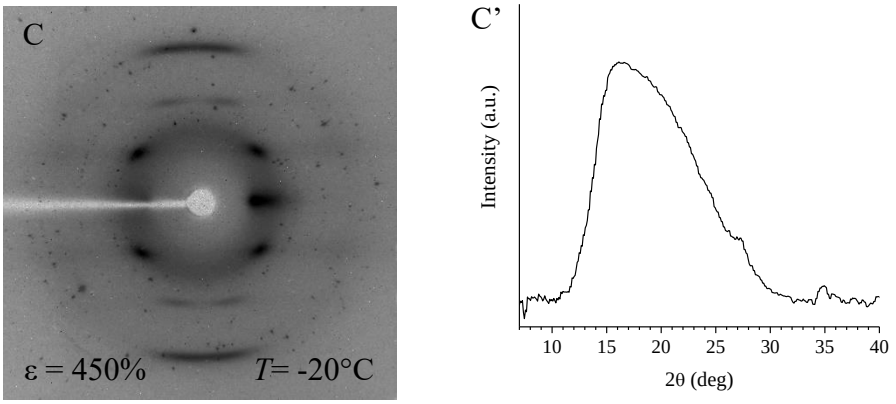

Figure 2.44 X-ray fiber diffraction patterns of the quenched sample of RDG-1-135P (w_{iPP}=0.44) recorded at the indicated temperatures stretched at 0% (A, B) and 450% (C) deformation and corresponding equatorial profiles (A', C').

In Figure 2.45 the X-ray diffraction patterns and the corresponding equatorial profiles of the sample RDG-1-139P (w_{iPP}=0.31) quenched from the melt are reported. For this sample, the crystallization of the PE-like crystals achieved in the unoriented specimen cooled at -10°C (B) is also observed in the specimen stretched at ε=400%. In fact, the X-ray diffraction pattern recorded at ε=400% and *T*= -10°C (C) shows the presence of the $(110)_{PE}$ reflection relative to the PE-like crystals. In addition, the $(110)_{PE}$ reflection appears polarized in a nearly meridional position, thus indicating that partial orientation of the PE-like crystallites is achieved. The polarization of the $(110)_{PE}$ reflection is better observed by comparing the azimuthal profiles at 2θ=21° (E) extracted from the diffraction patterns recorded at -10°C (curve a) and 25°C (curve b). In fact, it is apparent that at *T*= -10°C, in addition to intensity maxima in the range of χ ±60 - ±120°, common to the azimuthal profile b obtained at 25°, small maxima at χ= ±90° (meridian) are present (curve a). The polarization of the $(110)_{PE}$ reflection in a nearly meridional position indicates that the PE crystals are oriented with their *c*-axes almost perpendicular to the fiber axis. This is in agreement with what observed in the case of the same sample slowly crystallized from the melt (curve a in Figure 2.42 C). In that case a higher degree of orientation of the PE-like crystallites was observed, according with the higher degree of deformation of the sample, i.e. ε=600%.

A model showing the oriented crystallization of the PE-like crystals with chain axes in the perpendicular orientation with respect to the fiber axis, in oriented fibers, is shown in Figure 2.46.

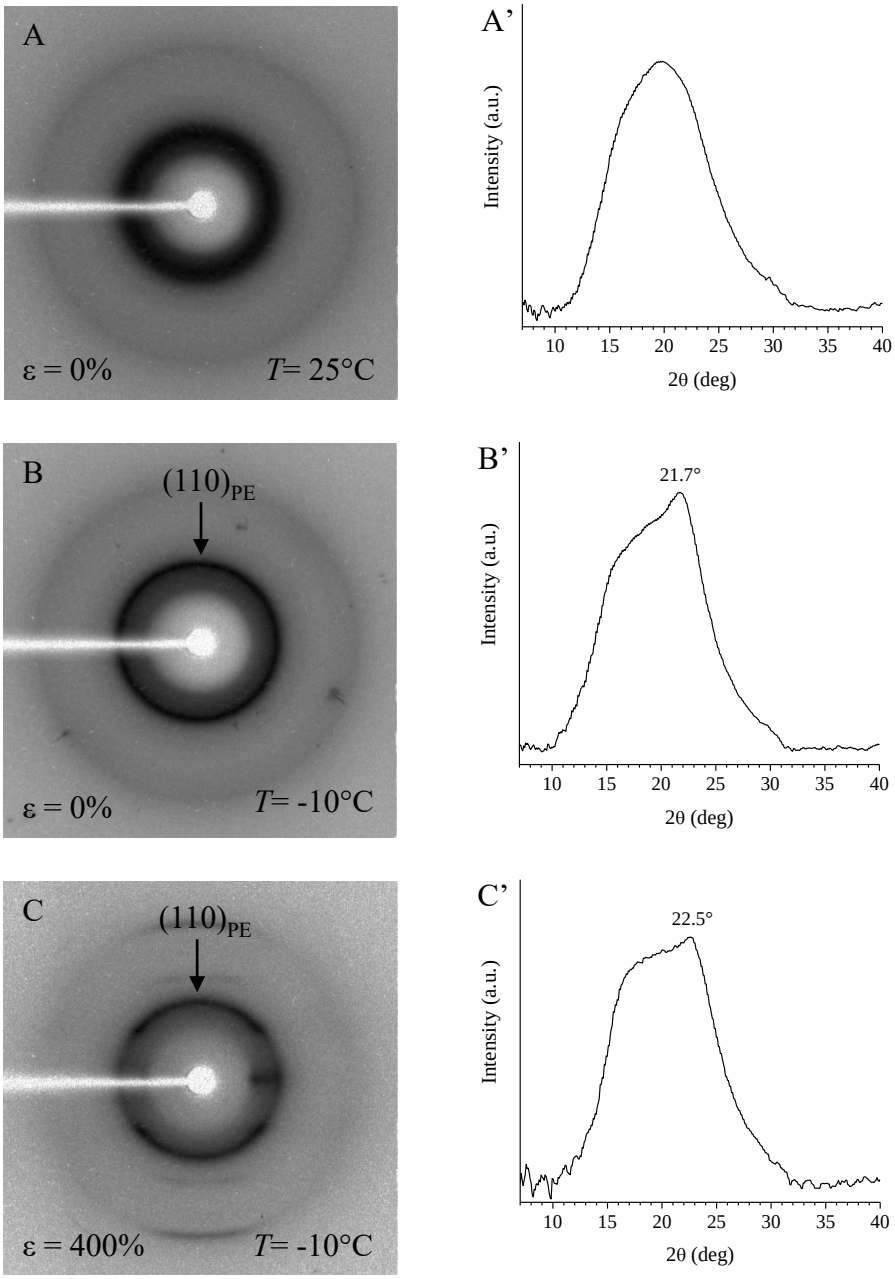

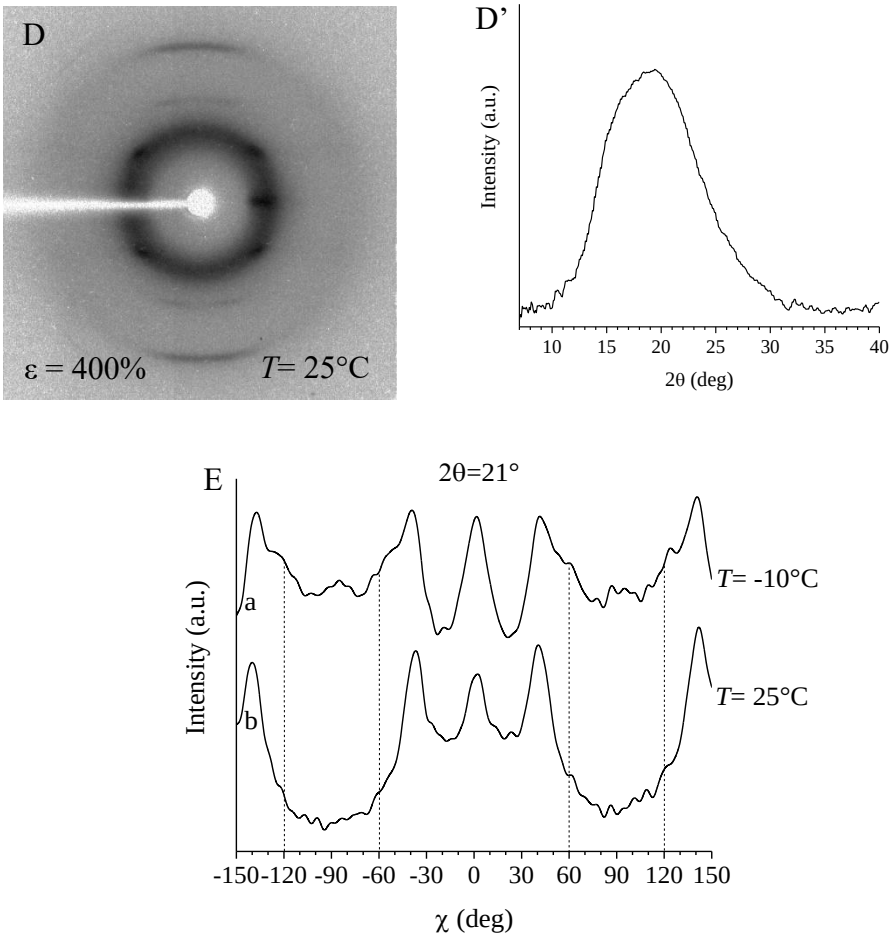

Figure 2.45 X-ray fiber diffraction patterns of the quenched sample of RDG-1-139P (w_{iPP}=0.31) collected at the indicated temperatures at 0% (A, B) and 400% (C, D deformation and corresponding equatorial profiles (A', D'). (E) Azimuthal profiles at 2θ=21° extracted from the X-ray diffraction patterns recorded at -10°C (a) and 25°C (b).

In conclusion, the low-temperature structural characterization of the oriented fibers of the iPP-*b*-P(P-*co*-C18) BCPs confirms that the crystallization of the PE-like crystallites in the P(P-*co*-C18) block occurs in all the samples when they are in an unoriented state. By cooling to sub-zero temperatures the stretched samples, the crystallization of the PE-like crystals still occurs, provided that the concentration, the average distance and mobility of side chains is high enough. That is to say that the deformation of the sample may induce an increase of the mean distance between the side chains of the C18 units, so that above a threshold deformation, they may become unable to crystallize. The threshold value of the deformation may be related to the

concentration of the C18 units and the state of organization of the main chains in the P(P-*co*-C18) blocks. In fact, for the samples RDG-1-148P (w_{iPP}=0.49) and RDG-1-139P (w_{iPP}=0.31), both having a C18 concentration around 24 mol%, the crystallization of the side chains is still observed at deformation values of 400% and 600%, respectively. On the contrary, for the sample RDG-1-135P (w_{iPP}=0.44) having a C18 concentration of 13 mol%, the crystallization of the side chain is not observed above 400% deformation.

The confined crystallization of the side chain in the P(P-*co*-C18) block domains leads to formation of unoriented PE-crystals by stretching the BCP sample RDG-1-148P with w_{iPP}=0.49, whereas in the case of the BCP sample RDG-1-139P with w_{iPP}=0.31, and therefore with higher mass fraction of P(P-*co*-C18) blocks, PE-crystals with chain axes nearly perpendicular to the fiber axis are obtained (Figure 2.46). The oriented crystallization of PE-like crystals in stretched fibers of the BCP with the highest mass fraction of P(P-*co*-C18) blocks suggests that only when the mass fraction of the compliant matrix is high enough, the PE-like crystals formed by the side chains may re-adjust their position, becoming oriented with the longest axis, perpendicular to the chain axis, parallel to the stretching direction.

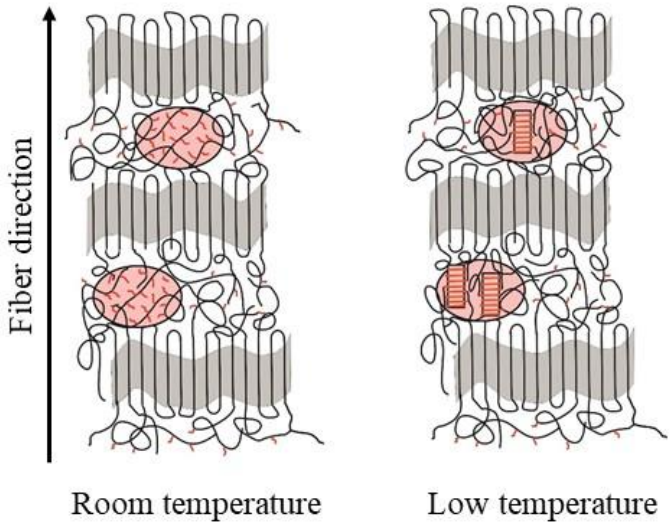

Figure 2.46 Scheme of the orientation of the PE-like crystals, with chain axes in the perpendicular orientation with respect to the fiber axis, in oriented fibers of the iPP-*b*-P(P-*co*-C18) BCPs.

2.2.8 Morphological characterization

The morphological characterization of the iPP-*b*-P(P-*co*-C18) BCPs at micrometer length scales has been carried out by polarized light optical microscopy (POM). The samples have been crystallized by cooling the melt from 180°C to room temperature at a rate of 10°C/min. The thickness of the polymer films is ≈100μm. The POM images of the analyzed samples are shown in Figure 2.47. For comparison, the POM image of the iPP homopolymer, (see section 2.1.7) is also reported. As discussed in section 2.1.7, the image of the iPP homopolymer RDG-1-41 shows the presence of bundle-like entities organized in a nearly 90° texture[35] that are typical of iPP samples in which both α and γ forms crystals are present.

The POM images of the iPP-*b*-P(P-*co*-C18) BCPs (B for RDG-1-148P (w_{iPP}=0.49), C RDG-1-135P (w_{iPP}=0.44) and D for RDG-1-139P (w_{iPP}=0.31)), on the contrary, show disordered lamellar aggregates of dimensions of 5-10μm, thus indicating that the presence of the amorphous block linked to the crystalline iPP block somewhat influences the morphology.

A) RDG-1-41 (w_{iPP}=1)

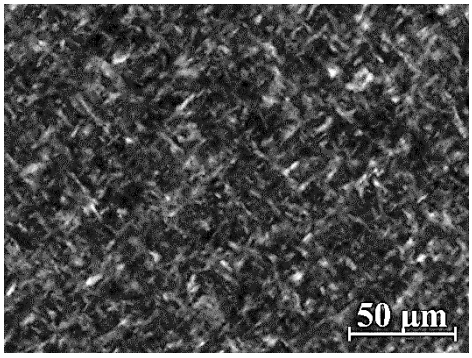

B) RDG-1-148P (w_{iPP}=0.49)

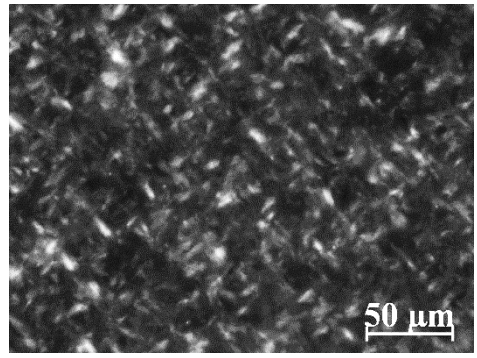

C) RDG-1-135P (w_{iPP}=0.44) D) RDG-1-139P (w_{iPP}=0.31)

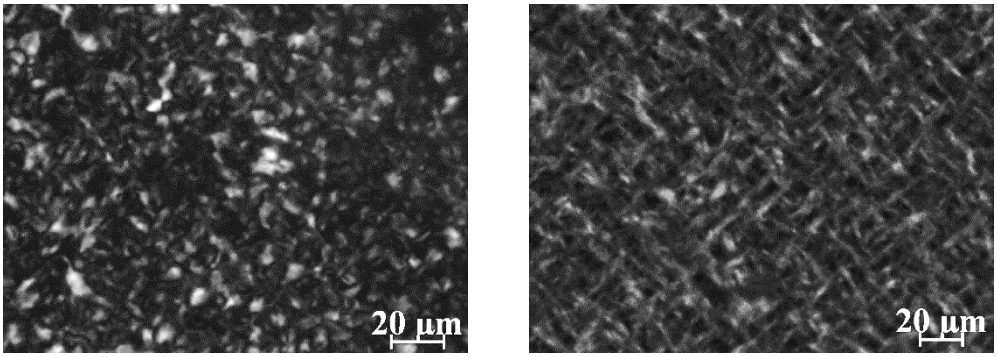

Figure 2.47 POM images of the samples crystallized from the melt at a cooling rate of 10°C/min of the iPP homopolymer RDG-1-41 (A) and of the iPP-*b*-P(P-*co*-C18) BCPs, RDG-1-148P (w_{iPP}=0.49) (B), RDG-1-135P (w_{iPP}=0.44) (C) and RDG-1-139P (w_{iPP}=0.31) (D).

In an attempt to observe the PE-like crystallites formed from the C18 side chains, the POM images of the random copolymer RDG-1-133P (Figure 2.48) and of the iPP-*b*-P(P-*co*-C18) BCPs (Figures 2.49-2.51) have been collected at *T*= -10°C and compared to those acquired at *T*=25°C. The POM analysis of the BCPs has been performed for the samples crystallized from the melt at slow (10°C/min, from 180°C to 25°C) and fast (quenching, from 180°C to 0°C) rates. In fact, the inhibition of the α form crystallization in the iPP block, by quenching of the sample, may permit to better observe the crystallization of the PE-like crystallites in the P(P-*co*-C18) block. For comparison, the POM image of P(C18) homopolymer is also shown (Figure 2.52).

The POM images of the P(P-*co*-C18) random copolymer acquired at 25°C does not shows significant birefringence (Figure 2.48 A), in agreement with the fact that at *T*=25°C the sample is amorphous. However, the cooling of the sample down to -10°C does not produce any increase of birefringence even though the crystallization of the PE-like crystals occurs (Figure 2.48 A'). The same behaviour is observed for the iPP-*b*-P(P-*co*-C18) BCPs (Figures 2.49-2.51). In fact, by comparing the images acquired for these samples at *T*=25°C and *T*= -10°C, any significant change of birefringence occurs, even though at *T*= -10°C the crystallization of the PE-like crystals occurs. The unchanged level of birefringence at -10°C may be due the sub-micrometer size of the PE-like crystals formed in confined environments.

It is worth noting that the POM image acquired for the P(C18) homopolymer at *T*= 25°C shows marked birefringence due to the presence of needle-like crystals formed by the side chains of the C18 units (Figure 2.52).

P(P-*co*-C18)

RDG-1-133P

A) RDG-1-133P *T*=25°C

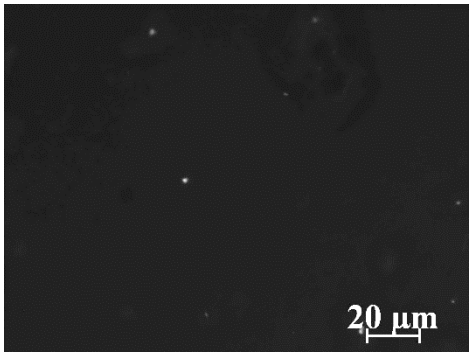

A') RDG-1-133P *T*= -10°C

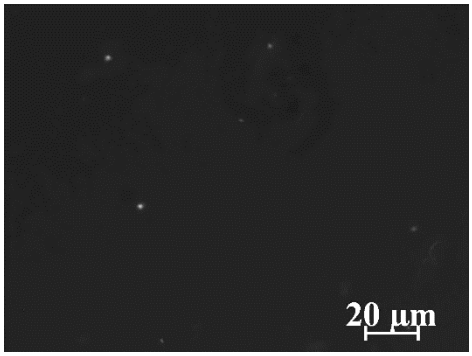

Figure 2.48 POM images of the P(P-*co*-C18) random copolymer, RDG-1-133P, acquired at *T*=25°C (A) and *T*= -10°C (A').

iPP-*b*-P(P-*co*-C18)

RDG-1-148P (w_{iPP}=0.49)

A) *T*=25°C

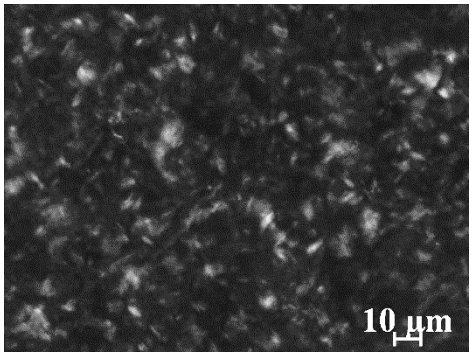

A') *T*= -10°C

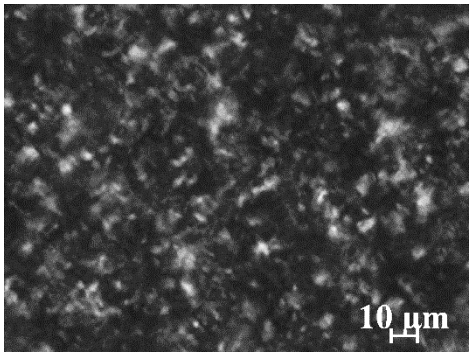

B) *T*=25°C

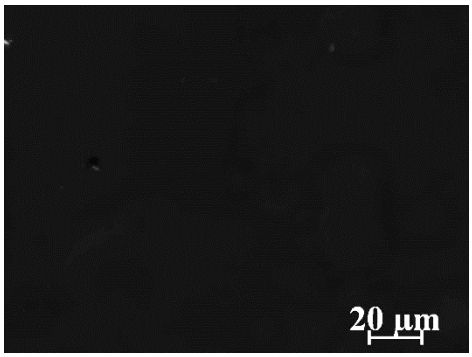

B') *T*= -10°C

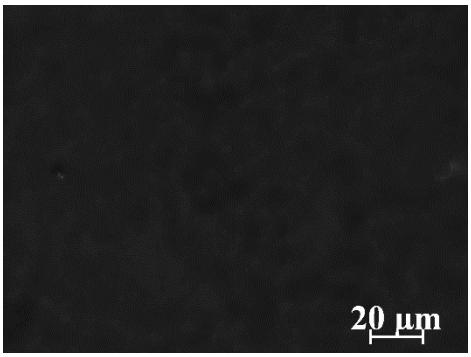

Figure 2.49 POM images of the iPP-*b*-P(P-*co*-C18) BCP RDG-1-148P (w_{iPP}=0.49) slowly crystallized from the melt (A and A') and quenched from the melt (B and B'), acquired at *T*= 25°C (A and B) and *T*= -10°C (A' and B').

RDG-1-135P (w_{iPP}=0.44)

A) *T*=25°C

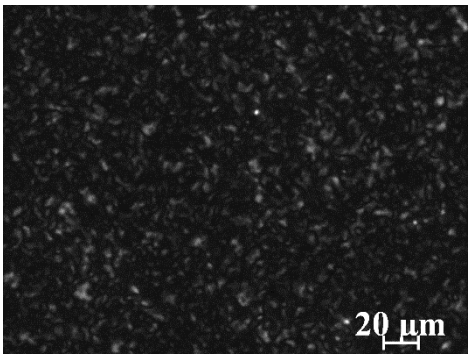

A') *T*= -10°C

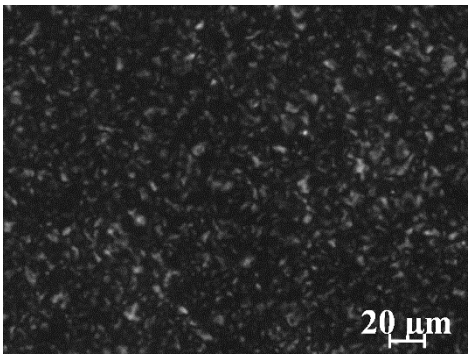

B) *T*=25°C

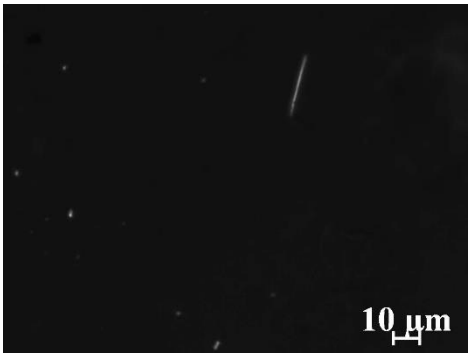

B') *T*= -10°C

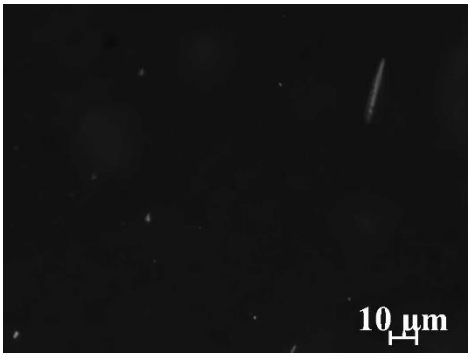

Figure 2.50 POM images of the iPP-*b*-P(P-*co*-C18) BCP RDG-1-135P (w_{iPP}=0.44) slowly crystallized from the melt (A and A') and quenched from the melt (B and B'), acquired at *T*= 25°C (A and B) and *T*= -10°C (A' and B').

RDG-1-139P (w_{iPP}=0.31)

A) *T*=25°C

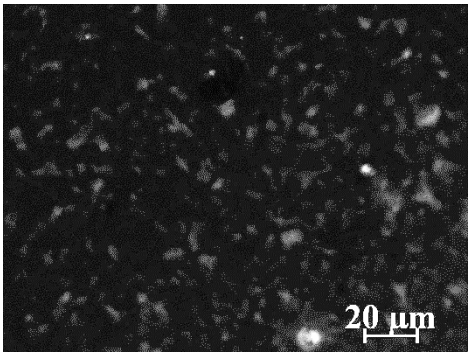

A') *T*= -10°C

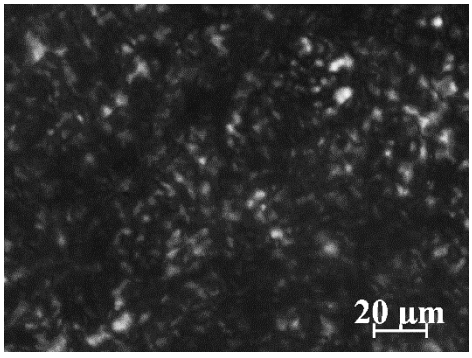

B) T=25°C

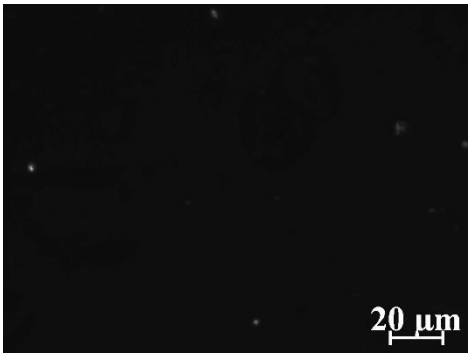

B') T= -10°C

Figure 2.51 POM images of the iPP-*b*-P(P-*co*-C18) BCP RDG-1-139P (w_{iPP}=0.41) slowly crystallized from the melt (A and A') and quenched from the melt (B and B'), acquired at T= 25°C (A and B) and T= -10°C (A' and B').

P(C18)

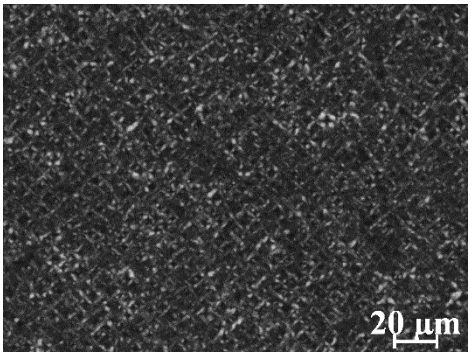

Figure 2.52 POM image of the poly(1-octadecene) (P(C18)) homopolymer slowly crystallized from the melt, acquired at T= 25°C.

The study of the morphology at nanometer length scales has been performed by Transmission Electron Microscopy (TEM). A thin film of the sample (thickness<100nm) has been deposited on a copper grid by casting from a diluted solution (0.5%wt) of the BCP in p-xylene. The thin polymer film thus obtained is then subjected to melting, maintained in the molten state for 5min and then quenched from the melt in order to inhibit the crystallization of the iPP blocks and, at the same time, obtain the vitrification of a possible nanostructure developing in the melt. For comparison, the TEM image of a thin polymer film subjected to slow crystallization from the melt has also been collected.

The sample RDG-1-148P (w_{iPP}=0.49) having a volume fraction of the iPP block (f_{iPP}) equal to 0.47 has been selected for the morphological analysis. On the basis of the value of f_{iPP}, the possible nanostructure developing in the

melt should have a lamellar morphology. The TEM images of the sample RDG-1-148P have been obtained after staining the thin polymer film with RuO_4, to enhance the contrast between the crystalline lamellae and the amorphous phase.

The TEM image obtained for the sample slowly crystallized from the melt (Figure 2.53 A) shows crystalline lamellae having thickness ≈10nm, which are relative to the iPP block crystallized in α form (Figure 2.53 A). The TEM image of the sample quenched from the melt after being kept at *T*=180°C for 5min (Figure 2.53 B), also shows lamellar entities with thickness ≈10-15nm, thus indicating that the quenching has not been efficient in inhibiting the crystallization of iPP blocks. A second quenching attempt has thus been performed, however in this case the thin film obtained by casting has been maintained at the temperature of 180°C for 3 days (in an oven at reduced pressure) in order to eliminate the crystalline memory of the melt. The so obtained TEM image shows that in this case crystallinity development has efficiently be inhibited (Figure 2.53 C), only small crystalline aggregates are observed (inset). In all cases the relative arrangement of the crystalline and amorphous phase is highly disorder, indicating that the possible phase separation at nanoscale of the crystalline (iPP) and amorphous (P(P-*co*-C18)) is not achieved either because crystallization occurs from a homogeneous melt, or because iPP crystallization breaks the nanostructured morphology.

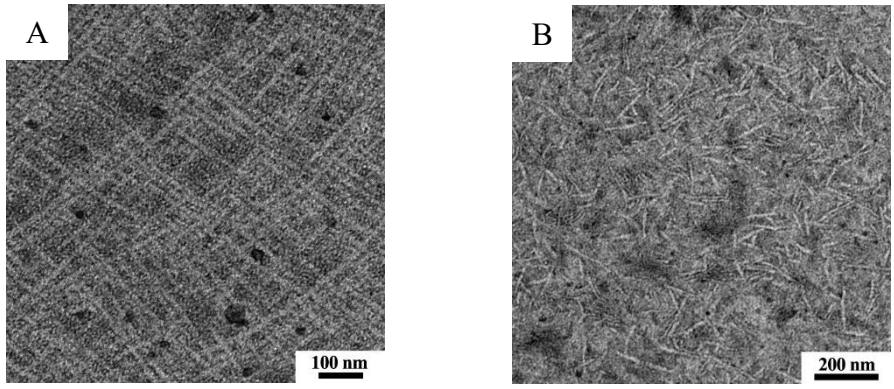

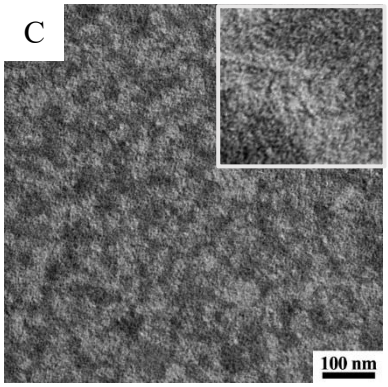

Figure 2.53 TEM images of the sample RDG-1-148P (w_{iPP}=0.49) quenched from the melt after 5min at 180°C (A) and after 3 days at 180°C (B), and of the sample slowly crystallized from the melt (C). Contrast is generated by staining with RuO_4.

The morphology of the iPP-*b*-P(P-*co*-C18) BCPs quenched from the melt has been studied by Atomic Force Microscopy (AFM). In particular, for this analysis, the sample RDG-1-148P, showing the highest mass fraction of the iPP blocks, i.e. w_{iPP}=0.49, has been selected.

The AFM images (Figure 2.54) show that the mesophase developing in the iPP block of the iPP-*b*-P(P-*co*-C18) BCPs does not show the nodular morphology observed for iPP homopolymer (Figure 2.19). We speculate that the presence of the amorphous P(P-*co*-C18) blocks covalently linked to the iPP blocks somewhat influences the overall morphology developing in iPP blocks.

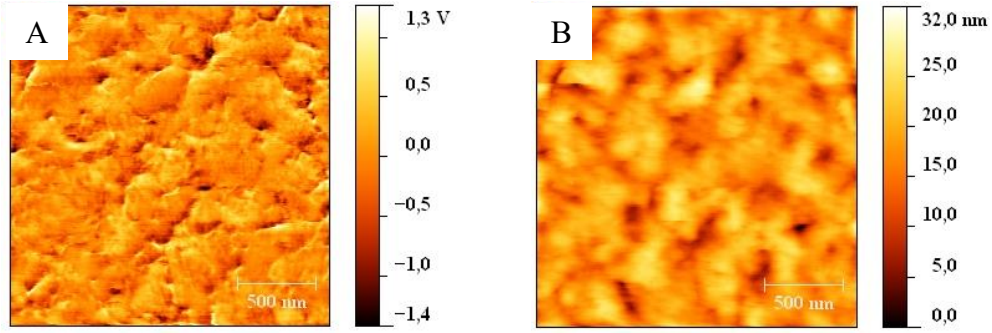

Figure 2.54 AFM phase (A) and height (B) images of the iPP-*b*-P(P-*co*-C18) BCP RDG-1-148P (w_{iPP}=0.49).

CHAPTER 3

Semicrystalline ethylene/norbornene-based multi-block copolymers

The insertion of cyclic comonomers in polyethylene chains produces micro-structural modifications into the polymer chains which typically result in the enhancement of the mechanical and thermal properties of the starting material. For instance, ethylene-norbornene random copolymers P(E-*co*-N) obtained by metallocene catalysis show high thermal resistance, high resistance to solvent dissolution, high gas barrier properties and high optical transparency.[45]

The first experiment of copolymerization of ethylene and norbornene was reported by Kaminsky et al. with the catalyst *rac*-[Et(Ind)2]ZrCl2/MAO.[46] Since then, many efforts have been made by academic and industrial research to deeply understand the microstructure of the ethylene/norbornene copolymers.[45,47] In fact, depending on the catalysts structure, norbornene units can arrange in alternating sequences (ENEN) or in short norbornene homosequences such as dyads (ENNE) and triads (ENNN).[48] The control of the copolymers microstructure, the N content and distribution, is extremely important since it enables to finely tune the properties of the resulting materials.

Recently, an attempt to synthesize ethylene/norbornene multi-block copolymers has been performed,[49,50] by using chain shuttling polymerization (CSP), firstly introduced by Dow Chemical Company in 2006 for the copolymerization of ethylene and 1-octene.[51]

The catalytic system of CSP is composed by three fundamental components: two catalysts with different propensity to incorporate the comonomeric units and one chain transfer agent (CTA) that “shuttles” the growing chain between two different catalytic centres. The CSP strategy allows to obtain multi-blocks copolymers where different microstructures are bonded together in an alternate sequence to form a polymer chain. The advantage of obtaining such molecular architectures is that the different properties of the diverse microstructural blocks are combined in a single polymer chain showing hybrid properties. In fact, in the case of ethylene/norbornene copolymers, CSP may allow to obtain a component rich

in ethylene and a component rich in norbornene, bonded in an alternate multi-block sequence, resulting in polymers showing, at the same time, elastic properties and rigidity typical of P(E-*co*-N) copolymers.

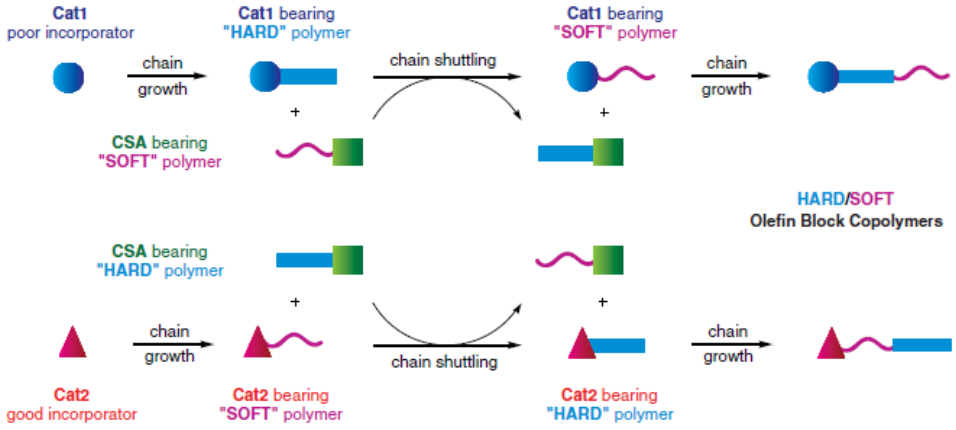

Figure 3.1 Scheme for the chain shuttling mechanism: Cat1 (●) and Cat2 (▲) represent catalysts with high and low monomer selectivity, respectively, whereas the CSA (■) facilitates the chain shuttling reaction. The polymer segment produced at the Cat1 active site is transferred by the CSA to the Cat2 active site and *vice versa*. Multiple repetitions of this event provide a multi-block architecture in the resultant polymer chain.[51]

In this chapter, E/N multi-block copolymers (MBCPs) obtained via CSP mechanism have been studied. The samples have been subjected to thermal and structural characterization. In particular, time/temperature resolved SAXS/WAXS analysis has been performed, in order to study, *in situ*, the melting and crystallization processes of the samples.

3.1 Materials and methods

The ethylene-norbornene multi-block copolymer (E/N MBCPs) samples studied in the present work were synthesized by CSP strategy,[50] by using two *ansa*-metallocene Zr-based catalysts activated with N,N-Dimethylanilinium tetrakis(pentafluorophenyl)borate (Figure 3.2), i.e. isopropyliden(3-methylcyclopentadienyl)(Fluorenyl)Zirconium dichloride and isopropyliden(cyclopentadienyl)(Indenyl)Zirconium dichloride, with low and high norbornene incorporation capability, respectively. The catalyst showing low norbornene incorporation capability, labelled as B1, tends to polymerize -NENE- alternating sequences in presence of a high comonomer feed ratio (N/E), whereas the catalyst showing low norbornene incorporation capability,

A3, tends to copolymerize ethylene and norbornene randomly. The chain transfer agent (CTA) used for this CSP system is diethyl zinc, $Zn(Et)_2$.
The comonomer feed ratio (N/E) is set equal to 1.3. In these reaction conditions, i.e. when the N/E feed ratio is not high, the chain transfer mechanism is optimized, even though chain termination events of chains coordinated at $ZnEt_2$ dormant site may not be excluded. The resultant products are a reactor blend of chains obtained from the sole catalyst A3 by chain shuttling from A3 to A3, from the sole catalyst B1 by chain shuttling from B1 to B1, multi-block copolymer chains deriving from the chain shuttling mechanisms between A3 and B1 and *viceversa*. The multi-block copolymer chains including blocks produced by the two different catalysts act as compatibilizer between the chains obtained from A3 and from B1.

The molecular characteristics of the studied samples are reported in Table 3.1.

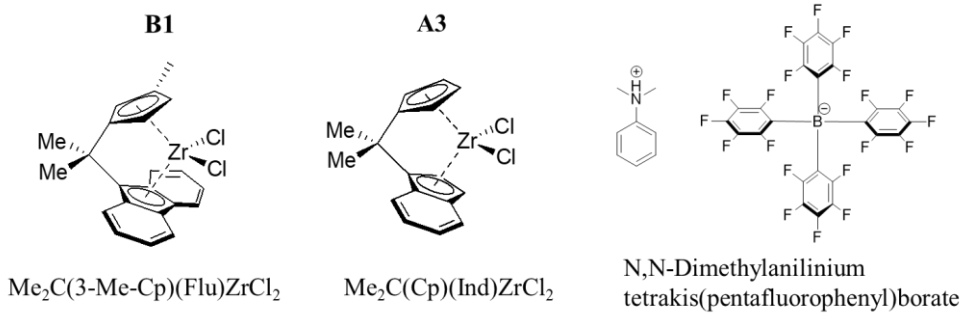

Figure 3.2 Structure of the isopropyliden(3-methylcyclopentadienyl)(Fluorenyl)Zirconium dichloride (B1) and isopropyliden(cyclopentadienyl)(Indenyl)Zirconium dichloride (A3) catalysts and of the N,N-Dimethylanilinium tetrakis(pentafluorophenyl)borate cocatalyst used for the synthesis of multi-block ethylene/norbornene copolymers.

Table 3.1 Catalyst (Cat) and amount of $Zn(Et)_2$ (expressed as Zn/Zr) used for the synthesis, value of the overall content of norbornene (N), of the glass transition temperature (T_g), of the molecular mass (M_w) and of the polydispersity index (M_w/M_n) of the ethylene/norbornene copolymers.

	SAMPLE	Cat	Zn/Zr	N[a] (mol%)	M_w[b] (Kg/mol)	$\frac{M_w}{M_n}$[b]
N/E feed ratio=1.3	DSC153	B1	198	21	-	-
	DSC157	A3	396	29	22.8	1.7
	DSC158	B1+A3	50	31	27	1.8
	DSC159	B1+A3	99	31	25.1	1.8

a evaluated from ^{13}C-NMR[50]; **b** evaluated from GPC analysis.[50]

The samples DSC158 and DSC159 have been synthesized in presence of both B1 and A3 catalysts using different amounts of CTA (expressed as Zn/Zr). The reference samples synthesized using the sole catalyst B1 and A3 (DSC153 and DSC157, respectively) in presence of diethylzinc have been also prepared. The two samples synthesized with B1+A3 catalysts show a norbornene content (N) of 31% mol, intermediate between the N content in the sample synthesized with the sole B1 catalyst (having lower N incorporation capability) and that in the sample synthesized with the sole A3 catalyst, corresponding to 21% mol and 29% mol, respectively.

The thermal characterization of the samples has been carried out by calorimetric measurements performed with a differential scanning calorimeter (DSC-822 by Mettler Toledo) in a flowing N_2 atmosphere and at a scanning rate of 10°C/min.

The structural characterization at different length scales has been carried out by X-ray scattering technique using a Ni-filtered CuKα radiation. Wide angle X-ray scattering (WAXS) analysis has been performed on unoriented (powder) using an automatic diffractometer (Philips).

Time/temperature resolved SAXS/WAXS analysis has been carried out on BM26B (DUBBLE) station at the European Synchrotron Radiation Facility (ESRF) in Grenoble, France. A modified DSC Linkam hot stage permitting the transmission of the X-rays through the sample has been employed for the in situ thermal treatment of the samples. The data have been acquired by using an acquisition time of 6 s, a delay time of 6 s and a wavelength of 1.0402 Å. The collection rate is 0.071frame/s both for WAXS and SAXS measurements.

3.2 WAXS and thermal analyses of as prepared samples

The X-ray powder diffraction profiles of the as prepared samples of the E/N copolymers are shown in Figure 3.3. The X-ray diffraction profile of the sample synthesized with the catalyst B1, i.e. DSC153 (curve a), shows an amorphous halo centered at 2θ=17.8° and two low-intensity crystalline peaks at 2θ=21° and 2θ=24° corresponding, respectively, to the (110) and (200) reflection of the orthorhombic form of PE. This indicates that the catalyst B1 produces rather long -EEEE- sequences along the polymer chains, which, therefore, are able to crystallize. On the contrary, the X-ray diffraction profile of the sample synthesized with the catalyst A3, i.e. DSC157 (curve b), only

shows an amorphous halo centered at 2θ=17.7°. This is due to the fact that the catalyst A3 has a higher N incorporation capability with respect to the catalyst B1, and that the distribution of N and E units along the polymer chains is random. The X-ray powder diffraction profiles of the two multi-block copolymer samples synthesized with B1+A3, i.e. DSC158 (curve c) and DSC159 (curve d), show, similarly to the sample DSC158, two low-intensity peaks at 2θ=21° and 2θ=24° due to the presence of small amounts of PE crystals. It is worth noting that the N content in the two multi-block copolymer samples (29% mol) is similar to that of the sample synthesized with the sole catalyst A3 (31% mol), nevertheless it shows a slight crystallinity. It confirms the multi-block nature of these copolymers, wherein slightly crystalline blocks synthesized by the catalyst B1 alternate with the amorphous blocks synthesized by the catalyst A3, and/or the presence of chains produced with the sole catalyst B1.

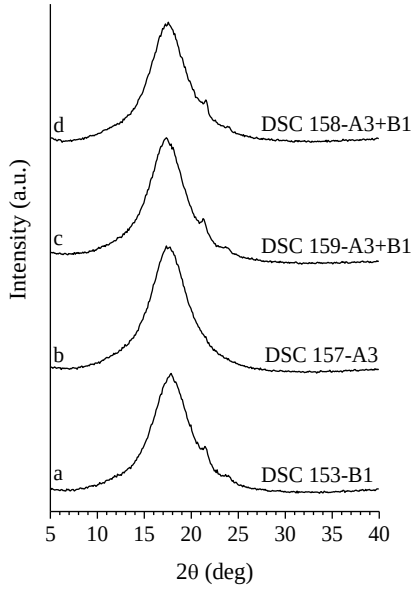

Figure 3.3 X-ray powder diffraction profiles of the E/N copolymers synthesized with the catalyst B1 (a), A3 (b) and with both B1 and A3 catalysts (c, d).

The DSC thermograms of the as prepared samples of the E/N copolymers are shown in Figure 3.4. The thermograms are recorded during the first heating from -40°C to 200°C (A), successive cooling from 200°C to -40°C (B) and second heating from -40°C to 200°C (C).

The thermogram recorded during the first heating of the sample synthesized with the catalyst B1, DSC153, (curve a in Figure 3.4 A), shows

an inflection point relative to the glass transition, followed by an endothermic relaxation phenomenon, at T=28°C (hysteresis). At higher temperatures, i.e. T=131°C, an endothermic peak relative to the melting of the PE crystals observed in WAXS analysis is also present. The DSC thermogram recorded during the cooling (curve a in Figure 3.4 B) and successive heating (curve a in Figure 3.4 C) shows the inflection point relative to the T_g and exothermic (during cooling)/endothermic (during heating) phenomena relative to the crystallization and successive melting of the PE like crystals, respectively.

The heating/cooling thermograms of the sample synthesized with the catalyst A3, DSC157, (curves b in Figure 3.4 A, B and C), only show the inflection point relative to the T_g at ≈42°C.

The heating thermograms of the samples synthesized with B1+A3 catalysts (curve c, d in Figure 3.4 A and C) show the endothermic peak relative to the melting of the PE crystals in the blocks synthesized by the catalyst B1, while the cooling thermograms (curves c, d in Figure 3.4 B) show the exothermic peak relative to the crystallization of PE-like crystals. For the sample DSC 158, a broad inflection indicating the T_g is also evident at ≈40°C.

The values of the melting temperature and enthalpy recorded during the first (T_m^I, ΔH_m^I) and second heating (T_m^{II}, ΔH_m^{II}), crystallization temperature and enthalpy (T_c, ΔH_c) and of the glass transition temperature (T_g) are reported in Table 3.2.

The high melting temperature of the PE crystals and the value of the T_g in the sample synthesized with the catalyst B1 indicates the presence, along the polymer chain, of rather long -EEE- sequences which, therefore, are able to crystallize, and sequences wherein the E-N units are randomly distributed, thus resulting in amorphous segments with a relatively high T_g.

The same may be said for the two samples synthesized with B1+A3 and CTA. However, in this case, the ethylene-rich sequences showing a T_m≈125°C and the E-N random sequences showing a T_g≈40°C are produced by two different catalysts, namely B1 and A3, respectively. In fact, the value of the T_g is comparable with that of the sample synthesized with the sole A3 catalyst.

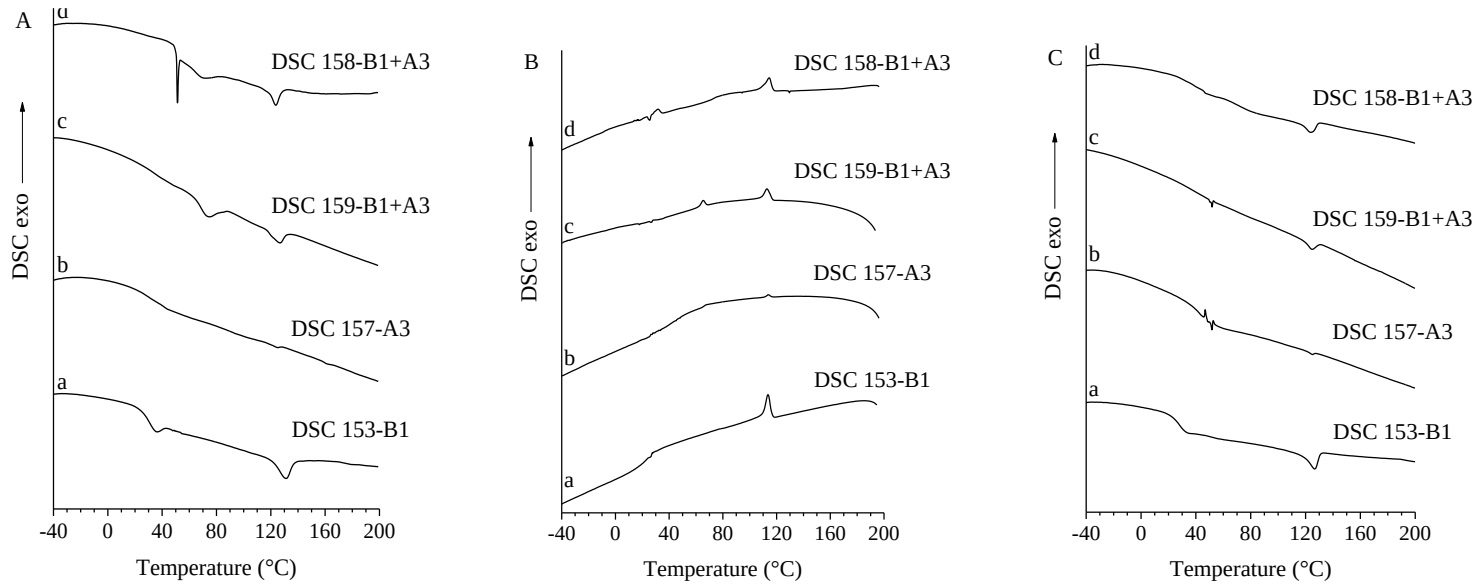

Figure 3.4 DSC thermograms recorded during heating (A), successive cooling (B) and second heating (C) of the as prepared samples of the E/N copolymers synthesized with the catalyst B1 (a), A3 (b) and with both B1 and A3 catalysts (c, d).

Table 3.2 Catalyst (Cat) used for the synthesis, value of the overall content of norbornene (N), melting temperature and enthalpy recorded during the first (T_m^I, ΔH_m^I) and second (T_m^{II}, ΔH_m^{II}) heating, crystallization temperature and enthalpy (T_c, ΔH_c) and glass transition temperature (T_g) of the as prepared samples of the ethylene/norbornene copolymers.

SAMPLE	Cat	N (%mol)	T_m^I (°C)	ΔH_m^I (J/g)	T_m^{II} (°C)	ΔH_m^{II} (J/g)	T_c (°C)	ΔH_c (J/g)	T_g (°C)
DSC153	B1	21	130	-9.2	127	-3.5	114	3.0	28
DSC157	A3	29	-	-	-	-	-	-	42
DSC158	B1+A3	31	124	-3.3	124	-1.2	114	1.9	≈40
DSC159	B1+A3	31	73;126	-4.4;-2.9	124	-1.3	65;113	0.5;1.4	-

3.3 Time/temperature resolved SAXS/WAXS analysis

The study of the structural organization of the E/N copolymers at different length scales has been performed by analyzing *in situ* the melting and crystallization processes in these samples, by means of SAXS/WAXS analysis through use of synchrotron radiation at ESRF.

For each sample, a small amount of the as prepared sample has been sandwiched between two kapton sheets and subjected to the following thermal treatment: rapid heating, at a rate of 30°C/min, up to 180°C or 200°C, isotherm at that temperature for 1 minute, cooling down to 25°C at a rate of 10°C/min and heating up to 180°C or 200°C at a rate of 10°C/min. An acquisition time of 6 s and a delay time of 6 s have been used. Selected SAXS/WAXS patterns recorded during the three different thermal ramps, and the corresponding Lorentz corrected intensity profiles, are shown for each sample in Figures 3.5-3.8.

The WAXS/SAXS and the Lorentz corrected intensity profiles of the sample DSC158 synthesized with B1+A3 and the CTA agent (Zn/Zr=50) are shown in Figure 3.5. The WAXS profiles confirm what previously observed from X-ray powder diffraction and thermal analyses. In fact, WAXS profiles recorded during the heating of the sample at a rate of 30°C/min (Figure 3.5 A), display that the sample shows slight PE crystallinity, as indicated by the two low-intensity reflections $(110)_{PE}$ and $(200)_{PE}$ (curve a). During heating at a rate of 30°C/min, the PE crystals are present up ≈130°C (curves b-f), while at higher temperatures the sample is totally in the melt state (curves g-h). The WAXS profiles recorded during the cooling at a rate of 10°C/min (Figure 3.5 B) show that PE crystallinity starts developing at ≈115°C (curve d). Crystallinity increases during cooling the sample down to 25°C (curves e-h). The amount of the crystallinity is small, as indicate by the low intensity of the (110) and (200) reflections of PE in the orthorhombic form. The WAXS profiles recorded during the successive heating at a rate of 10°C/min (Figure 3.5 C) show that the PE crystals are present up to ≈114°C (curves a-c), while at higher temperatures the sample is completely melt (curves d-h).

From the SAXS profiles simultaneously recorded with the WAXS data during the thermal treatment of the sample it is possible to gain further information. In fact, it is apparent that the SAXS profiles recorded during the heating at a rate of 30°C/min (Figure 3.5 A') and those recorded during the successive cooling (Figure 3.5 B') and heating at 10°C/min (Figure 3.5 C') always show

a broad correlation peak, even after Lorentz intensity correction (A'', B'', C'') extending from ≈0.6nm^{-1} to 0.9nm^{-1} (indicated by the arrows in curves a-f) in the whole temperature range from 25°C to 200°C. This correlation peak may not be due to the lamellar organization of PE crystals, because it does not disappear after melting of the PE crystals. It is probably due to the electron density contrast between phase separated domains of segments rich in norbornene units (produced with the catalyst A3) and those containing segment containing -EEE- sequences (produced with the catalyst B1). From the position of the correlation peak (q≈0.6-0.9nm^{-1}) it is possible to determine that the size of the phase separated domains falls in the range 7 - 10.5nm. It is worth noting that the SAXS profiles of the sample recorded below T≈114°C, that is upon crystallization of PE segments, do not show any additional correlation peak due to lamellar organization of PE crystals. These data indicate that PE crystals are present as isolated entities within the sample. Alternatively, the absence of a correlation peak related to the PE crystalline phase may be due to the fact that the degree of crystallinity is too low to produce significant SAXS intensity in the investigated q range.

The same considerations hold also for the sample DSC159 synthesized with B1+A3 using a doubled amount of CTA (Zn/Zr=99) with respect to the sample, DSC158. The WAXS/SAXS and the Lorentz corrected intensity profiles recorded during the thermal treatment are shown in Figure 3.6.

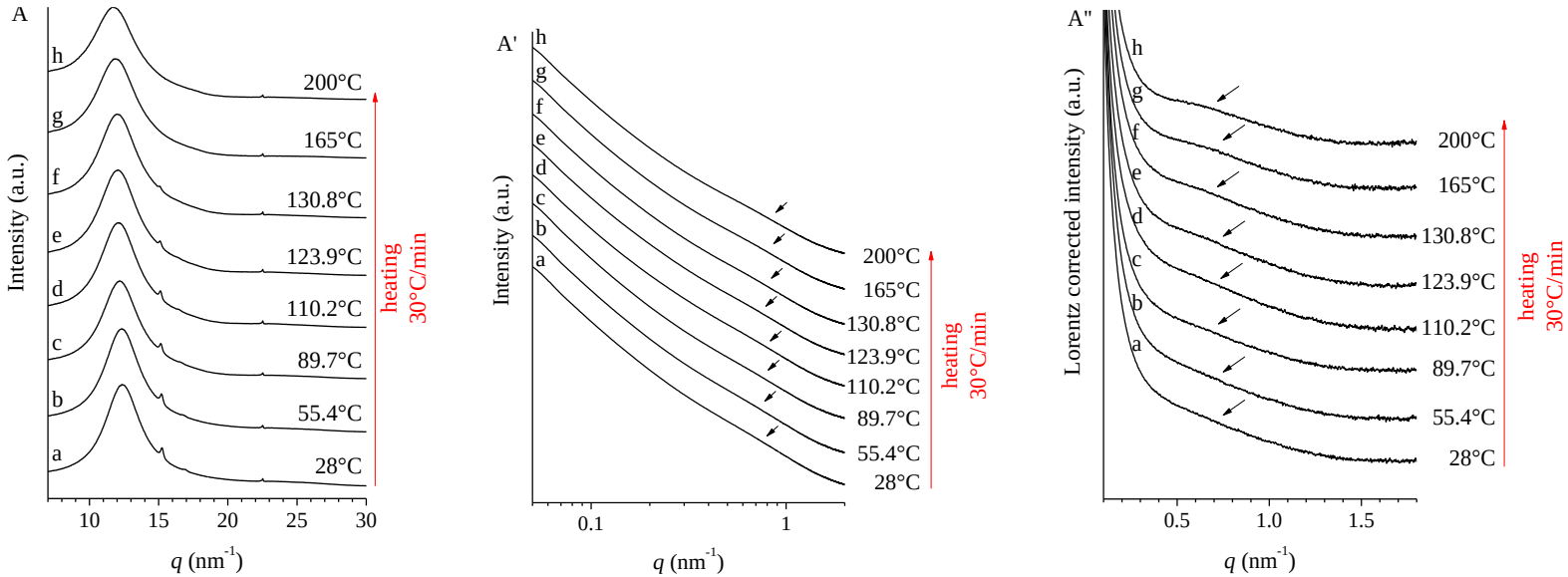
A
Intensity (a.u.)
h
g
f
e
d
c
b
a
200°C
165°C
130.8°C
123.9°C
110.2°C
89.7°C
55.4°C
28°C
heating
30°C/min
10
15
20
25
30
q (nm-1)
A'
Intensity (a.u.)
0.1
1
q (nm-1)
A"
Lorentz corrected intensity (a.u.)
0.5
1.0
1.5
q (nm-1)

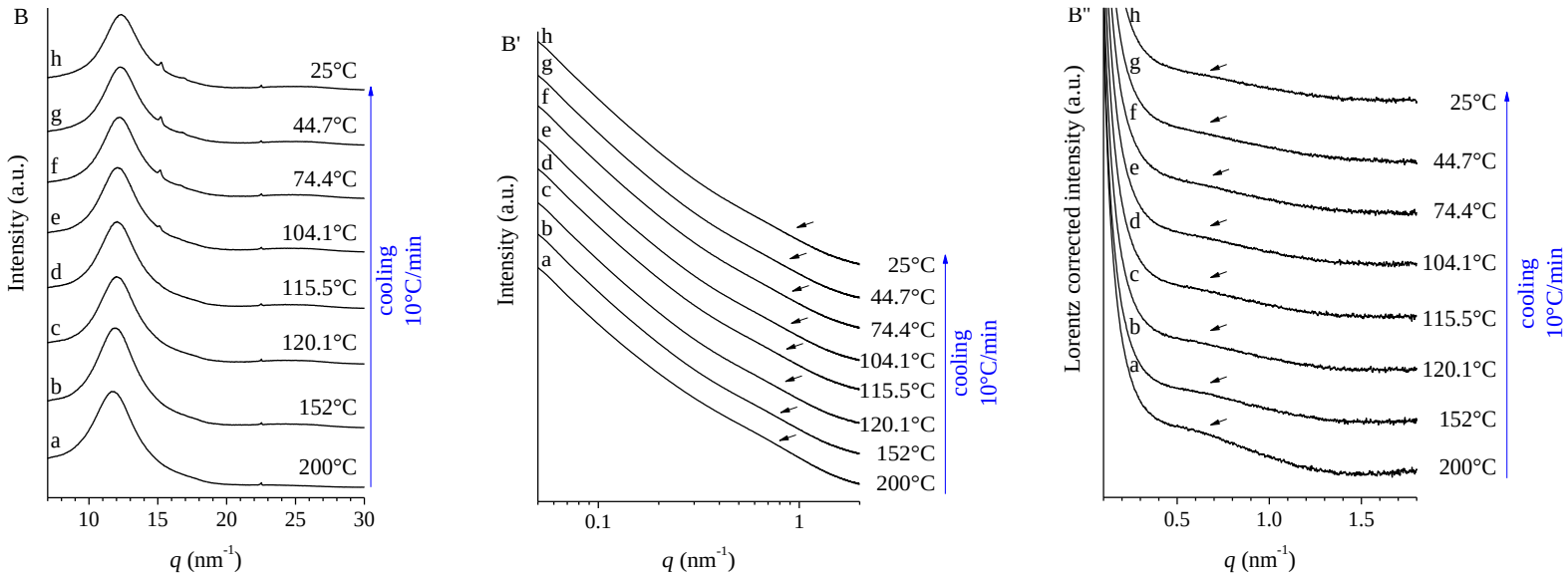
B
Intensity (a.u.)
h
g
f
e
d
c
b
a
25°C
44.7°C
74.4°C
104.1°C
115.5°C
120.1°C
152°C
200°C
cooling
10°C/min
10
15
20
25
30
q (nm-1)
B'
Intensity (a.u.)
0.1
1
q (nm-1)
B''
Lorentz corrected intensity (a.u.)
0.5
1.0
1.5
q (nm-1)

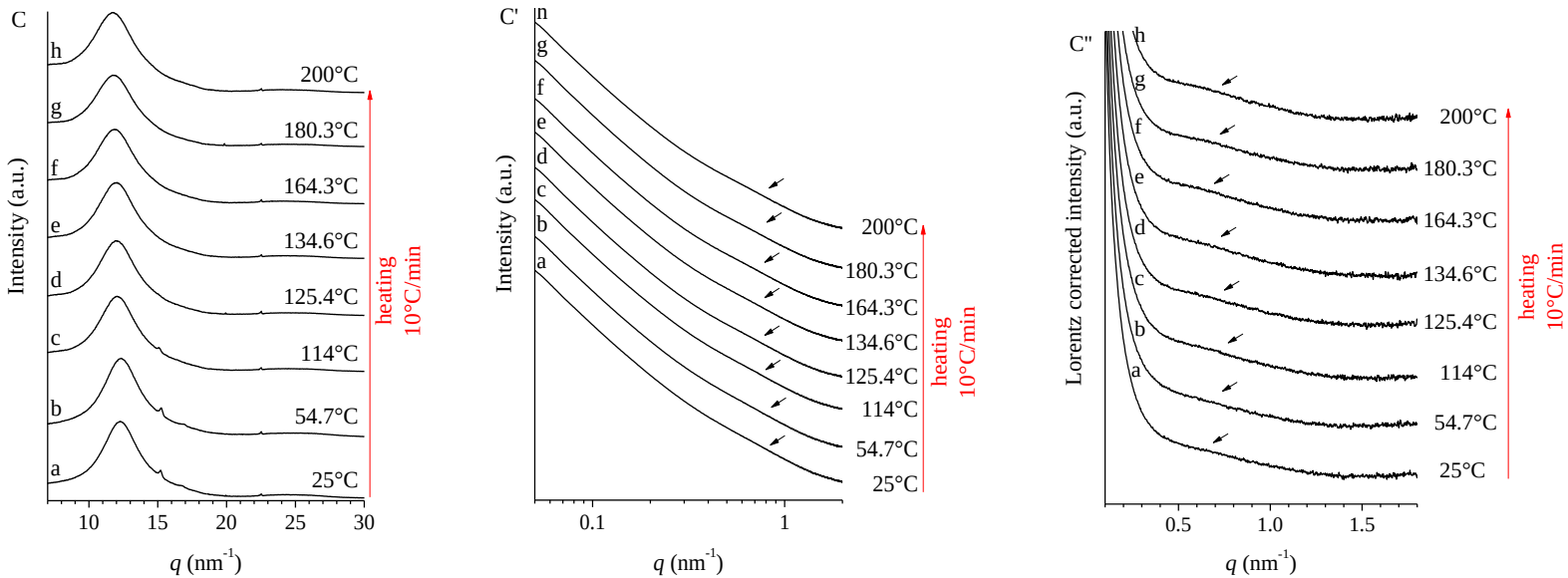

Figure 3.5 WAXS (A, B, C), SAXS (A', B', C') and Lorentz corrected (A'', B'', C'') intensity profiles of the E/N copolymer DSC158 synthesized with B1+A3 in presence of the CTA (Zn/Zr=50), recorded at the indicated temperatures during heating at a rate of 30°C/min (A, A', A''), cooling at a rate of 10°C/min (B, B', B'') and successive heating at a rate of 10°C/min (C, C', C'').

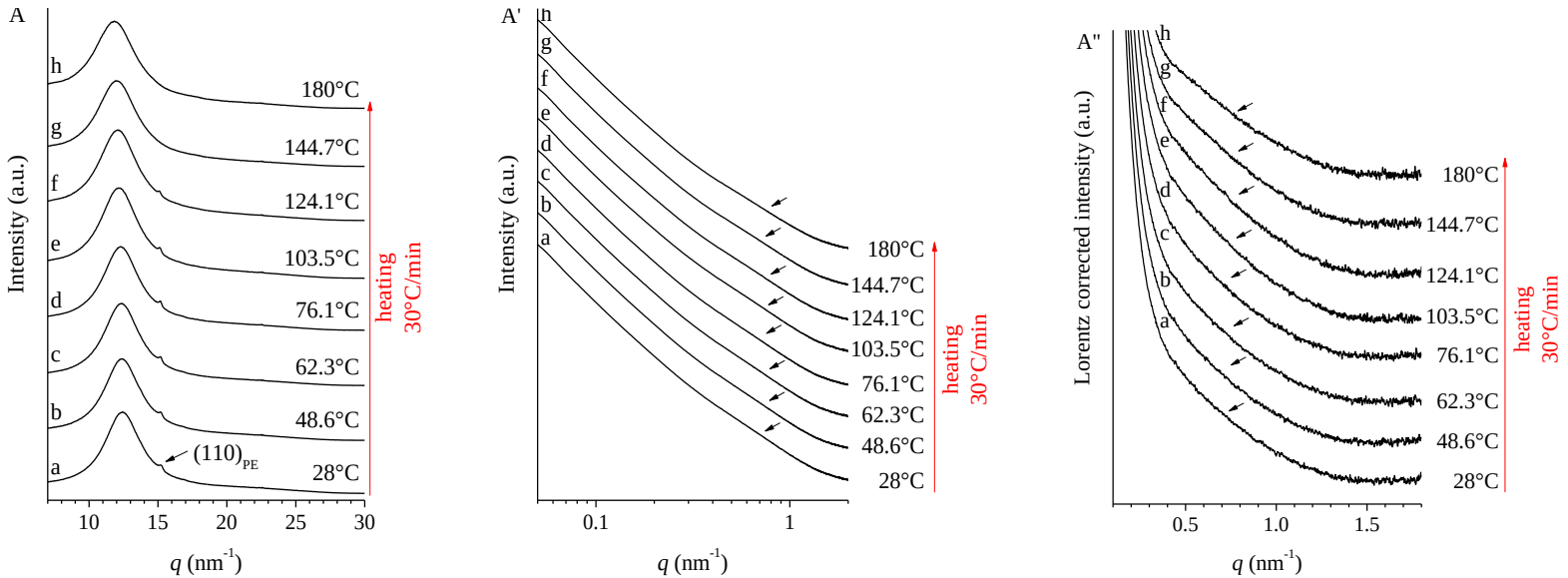
A
Intensity (a.u.)
h
g
f
e
d
c
b
a
180°C
144.7°C
124.1°C
103.5°C
76.1°C
62.3°C
48.6°C
28°C
(110)PE
heating
30°C/min
10
15
20
25
30
q (nm-1)
A'
Intensity (a.u.)
0.1
1
q (nm-1)
A"
Lorentz corrected intensity (a.u.)
0.5
1.0
1.5
q (nm-1)

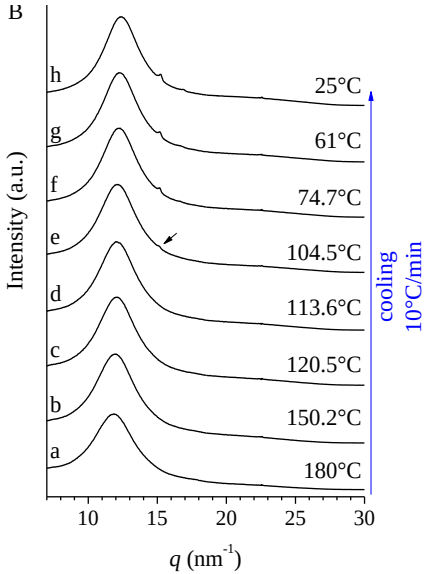
B
Intensity (a.u.)
h
g
f
e
d
c
b
a
25°C
61°C
74.7°C
104.5°C
113.6°C
120.5°C
150.2°C
180°C
cooling
10°C/min
10
15
20
25
30
q (nm-1)

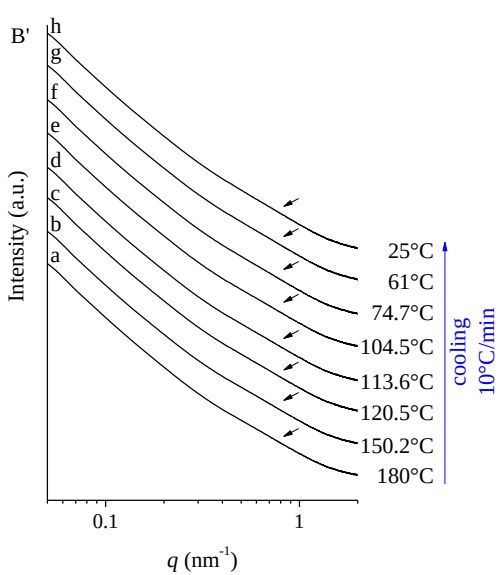
B'
Intensity (a.u.)
h
g
f
e
d
c
b
a
25°C
61°C
74.7°C
104.5°C
113.6°C
120.5°C
150.2°C
180°C
cooling
10°C/min
0.1
1
q (nm-1)

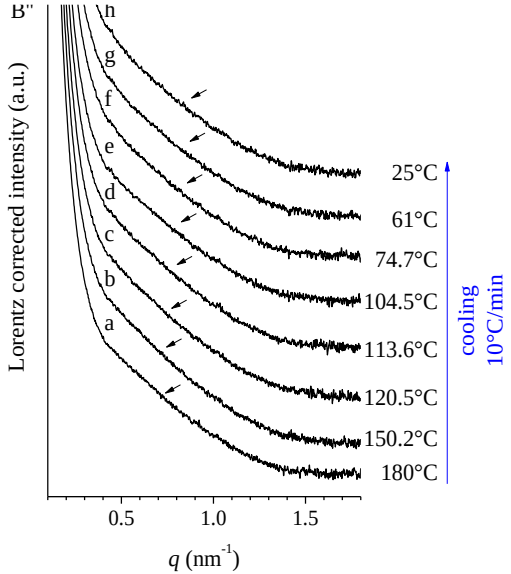
B''
Lorentz corrected intensity (a.u.)
h
g
f
e
d
c
b
a
25°C
61°C
74.7°C
104.5°C
113.6°C
120.5°C
150.2°C
180°C
cooling
10°C/min
0.5
1.0
1.5
q (nm-1)

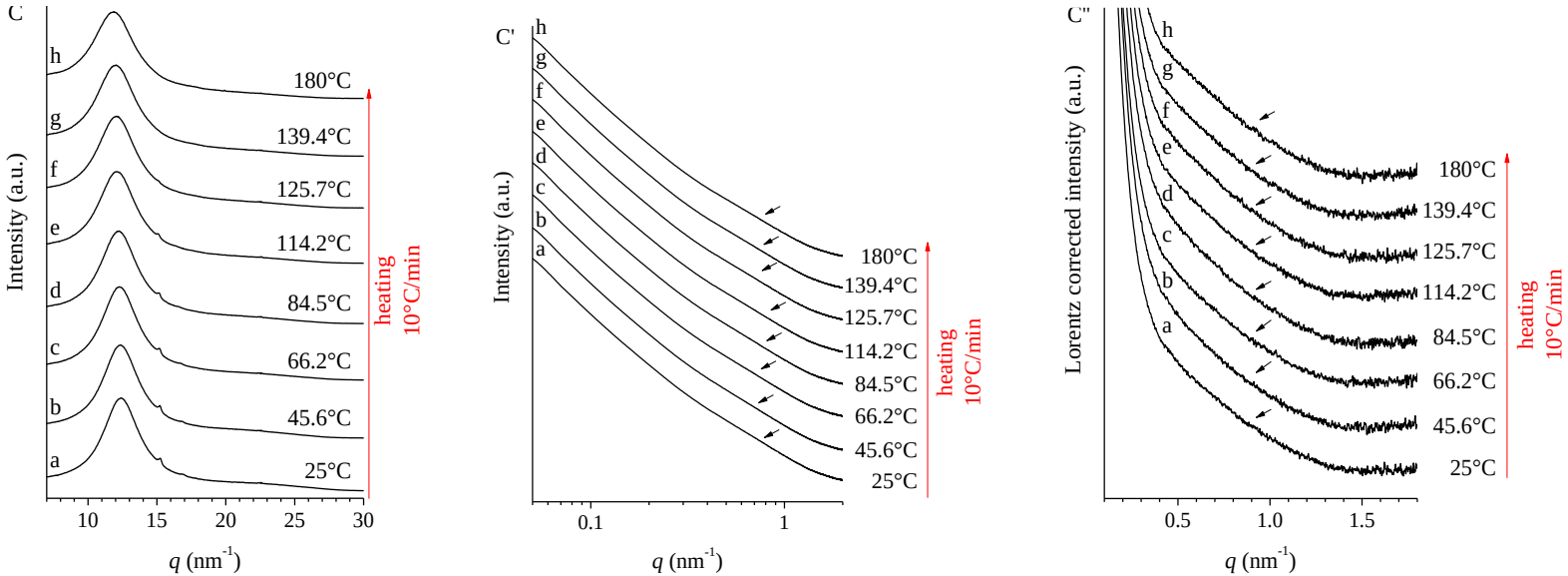

Figure 3.6 WAXS (A, B, C), SAXS (A', B', C') and Lorentz corrected (A'', B'', C'') intensity profiles of the E/N copolymer DSC159 synthesized with catalysts B1+A3 in presence of the CTA (Zn/Zr=99), recorded at the indicated temperatures during heating at a rate of 30°C/min (A, A', A''), cooling at a rate of 10°C/min (B, B', B'') and successive heating at a rate of 10°C/min (C, C', C'').

The WAXS/SAXS and the Lorentz corrected intensity profiles of the sample DSC153 synthesized with the catalyst B1 in presence of the CTA agent (Zn/Zr=198) are shown in Figure 3.7. The WAXS profiles recorded during the heating at a rate of 30°C/min (Figure 3.7 A) display the $(110)_{PE}$ and $(200)_{PE}$ reflections of PE in the orthorhombic form for $T \leq 131$°C (curves a-f). At higher temperatures the sample is completely melted (curves g-h) and only an amorphous halo centered at $2\theta=12°$ with a shoulder at $2\theta=15.5°$ is present. The WAXS profiles recorded during the cooling at a rate of 10°C/min (Figure 3.7 B) show that PE crystallinity starts developing at $T \approx 114$°C (curve d). The intensity of PE reflections increases by further cooling the sample down to 25°C (curves e-h). The WAXS profiles recorded during the successive heating at a rate of 10°C/min (Figure 3.7 C) reveal that the PE crystals melt at $T \approx 126$°C (curves a-f).

Also in this case, the SAXS profiles recorded during the thermal treatment (Figure 3.7 A', B' and C') show a broad correlation peak, even after Lorentz intensity correction (A'', B'', C''), extending from ≈0.6 to 0.9nm^{-1} in the whole temperature range 25-180°C, similarly to the samples DSC158 and DSC159 synthesized with both B1 and A3 catalysts. However, in the case of these samples, the correlation peak has been attributed to the presence of blocks synthesized by the two different catalysts, having different N contents and different microstructures resulting in an electron density contrast. In the case of the sample DSC153 synthesized with the sole catalyst B1 the correlation peak cannot be attributed to the presence of different blocks with different composition. Nevertheless, the electron density inhomogeneities in the sample may have the same origin, namely the contrast between ethylene-rich and norbornene-rich sequences along the chain. In fact, as previously stated in section 3.2, the copolymerization of E and N with catalyst B1 does not result in a completely random distribution of the two monomers, and rather long -EEEE- sequences along the polymer chains are formed, which, in fact are able to crystallize. Also in this case, the size of the different domains varies in the range 7-10.5nm.

For comparison, the WAXS/SAXS and the Lorentz corrected intensity profiles of the sample DSC157 synthesized with the catalyst A3 in presence of the CTA agent (Zn/Zr=396) are also shown in Figure 3.8. The WAXS profiles recorded during the thermal treatment of the sample show that the sample is amorphous in the whole temperature range from 25°C to 180°C (Figure 3.8 A, B and C). The corresponding SAXS profiles (Figure 3.8 A', B'

and C') and the Lorentz corrected intensity profiles (Figure 3.8 A'', B'' and C'') do not show any correlation peak thus indicating that in this sample no electron density contrast is present. In fact, the catalyst A3 tends to synthesize copolymers with a uniform distribution of E and N units, resulting in amorphous polymer chains.

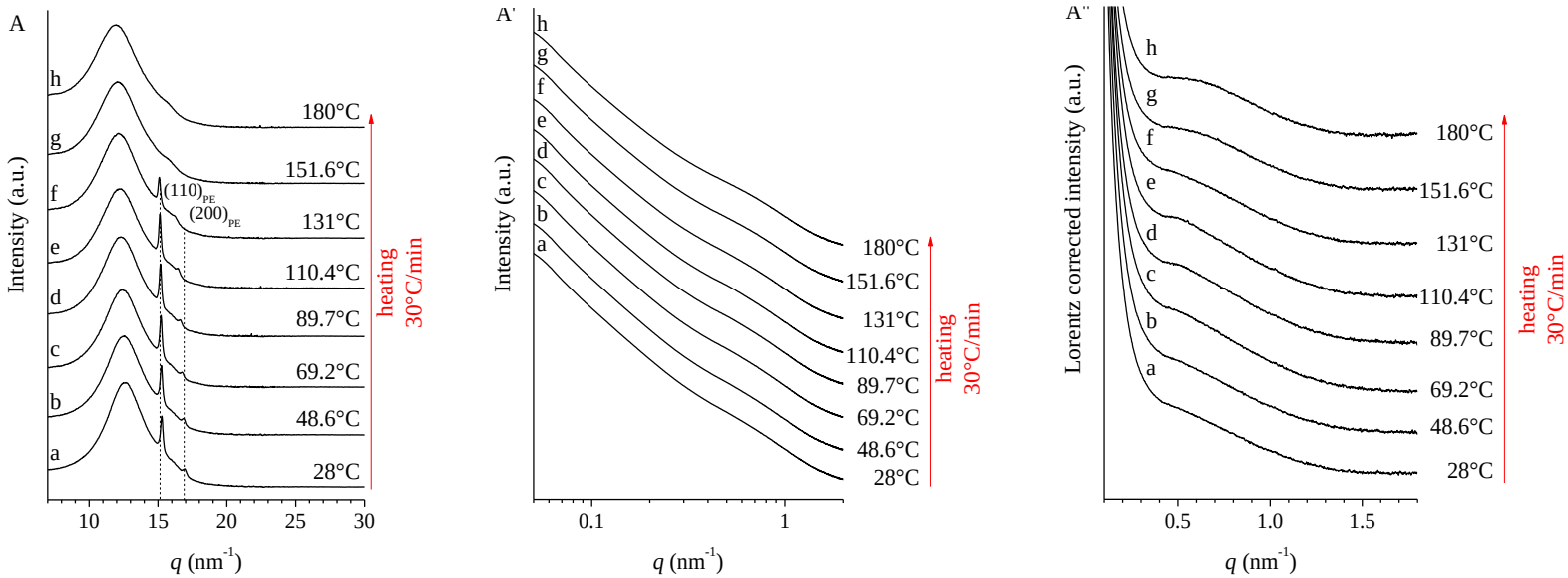
A
Intensity (a.u.)
h
g
f
e
d
c
b
a
180°C
151.6°C
131°C
110.4°C
89.7°C
69.2°C
48.6°C
28°C
(110)PE
(200)PE
heating
30°C/min
10
15
20
25
30
q (nm-1)
A'
Intensity (a.u.)
0.1
1
q (nm-1)
A''
Lorentz corrected intensity (a.u.)
0.5
1.0
1.5
q (nm-1)

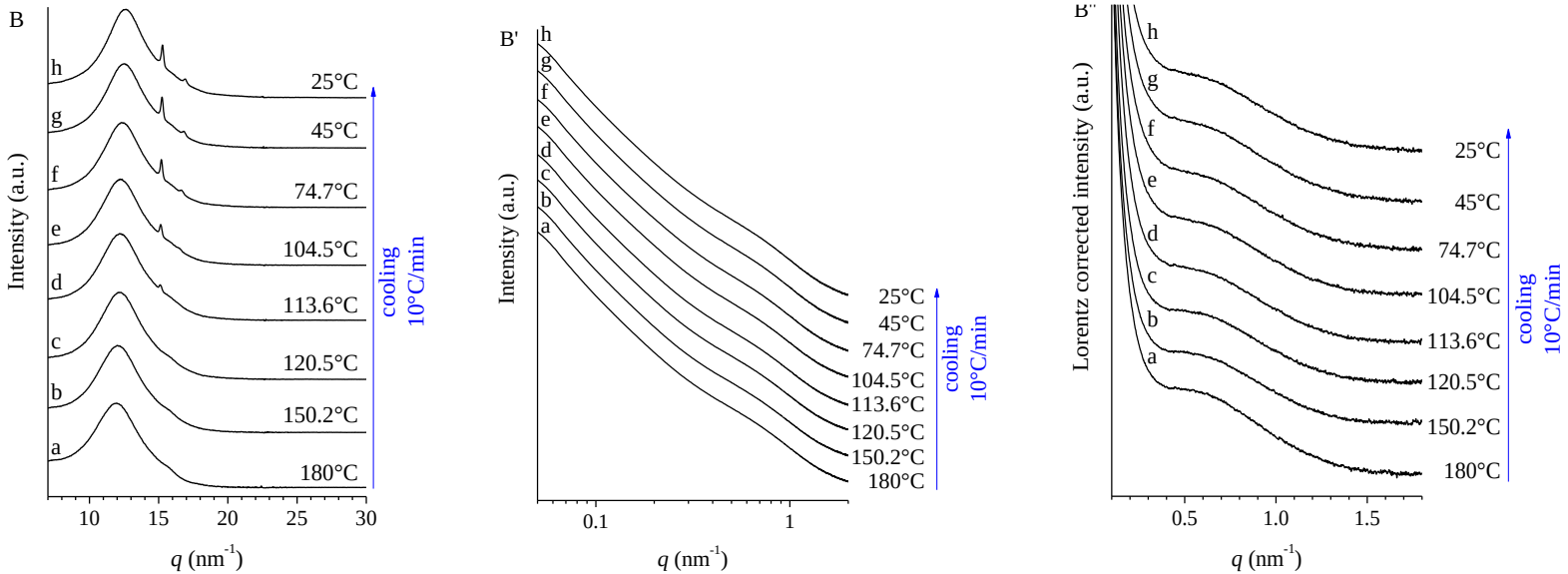
B
Intensity (a.u.)
h
g
f
e
d
c
b
a
25°C
45°C
74.7°C
104.5°C
113.6°C
120.5°C
150.2°C
180°C
cooling
10°C/min
10
15
20
25
30
q (nm-1)
B'
Intensity (a.u.)
0.1
1
q (nm-1)
B''
Lorentz corrected intensity (a.u.)
0.5
1.0
1.5
q (nm-1)

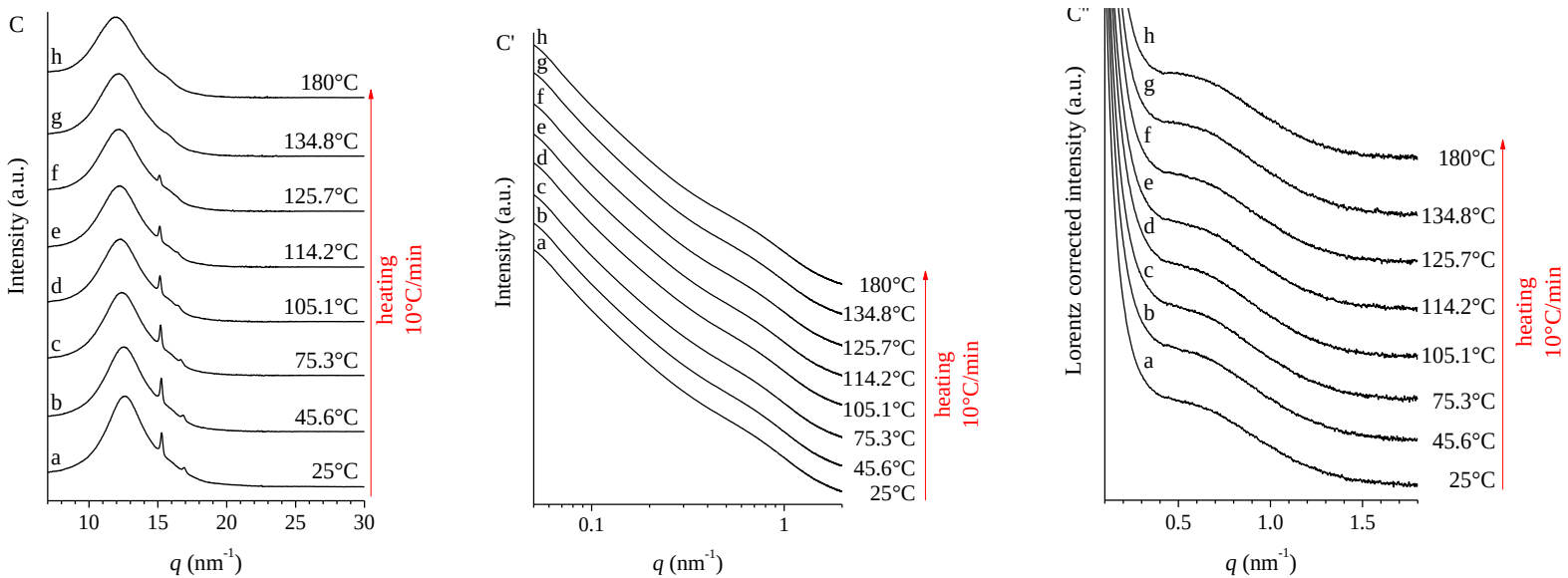

Figure 3.7 WAXS (A, B, C), SAXS (A', B', C') and Lorentz corrected (A'', B'', C'') intensity profiles of the E/N copolymer DSC153 synthesized with catalyst B1 in presence of the CTA (Zn/Zr=198), recorded at the indicated temperatures during heating at a rate of 30°C/min (A, A', A''), cooling at a rate of 10°C/min (B, B', B'') and successive heating at a rate of 10°C/min (C, C', C'').

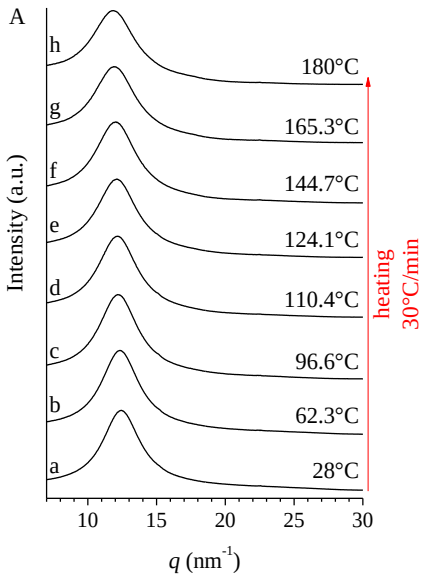
A
Intensity (a.u.)
h
g
f
e
d
c
b
a
180°C
165.3°C
144.7°C
124.1°C
110.4°C
96.6°C
62.3°C
28°C
heating
30°C/min
10
15
20
25
30
q (nm-1)

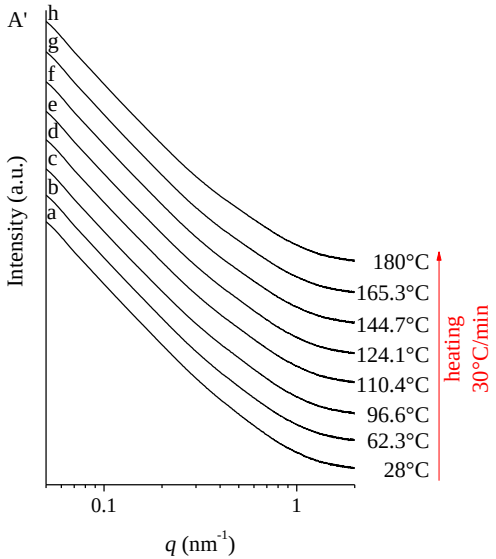
A'
Intensity (a.u.)
h
g
f
e
d
c
b
a
180°C
165.3°C
144.7°C
124.1°C
110.4°C
96.6°C
62.3°C
28°C
heating
30°C/min
0.1
1
q (nm-1)

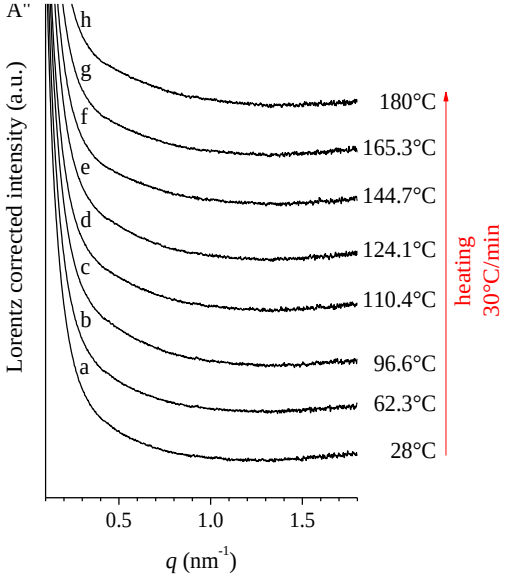
A''
Lorentz corrected intensity (a.u.)
h
g
f
e
d
c
b
a
180°C
165.3°C
144.7°C
124.1°C
110.4°C
96.6°C
62.3°C
28°C
heating
30°C/min
0.5
1.0
1.5
q (nm-1)

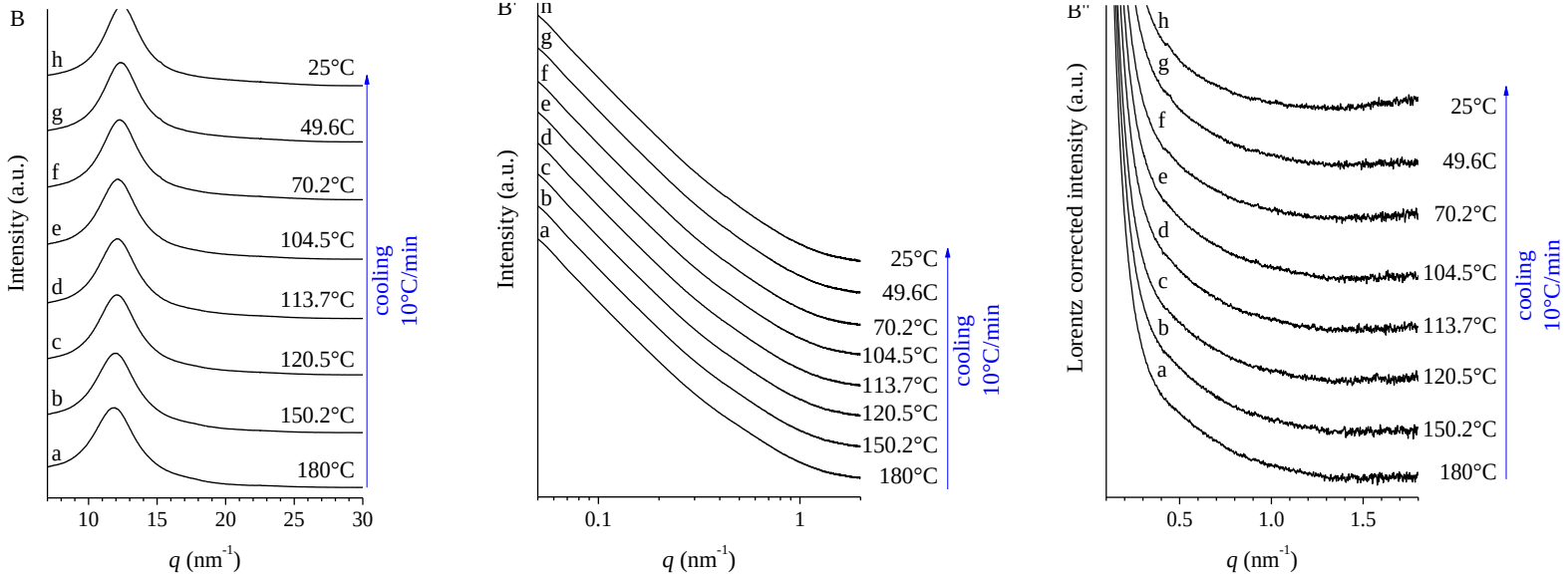
B
Intensity (a.u.)
h
g
f
e
d
c
b
a
25°C
49.6C
70.2°C
104.5°C
113.7°C
120.5°C
150.2°C
180°C
cooling
10°C/min
10
15
20
25
30
q (nm-1)
B'
0.1
1
B''
Lorentz corrected intensity (a.u.)
0.5
1.0
1.5

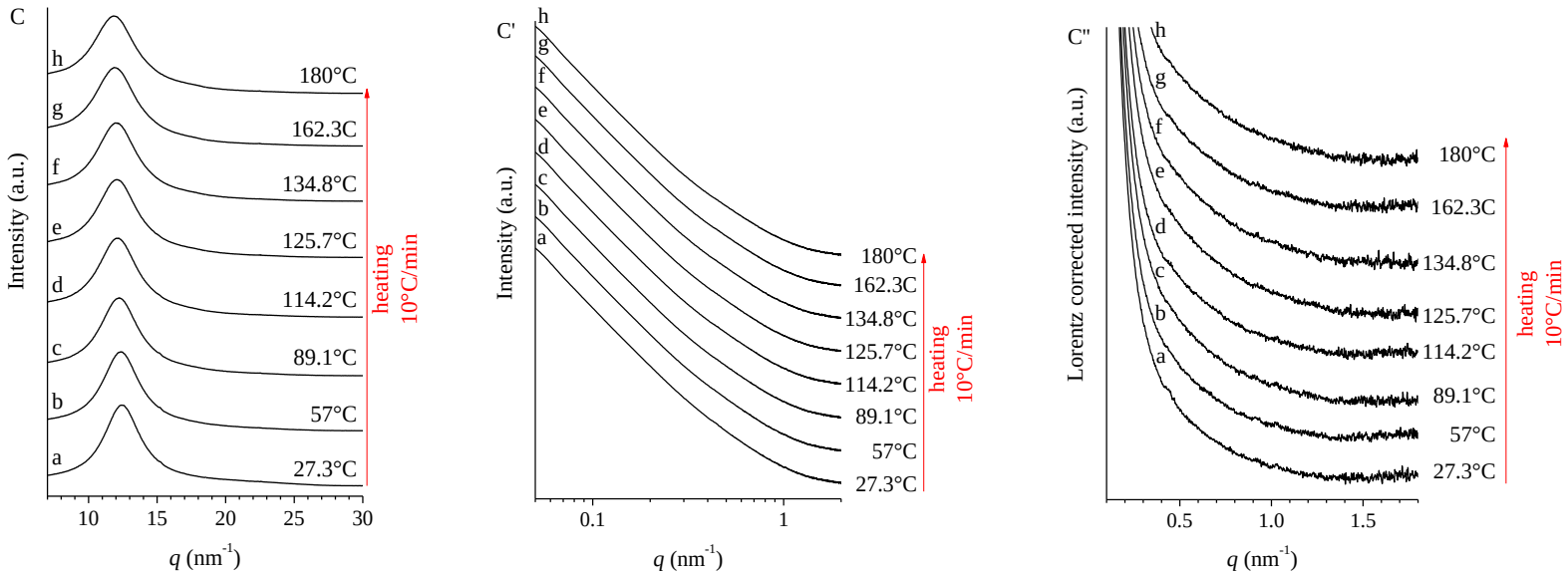

Figure 3.8 WAXS (A, B, C), SAXS (A', B', C') and Lorentz corrected (A'', B'', C'') intensity profiles of the E/N copolymer DSC157 synthesized with catalyst A3 (Zn/Zr=396), recorded at the indicated temperatures during heating at a rate of 30°C/min (A, A', A''), cooling at a rate of 10°C/min (B, B', B'') and successive heating at a rate of 10°C/min (C, C', C'').

The present results do not clearly indicate that the samples obtained with A3+B1 in presence of the CTA are truly multi-block copolymers. Indeed, the sample produced with the sole catalyst B1 already is characterized by heterogeneities at the same nanometer length scale as the copolymers produced in presence of £ and B1 in presence of the CSA. Therefore, the effect of CTA in presence of the *ansa*-metallocene catalysts B1+A3 in the copolymerization of E and N to multi-block architectures remains an open question.

CONCLUSIONS

In this work a structural and morphological characterization at different length scales, of different classes of polyolefin-based semicrystalline block-copolymers (BCPs) obtained through metallorganic catalysis have been performed. The physical properties of these BCPS have been also analyzed.

In chapter 1, two different classes of polyethylene-based (PE) semicrystalline BCPs are considered. In the first class the PE crystalline block is linked to an amorphous poly(1,5-hexadiene) (PHD) block (PE-*b*-PHD). Samples with different relative length of the blocks have been synthesized, by using a fluorinated bis(phenoxyimine) Ti complex. In particular, the mass fraction of the PE block (w_{PE}) varies in the range 0.27-0.79. The structural characterization reveals that these samples crystallize in the orthorhombic form of PE, with a crystallinity index (x_c) decreasing with decreasing w_{PE}, but after normalization of x_c for w_{PE}, the crystallinity index becomes more similar among the different samples. The DSC thermal characterization shows that the melting of the PE crystals occurs in the temperature range 100-120°C, slightly lower than the typical melting temperature of high density PE (HDPE) ($T_m \approx 130$°C), because of the presence of 1,5-hexadiene units within the PE block. The crystallization temperature of the PE crystals varies in the range 84-97°C. The glass transition temperature of the PE-*b*-PHD BCPs, which is due to the amorphous PHD block, occurs at -19°C.

The SAXS/WAXS analysis as a function of temperature reveals that when PE-*b*-PHD BCPs are melted, a non-homogeneous phase is obtained because of the scarce chemical affinity of the two blocks and the high molecular mass of the BCPs. This phase-separated melt is still present at high temperatures, i.e. 280°C, with correlation distances of the different domains varying in the range 28-60nm depending on the relative block length of the two blocks. These data also indicate that the crystallization of PE occurs from a microphase separated melt. The values of the average periodicity of the PE lamellar domains vary in the range 16-20 nm. By calculating the one-dimensional normalized (self-) correlation function of electron density fluctuations, further information about the structural organization in the crystalline PE block have been obtained, namely the thickness of the amorphous (l_a) and crystalline (l_c) layers of the stacked arrays of lamellar PE crystals. The values of l_c vary in the range 3.6–7nm, those of l_a in the range of

10.7-14.2nm. In particular, it has been observed that the higher the molecular mass of PE blocks, the shorter the thickness of lamellar crystals. We speculate that this is due to the different morphologies occurring in the melt, and therefore to the different geometries of the crystallisable PE domains.

The mechanical characterization performed on the PE-*b*-PHD samples shows extremely interesting results: PE-*b*-PHD BCPs span different mechanical behaviors depending on the relative block length of PE and PHD blocks. Therefore, by changing the sole mass fraction of one of the two blocks, it is possible to design materials with tailored properties ranging from those of stiff plastomers (similar to PE) at high w_{PE} values, to those of materials with high flexibility and ductility with partial elastomeric properties at lower w_{PE} values. In addition, it is worth mentioning that regardless of the mechanical properties, these BCPs also show a good thermal resistance due to the presence of the crystalline PE block having a melting temperature of ≈110°C.

The study of the stress-induced structural rearrangements of the PE-*b*-PHD BCPs reveals that upon deformation, gradual orientation of PE crystals in the stretching direction is obtained, and that the longer the relative length of PE blocks, the higher the degree of orientation achieved by PE crystals. In fact, the increase of the relative length of PE blocks implies the decrease of the volume fraction of the PHD amorphous blocks which, indeed, perform a damping effect, transmitting the stress to the crystals less efficiently.

In the second class of PE-based BCPs the PE crystalline block is linked to an amorphous block made of a random copolymer of ethylene and vinyl cyclohexene (P(E-*co*-VCH)). One PE-*b*-P(E-*co*-VCH) BCP sample with a mass fraction of the PE block equal to 0.59 has been synthesized with a C_s-symmetric pyridylamidohafnium dimethyl complex.

The structural characterization shows that the sample crystallizes in the orthorhombic form of PE. The thermal characterization shows that the PE crystals melt at T=133°C and crystallize at T=120°C. It is worth mentioning that in this case, according to the adopted synthetic procedure, no VCH units are present in the PE block, therefore the PE block shows a high melting temperature, comparable to that of HDPE. The SAXS/WAXS analysis as a function of temperature shows that when PE-*b*-P(E-*co*-VCH) BCP is melted, no inhomogeneities are observed, thus indicating that either phase separation does not occur, or that the periodicity of the phase separated domains of PE and P(E-*co*-VCH) incompatible blocks occurs at higher length scales than

those accessible in our measurements, i.e. >90nm. The analysis also shows that the lamellar crystals of PE of characteristic size equal to ≈8 nm are organized in stacks with a periodicity of ≈60nm, separated by amorphous domains of thickness equal to ≈56 nm.

The mechanical properties of the PE-*b*-P(E-*co*-VCH) BCP have been compared to those of an amorphous P(E-*co*-VCH) random copolymer synthesized with the same catalyst and in the same reaction conditions as the P(E-*co*-VCH) block in the PE-*b*-P(E-*co*-VCH) BCP. The random copolymer shows the typical behavior of an amorphous, rubbery material with low value of the Young's modulus, no yield point and high deformation at break. The mechanical characterization of the PE-*b*-P(E-*co*-VCH) BCP shows that by linking the crystalline PE block to the amorphous P(E-*co*-VCH) block, a rather rigid material is obtained, with higher value of the Young's modulus, lower value of the deformation at break and high strain hardening.

In chapter 2, two classes of iPP-based semicrystalline BCPs have been studied. In the first class the iPP block is linked to an amorphous block made of a random copolymer of propylene and vinyl cyclohexene (P(P-*co*-VCH)), while in the second class the iPP block is linked to an amorphous block made of a random copolymer of propylene and 1-octadecene (P-*co*-C18). Samples of iPP-*b*-P(P-*co*-VCH) and iPP-*b*-P(P-*co*-C18) BCPs differing in the relative lengths of the blocks have been synthesized with the same C_s-symmetric pyridylamidohafnium dimethyl complex also used for the synthesis of the PE-*b*-P(E-*co*-VCH) BCP. The structural and thermal characterization of these samples reveal that both classes of BCPs mainly crystallize in the α form of iPP, with melting and crystallization temperatures of the iPP blocks of 133°C and ≈95°C, respectively. In the case of iPP-*b*-P(P-*co*-C18) BCPs, additional PE-like crystallinity is observed when cooling the samples below room temperature, due to the crystallization of the side chains of the C18 units in the (P-*co*-C18) block. SAXS/WAXS analysis as a function of temperature reveals that for both the iPP-based BCPs classes, either a homogeneous melt is obtained or a possible phase separation due to chemical incompatibility between the two different blocks occurs at higher length scales than those accessible in our measurements. The crystallization of the iPP block from the melt results in lamellar stacks having a periodicity of ≈12-14nm, comparable to what observed for a iPP homopolymer synthesized with the same catalyst and in the same reaction conditions as the iPP-based BCPs. Moreover, for the

iPP-*b*-P(P-*co*-VCH) BCPs, a lamellar thickness of ≈11nm and an amorphous layer thickness of ≈3nm have also been evaluated by calculating the self-correlation function from the SAXS data recorded at 25°C. For the iPP-*b*-P(P-*co*-C18) BCPs, low temperature SAXS analysis reveals that the PE-like crystallites formed by the C18 units arrange in crystalline domains having dimensions of ≈5nm.

The mechanical behavior of the iPP-based BCPs has been compared to that of the iPP homopolymer. In the case of the iPP-*b*-P(P-*co*-VCH) BCPs, with values of w_{iPP} equal to 0.67 and 0.78, lower ductility, but similar values of the stress at the yield and break point with respect to iPP homopolymer are observed. In the case of the iPP-*b*-P(P-*co*-C18) BCPs with values of w_{iPP} equal to 0.31, 0.44, similar ductility, but lower values of the stress at yield and break point are observed with respect to the iPP homopolymer. These data indicate that when an amorphous block is linked to the crystalline iPP block, the mechanical behavior is changed. With high values of w_{iPP} the mechanical resistance due to the iPP block prevails, but a decrease of the ductility is observed, while at lower w_{iPP}, high ductility is achieved at the expense of the mechanical stress and rigidity.

The study of the stress-induced transformation reveals that while in the iPP homopolymer a complete transformation of the α form crystals into the mesophase occurs, in the case of the iPP-*b*-P(P-*co*-VCH) and iPP-*b*-P(P-*co*-C18) BCPs, only partial transformation of the α form crystals into mesophase occurs. As in the case of PE-*b*-PHD BCPs, this behavior is due to the presence of an amorphous random copolymer block, linked to the crystalline block, that performs a damping effect, so that the stress level experienced by amorphous tie chains is transmitted to the crystals less efficiently.

In the case of iPP-*b*-P(P-*co*-C18) BCPs, stretching experiments performed at low temperature while recording X-ray diffraction data reveal that the drawing of the samples induces the orientation of the PE-like crystallites formed by the C18 units with their chain axes perpendicular to the drawing direction. However, above a threshold value of deformation, which depends on the concentration of the C18 units in the P(P-*co*-C18) block, the PE-crystals are destroyed by effect of tension, probably because the mean distance between the side chains increases to an extent that they are not able to organize in PE-like crystallites anymore.

The ability of iPP-based BCPs to undergo the same structural change observed for iPP homopolymer when rapidly cooled (quenching) from the

melt, has been studied. For both iPP-based BCPs classes, the quenching of the samples from the melt down to 0°C induces the crystallization of the iPP block into the mesomorphic form, thus indicating that the presence of the amorphous block does not influences the properties of the iPP block.

The mechanical behavior of the iPP-*b*-P(P-*co*-C18) BCPs crystallized in iPP mesophase is similar in terms of ductility to that of the same samples crystallized in α form, but strain hardening is observed, thus leading to higher values of the stress at break. This mechanical behavior is probably dictated by the different morphology developing in the samples quenched from the melt, which may somehow influence the mechanisms of deformation and fracture. In fact, the study of the morphology by polarized optical microscopy (POM) shows that the all the samples slowly crystallized from the melt are characterized by the presence of birefringent lamellar aggregates of not well defined shape, and dimensions 5-10μm, which are relative to the iPP block crystallized in α form. When the iPP block crystallizes in the mesomorphic form, a different morphology is observed. POM images do not show birefringence. However, AFM analysis reveals a nodular morphology with aggregates having dimensions ≈90-100nm, resembling that of the iPP homopolymer, in the case of samples with high values of w_{iPP}. For BCP samples with low w_{iPP} values the nodular morphology is not observed. This may be due to the presence of a high amount of the amorphous block that prevents the formation of nodular aggregates. We speculate that for BCPS with low w_{iPP}. values, isolated mesomorphic aggregates are formed, which are not well discernible, by AFM analysis, from the surrounding amorphous matrix in which they are embedded.

The interest towards PE-based and iPP-based BCPs relies on the possibility of coupling crystalline blocks having high melting temperatures with amorphous blocks, to yield peculiar properties and therefore materials suitable for tailored application. For instance, the PE-*b*-PHD BCPs wherein the PE crystalline block is linked to a rubbery PHD block are interesting systems in which the final mechanical properties may be finely tuned by varying the relative block length of the two blocks, while preserving the high melting temperature due to the PE block. Moreover, since the polymerization of 1,5-hexadiene leads to the formation of vinyl groups as side chains, functional BCPs may be obtained. In this way, materials for advanced applications can be obtained, as a result of the combination of the good mechanical properties provided by the main chain of the BCP and the specific

properties provided by the functional side chains. Similar interest relies on the PE-*b*-P(E-*co*-VCH) BCPs and of the iPP-P(P-*co*-VCH) BCPs, because of the possibility to have high melting temperature functional thermoplastic materials. In fact, the VCH units in the amorphous blocks bear pendant reactive moieties that provide easy access to a wide range of functionalities. Moreover, in the case of the iPP-based BCPs, further interest arises from the polymorphism of iPP. In fact, by choosing the proper crystallization conditions, it is possible to choose the type of crystallinity developing in the material and hence tailor its final properties.
In the case of the iPP-*b*-P(P-*co*-C18) BCPs the interest relies on the possibility of combining the peculiar structural and thermal properties of the iPP and P(P-*co*-C18) blocks: on one hand the high melting temperature iPP block that can possibly crystallize in different crystalline forms depending on the thermal processing, on the other hand the P(P-*co*-C18) block that whilst amorphous at room temperature, can develop crystallinity when cooled below room temperature due to the crystallization of the side chains of the 1-octadecene (C18) units. Therefore, the linking of the two different blocks and the selection of the proper crystallization conditions allows tailoring the properties of this new class of materials.

In chapter 3, the study of the structural and thermal properties of multi-block ethylene-norbornene (E/N) semicrystalline multi-block copolymers (MBCPs) has been performed. The E/N MBCPs were synthesized via chain shuttling polymerization (CSP), by using two *ansa*-metallocene Zr-based catalysts, labelled B1 and A3, having different selectivity toward norbornene incorporation, and diethyl zinc ($Zn(Et)_2$) as chain transfer agent (CTA). The structure and properties of the E/N multi-block copolymers are compared with those of reference samples, obtained by copolymerization of E and N with the sole catalyst A3 and the sole catalyst B1. MBCPs and the reference samples were prepared by fixing the N/E feed ratio equal to 1.3, and using different concentrations of CTA. The copolymers prepared with the sole catalyst A3 are amorphous, and include a major amount of N units. The copolymers prepared with the sole catalyst B1, include a lower content of N units, and show a small degree of crystallinity, due to presence of long ethylene sequences melting at ≈120°C, and crystallizing from the melt at ≈115°C. Also the E/N MBCPs show a slight crystallinity due to the presence of long ethylene sequences, with melting and crystallization temperature similar to those of the

reference samples from catalyst B1, and glass transition temperatures intermediate between those of the reference samples from A3 and B1 catalysts. SAXS/WAXS analysis as a function of temperature reveals that the E/N BCPs and the reference sample synthesized with the sole B1 catalyst, show heterogeneities in the melt due to the presence of different chain sequences having different N contents and different microstructures. The size of the different domains forming in the melt is in the range 7-10.5nm. On the contrary, the melt of the reference sample synthesized with the sole A3 catalyst is homogeneous, confirming the homogeneous distribution of E and N along the polymer chain. The present results do not clearly indicate that the samples obtained with A3+B1 in presence of the CTA are truly multi-block copolymers. Therefore, the effect of CTA in presence of the *ansa*-metallocene catalysts A3+B1 in the copolymerization of E and N to multi-block architectures remains an open question.

The interest towards this class of materials obtained through CSP strategy relies on the possibility to obtain multi-blocks copolymers where different microstructures are bonded together in an alternate sequence to form a polymer chain. The advantage of obtaining such molecular architectures is that the different properties of the diverse microstructural blocks are combined in a single polymer chain showing hybrid properties. In fact, in this particular case of ethylene/norbornene copolymers, CSP may allow to obtain a component rich in ethylene and a component rich in norbornene, bonded in an alternate multi-block sequence resulting in polymers showing, at the same time, elastic properties and rigidity typical of P(E-*co*-N) copolymers.

APPENDIX 1

1. Composition of poly(1,5-hexadiene) homopolymer and of polyethylene-*b*-poly(1,5-hexadiene) di-block copolymers

It is well known that the polymerization of 1,5-hexadiene by the fluorinated bis(phenoxyimine) Ti catalyst results in a copolymer containing not only the expected comonomeric units of methylene-1,3-cyclopentane (MCP) but also 3-vinyl tetramethylene (VTM) units.[23]
The composition of the poly(1,5-hexadiene) homopolymer (PHD), in terms of MCP and VTM units, has been determined by ^{1}H-NMR analysis.

The spectrum obtained for the PHD homopolymer is shown in Figure A1.1. The amount of the MCP and VTM units has been determined by using Eq. I to IV: Eq. I sets the value of a proton belonging to a VTM unit, similarly, Eq. 2 sets the value of a proton belonging to a MCP unit. In this last case, in order to define the value of a proton belonging to a MCP unit, it is necessary to subtract the contribute of the aliphatic protons of the VTM unit (i.e. 7 protons) from the signals counting all the aliphatic protons (0.7-2.2 ppm) and then divide it by the number of protons in the MCP unit (i.e. 10). The concentration of VTM units and MCP units are calculated as mol % by using Eq. III and Eq. IV respectively.

Equations

(Eq. I) $$H_{VTM} = b$$

(Eq. II) $$H_{MCP} = \frac{(c+d_{1,2}+e_{1,2}+f_{1,2}+g+h_{1,2}+i+l_{1,2}+m_{1,2}+n_{1,2})-7H_{VTM}}{10}$$

(Eq. III) $$VTM\ (mol\%) = \frac{H_{VTM}}{H_{VTM}+H_{MCP}} \cdot 100$$

(Eq. IV) $$MCP\ (mol\%) = \frac{H_{MCP}}{H_{VTM}+H_{MCP}} \cdot 100$$

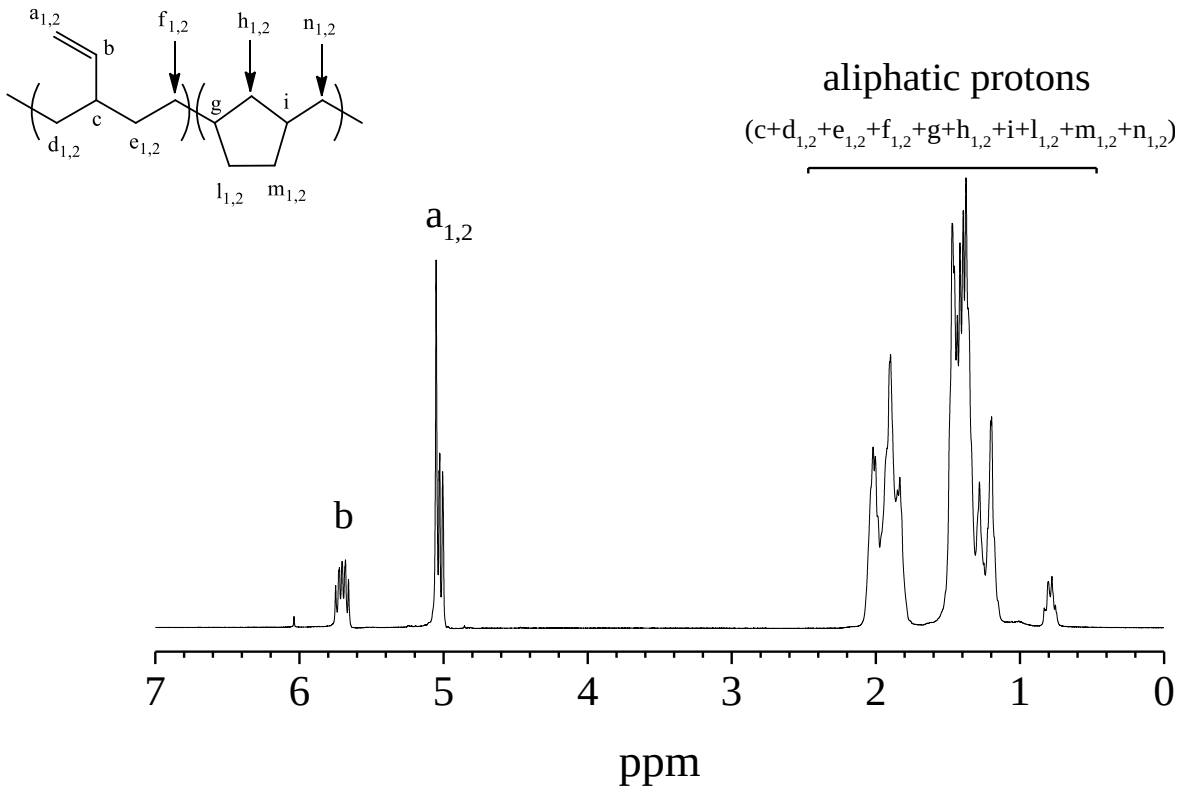

Figure A1.1 ^{1}H-NMR spectrum of the PHD homopolymer RDG-1-13.

The spectra obtained for all the PE-*b*-PHD BCPs, except for the RDG-1-29 (w_{PE}=0.44) sample, are shown in Figure A1.2-A1.5. The amount of the VTM units with respect to the overall BCP molecule has been determined by using Eq. V to Eq. VIII. As previously observed for the PHD homopolymer, Eq. V sets the value of a proton belonging to a VTM unit, Eq. 2 sets the overall value of all the protons belonging to ethylene (E) and MCP units; in fact, the contribution of the aliphatic protons of the VTM units has been subtracted from the signals counting all the aliphatic protons (0.7-2.2 ppm). The overall concentration of the E and MCP units (E+MCP) and of the VTM units is calculated as mol % by using Eq. VII and Eq. VIII respectively. The values of the concentration of the VTM units in the whole BCP molecule are reported in Table 1.1 and Table A1.1. It is worth noting that the concentration of the VTM units in the sole PHD blocks calculated from the molecular mass of the blocks and the concentration of the VTM units in the whole BCP chains is different that of the PHD sample RDG-1-13, synthesized with the same catalyst and in the same reaction conditions as the PE-*b*-PHD BCPs, equal to ≈33mol%. These differences are higher the higher the molecular mass of the PE blocks in the BCPs, and are due to the large relative errors (±20%) affecting the values of the molecular mass of the blocks.

Equations

(Eq. V) $$H_{VTM} = b$$

(Eq. VI) $$H_{TOT\,(E+MCP)} = \left(et_{1,2} + c + d_{1,2} + e_{1,2} + f_{1,2} + g + h_{1,2} + i + l_{1,2} + m_{1,2} + n_{1,2}\right) - 7H_{VTM}$$

(Eq. VII) $$E + MCP\ (mol\%) = \frac{H_{TOT\,(E+MCP)}}{H_{TOT\,(E+MCP)} + 7H_{VTM}} \cdot 100$$

(Eq. VIII) $$VTM\ (mol\%) = 100 - (E + MCP)$$

Table A1.1 Total molecular mass ($M_{n\ TOT}$), molecular mass of the PHD block ($M_{n\ PHD}$) and of the PE block ($M_{n\ PE}$), polydispersity index (M_w/M_n), mass fraction (w_{PHD}) and volume fraction (f_{PHD}) of the PHD block, mass fraction of the PE block (w_{PE}), concentration of the 3-vinyl tetramethylene units in the overall BPC (VTM $_{PE\text{-}b\text{-}PHD}$).

SAMPLE	M_n[a] $_{TOT}$ (Kg/mol)	M_n[a] $_{PHD}$ (Kg/mol)	M_n[b] $_{PE}$ (Kg/mol)	$\frac{M_w}{M_n}$[a]	w[c] $_{PHD}$	f[d] $_{PHD}$	w[c] $_{PE}$	VTM[e] (mol%)
RDG-1-13	78.4	-	-	1.34	1	1	0	-
RDG-1-26	146.4	106.7	39.7	1.53	0.73	0.74	0.27	16
RDG-1-20	175.7	113.4	62.3	1.33	0.64	0.66	0.36	18
RDG-1-29	203.5	114.3	89.2	1.29	0.56	0.58	0.44	-
RDG-1-36	232.6	68.8	163.8	1.29	0.30	0.31	0.70	10
RDG-1-15	466.4	97.6	368.8	1.45	0.21	0.22	0.79	3.9

a evaluated from GPC analysis; **b** calculated from $M_{n\ TOT}$ and $M_{n\ PHD}$ as $M_{n\ PE}=M_{n\ TOT}-M_{n\ PHD}$; **c** calculated as $M_{n\ PHD}/M_{n\ TOT}$; **d** calculated from the molecular masses $M_{n\ PHD}$ and $M_{n\ PE}$ and the densities of PHD (0.940 g/cm^3) and PE (0.996 g/cm^3) as $f_{PHD}=(M_{n\ PHD}/0.940)/((M_{n\ PHD}/0.940)+(M_{n\ PE}/0.996))$. The density of the PHD has been experimentally determined by flotation (see Appendix 3) using a PHD homopolymer synthesized with the same Ti-based catalyst used for the synthesis of the PE-*b*-PHD copolymers; the density of PE is the theoretical value for a sample having 100% crystallinity; **e** evaluated from ^{1}H-NMR as described above; in the case of the sample RDG-1-13, it indicates the amount of VTM units in PHD homopolymer, while in the case of the BCPs samples (from RDG-1-26 to RDG-1-15) it indicates the amount of VTM in the whole BCP molecule.

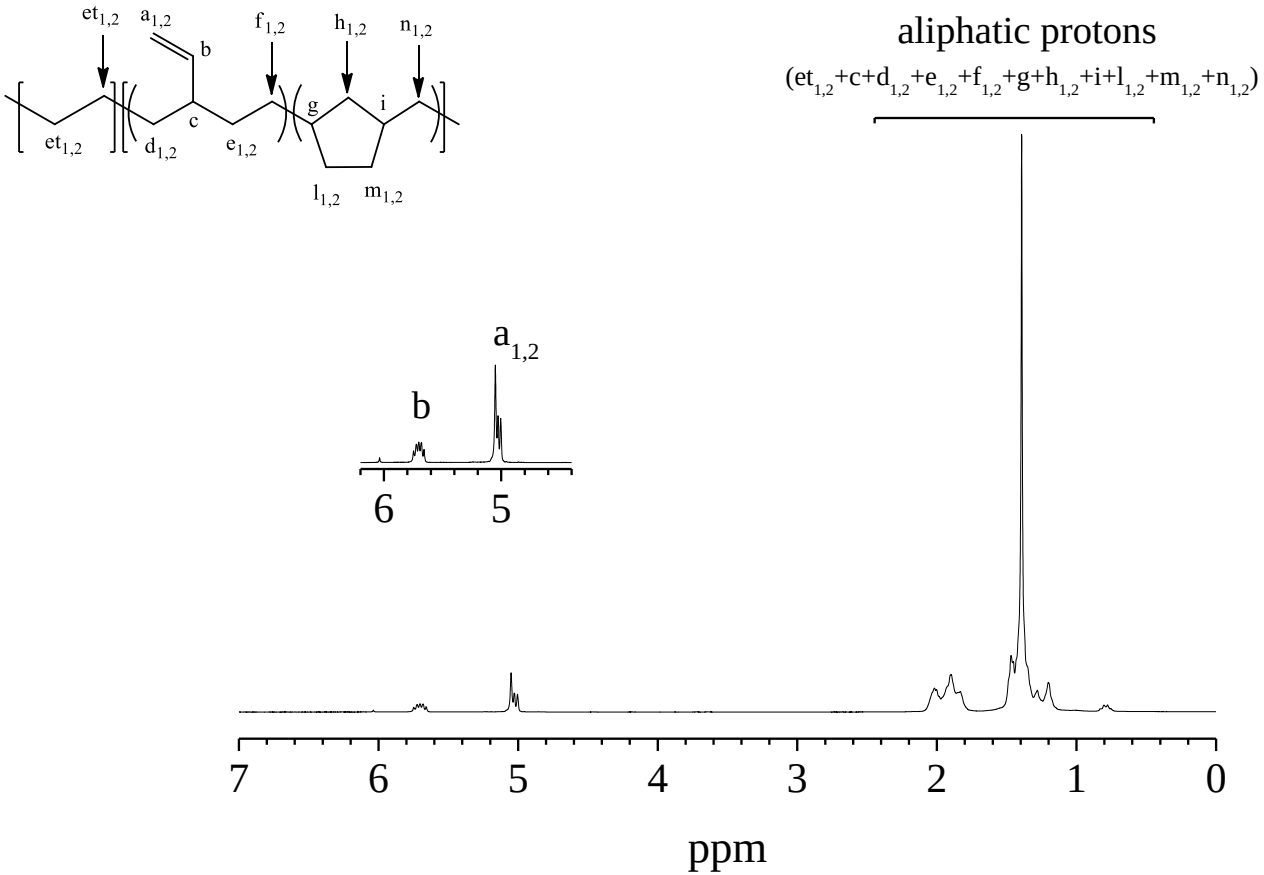

Figure A1.2 ^{1}H-NMR spectrum of the PE-*b*-PHD block copolymer RDG-1-26 (w_{PE}=0.27).

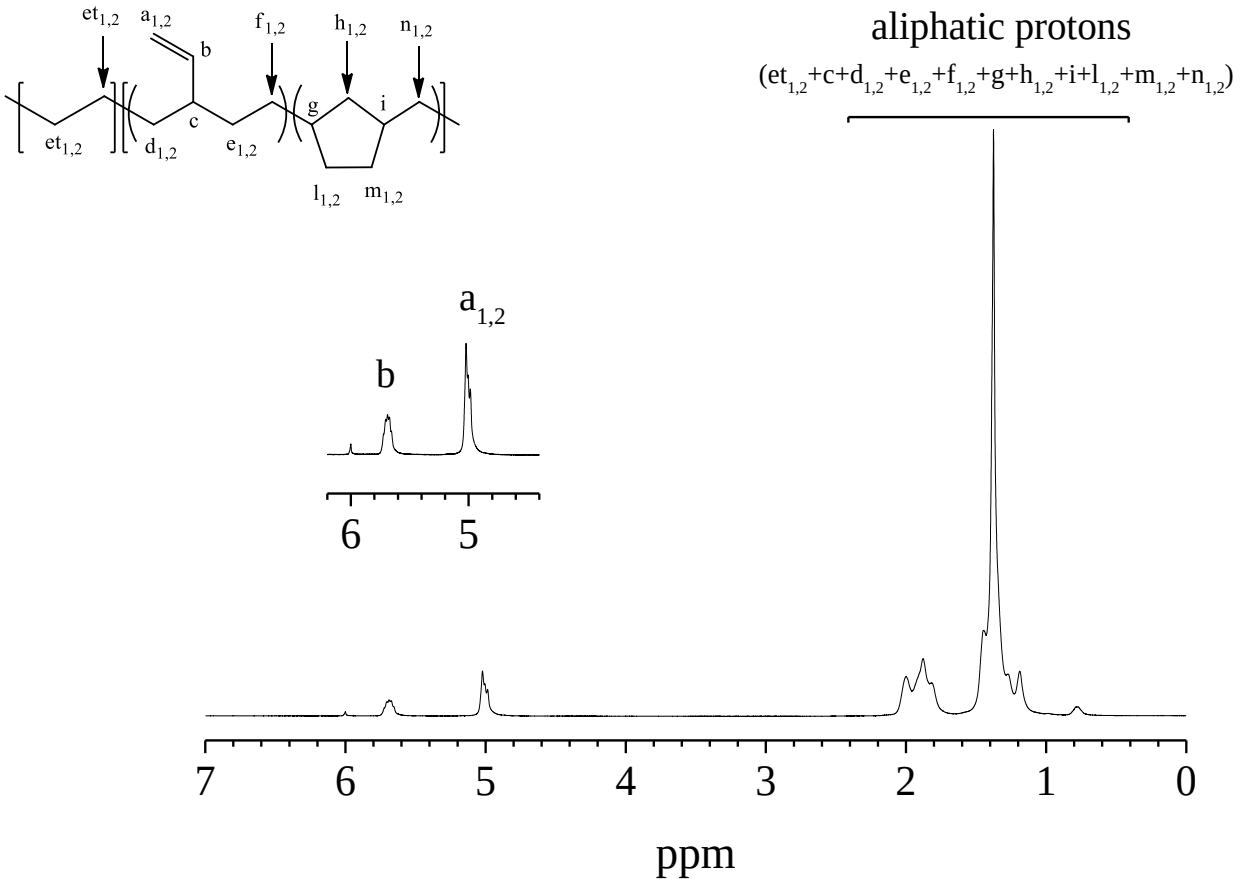

Figure A1.3 ^{1}H-NMR spectrum of the PE-*b*-HD block copolymer RDG-1-20 (w_{PE}=0.44).

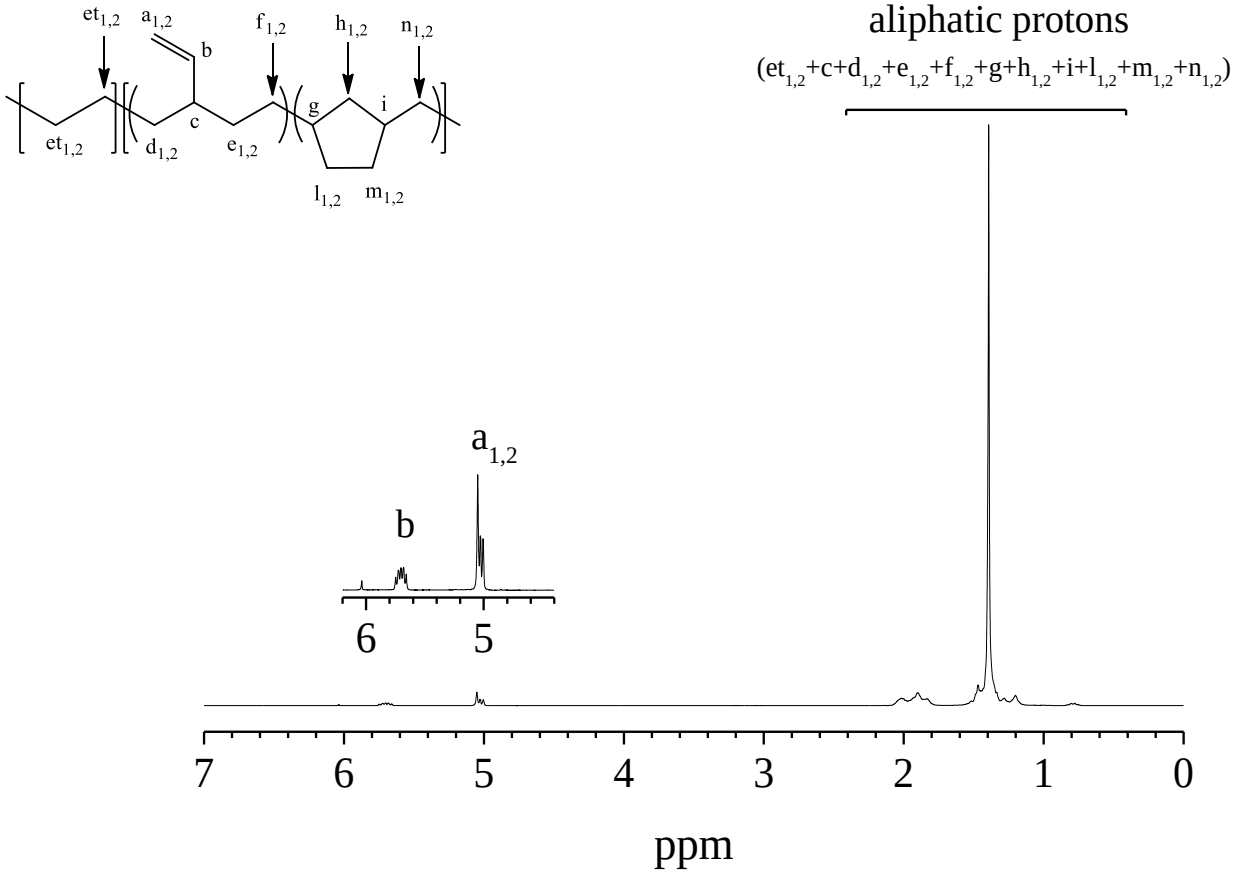

Figure A1.4 ^{1}H-NMR spectrum of the PE-*b*-HD block copolymer RDG-1-36 (w_{PE}=0.70).

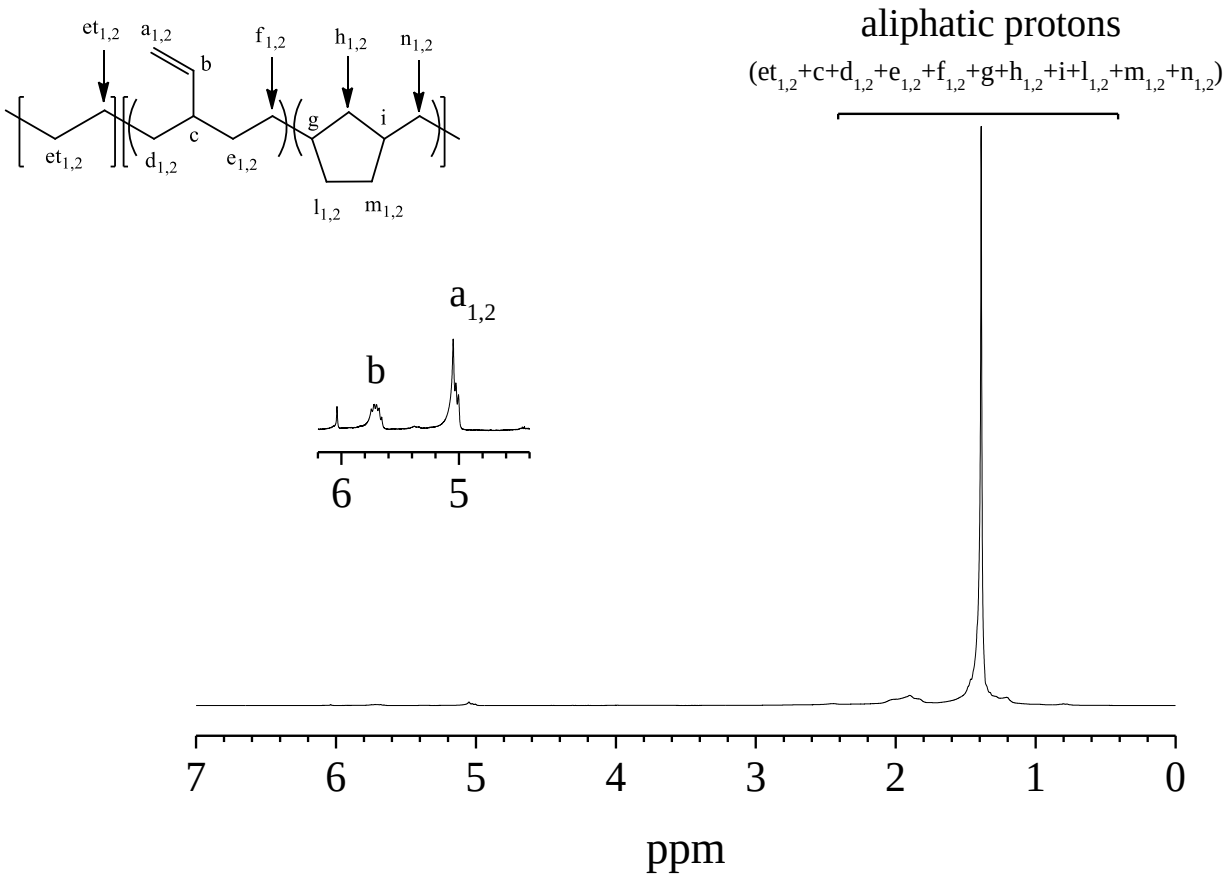

Figure A1.5 ^{1}H-NMR spectrum of the PE-*b*-HD block copolymer RDG-1-15 (w_{PE}=0.79).

2. Composition of poly(ethylene-*co*-vinyl cyclohexene) random copolymer

The composition of the poly(ethylene-*co*-vinyl cyclohexene) (P(E-*co*-VCH)) random copolymer has been determined by ^{13}C-NMR analysis. The spectrum has been obtained with a Bruker Advance spectrometer (400 MHz) equipped with a 5 mm high temperature cryoprobe operating on 50 mg/mL solutions in 1,1,2,2-tetrachloroethane-d2 at 120 °C.

The spectrum obtained for the P(E-*co*-VCH) random copolymer is shown in Figure A1.6. The resonances have been identified by comparing the experimental spectrum with the spectrum of a P(E-*co*-VCH) random copolymer obtained by using a half-titanocene catalyst exhibiting efficient comonomer incorporation.[52] The same is expected for the C_s-symmetric pyridylamidohafnium dimethyl complex used for the synthesis of the P(E-*co*-VCH) random copolymer.

The composition of the P(E-*co*-VCH) random copolymer has been determined by using Eq. IX to XII: Eq. IX counts all the signals that can be attributed to a C atom belonging to an ethylene unit (C_E). Similarly, Eq. X counts all the signals that can be attributed to a secondary C atom belonging to a vinylcyclohexene unit (C_{VCH}). The concentration of ethylene units and vinylcyclohexene units are calculated as mol % by using Eq. XI and Eq. XII respectively. The C_E in Eq. XI and Eq. XII is divided by 2 since an ethylene unit comprises two C atoms.

Equations

(Eq. IX) $$C_E = {}^1\!/_2\,\alpha\delta^+ + \beta\delta^+ + \gamma\delta^+ + \delta^+\delta^+ + {}^1\!/_2\,\alpha\gamma^+ + \beta\beta$$

(Eq. X) $$C_{VCH} = {}^1\!/_2\,\alpha\delta^+ + {}^1\!/_2\,\alpha\gamma^+$$

(Eq. XI) $$E\ (mol\%) = \frac{\frac{C_E}{2}}{\frac{C_E}{2}+C_{VCH}} \cdot 100$$

(Eq. XII) $$VCH\ (mol\%) = \frac{C_{VCH}}{\frac{C_E}{2}+C_{VCH}} \cdot 100$$

The concentration of the P(E-*co*-VCH) block of the PE-*b*- P(E-*co*-VCH) BCP is considered the same as that of the P(E-*co*-VCH) random copolymer since the two copolymers are synthesized with the same catalyst, and since the reaction conditions used for the synthesis of the P(E-*co*-VCH) block are the same as those used for the synthesis of the P(E-*co*-VCH) random copolymer. The values of the concentration of the VCH units in the P(E-*co*-VCH) random copolymer and in the P(E-*co*-VCH) block of the PE-*b*- P(E-*co*-VCH) BCP are reported in Table 1.8 and A1.2.

Table A1.2 Total molecular mass ($M_{n\ TOT}$), molecular mass of the PE block ($M_{n\ PE}$) and P(E-*co*-VCH) block ($M_{n\ PEVCH}$), polydispersity index (M_w/M_n), mass (w_{PE}) and volume (f_{PE}) fractions of the PE block, content of vinyl cyclohexene monomer in the P(E-*co*-VCH) block.

SAMPLE	M_n[a] TOT (Kg/mol)	M_n[a] PE (Kg/mol)	M_n[b] PEVCH (Kg/mol)	$\frac{M_w}{M_n}$[a]	w_{PE}[c]	f_{PE}[d]	VCH (mol%)
RDG-1-126	113.8	-	-	1.23	1	1	27
RDG-1-130	121.3	71.6	49.7	1.28	0.59	0.55[d]	27

a evaluated from GPC analysis; **b** calculated from $M_{n\ TOT}$ and $M_{n\ PE}$ as $M_{n\ PEVCH}=M_{n\ TOT}-M_{n\ PE}$; **c** calculated as $M_{n\ PE}/M_{n\ TOT}$; **d** calculated from the molecular masses $M_{n\ PE}$ and $M_{n\ TOT}$ and the densities of PE (0.996 g/cm^3) and of the PE-*b*-P(E-*co*-VCH) BCP (0.929 g/cm^3) as $f_{PE}=(M_{n\ PE}/0.996)/(M_{n\ TOT}/0.929)$. The density of PE is the theoretical value for a sample having 100% crystallinity, the density of the PE-*b*-P(E-*co*-VCH) BCP has been experimentally determined by flotation (see Appendix 3).

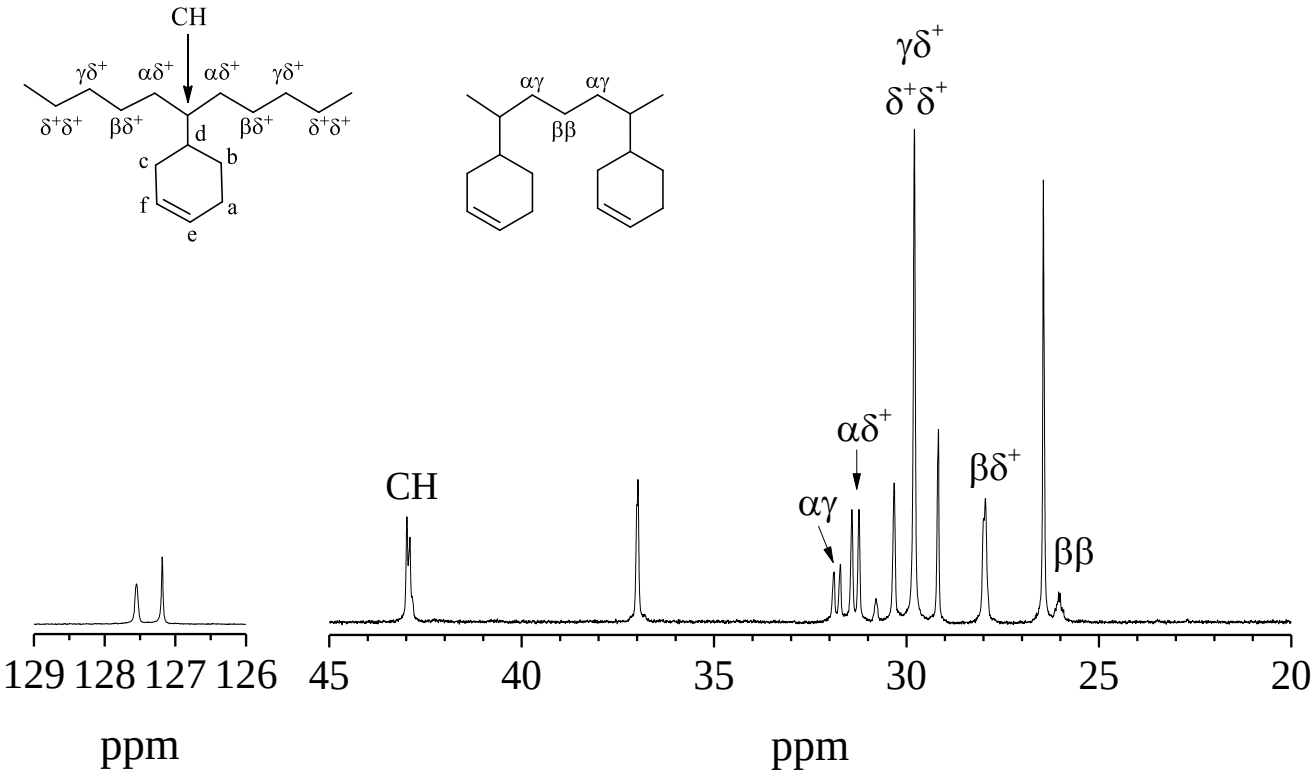

Figure A1.6 ^{13}C-NMR spectrum of the P(E-*co*-VCH) random copolymer RDG-1-126.

3. Composition of poly(propylene-*co*-vinylcyclohexene) random copolymer and of isotactic polypropylene-*b*-poly(propylene-*co*-vinylcyclohexene) di-block copolymers

The composition of the poly(propylene-*co*-vinylcyclohexene) (P(P-*co*-VCH)) random copolymer has been determined by ^{13}C-NMR analysis. The spectrum has been obtained with a Bruker Advance spectrometer (400 MHz) equipped with a 5 mm high temperature cryoprobe operating on 50 mg/mL solutions in 1,1,2,2-tetrachloroethane-d2 at 120 °C.

The spectrum obtained for the P(P-*co*-VCH) random copolymer is shown in Figure A1.7. The resonances have been estimated starting from the resonances of the C atoms of the P(E-*co*-VCH) random copolymer synthesized with the same catalyst (section 2), to which the contributions due to the presence of the methyl group of the propylene units have been added by using the Paul and Grant rules.[53]

The composition of the P(P-*co*-VCH) random copolymer has been determined by using Eq. XIII to XVI: Eq. XIII counts all the secondary C atoms that can be attributed to a propene unit (C_P). Similarly, Eq. XIV counts all the secondary C atoms that can be attributed to a vinylcyclohexene unit (C_{VCH}). The concentration of propylene units and vinylcyclohexene units are calculated as mol % by using Eq. XV and Eq. XVI respectively.

The spectrum obtained for the iPP-*b*-P(P-*co*-VCH) BCP RDG-1-143 (w_{iPP}=0.78) is shown in Figure A1.8. The resonances have been attributed as in the case of P(P-*co*-VCH) random copolymer. The composition has been calculated by using the same equations used for the P(P-*co*-VCH) random copolymer. However, in this case, the concentration of P and VCH calculated by using Eq. XIII to XVI are relative to the whole BCP molecule. The concentration of P and VCH within the sole P(P-*co*-VCH) block is calculated by combining the results obtained from ^{13}C-NMR analysis and from GPC analysis (i.e. the mass fraction of the two blocks) through Eq. XVII to XX.

In the case of the sample RDG-1-145 (w_{iPP}=0.78) sample, ^{13}C-NMR analysis we have assumed that the concentration of vinylcyclohexene in the P(P-*co*-VCH) block (VCH (mol%)) is the same as that calculated for the RDG-1-143 BCP. These values are reported in Table 2.1 and A1.3.

Equations

(Eq. XIII) $$C_P = CH_2\ PP + {}^1/_2\ CH_2\ PVCH$$

(Eq. XIV) $$C_{VCH} = {}^1/_2\ CH_2 PVCH$$

(Eq. XV) $$P\ (mol\%) = \frac{C_P}{C_P + C_{VCH}} \cdot 100$$

(Eq. XVI) $$VCH\ (mol\%) = \frac{C_{VCH}}{C_P + C_{VCH}} \cdot 100$$

(Eq. XVII) $$VCH\ (wt\%) = \frac{VCH\ (mol\%) \cdot 108}{P\ (mol\%) \cdot 42 + VCH(mol\%) \cdot 108} \cdot 100$$

(Eq. XVIII) $$VCH_{PVCH}\ (wt\%) = \frac{VCH\ (wt\%)}{(1 - w_{iPP})}$$

(Eq. IX) $$VCH_{PVCH}\ (mol\%) = \frac{\frac{VCH_{PVCH}\ (wt\%)}{108}}{\frac{VCH_{PVCH}\ (wt\%)}{108} + \frac{100 - VCH_{PVCH}\ (wt\%)}{42}} \cdot 100$$

(Eq. XX) $$P_{PVCH}(mol\%) = 100 - VCH_{PVCH}\ (mol\%)$$

Table A1.3 Total molecular mass ($M_{n\ TOT}$), molecular mass of the iPP block ($M_{n\ iPP}$) and of the P(P-*co*-VCH) block ($M_{n\ PPVCH}$), polydispersity index (M_w/M_n), mass fraction (w_{iPP}) and volume fraction (f_{iPP}) of the iPP block, concentration of the vinylcyclohexene units in the P(P-*co*-VCH) block (VCH).

SAMPLE	M_n[a] TOT (Kg/mol)	M_n[a] iPP (Kg/mol)	M_n[b] PPVCH (Kg/mol)	$\frac{M_w}{M_n}$[a]	w_{iPP}[c]	f_{iPP}[d]	VCH (mol%)
RDG-1-142	45	-	-	1.31	-	-	3
RDG-1-41	139.8	-	-	1.29	1	1	-
RDG-1-143	55.9	43.5	12.4	1.36	0.78	0.75	7
RDG-1-145	80.5	54.2	26.3	1.39	0.67	0.65	7

a evaluated from GPC analysis; **b** calculated from $M_{n\ TOT}$ and $M_{n\ iPP}$ as $M_{n\ PPVCH} = M_{n\ TOT} - M_{n\ iPP}$; **c** calculated as $M_{n\ iPP}/M_{n\ TOT}$; **d** calculated from the molecular masses $M_{n\ iPP}$ and $M_{n\ TOT}$ and the densities of iPP (ρ_{iPP}=0.936 g/cm^3) and of the iPP-*b*-P(P-*co*-VCH) BCPs ($\rho_{iPP\text{-}b\text{-}P(P\text{-}co\text{-}VCH)}$) as $f_{iPP} = (M_{n\ iPP}/\rho_{iPP})/(M_{n\ TOT}/\rho_{iPP\text{-}b\text{-}P(P\text{-}co\text{-}VCH)})$. The density of iPP is the theoretical value for a sample having 100% crystallinity, the densities of the iPP-*b*-P(P-*co*-VCH) BCPs have been experimentally determined by flotation (see Appendix 3).

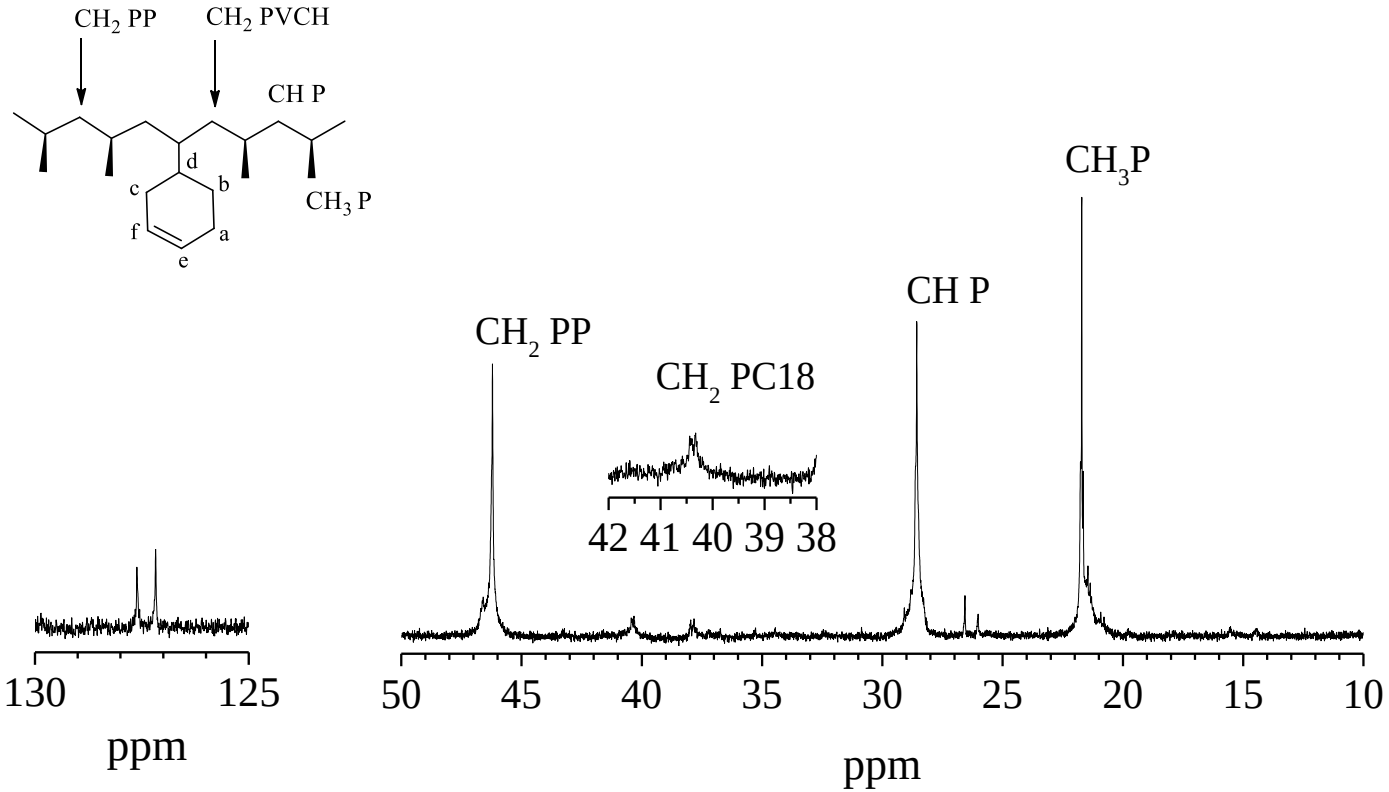

Figure A1.7 ^{13}C-NMR spectrum of the P(P-*co*-VCH) random copolymer RDG-1-142.

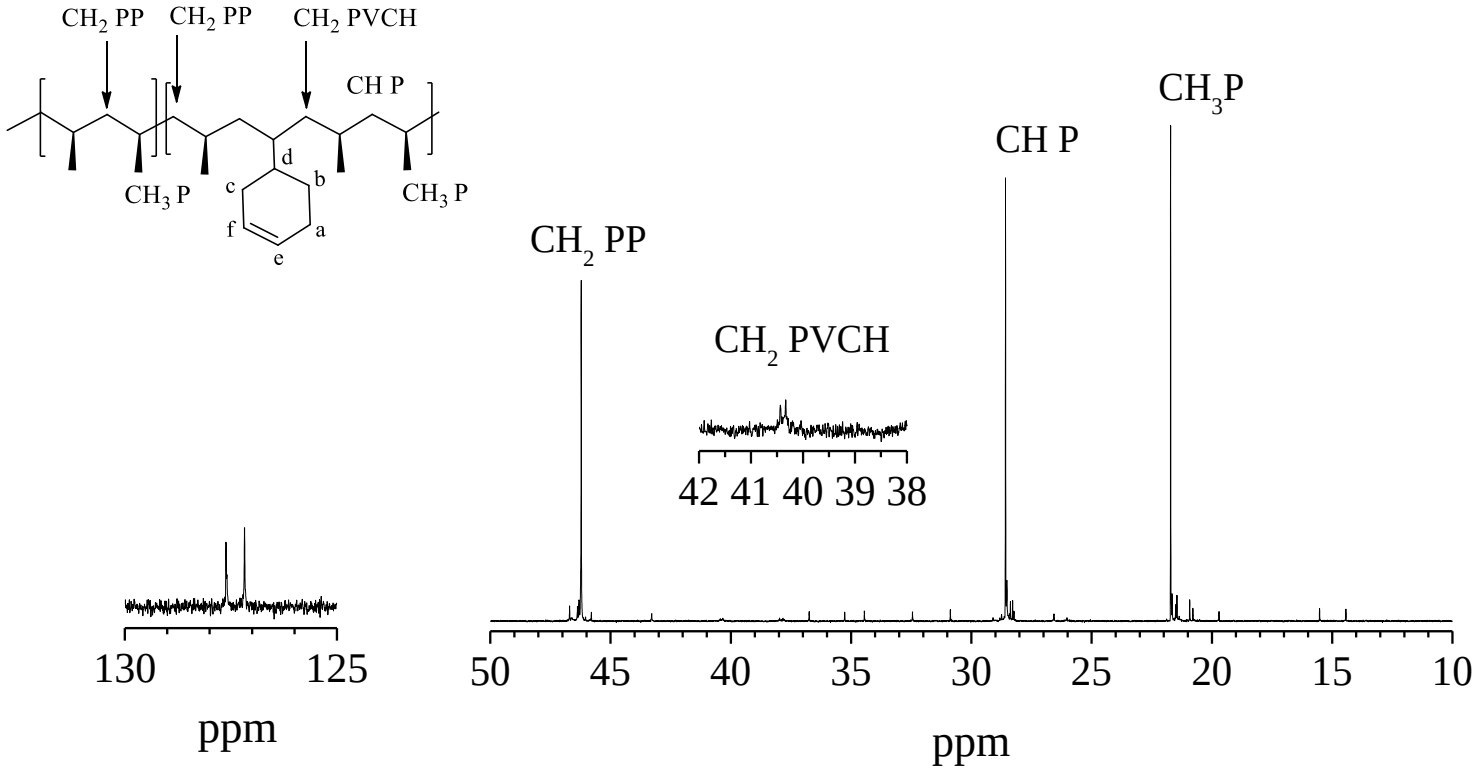

Figure A1.8 ^{13}C-NMR spectrum of the iPP-*b*-P(P-*co*-VCH) block copolymer RDG-1-143 (w_{iPP}=0.78).

4. Composition of poly(propylene-*co*-1-octadecene) random copolymer and of isotactic polypropylene-*b*-poly(propylene-*co*-1-octadecene) di-block copolymers

The composition of the poly(propylene-*co*-1-octadecene) (P(P-*co*-C18)) random copolymer has been determined by ^{13}C-NMR analysis. The spectrum has been obtained with a Bruker Advance spectrometer (400 MHz) equipped with a 5 mm high temperature cryoprobe operating on 50 mg/mL solutions in 1,1,2,2-tetrachloroethane-d2 at 120 °C.
The spectrum obtained for the P(P-*co*-C18) random copolymer is shown in Figure A1.9. The resonances have been assigned according to ref. 54.
The composition of the P(P-*co*-C18) random copolymer has been determined by using Eq. XXI to XXIV: Eq. XXI counts all the secondary C atoms that can be attributed to a propene unit (C_P). Similarly, Eq. XXII counts all the secondary C atoms that can be attributed to a 1-octadecene unit (C_{C18}). The concentration of propylene units and 1-octadecene units are calculated as mol % by using Eq. XXIII and Eq. XXIV respectively.

The spectrum obtained for the iPP-*b*-P(P-*co*-C18) BCPs are shown in Figure A1.10-A1.12. The resonances have been attributed as in the case of the P(P-*co*-C18) random copolymer. The composition has been calculated by using the same equations used for the P(P-*co*-C18) random copolymer. However, in this case, the concentration of P and C18 calculated by using Eq. XXI to XXIV are relative to the whole BCP molecule. The concentration of P and C18 within the sole P(P-*co*-C18) block is calculated by combining the results obtained from ^{13}C-NMR analysis and from GPC analysis (i.e. the mass fraction of the two blocks) through Eq. XXV to XXVIII. The results are reported in Table 2.7 and A1.4.
In the case of the iPP-*b*-P(P-*co*-C18) BCP RDG-1-148P (w_{iPP}=0.49) the concentration of C18 within the P(P-*co*-C18) block is assumed to be equal to that calculated for the sample RDG-1-139P, since the melting and crystallization temperatures of the side chains of the C18 units in the two samples are close.

Equations

(Eq. XXI) $$C_P = CH_2\ PP + {}^1/_2\ CH_2\ PC18$$

(Eq. XXII) $$C_{C18} = {}^1/_2\ CH_2 PC18$$

(Eq. XXIII) $$P\ (mol\%) = \frac{C_P}{C_P + C_{C18}} \cdot 100$$

(Eq. XXIV) $$C18\ (mol\%) = \frac{C_{C18}}{C_P + C_{C18}} \cdot 100$$

(Eq. XXV) $$C18\ (wt\%) = \frac{C18\ (mol\%) \cdot 252.5}{P\ (mol\%) \cdot 42 + C18\ (mol\%) \cdot 108} \cdot 100$$

(Eq. XXVI) $$C18_{PC18}\ (wt\%) = C18\ (wt\%)/(1 - w_{iPP})$$

(Eq. XXVII) $$C18_{PC18}\ (mol\%) = \frac{\frac{C18_{PC18}\ (wt\%)}{252.5}}{\frac{C18_{PC18}\ (wt\%)}{252.5} + \frac{100 - C18_{PC18}\ (wt\%)}{42}} \cdot 100$$

(Eq. XXVIII) $$P_{PC18}(mol\%) = 100 - C18_{PC18}\ (mol\%)$$

Table A1.4 Total molecular mass ($M_{n\ TOT}$), molecular mass of the iPP block ($M_{n\ iPP}$) and of the P(P-*co*-C18) block ($M_{n\ PPC18}$), polydispersity index (M_w/M_n), mass fraction (w_{iPP}) and volume fraction (f_{iPP}) of the iPP block, concentration of the 1-octadecene units in the P(P-*co*-C18) random block (C18).

SAMPLE	M_n[a] TOT (kg/mol)	M_n[a] iPP (kg/mol)	M_n[b] PPC18 (kg/mol)	$\frac{M_w}{M_n}$[a]	w iPP[c]	f iPP[d]	C18 (mol%)
RDG-1-133P	250.1	-	-	1.39	-	-	18
RDG-1-41	139.8	-	-	1.29	1	1	-
RDG-1-148P	135	66.8	68.2	1.30	0.49	0.47	24
RDG-1-135P	114.4	50.3	64.1	1.27	0.44	0.41	13
RDG-1-139P	124.9	38.3	86.6	1.30	0.31	0.28	≈24

a evaluated from GPC analysis; **b** calculated from $M_{n\ TOT}$ and $M_{n\ iPP}$ as $M_{n\ PPC18}=M_{n\ TOT}-M_{n\ iPP}$; **c** calculated as $M_{n\ iPP}/M_{n\ TOT}$; **d** calculated from the molecular masses $M_{n\ iPP}$ and $M_{n\ TOT}$ and the densities of iPP (ρ_{iPP}=0.936 g/cm^3) and of the iPP-*b*-P(P-*co*-C18) BCPs ($\rho_{iPP\text{-}b\text{-}P(P\text{-}co\text{-}C18)}$) as $f_{iPP}=(M_{n\ iPP}/\rho_{iPP})/(M_{n\ TOT}/\rho_{iPP\text{-}b\text{-}P(P\text{-}co\text{-}C18)})$. The density of iPP is the theoretical value for a sample having 100% crystallinity, the densities of the iPP-*b*-P(P-*co*-C18) BCPs have been experimentally determined by flotation (see Appendix 3).

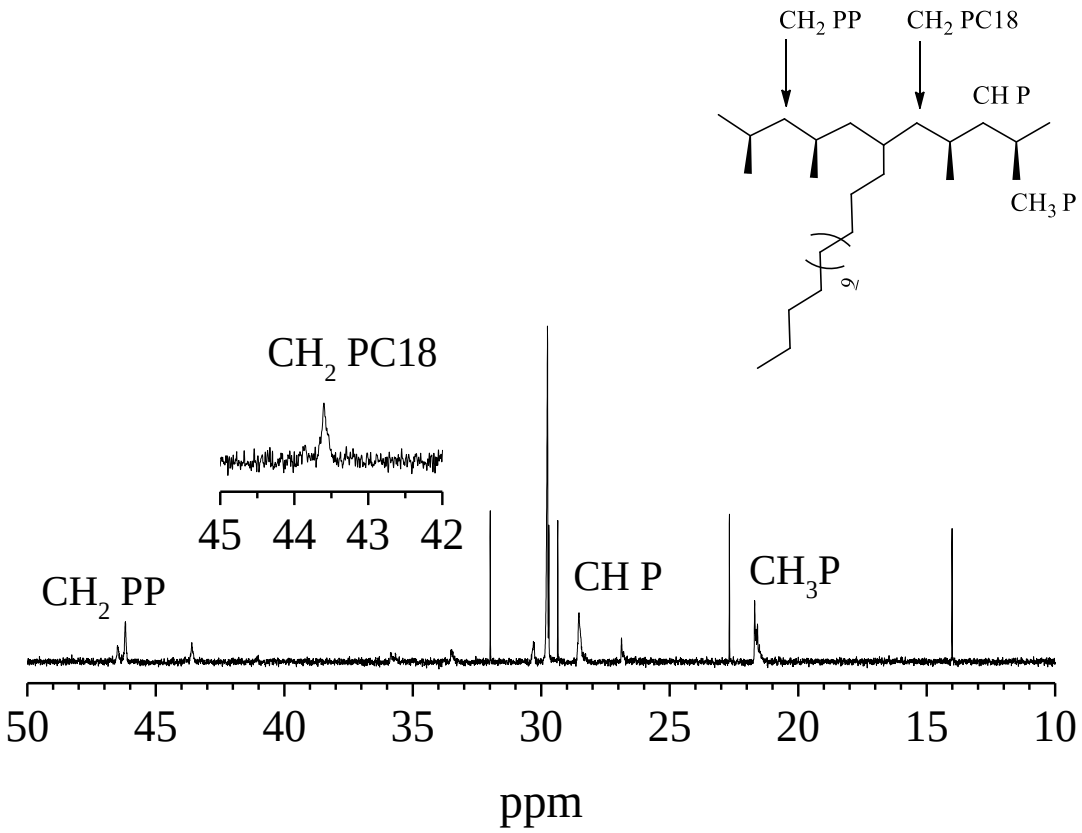

Figure A1.9 ^{13}C-NMR spectrum of the P(P-*co*-C18) random copolymer RDG-1-133P.

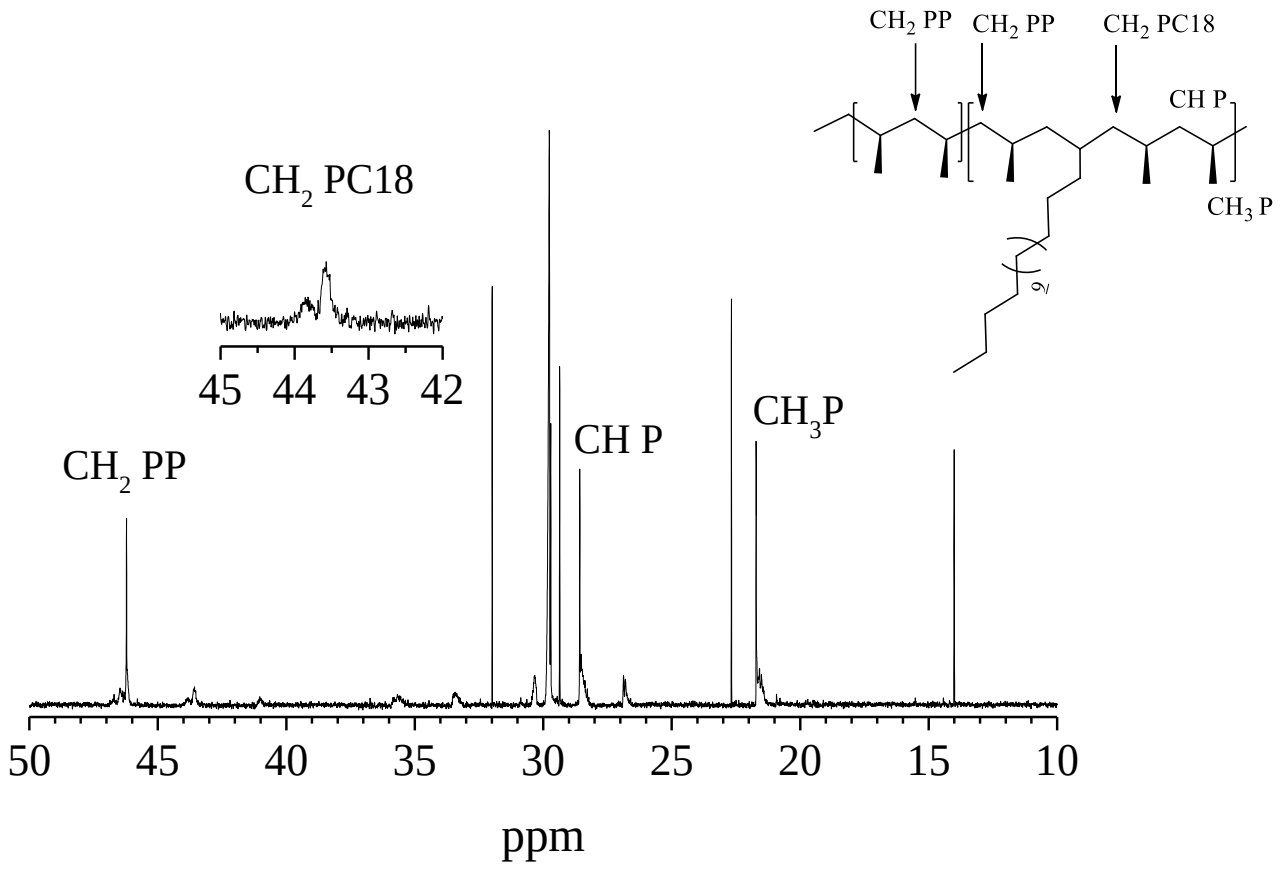

Figure A1.10 ^{13}C-NMR spectrum of the iPP-*b*-P(P-*co*-C18) block copolymer RDG-1-148P (w_{iPP}=0.49).

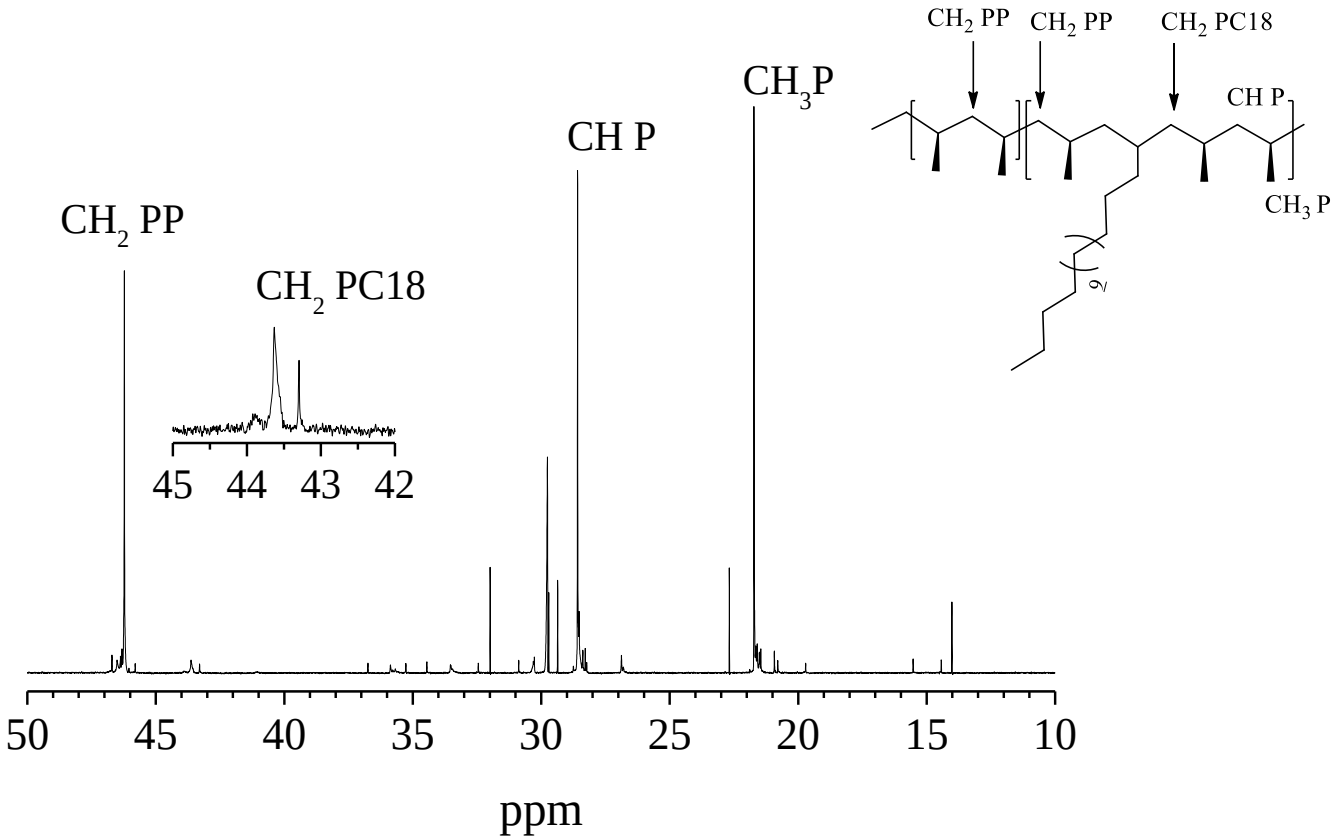

Figure A1.11 ^{13}C-NMR spectrum of the iPP-*b*-P(P-*co*-C18) block copolymer RDG-1-135P (w_{iPP}=0.44).

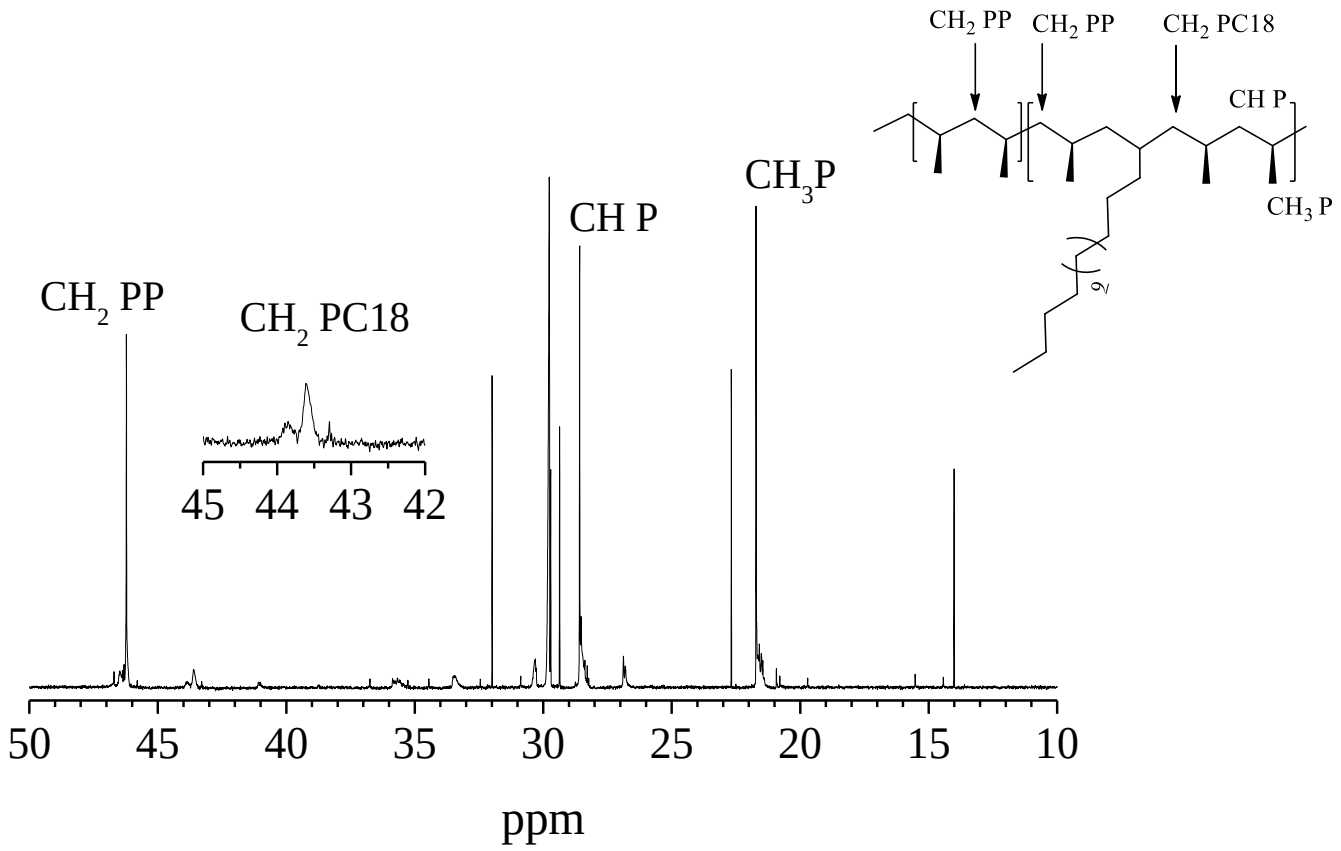

Figure A1.12 ^{13}C-NMR spectrum of the iPP-*b*-P(P-*co*-C18) block copolymer RDG-1-139P (w_{iPP}=0.31).

APPENDIX 2

Crystal structures of α and γ forms of isotactic polypropylene (iPP)

The crystal structures of α and γ forms of iPP are very similar. The limit-ordered structural models proposed for the α and γ forms are shown in Figure A2.1. Both the α and γ forms are characterized by chains in the 3/1 helical conformation (chain periodicity c=6.5Å), organized to form bilayers. However, α form is characterized by a regular stacking of bilayers along the b_α-axis direction with chain axes all parallel[55] (Figure A2.1 A), whereas the γ form is characterized by a regular packing along the c_γ-axis direction of bilayers of chains with axes oriented alternatively along two nearly perpendicular directions[56] (Figure A2.1 C). The angle between the axes of the chains belonging to consecutive bilayers is 98.6° (or equivalently 81°), close to the angle β_α of the monoclinic unit cell of the α form.

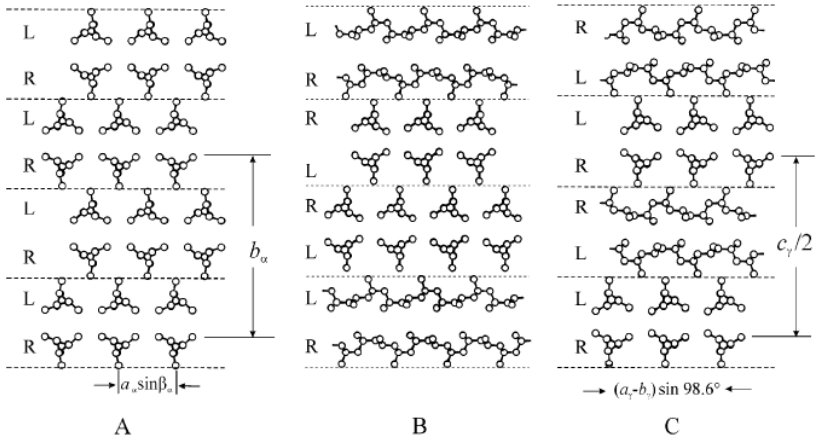

Figure A2.1 Limit ordered models of packing proposed for α (A) and γ (C) forms of iPP and model of the α/γ disordered modifications intermediate between α and γ forms (B). The dashed horizontal lines delimit bilayers of chains. Subscripts α and γ identify unit cell parameters referred to the monoclinic and orthorhombic unit cells of the α and γ forms, respectively. In the disordered model (B), consecutive bilayers of chains are stacked along b_α (c_γ) with the chain axes either parallel, as in the α form, or nearly perpendicular, as in the γ form. Symbols R and L indicate rows of all right- and left-handed helical chains, respectively.

As a consequence of the structural similarity, the X-ray diffraction patterns of α and γ forms of iPP are very similar (Figure A2.2 A for α form and B for γ form). The most characteristics reflections of the α and γ forms, the corresponding 2θ values relative to the CuKα radiation and *q* values and the corresponding Bragg distances are reported in Table A2.1 and Table A2.2 respectively.

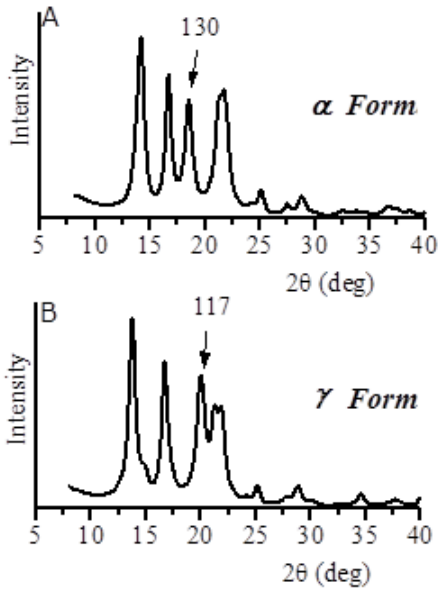

Figure A2.2 X-ray powder diffraction profile of iPP crystallized in α form (A) and γ form (B).

Table A2.1 Miller indexes $(hkl)_\alpha$, diffraction angles for the CuK_α radiation (2θ), values of the scattering vector (*q*) and Bragg distances (*d*) relative to the most characteristics reflections of the α form of iPP.

$(hkl)_\alpha$	2θ (°) (CuKα)	*q* (nm^{-1})	*d* (Å)
1 1 0	14.2	10	6.25
0 4 0	17.1	12.1	5.18
1 3 0	18.6	13.2	4.76
1 1 1	21.1	14.9	4.21
$\bar{1}$ 3 1, 0 4 1	21.9	15.5	4.06

Table A2.2 Miller indexes $(hkl)_\gamma$, diffraction angles for the CuKα radiation (2θ), values of the scattering vector (q) and Bragg distances (d) relative to the most characteristics reflections of the γ form of iPP.

$(hkl)_\gamma$	2θ (°) (CuKα)	q (nm^{-1})	d (Å)
1 1 1	13.8	9.8	6.40
0 0 8	16.7	11.8	5.30
1 1 7	20.1	14.2	4.42
2 0 2	21.2	15	4.19
0 2 6	21.9	15.5	4.06

The only remarkable difference in the diffraction patterns of α and γ forms is in the position of the third strong peak which occurs at 2θ=18.6° ($(130)_\alpha$ reflection) for the α form, and at 2θ=20.1° ($(117)_\gamma$ reflection) for the γ form.

An example of a disordered modification is shown in Figure A2.1 B. In this structure, consecutive bilayers of chains may face each other with the chain axes either parallel (like in the α form) or nearly perpendicular (like in the γ-form). The X-ray diffraction profile of a sample of iPP crystallized in a disordered modification intermediate between α and γ forms shows a diffuse scattering concentrated in very narrow regions of the diffraction pattern, i.e. at $2\theta\approx14°$, around the $(110)_\alpha$ and $(111)_\gamma$ reflections of the α and γ forms respectively, and in the 2θ range 18°-20°, around the $(130)_\alpha$, and $(117)_\gamma$ reflections of the α and γ forms respectively.[42,57,58] The intensities and the positions of the $(040)_\alpha$ and $(008)_\gamma$ reflections at 2θ=17° and of the $(111)_\alpha$ and $(202)_\gamma$ reflections at 2θ=21° are not affected by the presence of α/γ disorder.[57,58] Therefore, the inclusion of a high degree of α/γ structural disorder in the crystalline domains implies that the $(130)_\alpha$ and $(117)_\gamma$ reflections are almost absent and only a diffuse scattering is observed in the corresponding 2θ range.

APPENDIX 3

Density determination of polymer samples through flotation method

For some of the samples analysed in this work, density measurements have been performed. The flotation method has been employed.

In the flotation method, the density of a liquid, in which the object of interest floats, is determined. Typically, the liquid is a mixture of two miscible solvents with different densities, one lower and one higher than the density of the object of interest. The density of the liquid mixture is determined through weight measurement of a well-defined volume of the liquid mixture.

For the density determination of the polymer samples analysed in this work, compression-molded films with no bubbles and no defects on the surface, are prepared. An odd number of small pieces (≈ 2mm × 2mm) are cut from the polymer film and are immersed in ethanol (ρ=0.798g/cm^3) in which they sink. Then, water (ρ=0.997g/cm^3) is added in small volumetric intervals until the polymer pieces start floating in the liquid mixture. Distilled water, boiled for ≈1h and then cooled to room temperature, has been used. The ethanol/water mixture in which the polymer pieces float is put in a 10mL pycnometer, previously tared, and at least three weight measurements are carried out. The density of the liquid, and therefore of the polymer sample, is determined as the ratio of the average weight and the volume (10mL) of the liquid mixture. The density is determined at T=25°C.

The values of the densities determined for the poly(1-hexadiene) (PHD) homopolymer and for the polyethylene-*b*-poly(propene-*co*-vinyl cyclohexene) (PE-*b*-P(E-*co*-VCH)), isotactic polypropylene-*b*-poly(propene-*co*-vinyl cyclohexene) (iPP-*b*-P(P-*co*-VCH)) and isotactic polypropylene-*b*-poly(propene-*co*-1-octadecene) (iPP-*b*-P(P-*co*-C18)) block copolymers are reported in Table A3.1.

Table A3.1 Values of the density (ρ) experimentally determined by flotation, at 25°C, in ethanol/water solutions, for the PHD homopolymer and for the PE-*b*-P(E-*co*-VCH), iPP-*b*-P(P-*co*-VCH), iPP-*b*-P(P-*co*-C18) BCPs samples.

SAMPLE	**ρ (g/cm^3)**
PHD	
RDG-1-13	0.940±0.002
PE-*b*-P(E-*co*-VCH)	
RDG-1-130 (w_{PE}=0.59)	0.9289±0.0007
iPP-*b*-P(P-*co*-VCH)	
RDG-1-143 (w_{iPP}=0.78)	0.908±0.003
RDG-1-145 (w_{iPP}=0.67)	0.9072±0.0005
iPP-*b*-P(P-*co*-C18)	
RDG-1-148 (w_{iPP}=0.49)	0.887±0.003
RDG-1-135 (w_{iPP}=0.44)	0.863±0.004
RDG-1-139 (w_{iPP}=0.31)	0.860±0.006

APPENDIX 4

Isotactic poly(1-octadecene) RDG-1-71P

An isotactic poly(1-octadecene) (P(C18)) homopolymer, RDG-1-71P, has been synthesized by means of an octahedral group IV bis(phenolate) catalyst (Figure A4.1) by using the following procedure: a 100 mL glass reactor was charged under nitrogen with dry toluene, distilled 1-octadecene and dried PMAO (poly(methylalumoxane)). The polymerization was initiated by injection of the bis(phenolate) catalysts solution (Hf precatalyst in chlorobenzene) and allowed to proceed for 20 min. Then, the reaction was terminated by injecting a methanol/HCl solution. The polymer was precipitated into copious methanol and allowed to stir overnight; it was then collected via filtration and dried in vacuo to constant weight.

The molecular characteristics of the sample are reported in Table A4.1.

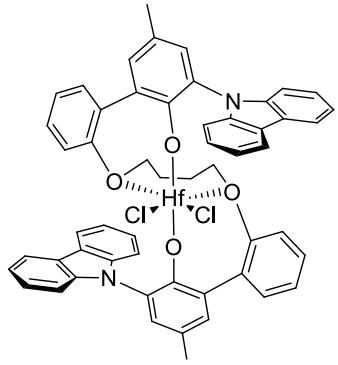

Figure A4.1 Structure of the octahedral group IV bis(phenolate) catalyst catalyst used for the synthesis of the poly(1-octadecene) homopolymer RDG-1-71.

Table A4.1 Number average molecular mass (M_n), weight average molecular mass (M_w) and polydispersity index (M_w/M_n) of the poly(1-octadecene) homopolymer RDG-1-71P evaluated from GPC analysis.

SAMPLE	M_n[a] (Kg/mol)	Mw[a] (Kg/mol)	$\frac{M_w}{M_n}$[a]
RDG-1-71P	25.6	45.0	1.75

The as prepared sample has been subjected to structural thermal characterization.

The small (SAXS) and wide (WAXS) angle structural characterization has been carried out by using synchrotron radiation at ESRF beamline BM26B (DUBBLE) in Grenoble. The data have been acquired at T=25°C by using a wavelength of 1.0402Å and an acquisition time of 6s.

The thermal characterization of the sample has been carried out by a calorimetric measurement performed with a differential scanning calorimeter (DSC-1 by Mettler Toledo) in a flowing N_2 atmosphere, at a scanning rate of 10°C/min in the temperature range -150 - 100°C.

The WAXS and SAXS profiles are shown in Figure A4.2 A and A' respectively and in Figure 2.28, while the DSC heating thermogram is shown in Figure A4.3.

In this sample, the crystallinity is due to the organization of the methylene sequences of the side chains of the C18 units into PE-like crystals. In fact, the WAXS profile (A) recorded at 25°C shows a sharp reflection at q=15nm^{-1}, corresponding to a Bragg distance d=4.1Å, which is similar to the Bragg distance relative to the (110) planes of the orthorhombic form of PE. The corresponding SAXS profile (A') shows a well-defined correlation peak at q=0.88nm^{-1}, corresponding to a periodicity L_B=7nm. The melting of the PE-like crystals occurs in the range of temperature 40-60°C as indicated by the double, high-intensity endothermic peak in the heating thermogram shown in Figure A4.3.

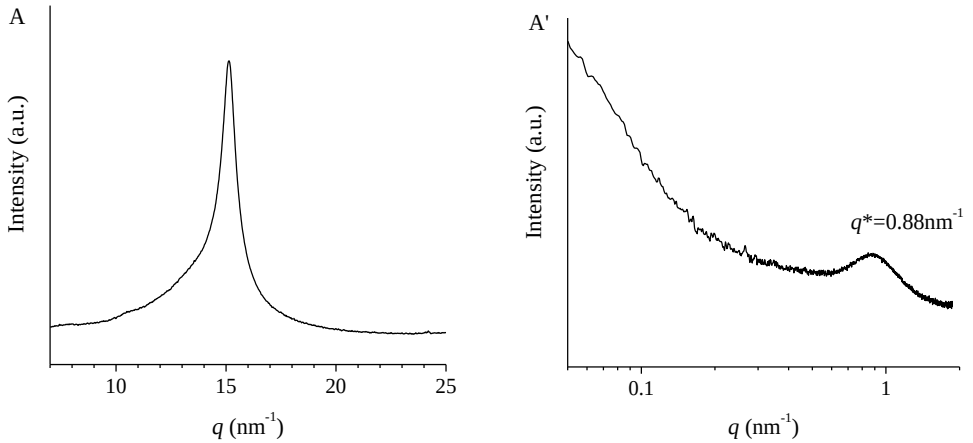

Figure A4.2 SAXS (A) and WAXS (A') intensity profiles of the P(C18) homopolymer recorded at 25°C.

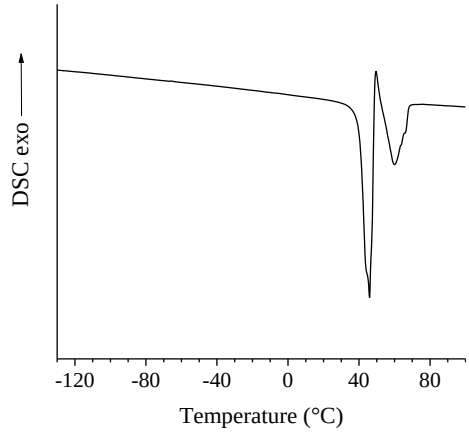

Figure A4.3 DSC heating thermogram recorded during the heating of the P(C18) homopolymer RDG-1-71P from -150°C to 100°C at a rate of 10°C/min.

REFERENCES

1. F.S. Bates, G.H. Fredrickson; *Annu. Rev. Phys. Chem.* **1990**, *41*, 525.
2. M.J. Fasolka, A.M. Mayes; *Annu. Rev. Mater. Res.* **2001,** *31*, 323.
3. (a) I.W. Hamley; *The Physics of Block Copolymers*, New York: Oxford University Press **1998**.
   (b) I.W. Hamley; *Development in Block Copolymer Science and Technology*, John Wiley & Sons. Chichester **2005**.
4. (a) G.W. Coates, P.D. Hustad, S. Reinartz; *Angew. Chem. Int. Ed.* **2002**, *41*, 2236.
   (b) G.J. Domski, J.M. Rose, G.W. Coates, A.D. Boling, M. Brookhart; *Prog. Polym. Sci.* **2007**, *32*, 30.
5. J. Tian, P.D. Hustad, G.W. Coates; *J. Am. Chem. Soc.* **2001**, *123*, 5134.
6. A.F. Mason, G. W. Coates; *J. Am. Chem. Soc.* **2004**, *126*, 16326.
7. A.E. Cherian, J.M. Rose, E.B. Lobkovsky, G.W. Coates; *J. Am. Chem. Soc.* **2005**, *127*, 13770.
8. (a) V. Busico, R. Cipullo, N. Friederichs, S. Ronca, M. Togrou; *Macromolecules* **2003**, *36*, 3806.
   (b) V. Busico, R. Cipullo, N. Friederichs, S. Ronca, G. Talarico, M. Togrou, B. Wang; *Macromolecules* **2004**, *37*, 8201.
9. G.W. Coates; PCT Int. Appl. WO2008/112133.
10. S. Nojima, K. Kato, S. Yamamoto, T. Ashida; *Macromolecules*, **1992**, *25*, 2237.
11. S. Nojima, H. Nakano, T. Ashida; *Polymer*, **1993**, *34*, 4168.
12. S. Nojima, H. Nakano, Y. Takahashi, T. Ashida; *Polymer*, **1994**, *35*, 3479.
13. P. Rangarajan, R.A. Register, D.H. Adamson, L.J. Fetters, W. Bras, S. Naylor, A.J. Ryan; *Macromolecules*, **1995**, *28*, 1422.
14. L.B.W. Lee, R.A. Register; *Macromolecules*, **2004**, *37*, 7278.
15. S. Nojima, K. Kato, S. Yamamoto, T. Ashida; *Macromolecules*, **1992**, *25*, 2237.
16. P. Rangarajan, R.A. Register, L.J. Fetters, W. Bras, S. Naylor, A.J. Ryan; *Macromolecules*, **1995**, *28*, 4932.
17. S. Li, R.A. Register, J.D. Weinhold, B.G. Landes; *Macromolecules*, **2012**, *45*, 5773.
18. G. Floudas, C. Tsitsilianis; *Macromolecules*, **1997**, *30*, 4381
19. P.H. Richardson, R.W. Richards, D.J. Blundell, W.A. Macdonald, P. Millis; *Polymer*, **1995**, *36*, 3059.

20. Y.L. Loo, R.A. Register, A.J. Ryn, G.T. Dee; *Macromolecules*, **2002**, *35*, 2365.
21. A.J. Ryan, I.W. Hamley, W. Bras, F.S. Bates; *Macromolecules* **1995**, *28*, 3860.
22. (a) G. Floudas, R. Ulrich, U. Wiesner; *J. Chem. Phys.*, **1999**, *110*, 652.
    (b) G. Floudas, B. Vazajou, F. Schipper, R. Ulrich, U. Wiesner, H. Iatrou, N. Hadjichristidis; *Macromolecules*, **2001**, *34*, 2947.
23. P.D. Hustad, G.W. Coates; *J. Am. Chem. Soc.*, **2002**, *124*, 11578.
24. C. Vonk; *J. Appl. Cryst.*, **1957**, *8*, 340.
25. (a) G.R. Strobl, M.J. Schnieder; *J. Polym. Sci., Polym. Phys. Ed.*, **1980**, *18*, 1343.
    (b) W. Ruland; *J. Appl. Cryst.*, **1971**, *4*, 70.
26. O. Ruiz de Ballesteros, F. Auriemma, G. Guerra, P. Corradini; *Macromolecules*, **1996**, *29*, 7141.
27. W. Kaminsky, D. Arrowsmith, H.R. Winkelbach; *Polym. Bull.*, **1996**, *36*, 577.
28. S. Bruckner, S.V. Meille, V. Petraccone, B. Pirozzi; *Prog. Polym. Sci.*, **1991**, *16*, 361.
29. A.J. Müller, M.L. Arnal, V. Balsamo; *Lect. Notes Phys.*, **2007**, *714*, 229.
30. C. De Rosa, F. Auriemma, R. Di Girolamo, O. Ruiz de Ballesteros; *J. Polym. Sci., Part B: Polym. Phys.*, **2014**, *52*, 677.
31. I. Coccorullo, R. Pantani, G. Titomanlio; *Polymer*, **2003**, *44*, 307.
32. J. Zhao J, Z. Wang, Y. Niu, B.S. Hsiao, S. Piccarolo; *J. Phys. Chem. B*, **2012**, *116*, 147.
33. C. De Rosa, F. Auriemma, *Crystals and Crystallinity in Polymers*; Wiley: Hoboken, NJ, **2014**.
34. C. De Rosa, F. Auriemma, G. De Lucia, L. Resconi; *Polymer*, **2005**, *46*, 9461.
35. C. De Rosa, F. Auriemma, R. Di Girolamo, O. Ruiz de Ballesteros, M. Pepe, O.Tarallo, A. Malafronte; *Macromolecules*, **2013**, *46*, 5202.
36. Q. Zia, H.J. Radusch, R. Androsch; *Polym. Bull.*, **2009**, *63*, 755.
37. H.P. Nadella, H.M. Henson, J.E. Spruiell, J.L. White; *J. Appl. Polym. Sci.*, **1977**, *21*, 3003.
38. P.Y.F. Fung, E. Orlando, S.H. Carr; *Polym. Eng. Sci.*, **1973**, *13*, 295.
39. P.G. Anderson, S.H. Carr; *J. Mater. Sci.*, **1975**, *10*, 870.
40. F.M. Lu, J.E. Spruiell; *J. Appl. Polym. Sci.*, **1987**, *34*, 1521.

41. B. Lotz, J.C. Wittman; *J. Polym. Sci., Part B: Polym. Phys.*, **1986**, *24*, 1541.
42. F. Auriemma, C. De Rosa; *Macromolecules*, **2006**, *39*, 7635.
43. C. De Rosa, F. Auriemma, R. Di Girolamo, L. Romano, M.R. De Luca; *Macromolecules*, **2010**, *43*, 8559.
44. H. Palza, J.M. Lopez-Majada, R. Quijada, R. Benavente, E. Perez; M.L. Cerrada; *Macromol. Chem. Phys.*, **2005**, *206*, 1221.
45. I. Tritto, L. Boggioni, D.R. Ferro; *Coord. Chem. Rev.*, **2006**, *250*, 212.
46. (a) W. Kaminsky, R. Spiehl; *Macromol. Chem. Phys.*, **1989**, *190*, 515.
(b) W. Kaminsky, A. Bark; *Makromol. Chem. Macromol. Symp.*, **1991**, *47*, 83.
47. Tritto, L. Boggioni, C. Zampa, M. C. Sacchi, D. R. Ferro; *Topics in Catalysis*, **2006**, *40*, 151.
48. A. Provasoli, D.R. Ferro, L. Boggioni, I. Tritto; *Macromolecules*, **1999**, *32*, 6697.
49. I. Tritto, L. Boggioni, G. Scalcione, D. Sidari, N. Galotto Galotto; *J. Organomet. Chem.*, 2015, *798*, 367.
50. D. Sidari, *Cyclolefin Copolymers via Chain Shuttling*, XXVII cycle Doctorate in Chemical Sciences, Università Degli Studi Di Milano Bicocca, **2015**.
51. D.J. Arriola, E.M. Carnahan, P.D. Hustad, R.L. Kuhlman, T.T. Wenzel; *Science*, **2006**, *312*, 714.
52. K. Itagaki; K. Nomura; *Macromolecules*, **2009**, *42*, 5097.
53. D.M. Grant, E.G. Paul; *J. Am. Chem. Soc.*, **1964**, *86*, 2984.
54. (a) T. Usami, S. Takayama; *Macromolecules*, **1984**, *17*, 1756.
(b) U.M. Wahner, I. Tincul, D.J. Joubert, E.R. Sadiku, F. Forlini, S. Losio, I. Tritto, M.C. Sacchi; *Macromol. Chem. Phys.*, **2003**, *204*, 1738.
(c) Y.V. Kissin, A.J. Brandolini; *Macromolecules*, **1991**, *24*, 2632.
55. G. Natta, P. Corradini; *Nuovo Cimento Suppl.*, **1960**, *15*, 40.
56. S. Bruckner, S.V. Meille; *Nature*, **1989**, *340*, 455.
57. F. Auriemma, C. De Rosa; *Macromolecules*, **2002**, *35*, 9057.
58. F. F. Auriemma, C. De Rosa, T. Boscato, P. Corradini; *Macromolecules*, **2001**, *34*, 4815.